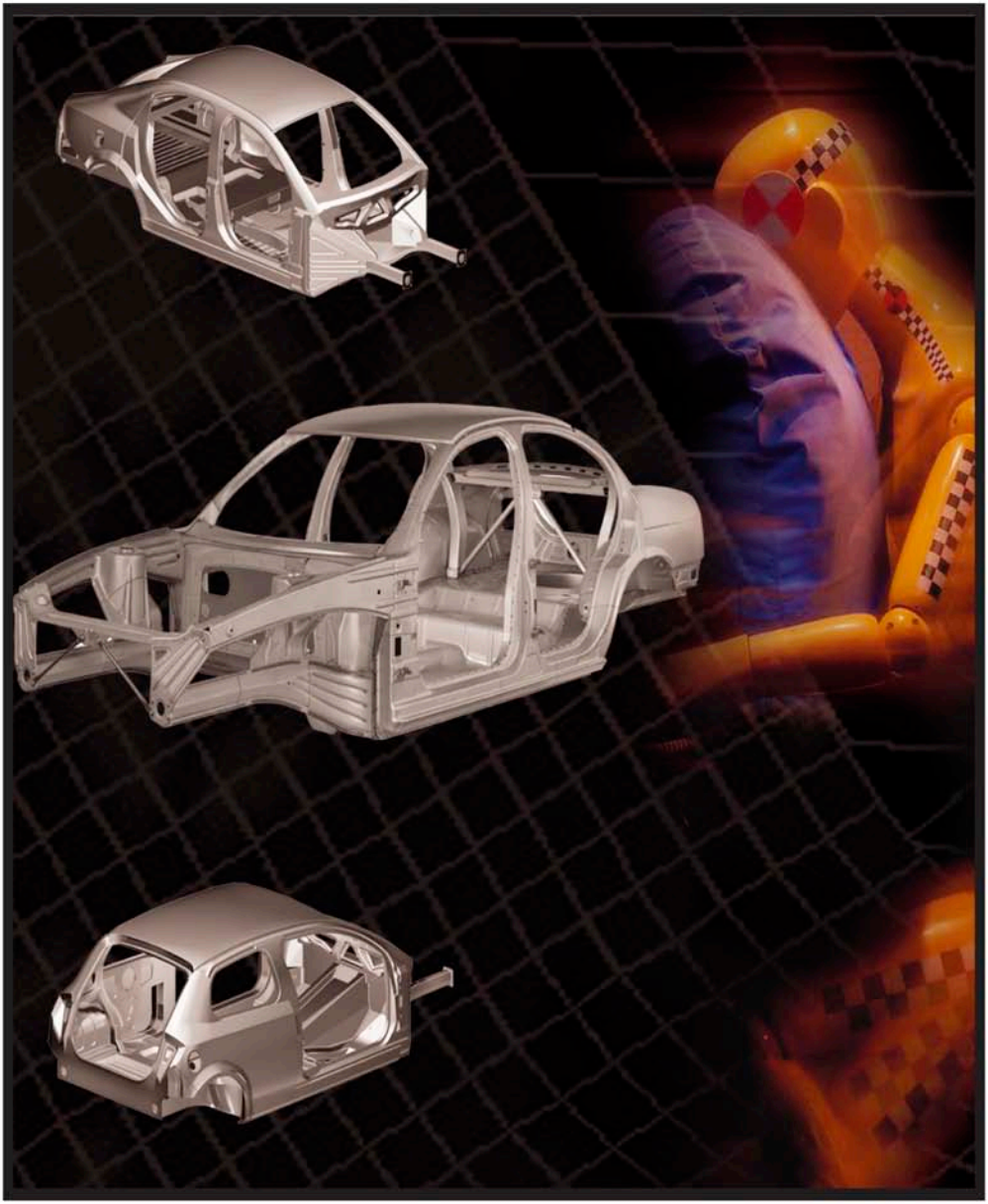

VEHICLE CRASHWORTHINESS AND OCCUPANT PROTECTION

American Iron and Steel Institute

American Iron and Steel Institute
2000 Town Center, Suite 320
Southfield, MI 48075
1-877-STEELINDUSTRY
www.autosteel.org

The New Steel

VEHICLE CRASHWORTHINESS AND OCCUPANT PROTECTION

Paul Du Bois
Clifford C. Chou
Bahig B. Fileta
Tawfik B. Khalil
Albert I. King
Hikmat F. Mahmood
Harold J. Mertz
Jac Wismans

Editors:

Priya Prasad
Jamel E. Belwafa

Sponsored by:

Automotive Applications Committee
American Iron and Steel Institute
Southfield, Michigan

Disclaimer

The opinions included in this publication are those of the individual authors and in no way represent endorsement of the Editors or American Iron and Steel Institute (AISI) Safety Panel members.

American Iron and Steel Institute
2000 Town Center
Southfield, Michigan 48075

Contents

Preface

Automotive historians will remember the 1990's as the renaissance decade of automotive safety. During that decade occupant safety established itself as a leading marketing characteristic of motor vehicles. Vehicle crashworthiness as measured in standardized crash tests is currently ranked at equal level to quality, styling, ride and handling, and fuel economy. Auto manufacturers, government agencies, insurance underwriters, and the news media provide consumers with assessments of automotive safety.

Safety features such as energy absorbing front and side structures, air bags, seats with integrated seat belts, and various crash avoidance devices are just some of the safety features offered as standard equipment on many vehicles. Future safety devices may include "smart" safety devices that would protect occupants based on age, gender, location in the vehicle, and crash severity. The focus on vehicle safety, meaning structural crashworthiness and reduction in occupant fatalities and harm, will undoubtedly continue to sharpen during the next decades in response to consumer demands, increasing government regulation and globalization of the industry.

Achieving vehicle safety involves an iterative process that starts with the definition of a design concept and ends when the vehicle is recycled. It is a cross-functional, multidisciplinary process with one objective – continuous improvement in occupant protection. It relies primarily on multidisciplinary knowledge of human factors, injury biomechanics, and structural mechanics. In the past, safety meant a relatively low vehicle deceleration pulse that was achieved by increasing the vehicle crush space, and consequently, its mass. The short front ends of today's vehicle structures are designed and built with optimized architectures to satisfy fuel economy constraints and recyclability requirements. The structure must be lightweight, yet sufficiently stiff to satisfy crashworthiness requirements in front, side, rear, and rollover crashes. In addition, designers must provide occupant restraints to mitigate the potential of injury from a second impact.

These constraints, together with the ever-shrinking design cycle time, have challenged the traditional thinking of safety engineers. As a result, established test methods that relied primarily on prototype testing to assess the vehicle safety performance are no longer competitive. Safety engineers develop and use alternative analytical tools, coupled with a minimum number of prototype tests, to assess literally hundreds of design alternatives. To assure occupant safety in the event of a crash, virtually all vehicle

manufacturers currently use analytical tools at different levels of sophistication.

Over the past three decades, safety experts have published hundreds of research papers to address structural crashworthiness, restraint systems, and injury biomechanics. However, these are not available in a single source for quick reference. The objective of this book is to provide essential design safety information in a single publication for the convenience of the safety engineer. The Chapter 1 provides an introduction to vehicle safety with definitions of basic concepts.

Chapter 2 discusses design and the evolution of body structures to achieve crashworthiness. Considerations include different architectures, crush space, section size, load path and occupant compartment design. Fundamental concepts of collapse mechanics and crash energy management at the component level are presented.

Chapter 3 continues the theme of vehicle body design technology by detailing finite element methods. The chapter provides a history of finite element modeling in crashworthiness, and outlines a brief theoretical background of the technology. Finite element applications to components, substructures, and full-scale vehicle models are provided and discussed.

Chapter 4 reviews the protection benefits provided by restraint devices such as seat belts, air bags and steering columns. The chapter reviews fundamental kinematics and laws of mechanics that can be used to determine occupant motion and associated forces and moments. Also identified are the characteristics of a well-designed restraint device, on the basis of human anatomical and injury considerations.

Chapter 5 deals with analytical methods of determining occupant motion and associated loads when the occupant is subject to a crash pulse.

Chapter 6 presents biomechanics issues of human injury from head to toe, including discussions of mechanisms and tolerance limits.

Lastly, Chapter 7 deals with current anthropomorphic test devices, or dummies, used in safety tests in the automotive industry. Safety engineers design, build and instrument these mechanical devices to mimic human response in crash conditions. The devices are routinely used to assess the effectiveness of restraint systems in occupant protection.

The American Iron and Steel Institute (AISI), Automotive Applications Committee (AAC) , sponsored the development of the text and publication of this book. Direct oversight was provided by the Committee's Safety Panel, which was populated by representatives of most North American steel companies producing automotive sheet steels.

The AISI and AAC would like to acknowledge the contributions of several people: Mike Sheh, who at the start of this project was employed by Cray Research (and who is currently a vice president of automotive industry for Engineous Software), for proposing the concept and bringing together the author team that prepared the chapters; Priya Prasad of Ford Motor Company for his valuable comments and final review; Jamel Belwafa of Ford Motor Company who performed admirably as technical consultant and final review editor; Darryl Martin, senior director of automotive applications for AISI and communications consultant Jon Harrington for their encouragement, patience, and project coordination during the period necessary to complete this effort. The Institute and Committee would also like to give a special thanks to the authors, representing some of the top safety engineers in the world, for their time and talents in skillfully writing and editing chapters.

Introduction

Tawfik B. Khalil

1.1 Motor Vehicle Safety

The first motor vehicle fatality occurred in 1889 in New York City. Arguably this event led to the birth of automotive safety as a field of study. Over the past century, occupant safety has become an important design objective among all the performance criteria of ground transportation vehicles. Manufacturers realized early on the need to demonstrate occupant protection before the public accepted the automobile as a viable means of transportation. There are three distinct periods in the development history of automotive safety.

An early period of safety from the turn of the century to 1935 was a period of genesis, growth, and development to understanding the extremely complex process of vehicle collisions. The vehicle collision is a consequence of circumstances that produce abnormal operating conditions for the vehicle. Whether the collision occurs with another vehicle or with a stationary obstacle, it subjects the vehicle structure to forces and deformations. If the forces involved exceed the energy absorbing capability of the vehicle structure, occupants may be injured or killed.

This early period focused on basic improvements such as reduction of tire blowouts to avoid loss of vehicle control; introduction of the self-starter to eliminate injuries associated with engine cranking; incorporation of headlamps to provide for night visibility, installing laminated glass to reduce facial lacerations, and adopting an all-steel body structure for better occupant protection. In addition, the first full-scale crash tests were conducted in the early 1930's. These tests involved rollover simulations and car-to-barrier impact. Statisticians estimated that the fatality rate in 1935 was approximately 17 per 100 million vehicle miles traveled.

The second period from 1936 to 1965 was an intermediate safety period. Early in this period, auto manufacturers introduced many crash avoidance devices including turn signals, dual windshield wipers, improved headlamps, a test to simulate head impact into the instrument panel, and high penetration-resistant windshield glass. In addition, General Motors conducted the first car-to-barrier frontal crash test, launching a vehicle into a retaining wall. These early tests were quite rudimentary by today standards. Neither dummies nor electronic

instrumentation were sufficiently developed for use in crash testing. Evaluation of the vehicle structural performance was based on observations of the crushed vehicle. Perhaps the most significant safety device of that era was the introduction of seat belts as an option in 1956.

The third period starts in 1966, when President Lyndon Johnson signed into law the Highway Safety Act, and authorized the creation of the National Highway Traffic Safety Administration (NHTSA). During this post-regulation period, many mandatory safety standards, known as Federal Motor Vehicle Safety Standards (FMVSS), were introduced. These standards regulate several aspects of vehicle crashworthiness and crash avoidance performance. Appendix A includes a brief description of these standards.

Interestingly, long before 1966, occupant safety and security had been an integral part of the vehicle development process. Vehicle safety improvements over the past seven decades have focused on crash avoidance technology, structural crashworthiness, and occupant protection devices. The influence of the collective vehicle safety technologies, together with improvements to highways and better driver education has contributed to an impressive drop in the rate of traffic fatalities. The fatality rate in 1996 was about 1.6 per 100 million miles traveled. This is about ten percent of the fatality rate of 1935, and approximately equivalent to one fatality per 20,000 trips between New York City and San Francisco.

In spite of continuous declines in the traffic fatality rate, the statistics of highway injuries and death remain staggering. In 1994, the National Safety Council estimated that 20 million vehicle crashes occurred on roads in the United States, resulting in 43,000 fatalities and 2.1 million injuries requiring hospitalization. From a public health perspective, motor vehicle crashes are the fourth leading cause of death after heart disease, cancer and stroke.

Today, transportation safety efforts focus on crashworthiness, crash avoidance, driver performance, and highway construction. Over the past decade automakers have added many features to help the driver avoid a crash, such as anti-lock braking systems, traction control devices and daytime running lamps. Vehicles also include many crashworthiness features such as rigid steel occupant-cells surrounded by strategically placed, energy absorbing components. In addition, vehicles are equipped with an impressive array of restraint systems such as energy-absorbing steering columns, three-point belts, front and side air bags and head restraints to reduce the risk of injury. The contents of this treatise deal only with structural crashworthiness and related injury biomechanics issues. Before introducing crashworthiness, it seems appropriate to briefly discuss the evolution of the vehicle structure and the materials used in its fabrication.

1.2 The Automobile Structure

Safety engineers design and manufacture vehicle body structures to withstand static and dynamic service loads encountered during the vehicle life cycle. Exterior shapes provide low aerodynamic drag coefficient. The interior provides adequate space to comfortably accommodate its occupants. The vehicle body together with the suspension is designed to minimize road vibrations and aerodynamic noise transfer to the occupants. In addition, the vehicle structure is designed to maintain its integrity and provide adequate protection in survivable crashes.

The automobile structure has evolved over the last ten decades to satisfy consumer needs and demands subject to many constraints, some of which may be in conflict with each other. Among these constraints are materials and energy availability, safety regulations, economics, competition, engineering technology and manufacturing capabilities. Current car body structures and light trucks include two categories: body-over-frame structure or unit-body structure. The latter designation including space-frame structures.

The body-over frame structure of a passenger car or a sport utility vehicle consists of a vehicle body, frame, and front sheet metal. A light duty truck consists of a frame, cab, and box. The vehicle body provides most of the vehicle rigidity in bending and in torsion. In addition, it provides a specifically designed occupant cell to minimize injury in the event of crash. The chassis frame supports the engine, transmission, powertrain, suspension and accessories. In frontal impact, the frame and front sheet metal absorb most of the crash energy by plastic deformation. The three structural modules are bolted together to form the vehicle structure. The vehicle body is attached to the frame by shock absorbing body mounts, designed to isolate from high frequency vibrations. Figure 1.2.1 is a photograph showing a typical vehicle with this type of structure.

Unit-body structures, shown in Figure 1.2.2, comprise most passenger cars introduced in the U.S. since the early 1980's. These vehicles combine the body, frame, and front sheet metal into a single unit constructed from stamped sheet metal and assembled by spot welding or other fastening methods. The construction of the unit body structure, also known as unit-frame-and-body or frame-less body, is claimed to enhance whole vehicle rigidity and provide for weight reduction.

Fig. 1.2.1 **Typical body-on-frame vehicle**

1.3 Materials

Steel, the material typically used in vehicle structures, allowed for the economic mass production of millions of units over the past seven decades. Basic requirements for body structure materials include good formability, corrosion resistance, and recyclability. Body materials should also posses sufficient strength and controlled deformations under load to absorb crash energy, yet maintain sufficient survivable space for adequate occupant protection should a crash occur. Further, the structure should be lightweight to reduce fuel consumption. The majority of mass-produced vehicle bodies over the last six decades were manufactured from stamped steel components. Manufacturers build only a few limited production and specialty vehicle bodies from composite materials or aluminum.

Although a patent for an all-steel body was granted in 1900, until the 1920's, automakers built vehicle bodies from a composite of wood panels joined with steel brackets. Steel sheets were added over the panels to provide a better surface to hold the paint. As metallurgists improved the formability of sheet steel and toolmakers built durable dies capable of stamping millions of parts and spot weld technology allowed for joining large body shells, the all-steel vehicle body became a reality. Dodge built an all-steel vehicle body in 1924.

1.4 Crashworthiness

First used in the aerospace industry in the early 1950's, the term "crashworthiness" provided a measure of the ability of a structure and any of its components to

Fig. 1.2.2 **Body-In-White image of a typical unibody construction**

protect the occupants in survivable crashes. Similarly, in the automotive industry, crashworthiness connotes a measure of the vehicle's structural ability to plastically deform and yet maintain a sufficient survival space for its occupants in crashes involving reasonable deceleration loads. Restraint systems and occupant packaging can provide additional protection to reduce severe injuries and fatalities. Crashworthiness evaluation is ascertained by a combination of tests and analytical methods.

1.5 Crashworthiness Goals

Vehicle crashworthiness and occupant safety remain among the most important and challenging design considerations in the automotive industry. Early in the history of vehicle structural developments, vehicle bodies were manufactured from wood, and the goal of crashworthiness was to avoid vehicle deformations as much as possible. Over the years, the body structures evolved to include progressive crush zones to absorb part of the crash kinetic energy by plastic deformations. At present, vehicle bodies are manufactured primarily of stamped

steel panels and assembled using various fastening techniques. Designers create vehicles to provide occupant protection by maintaining integrity of the passenger compartment and by simultaneously controlling the crash deceleration pulse to fall below the upper limit of human tolerance. A crash deceleration pulse with an early peak in time and a gradual decay is more beneficial for protection of a restrained occupant. Therefore, the goal of crashworthiness is an optimized vehicle structure that can absorb the crash energy by controlled vehicle deformations while maintaining adequate space so that the residual crash energy can be managed by the restraint systems to minimize crash loads transfer to the vehicle occupants.

Real world vehicle collisions are unique dynamic events where the vehicle may collide with another vehicle of similar or different shape, stiffness and mass; or it may collide with another stationary object such as a tree, utility pole or bridge abutment. Generally, for the purpose of body development, safety experts classify vehicle collisions as frontal, side, rear or rollover crashes. Further, the vehicle may experience a single impact or multiple impacts. Moreover, vehicle crashes occur over a wide range of speeds, persisting for a fraction of a second, such as when a vehicle hits a tree, or for few seconds as in rollover events. These factors illustrate some of the complex tasks involved in the design of vehicle structures to satisfy crashworthiness constraints for all collision scenarios.

Accident reconstruction and analysis of motor vehicle crashes provide important information regarding the safety performance of vehicle in the traffic environment. These methods do not provide sufficient quantitative information necessary for vehicle design, such as deceleration pulse, occupant kinematics or occupant loads. So, design engineers rely on a combination of standard laboratory tests, proving ground evaluations, and analysis to achieve safety objectives. Currently vehicle crashworthiness is evaluated in four distinct modes: frontal, side, rear and rollover crashes.

1.6 Crashworthiness Requirements

The vehicle structure should be sufficiently stiff in bending and torsion for proper ride and handling. It should minimize high frequency fore-aft vibrations that give rise to harshness. In addition, the structure should yield a deceleration pulse that satisfies the following requirements for a range of occupant sizes, ages, and crash speeds for both genders:

- Deformable, yet stiff, front structure with crumple zones to absorb the crash kinetic energy resulting from frontal collisions by plastic deformation and prevent intrusion into the occupant compartment, especially in case of offset crashes and collisions with narrow objects such as trees. Short vehicle front ends, driven by styling considerations, present a challenging task to the crash-

worthiness engineer.

- Deformable rear structure to maintain integrity of the rear passenger compartment and protect the fuel tank.
- Properly designed side structures and doors to minimize intrusion in side impact and prevent doors from opening due to crash loads.
- Strong roof structure for rollover protection.
- Properly designed restraint systems that work in harmony with the vehicle structure to provide the occupant with optimal ride down and protection in different interior spaces and trims.
- Accommodate various chassis designs for different power train locations and drive configurations.

1.7 Achieving Crashworthiness

The task of the structural crashworthiness engineer is indeed unique when compared with that of the traditional structural analyst. Designers typically engineer structures using elastic analysis to withstand service loads without yielding or collapsing. Automotive structures, however, must meet all previously mentioned service load requirement, plus it must deform plastically in a short period of time (milliseconds) to absorb the crash energy in a controllable manner. It must be light, and able to be economically mass-produced. Further, the structural stiffness must be tuned for ride and handling, NVH and must be compatible with other vehicles on the road, so it is not too soft or too aggressive.

In addition, the automotive safety engineer is responsible for packaging the occupants, so whatever decelerations transmitted to the occupants are manageable by the interior restraints to fall within the range of human tolerance. The ultimate goal of the safety engineer is to reduce occupant harm. Typically, designers accomplish this goal using a combination of crash avoidance and crashworthiness measures. Crash avoidance tools are beyond the scope of this treatise, and therefore this book will focus on crashworthiness tools and related biomechanics issues only.

During the early years of automotive evolution, structural design relied primarily on extensive testing and experience. Available analytical tools were limited to strength of material calculations for idealized components. Engineers could not assess the overall vehicle crashworthiness until a vehicle prototype was built and tested. The earliest crashworthiness evaluations were rollover tests conducted in the 1930's. In 1934, General Motors Corporation initiated vehicle frontal crash testing by launching a vehicle into a rigid barrier.

In recent years, however, the demands on vehicle design have increased enor-

mously to satisfy safety regulations, fuel economy, cost of manufacturing and reduction in design cycle time. These requirements have provided an impetus for the development of mathematical tools for crashworthiness evaluations that go beyond simple strength of materials calculations. Currently, a combination of robust analytical tools is routinely used in crashworthiness evaluations. These vary from simple lumped-parameter models with few degrees of freedom to detailed finite element models with millions of degrees of freedom. Chapters 2 and 3 discuss the various analytical tools currently used in vehicle structural design evaluations. The following section is a brief discussion of test methods used in crashworthiness assessment.

1.8 CrashworthinessTests

In spite of the tremendous progress achieved in crashworthiness simulations of vehicle structures from components to full-scale vehicles, using the latest techniques in computational mechanics and super computers, final crashworthiness assessment still relies on laboratory tests. This is especially true in vehicle certification.

There are three categories of tests: component tests, sled tests, and full-scale barrier impacts. The complexity of the test and associated variables increase from component to full-scale tests. This may cause a decline in test repeatability – a reality that may not be realized from the mathematical models. The component test determines the dynamic and/or quasi-static response to loading of an isolated component. These component tests are crucial in identifying the crush mode and energy absorption capacity. Understanding their performance is also essential to the development of prototype substructures and mathematical models.

In a sled test, engineers use a vehicle buck representing the passenger compartment with all or some of its interior components such as the seat, instrument panel, steering system, seat belts, and air bags. Mechanical surrogates of humans (anthropomorphic test devices - “dummies”) or cadaver subjects are seated in the buck to simulate a driver and/or passenger and subjected to dynamic loads, similar to a vehicle deceleration-time pulse, to evaluate the occupant response in a frontal impact or side impact. The primary objective of a sled test is evaluation of the restraints. This is accomplished by high-speed photography of the dummy kinematics. In addition, various sensors located in the dummy and on the restraints monitor the forces and moments to help determine the impact severity and the effectiveness of the restraint system in reducing loads transferred to the occupant.

The typical full-scale barrier test involves collision of a guided vehicle, propelled

into a barrier at a predetermined initial velocity and angle. Typically, a barrier test uses a complete vehicle. To evaluate individual substructures, a sled test can be equally effective, especially in evaluation of the restraint systems.

Safety engineers run this barrier test to ensure vehicle structural integrity and compliance with government-mandated regulations, for example, United States Federal Motors Vehicle Safety Standard (FMVSS) 208. A fully instrumented vehicle with numerous load cells, accelerometers and instrumented dummy (or dummies) in the driver (and passenger) seat(s) impacts a rigid barrier at zero degrees, plus 30 degrees, and minus 30 degrees, respectively, from an initial velocity of 13.4 m/s (30 mph). The barrier face is instrumented with several load cells to monitor the impact force-time history. For compliance with FMVSS 208, the unrestrained dummies in the driver and right front passenger must score injury assessment values below those established for human injury thresholds for the head, chest, and legs.

In addition, the dummy performance is assessed at a higher impact speed of 35 miles per hour (mph). in what is known as the NCAP (New Car Assessment Program) test. Typically in the NCAP test, the dummy is restrained by three-point lap/shoulder belt system, in addition to the supplemental restraint air bag. Vehicle impact into a rigid barrier provides a method to assess the effectiveness of the restraint system, as it typically subjects the structure to high deceleration loads.

Another type of testing has emerged over the past few years to evaluate the structural integrity of the vehicle when subjected to frontal offset impact with 40 to 50 percent overlap. The impact target may be rigid or deformable. In this type of test the vehicle front structure is subject to more deformations and potential intrusion and relatively less severe deceleration.

Safety experts conduct similar full-scale tests for side impact, launching a deformable barrier of a particular mass and stiffness into the left or right side of the vehicle from some initial speed and crabbed at a certain angle (FMVSS 214). In this test, side impact dummies (“SID” For the US and “EURO SID1” for Europe) are used in the driver and outboard rear seat locations.

In addition, full-scale tests are conducted on the vehicle rear structure, either by a deformable barrier or by a bullet car to assess the integrity of the fuel tank. To evaluate roof strength according to FMVSS 216, engineers apply a quasi-static load on the “greenhouse,” and ensuring that the roof deformation falls below a certain level for the applied load.

Testing is both time consuming and expensive, particularly at the early stages in

vehicle development, where only prototypes are available. To ensure the crashworthiness and compliance with U.S. and international regulations of a vehicle platform, the manufacturer may test more than 100 prototype vehicles, with each early prototype costing between $400,000 - $750,000. For decades, design engineers have expressed the need to simulate the crash event using mathematical models. Accurate and robust analytical tools using state-of-the-art in computational mechanics and computer hardware are indispensable for crash simulations.

To meet ever-increasing safety demands, especially those associated with air bags, vehicle design has evolved into a complementary mix of testing and mathematical modeling. The expected performance and the design stage determine the type of test and level of test complexity. Whether assessing crashworthiness by a test, by a computer simulation, or by a combination of both, the ultimate objective is to determine the potential for human injury due to exposure to real world crash conditions. Unfortunately, each real world crash is a unique event, and therefore attempting to duplicate all real world crash conditions is a formidable task that is both time-consuming and expensive. Accordingly, engineers use selective laboratory crash modes that appear to be most relevant to reducing injuries and saving human lives.

1.9 Crashworthiness Models Requirements

The models should satisfy at a minimum the following overall requirements:

- Accuracy – the model should be able to yield reasonably accurate predictions of the essential features being sought
- Speed – the model should be executable with a reasonable turnaround time, not to exceed 12 hours regardless of its size, to allow for iterations and parameter studies
- Robustness – small variations in model parameters should not yield large model responses
- Development time – the model could be built in a reasonably short period of time, not to exceed two weeks

Design of Vehicle Structures for Crash Energy Management

Hikmat F. Mahmood and Bahig B. Fileta

2.1 Introduction

Historically, styling and packaging considerations drove the design of vehicle body structures. The final design was the product of a long evolution guided primarily by testing, supported by simple linear strength of material methods. With the advances in computer hardware and software, several analytical design capabilities evolved, providing engineers with a variety of tools to design modern vehicle structures that can meet the growing customer demands for better crashworthiness performance, quieter ride and reliability. These tools include simple spring-mass models, beam element models, hybrid models and finite element models. Although these tools vary in complexity, each is based on structural mechanics principles that require conservation of mass, momentum and energy. The selection of a particular analysis tool depends on the task at hand and on the particular design phase. For example, a simple beam model may be more appropriate at concept initiation to determine section geometry, size and thickness, whereas a full-scale finite element analysis of the vehicle may be more suitable when a prototype is built. Correspondingly, the time required to develop a model and the amount of information provided vary by model complexity.

In recent years, the auto industry has experienced the greatest demand from customers, regulators, and the media to provide safer vehicles. This translates into better crashworthiness of the vehicle structure and effective restraint systems. Examples are: Federal Motor Vehicle Safety Standard (FMVSS) , New Car Assessment Program (NCAP) test, Insurance Institute for Highway Safety (IIHS) tests, compatibility testing, and testing to insure protection of children and small adult occupants. In other words, a broader view of vehicles' crashworthiness is now needed.

In addition, competition in the industry to build products of high quality within short design cycles is driving the use of analytical tools and replacing testing except when absolutely necessary. This dramatic change in vehicle structural design, especially in vehicle crash, signals the need for design tools that are effective in analyzing the crash phenomena. Understanding the effect of the

collapsing structure on the vehicle's deceleration-time history, and learning about the interaction between the occupants and the vehicle during crash are examples of the needed knowledge. Efficient methods and tools are necessary to enable initiation of a sound design at the early concept phases of development.

In this chapter, methods and tools for designing structures for crashworthiness are described with emphasis on frontal crashes. The reason for emphasis on designing for frontal crashes is that these are considered to be responsible for more traffic fatalities and injuries than any other crash mode. In Section 2.2 – Current Design Practice, the current modeling and design processes are reviewed while identifying the shortcomings for early design stages. In Section 2.3 – Crash/Crush Design Techniques for Front Structures, techniques are examined for analyzing the front-end system and computing the performance design objectives of subsystems and components. Section 2.4 – Analytical Design Tools, introduces component design methods that enable the designer to create structural concepts for energy absorption and strength. Section 2.5 – Vehicle Front Structure Design for Different Impact Modes, discusses strategy for designing structures for different frontal impact modes, including vehicle-to-vehicle crashes.

2.2 Current Design Practice

The primary aim of the crashworthiness design process is to secure dummy response results that measure below or at acceptable injury risk values. The crash pulse, typically generated from a frontal crash of the vehicle into a rigid barrier, is the essential feature in the design process. It is used as input to occupant models. Currently, the design process relies on calculating the crash pulse from either Lumped Mass-Spring (LMS) models or Finite Element (FE) models. Figures 2.2.1 and 2.2.2 provide a schematic description of the two processes. LMS models were introduced in the early 1970's, and relied on static crush tests to establish the spring stiffness. Nonlinear FE models were introduced in the mid-1980's and rapidly gained acceptance among structural analysts. This acceptance was fueled by continually increasing computer capabilities such as speed, memory, storage space, graphics, and numerical structural mechanics techniques. Other factors, such as detailed design of components layout and surfaces, facilitated the development of vehicle models by shell finite elements since most of the geometry of the structural surfaces was already on computer graphic files. In addition to the advancement in computer technology, many enhancements have been made to the dynamic crash analysis computer codes. These include efficient computation for speed as well as user-friendly software for preparing input data

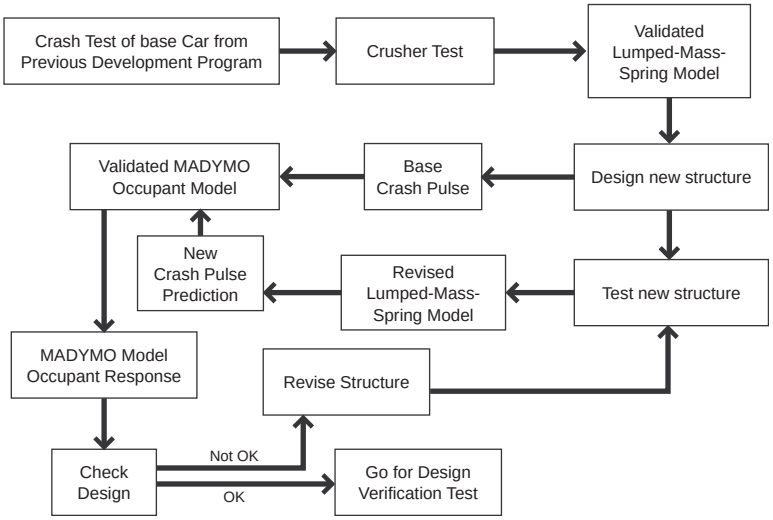

Fig. 2.2.1 **Current process of vehicle structure design for crash: lumped mass-spring modeling**

and processing the analysis results. These enhancements increased the popularity of using finite element codes for the analysis and design of vehicle structures for crash. In fact, the use of the finite element method becomes even more appealing when changes from the base vehicle design to the new vehicle design are small. In this case, validated finite element models as well as tuned occupant simulation models are usually available. More details on FE analysis of vehicle crashworthiness and occupant simulation models are presented in other chapters.

2.2.1 Comparison Between LMS and FE-Based Crashworthiness Processes

Examination of the two design processes for vehicle front-end crash, depicted in Figures 2.2.1 and 2.2.2, reveals ideas with some similarities and differences.

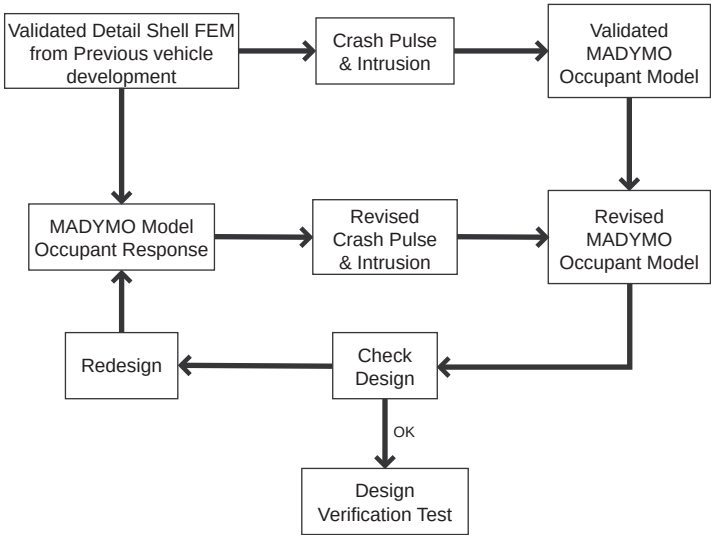

Fig. 2.2.2 **Current process of vehicle structure design for crash: detailed FE modeling**

In both processes, designing vehicle front-end structures for crash performance is divided into two primary tasks. The first includes the vehicle body structure and major components packaged ahead of the front occupants, such as the powertrain, while the second deals with designing the occupant environment such as the dummy, restraints, and vehicle interior surfaces. Modeling the vehicle front-end structure and major components and masses simulates the way these parts crush and move during impact with a barrier. The output of the vehicle crash (impact) simulation is the deceleration-time history at the rocker near the B-pillar. Meanwhile, modeling the front dummy and its environment uses the vehicle deceleration-time history (referred to here as crash pulse), that is predicted, measured, or assumed as input. The simulation output is the dummy's response that is compared with a given injury criteria. Thus, the interface that links the events of the two models is a common crash pulse. In some cases, the additional interface parameter, of deformation in the foot well area (intrusion), is used. The two subsystems and common interface are shown schematically on Figure 2.2.1.1.

In addition to the generic split of the front-end system, both processes use an occupant simulation computer code for predicting the dummy response during

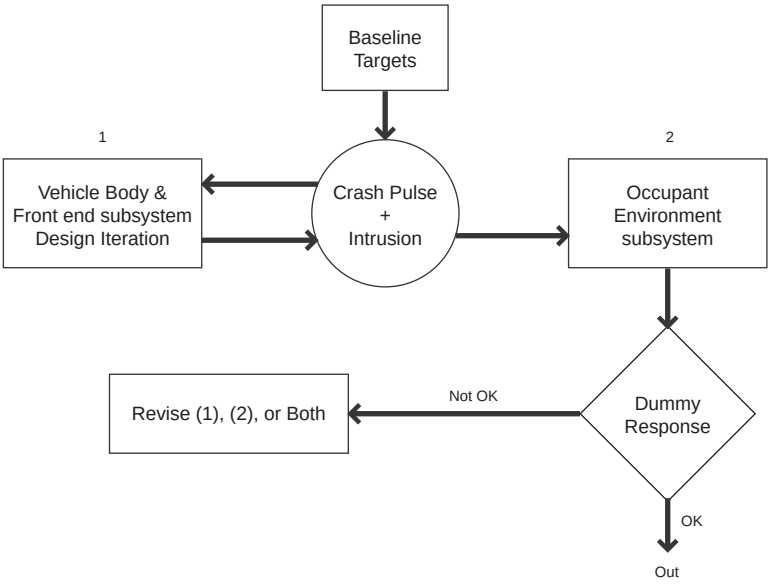

Fig. 2.2.1.1 **Structural and dummy modeling: parallel analysis**

vehicle impact such as MADYMO. However, for modeling the vehicle's front-end structure, detailed FE analysis that relies solely on geometry and material properties is used. LMS models rely on few discrete masses and springs whose properties are generated from crush tests

Both processes require a vehicle crash test to validate the simulation prior to using the results with confidence.

The tools used to simulate the vehicle impact and predict its response in both processes are extreme in two areas. FE analysis requires a complete and detailed description of the components' geometry and associated material properties. This information is readily available after "freezing" the design status, and solutions for potential problems are limited to minor modifications. By contrast, LMS analysis uses simple simulation models that synthesize the design and determine the functions of the structural parts through an experimental procedure.

Furthermore, the quality of the LMS model data and the simulation results are highly dependent on the experience of the crash engineer.

In addition to structural analysis by FE and LMS methods, other techniques based on deformable beam elements have been used. These methods are reviewed in later sections. For more information on MADYMO modeling of dummy response and finite element modeling of vehicle structures, the reader is referred to specific treatises on these subjects offered in this book.

2.2.2 Lumped Mass-Spring Models

In 1970, Kamal [1] developed a relatively simple, but powerful model for simulating the crashworthiness response of a vehicle in frontal impact. This model, known as the Lumped Mass-Spring (LMS) model, became widely used by crash engineers because of its simplicity and relative accuracy. This model is shown in Figure 2.2.2.1. The vehicle is approximated by a one-dimensional lumped mass-spring system, an over simplification that is quite acceptable for modeling the basic crash features in frontal impact. Because of its simplistic representation of the crash event, an LMS model requires a user with extensive knowledge and understanding of structural crashworthiness, and considerable experience in deriving the model parameters and translating the output into design data. The crush characteristics (spring parameters) were determined experimentally in a static crusher, as shown in Figure 2.2.2.2.

Several versions of the LMS models have been successfully used in simulations of front, side and rear impact vehicle crashes [2-4]. Figures 2.2.2.3 through 2.2.2.6, taken from [2], show one such model and demonstrate the simulation capabilities and some of its limitations. Figure 2.2.2.3 shows an LMS simulation model of a vehicle impacting a fixed barrier at 35 mph. The configuration of the model is arrived at from the study of an actual barrier test, which identifies pertinent masses and "springs" and their mode of collapse. The model is "tuned" by adjusting the load-deflection characteristics of the "springs" to achieve the best agreement with test results in the timing of the crash events. Figure 2.2.2.4 compares the simulated acceleration histories with those obtained from the test, and it shows that very good agreement can be achieved.

LMS models proved to be very useful in developing vehicle structures for crash, enabling the designer to develop generically similar crash energy management systems, that is, development of vehicle derivatives or structural upgrading for crash. Also, LMS models provide an easy method to study vehicle/powertrain kinematics, and give directional guidance to the designer by establishing component objectives.

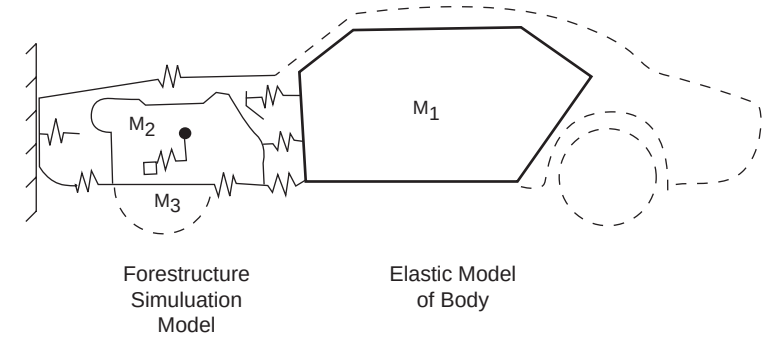

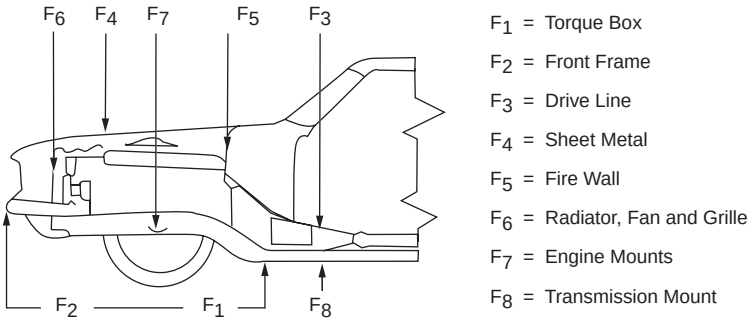

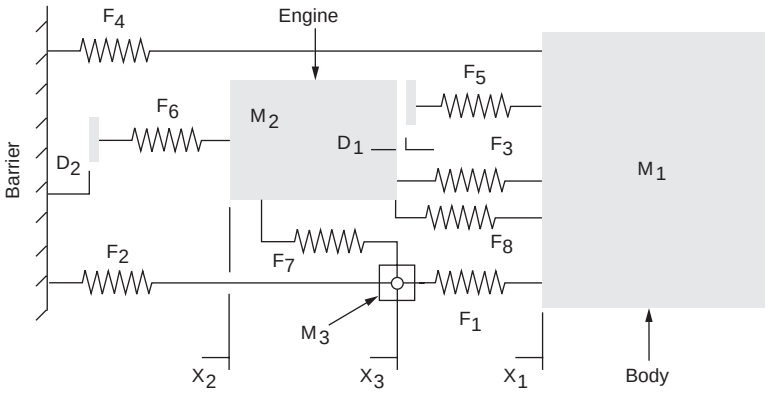

Fig. 2.2.2.1 **Kamal's model [1]**

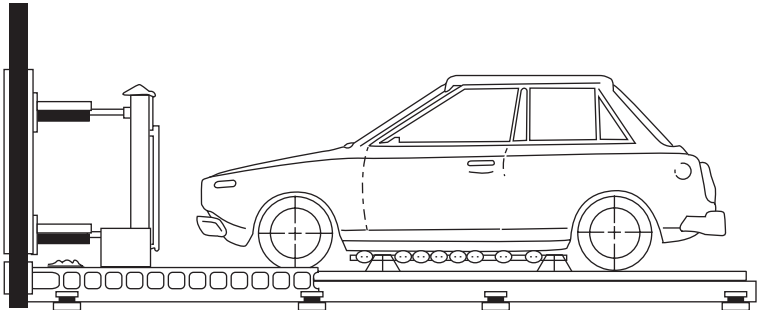

Fig. 2.2.2.2 **Static crush setup**

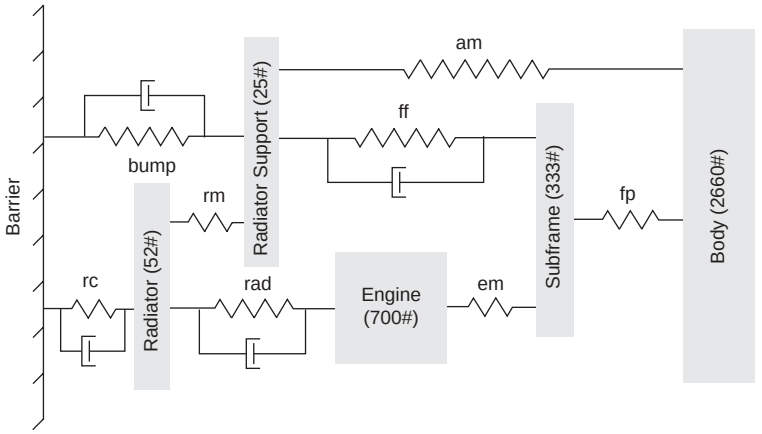

Fig. 2.2.2.3 **1-D LMS frontal barrier impact simulation**

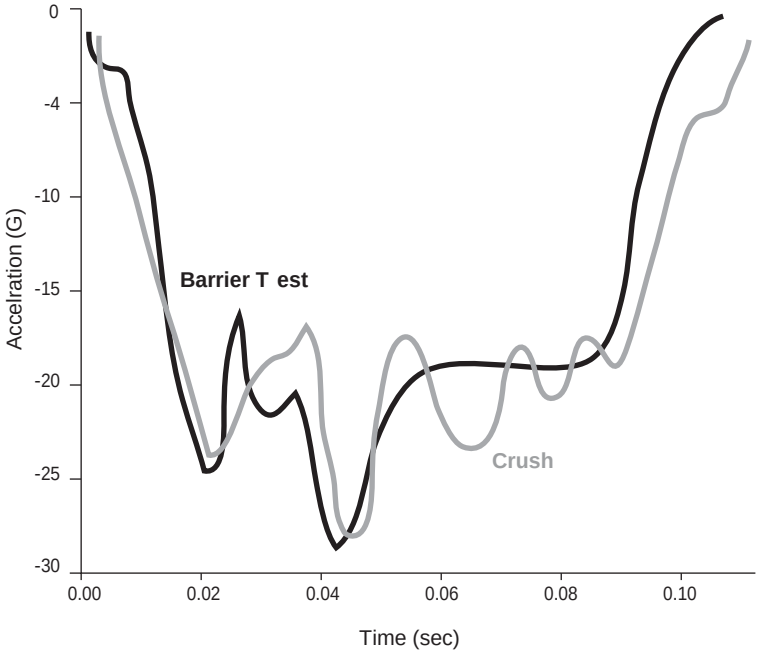

Fig. 2.2.2.4 **Crush simulation of acceleration histories in frontal barrier impact [2]**

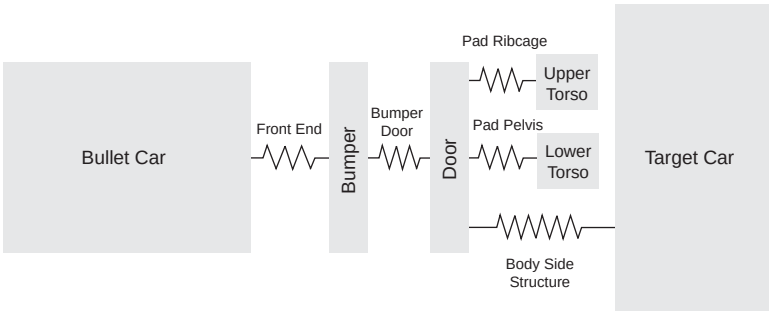

Fig. 2.2.2.5 **LMS model: vehicle-to-vehicle side impact [3]**

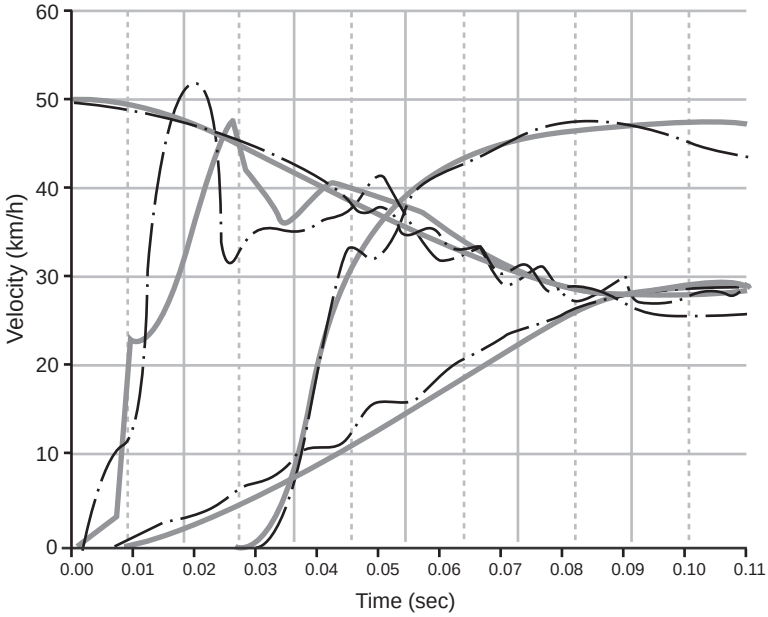

Fig. 2.2.2.6 **LMS side impact simulation of velocity histories [3]**

An LMS model schematic for a bullet vehicle impacting a target vehicle 's side at 50 km/h is depicted in Figure 2.2.2.5. Although these modeling techniques have shortcomings as design aids, each has a good theoretical basis, and with further development in modeling of crash events, they should be able to guide future designs. As mentioned in Section 2.2.2 – Lumped Mass-Spring Models, the usefulness and effectiveness of these models in guiding structural design of the vehicle to meet the stringent requirements of crash energy management depend upon the skill, experience and extent of knowledge and understanding of crash/ crush mechanics on the part of the user.

2.2.3 Limitations of LMS Models

In skilled hands, the "simple" model, shown in Figure 2.2.2.1, can be an effective design aid in modifying a vehicle for improved crash performance or guiding the design at early conceptual stages. Because of the simplicity of the model and the fast turnaround time, parametric studies, normally conducted in the early stages

of design, can be conveniently executed and preliminary design parameters established. It is important to note that there is a drawback to the LMS model as a design aid in new structural concepts. It requires prior knowledge of spring characteristics. This must be determined experimentally, obtained from existing data, or calculated from FE models or any equivalent procedure.

In addition the LMS model is 1-D. With the current trends towards lighter vehicles, shorter overhangs and a more efficient utilization of space, new concepts for managing crash energy more efficiently to achieve desired crash performance, weight and cost objectives are being explored. Thus, the ability to predict in the early design stages the kinematics of the vehicle and its major components and the effects of kinematics on occupant behavior increases in importance. The one-dimensional model is no longer sufficient, and more advanced two- and three-dimensional models are needed to guide the structural designs during development to meet the vehicle crash performance objectives.

To overcome some of these limitations, finite element modeling of deformable components can be substituted for testing to provide the spring characteristics. The one-dimensional LMS model, shown in Figure 2.2.3.1 taken from [5], is an example where the authors used finite element models to extract the spring properties. The comparison between the test and final simulation results is given in Figure 2.2.3.2. The reference, however, does not describe how the finite element

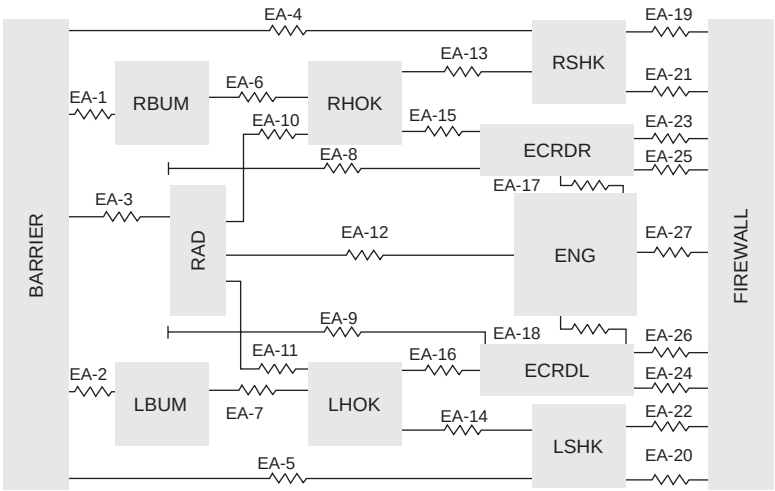

Fig. 2.2.3.1 **Lumped parameter model for zero degree frontal simulation [5]**

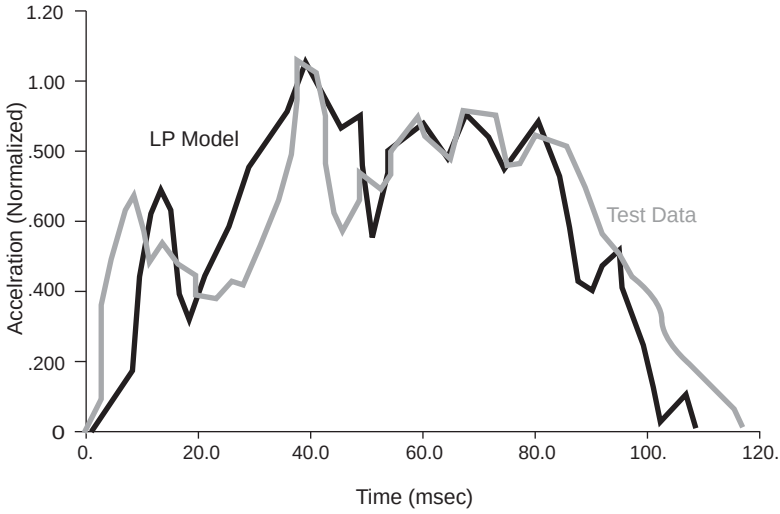

Fig. 2.2.3.2 **Comparison of deceleration pulse of test and simulation results**

method was used to extract the spring properties. The authors used the same technique to create 1D-LMS for offset deformable barrier impact case. This appears to be quite an extension beyond the capabilities of the 1-D model.

The idea to obtain load-deflection data of components and substructures has been shown successfully in [6]. Figure 2.2.3.3 shows a detailed shell finite element modeling of a substructure consisting of front rails and a power train. The crushed substructure is shown on Figure 2.2.3.4, which according to the authors, compares very well with the collapse of the rails in the full vehicle analysis model. The paper also shows the correlation between the substructure test results and the simulation (Figure 2.2.3.5).

As for the limitation of 1-D simulation of LMS models, some researchers, [7,8], modeled the vehicle front-end structure in three-dimensional space as a frame using the MADYMO simulation computer program. The model uses the typical rigid body dynamics library of springs, masses, and rigid bodies. Again, finite element modeling was used to compute the spring properties needed for the frame model. The model also includes the power train external surfaces to accurately capture contact with the barrier. The authors of [7] show reasonable

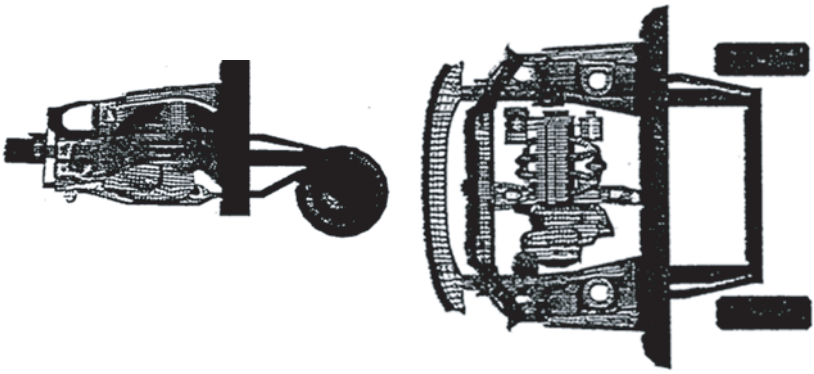

Fig. 2.2.3.3 **Suggested model of substructure vehicle**

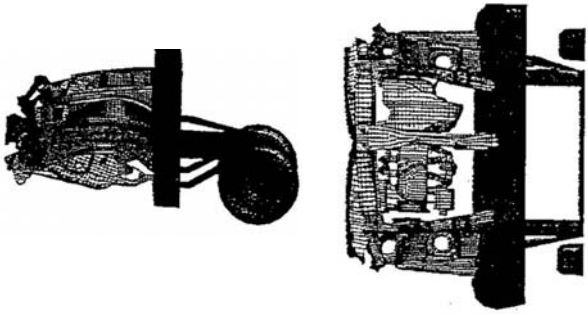

Fig. 2.2.3.4 **Deformed shape of engine room of substructure model BASE @80 msec**

correlation between results from the simplified 3-D frame and the full scale FE model (Figures 2.2.3.6 and 2.2.3.7). Furthermore, collapse mode of the frame appears to be similar to that found by the full scale FE model (Figure 2.2.3.8). Additional results are also computed by this modeling approach. Not easily computed in 1-D modeling, are the dash-panel intrusions as shown on Figure

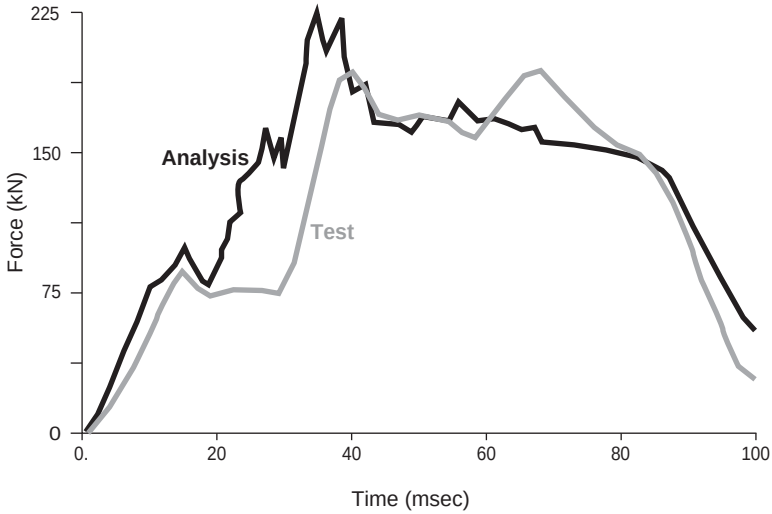

Fig. 2.2.3.5 **Force-time curve of test and analysis**

Fig. 2.2.3.6 **3-D space frame model for MADYMO [7]**

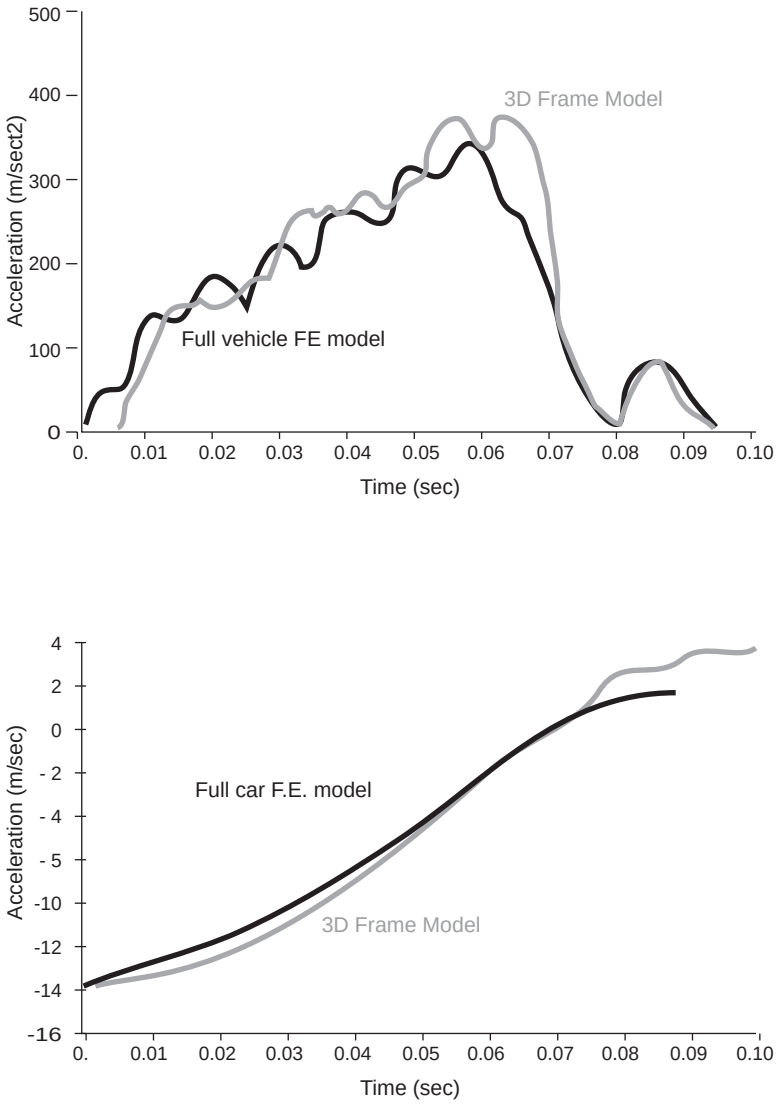

Fig. 2.2.3.7 **Results comparison: 3-D frame and full car FE model [7]**

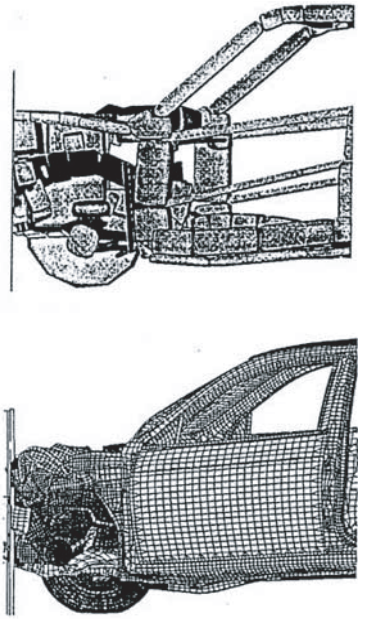

Fig. 2.2.3.8 **Comparison: collapse mode predictions for 3-D frame and full car FE model [7]**

2.2.3.9. The 3-D modeling of the vehicle front end was extended [1] to simulate other frontal impact modes such as offset impact with deformable barrier and car-to-car impact (Figures 2.2.3.10 and 2.2.3.11).

2.3 Crash/Crush Design Techniques for Front Structures

Designing for crash energy management, like any other design process that deals with many diverse systems of a vehicle, is a multidisciplinary process involving very close interaction of many diverse engineering disciplines such as biomechanics, structures, vehicle dynamics, packaging, engineering analysis and manufacturing. To meet the intended performance and cost objectives effectively, design for crash must be closely integrated with all other aspects of vehicle design. This requires an improved quantitative design process with the capability of predicting the various functions a system or a component is designed to perform.

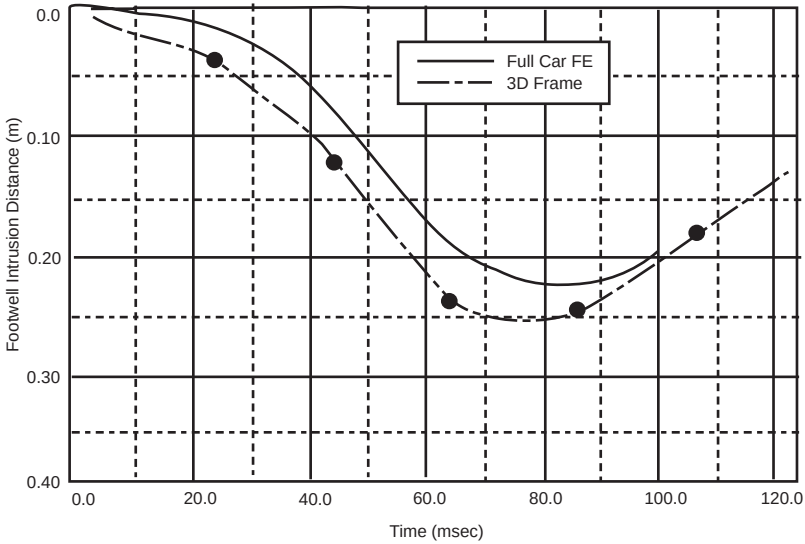

Fig. 2.2.3.9 **Comparison: footwell intrusion time history for finite and frame model in AMS [7]**

Fig. 2.2.3.10 **Frontal offset 40 mph [8]**

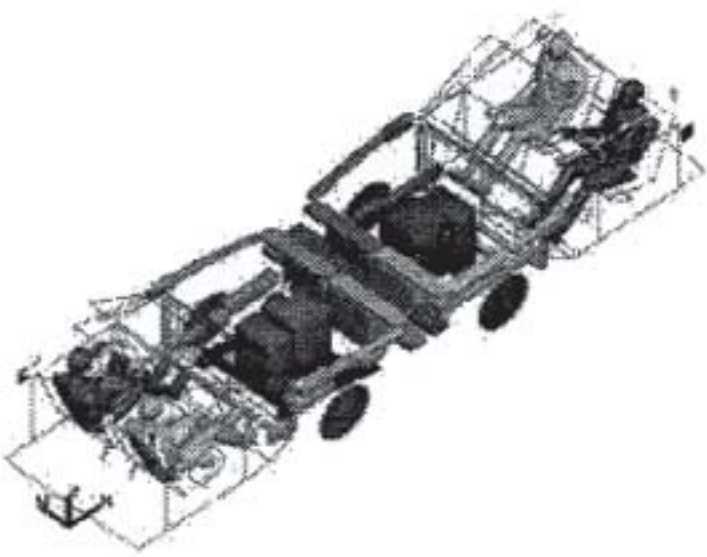

Fig. 2.2.3.1.1 **Full frontal car-to-car 70 mph [8]**

Therefore, to facilitate rational design decisions early in a vehicle's development program, without the very expensive and time-consuming modeling and possible testing, some of the basic principles of designing for crash energy management will be outlined. Existing techniques and new developments in analytical design aids for crash energy management are reviewed, and the way these are integrated into a comprehensive, yet practical design methodology are covered.

2.3.1 Some Basic Principles of Designing for Crash Energy Management

After many years of designing for frontal rigid barrier impact, most safety or crash engineers have come to agree on some basic features that should be included in the design in order to have a crashworthy vehicle.

2.3.1.1 Desired Dummy Performance

Crash energy management means controlling, by design, the dynamic behavior of multiple systems in a very violent and complex environment of a collision. To achieve this control over crash behavior, without sacrificing rigorous performance and cost objectives, requires a very close interdisciplinary interaction. The design process of crash energy management must, for obvious reasons, begin with the biomechanical considerations involving the interaction of the occupants with their restraint systems in response to a dynamic crash pulse generated in the vehicle by impact.

Various occupant simulation models are used to study interactions between dummy, restraint system and the vehicle. As a result, a family of crash pulses or signatures that successfully meet specific injury criteria are easily defined. These pulses, in turn, define objective criteria for vehicle design. Using spring-mass models, or any other simplified system modeling; these criteria are translated into discrete spring and mass elements to whatever degree of complexity the designer or analyst chooses. The logical choice would be to start with the simplest models and progressively increase their complexity as the design evolves.

Since design for crash energy management requires a system approach, several models would be constructed in parallel to investigate synergy, if any, between the major modes of frontal collisions, namely: 31 mph frontal, 35 mph frontal, and 40 mph offset frontal impacts. At this stage, the desired crush sequence and mode will need to be selected and crush zones identified to assure that the structural pulse parameter can be realized, that is, the force amplitude and the maximum crush distance, as determined in occupant model studies. Also, at this stage in the design process, parametric studies are conducted in conjunction with other parallel design studies, such as packaging and vehicle dynamics to explore various design alternatives.

2.3.1.2 Stiff cage Structural Concept

Designing crashworthy vehicles means providing protection for the occupants in all modes of survivable collisions. A fundamental concept that helps in achieving this objective is to design a stiff passenger compartment structure. This structure would have a peak load capacity to support the energy absorbing members in front of it, without exhibiting excessive deformation. The compartment structure should also be an efficient energy absorbing structure that limits the compartment deceleration and the intrusion during crash.

For front (and rear) structures, the mode of deformation and its efficiency will depend on the particular design configuration. The high crush loads, generated while crushing the energy-absorbing structures which decelerate the occupant

compartment, are transferred to it by way of the structural interface between the energy absorbing and compartment structures. The manner in which this is accomplished will dictate how well the compartment withstands these extreme loads and the severity of its deformation. This idea of having the passenger compartment structure central to the design is shown schematically in Figure 2.3.1.2.1.

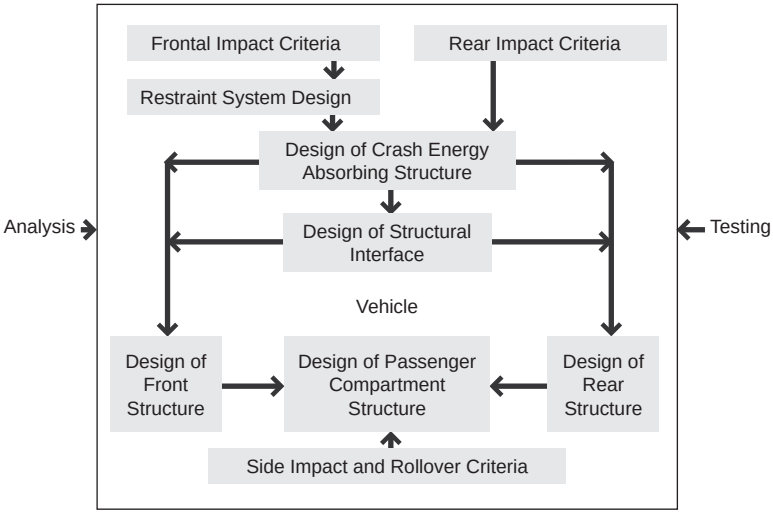

Fig. 2.3.1.2.1 **Design elements for crash energy management**

2.3.1.3 Controlled Progressive Crush or Deformation With Limited Intrusion

Current front, rear, roof, and side impact energy-absorbing structures deform upon direct impact in a mixed axial and bending mode, with bending being the dominant mode of collapse because of its lower energy content. Therefore, bending is considerably less efficient than the axial mode, and consequently will result in much heavier designs. In designs where light weight is desirable, axial mode will be a more appropriate candidate for energy absorption, provided the question of stability of the crush process can be resolved within given packaging constraints. The axial mode will be shown in the subsequent sections to be the most efficient of all structural collapse modes. When successfully executed, the primary crush zone will be characterized by a relatively uniform, progressive structural collapse.

The secondary crush zone involves the structural interface between the energy absorbing and occupant compartment structures. This structural interface must provide a stable platform for the progressively collapsing energy absorbing structure and transfer the loads to the occupant compartment, as efficiently as possible. The general idea, in this case, is to avoid excessive load concentrations that will make the control of the compartment intrusion difficult. The structure topology is very complex in this zone and the prevailing crash mode will be variations of compound axial/bending modes.

Following these ideas in frontal impact, three distinct crush zones are identified. They are differentiated by their function and/or crush events that occur. As a design strategy, there will be a soft front zone, designed to reduce the vehicle's aggressivity in pedestrian-to-vehicle and vehicle-to-vehicle collisions. The soft zone will be generally followed by two stiffer zones, which will be referred to as primary and secondary. The primary zone is composed of the main energy absorbing structure, in the fore section of the powertrain compartment. The secondary crush zone involves the structural interface between the absorber and the compartment. The latter will, generally, extend into the passenger compartment at the dash panel (firewall) and toe-board areas. The respective lengths of the structural crush zones, which constitute the total structural crush, will vary with the location and mounting of the powertrain and suspension systems and the solid stacking of non-structural components in the forward/powertrain compartment.

2.3.1.4 Weight Efficient Energy Absorbing Structures and Supporting Frame

The definition of structural topology, known also as the architecture of the structural frame, must be done in conjunction with the packaging studies. In the case of front and rear end structures, selection of topology will depend on the ability to design in the crush mode for the primary crush zones for the energy absorption, that is, folding, bending, or mixed folding and bending.

Simplified modeling of the vehicle's front-end system, shown in Figure 2.3.1.4.1, is a very good technique to study alternative topologies of the structure in a given vehicle package. An advantage of this technique is the ability to include the inertial effects of the major masses such as the powertrain, as well as the 3-D simulation of the shape and size of the masses and the structural members. Some elements in building this type of model will be discussed later in this section.

Once a skeleton vehicle structure has been constructed, design loads of structural members (energy absorbers and support frames) can be determined and detailed

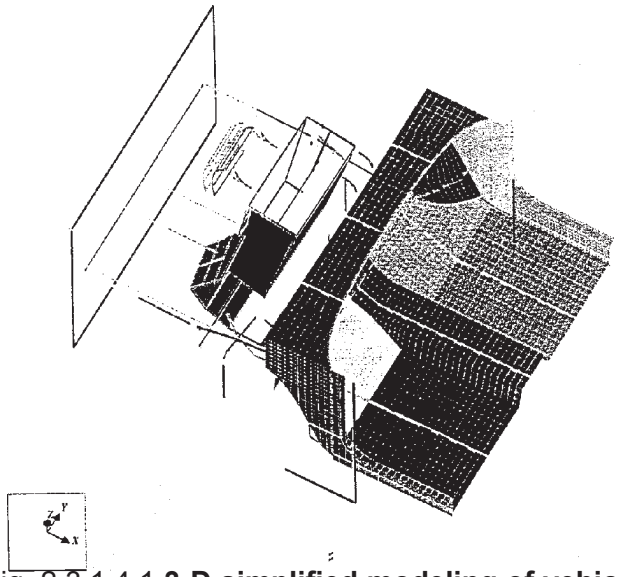

Fig. 2.3.1.4.1 **3-D simplified modeling of vehicle front end**

features can be initiated. This is accomplished using relatively simple quasi-analytical formulations, such as developed by Mahmood and Paluszny [9], for determining crush characteristics of thin-wall structures. A computer code such as SECOLLAPSE, [10] may be used to size structural components, once design loads are determined.

Because of the very demanding requirements of crash, it is safe to assume that the crush criteria will dictate the structural design, including the configuration and the sizing of various structural components and systems. Engineers designing crashworthy structures are able to accommodate any requirement set by noise, vibration and harshness (NVH) and durability early in the design process.

2.3.2 Review of Analytical Design Tools for Crash Energy Management

2.3.2.1 Hybrid Models

In an attempt to overcome some of the limitations of the LMS method, "hybrid" models were used. An approach is termed 'hybrid' because it combines test results of components and substructures into a simplified finite element (FE) model. Also, when a complete front end of a vehicle is modeled using multiple types of elements such as shells, beams, springs and masses, the model is

sometimes called hybrid model. Explicit FE crash codes are usually used for analysis or simulation, which allow enough flexibility to use as many elements as necessary to conduct the crash simulation.

The hybrid modeling approach was originally conceptualized by McIvor [11] in 1974 with the intent of combining the simplicity of the LMS method with the flexibility and iteration convenience of FE or other similar methods. The combination is an important feature in the early stages of design, as it provides quick analysis of many different design alternatives. The determination of "spring"/crush characteristics is calculated by FE or finite difference analytical models. The method has its limitations. The crush characteristics of structural components or systems are generally nonisotropic, that is, they vary with loading direction and boundary conditions. Since the method uses derived load-deflection characteristics, it is load-path dependent. Furthermore, in many instances, the internal effects will alter the mode of collapse and the crush characteristics of the system. Thus, extensive experience and understanding of vehicle crash on the part of the user become indispensable when designing with these tools.

In 1990, Liaw and others from Cranfield Institute of Technology used the hybrid modeling approach [12] for the simulation of vehicle impact with rigid barrier. In this case, modeling of system dynamics was also implemented using an earlier developed computer program, KRASH, an explicit dynamic code developed for aircraft crash simulation. The structure is modeled by deformable beam element in which the collapse characteristic is acquired from actual testing of the structural components.

For the hybrid modeling in KRASH, further development was needed on the element level and stability of solution during execution. In addition, investigation on appropriate damping factors for the beams and model was required in order to control the oscillations of the various masses and have reasonable calculations for the peak accelerations of the masses.

More on hybrid modeling usage is given in [13] for the purpose of developing 3-dimensional modeling capability while maintaining some of the one-dimensional elements. In this case, a hybrid element was developed to allow the modeling of rails as collapsible beam elements capable of connecting with spring-mass elements. An analysis program (FEMASS) was developed to combine the finite elements and the lumped-mass programs. The approach seemed to overcome many problems of solution instabilities and capability regarding large deformations. However, the collapsible beam element formulation neglects the effect of local buckling and crippling of the plates comprising the cross-section of the beam as well as the dimensional collapse of that section. For this reason, comparing the

computed load-deflection results by this method and the results from testing showed poor correlation (Figure 2.3.2.1.1).

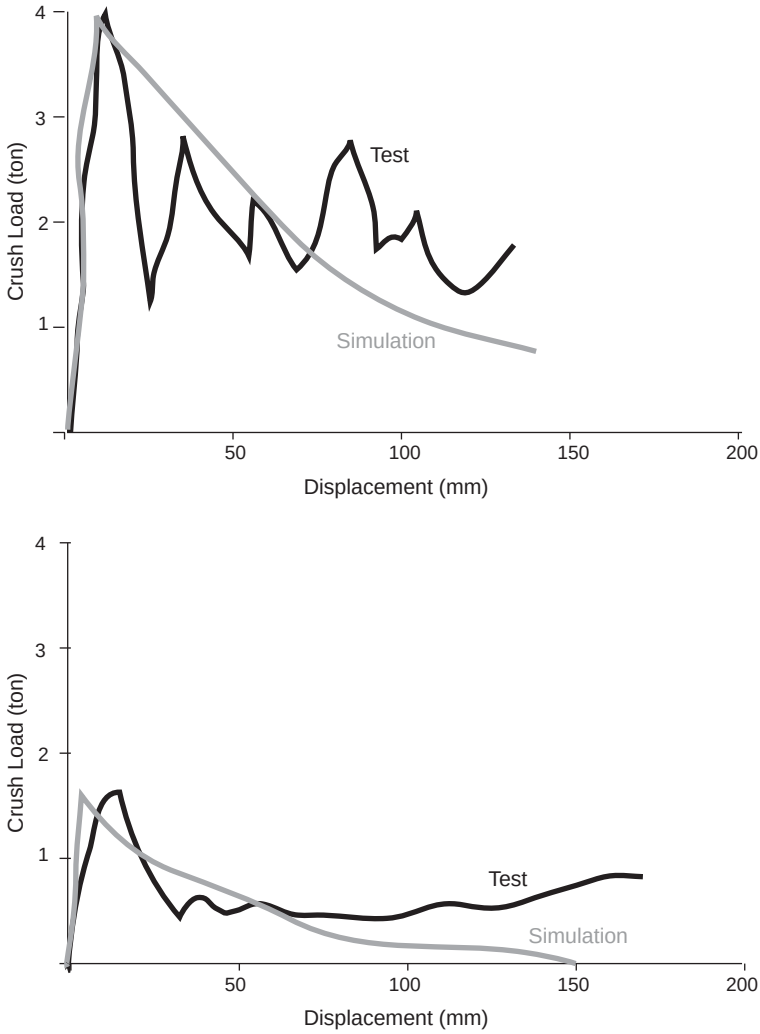

Fig. 2.3.2.1.1 **Discrepancy between simulation and test results in beam formulation [13]**

Clearly, the above description of hybrid modeling shows benefits in 3-D simulations of vehicle crashes. This leads to the development of better or improved collapsible beam element models.

2.3.2.2 Collapsible Beam Finite Element

Collapsible beam element is an important tool for crashworthiness design of vehicle structures. Many researchers tried formulations that were hybrid in nature, but used different ideas and concepts for the formulation. Some of these are summarized as follows:

2.3.2.2.1 Elastic-Plastic Beam With Plastic-Hinge Model

The plastic hinge concept was used extensively to model the bending collapse of beams, particularly when bending involves large rotation angles (referred to as deep collapse in some literature). The concept in the context of modeling with finite beam elements is activated when a yield criterion of a complex loading is satisfied. Prior to the formation of the plastic hinge, elastic-plastic beam behavior is followed. The combination of an elastic-plastic beam and a plastic hinge at either end of the beam offers a method by which simplified crash or crush analysis of vehicles structural frames were quickly made for the purpose of creating the geometrical layout and calculating the cross-section sizes. The most popular configuration demonstrated [14, 15, 16] by this approach is the S-frame structure, which is typical of front (or rear) rail support at the vehicle's passenger compartment.

S-frame crush in [14] was limited to a planer frame. Elastic-perfectly plastic material was assumed. At the structural hinges, the stiffness of the elements was modified according to a method that predicts the local collapse of the section versus local rotation. In [15], rotational springs were added at one end of the elastic-plastic beam to represent the plastic hinge after some it met yield criterion. The springs allow the simulation of different types of behavior (as the slopes shown in Figure 2.3.2.2.1.1) after the hinge is formed. The characteristics of the springs are determined analytically or experimentally, and represent the way different types of cross-section shapes and dimensions deform during large rotations.

The S-frame crush was also studied by modeling with rigid beams and rotational springs rather than the elastic-plastic beam [16], an idea being used to simulate the crush of structures using the rigid body dynamics computer programs. In [16], the crush was compared using the two types of modeling, which showed that the elastic-plastic beam with a plastic-hinge at the end is a more accurate method of modeling. Although this model can be helpful in design of structures dominated by bending, it has severe limitations when designing for energy

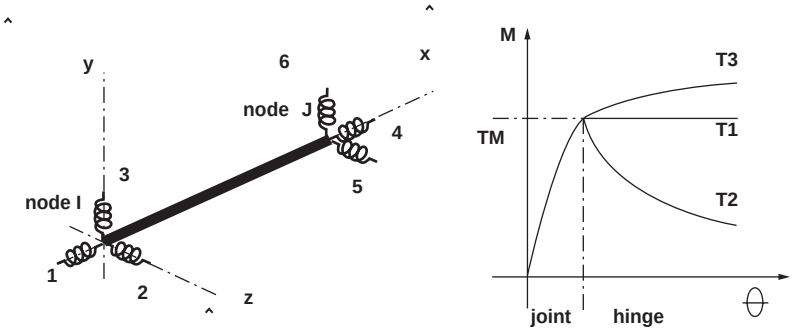

Fig. 2.3.2.2.1.1 **Simulation of elastic-plastic hinge in beams using rotational springs [15]**

absorption by axial folding. When the structure is subjected to combined axial load and biaxial bending, this approach fails and a formulation such as the super-collapsible beam described in Section 2.3.2.2.2 – Super-collapsible Beam Element, can be used to overcome these limitations.

2.3.2.2.2 Super-Collapsible Beam Element

This is an advanced beam element formulation capable of handling combined axial loads in the presence of multi-plane bending. Therefore, it is exceptionally useful in analyzing the crush behavior of front and rear vehicle structures where the rails first fold axially, then deform in bending near the vehicle's passenger compartment. Details of the formulation are given in [17] and [18]. The element has been incorporated in a specialized computer program, VCRUSH. More discussion about that element is presented in the Section 2.4.2—Design of Substructures.

2.3.2.3 Dynamic Effects

Dynamic effects originate from two sources. First are the effects of strain-rate on the yield and flow strengths of the material. Second are the inertia effects on the internal load distribution that may affect both the overall and local collapse modes. These effects in LMS models are combined into a single dynamic factor derived empirically and applied to statically determined "spring" characteristics. These factors are usually related to the crash rate, and the relationships vary with the investigators. Some assume the relationship varies linearly, others logarithmically. Prasad and Padgaonkar [19] conducted an extensive study on vehicles with framed structures and unit body cars, and developed dynamic factors by exercising the LMS models with different amplification factors and comparing model results with tests. They concluded that the factors that best explained the crash tests

varied with the construction of the vehicle. This is only natural since the collapse modes of these vehicles varied and so did the inertial effects associated with these modes, both of which were reflected in the amplification factors.

Davis and Magee studied the effect of strain-rate upon tensile properties using tensile [20] and four-point bending tests [21]. The strain-rates investigated in tensile experiments covered a range from 0.001 to 103 s^{-1}, which corresponds to crosshead speeds of ~0.42 mm/s and 22.35 m/s respectively, while the crosshead rates in the bending tests varied from 0.42 mm/s to 4.2 m/s. The authors show that, when the strength level and strengthening mechanisms are properly accounted for; the flow stress varies logarithmically with strain-rate.

$$\Delta\sigma = k_r \log V_2 / V_1 \qquad (2.3.2.3.1)$$

where $\Delta\sigma$ is the change in strength due to change in strain-rate quasi-static to dynamic, V_2 and V_1 are the high and quasi-static rates respectively, and k_r is experimentally determined and equals the slope of the line represented by Eq. (2.3.2.3.1). It was also observed that there was no significant change in the tensile ductility.

Kassar and Yu [22] conducted a fairly comprehensive experimental study on the strain rate effects for various steels in a project sponsored by AISI. Given two values of flow stress (σ_1 and σ_2) obtained at two different strain-rates (ε_1 and ε_2), the strain rate sensitivity exponent, m, is computed using logarithmic relationship.

$$m = ln\,(\sigma_2 / \sigma_1) / ln(\varepsilon_2 / \varepsilon_1) \qquad (2.3.2.3.2)$$

The magnitude of m can be determined empirically, and for most materials it is said to be usually between 0 and 0.03.

Thornton [23], in his study on static and dynamic collapse characteristics of scale model corrugated columns (axial collapse), which involved a more complex test mode (bending and biaxial shear in the individual hinge mechanisms), confirmed Davis' and Magee's findings. Thornton also showed that the dynamic response of a structure, in which the hinge mechanisms were "designed" into the test coupon, is governed solely by the strain-rate effects. This was found by the author to hold true for axially collapsing structures, in which the collapse process is progressive and thus involves only the immediate crush zone. In addition, since the crush zone is very localized, the inertial effects are minimal and can be neglected.

Abramowicz and Jones [24] used the empirical Cowper-Symonds uniaxial constitutive equation for mild steel in deriving the dynamic factor for an axially crushing square column.

$$(\sigma_y)_d / \sigma_y = 1 + (\varepsilon / 6844)^{1/3.91} \quad (2.3.2.3.3)$$

where σ_y is material yield strength, $(\sigma_y)_d$ its dynamic yield strength and ε the strain rate. The average strain rate in an axially crushing square tube is approximated with

$$\varepsilon = t V_m / 2r\delta \quad (2.3.2.3.4)$$

Here, t is the wall thickness, V_m the average crush velocity, r the small radius of a toroidal surface over which material is deformed [25]) and δ the effective crushing distance (see [26]). Additional information on dynamic factors for axially crushing columns may be found in the paper by Wierzbicki and Akerstorm [27], as derived in the context of a crush mechanism.

It is obvious that strain-rates vary during a crushing process not only with the crush velocity, but also with the prevailing mechanisms of collapse. The crush velocity diminishes as the crush progresses and its rate of decay may not necessarily be constant, but will vary with the decelerating force. In addition, as mentioned in Section 2.3.2.3 – Dynamic Effects, inertial effects contribute to the dynamic factor, and these will vary with the model. Thus, considerable experience is required in determining the dynamic factor that is appropriate for a given modeling technique. This is where non-linear FE analysis can automatically compensate for the dynamic effects of both the strain-rate and inertial origin. To correctly capture these effects, very detailed models may be required, which may make this approach cost-prohibitive, particularly in the early stages of vehicle design.

2.3.3 New Design Methodology

A design methodology that is practical and efficient in helping to create innovative structural concepts and advanced designs has been developed [28]. It integrates the simplified modeling and analysis techniques, and also implements design synthesis [29] and system engineering fundamentals. These ideas are highly valued by design engineers because the methodology satisfies their needs. On the other hand, the typical crash analysts may have difficulty in implementing these ideas because of the understanding that is required in crash behavior and in designing vehicle structures.

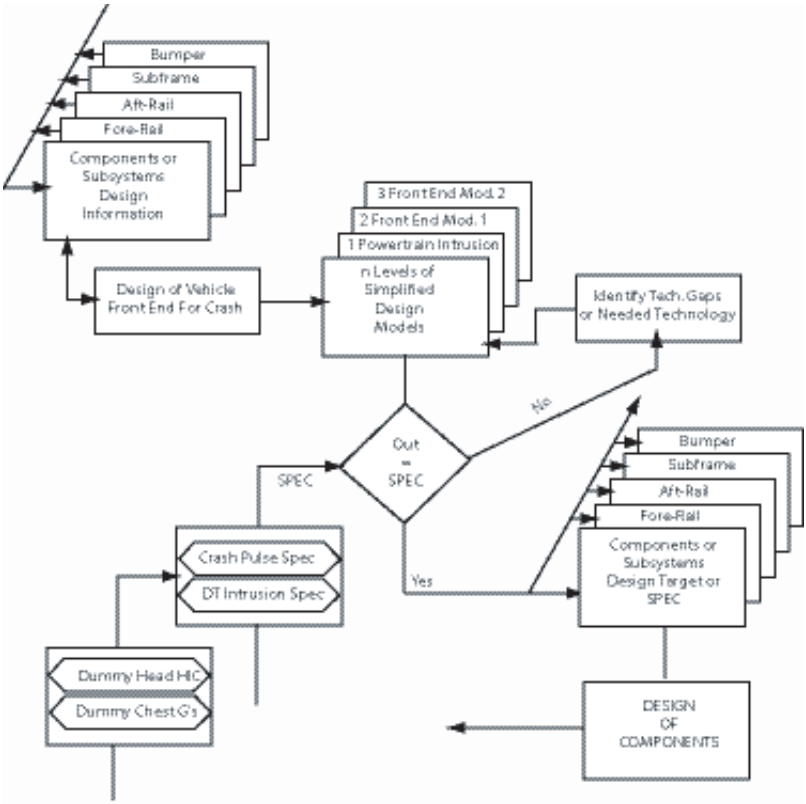

Fig. 2.3.3.1 **Front-end system design approach [28]**

In this new design methodology, the elements of the system are synthesized [29]. Their functional performances are derived by dividing the system into its constituent subsystems (Figure 2.3.3.1), components, and defining appropriate interfaces on its boundaries. Thus, there is no need to have a complete design initially. However, from the analyst's viewpoint, a complete design in which models are integrated to include every detail in the system is required, which is an unreasonable expectation when starting to define a design concept.

By this new design methodology, system modeling is performed using collapsible beam element or 3D hybrids [28,30] rather than only lumped masses and springs (Figure 2.3.3.2). This approach adds the ability to analyze asymmetrical impacts,

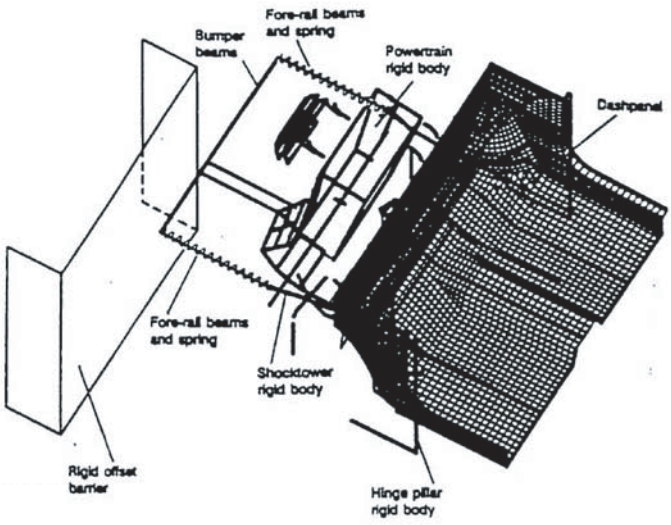

Fig. 2.3.3.2 **3-D hybrid modeling of front end system [28, 30]**

such as offset. Also, the system model progressively grows as components are designed, rather than having all detailed modeling or all simplified, that is, the mix of elements of the hybrid model changes as the design progresses and detailed information becomes available. Consequently, the designed structural components or substructures are readily analyzed in a system environment. A schematic of model growth is shown in Figure 2.3.3.3 as envisioned by the authors and other researchers [31].

2.4 Analytical Design Tools

2.4.1 Component Design

The terminology used in subsequent sections may differ from definitions found in the literature. Also, some of the concepts described may be unfamiliar to the

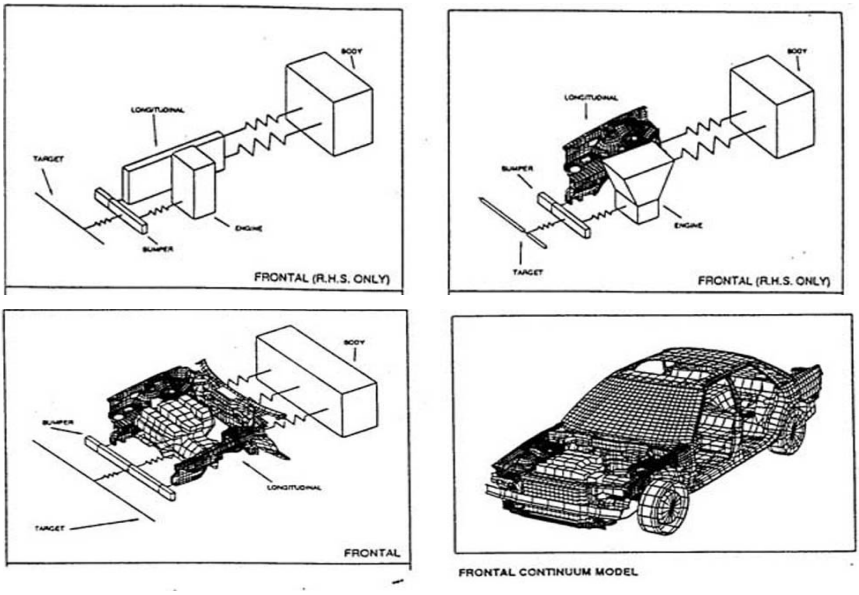

Fig. 2.3.3.3 **Evolving front-end system modeling [31]**

reader. To clarify, a structural member will be called a column if it is axially loaded in compression. Alternatively, it will be referred to as a beam if it is subjected to bending or combined bending and axial compression. Buckling/collapse of a structural component is called local when the deformations (buckle/fold) are of local character and the collapse is confined to an isolated area of the component. It is global (an example is an Euler-type column buckling) when the whole component becomes deformed and subsequently collapses in a linkage fashion (rigid sections of the component connected like links in a mechanism by discrete rotational plastic hinges that originate from local collapse phenomena).

2.4.1.1 Collapse Modes

There are two major considerations in the design of automotive structures for crash energy management: absorption of the kinetic energy of the vehicle and the crash resistance or strength to sustain the crush process and/or maintain passenger compartment integrity. As for energy absorption, two basic modes or mechanisms are encountered in thin wall sheet metal beam-type structures commonly found in automobiles: axial collapse and bending. Pure axial collapse can be achieved only in the energy-absorbing structures and only during direct frontal/rear or slightly off-angle (5°-10°) impacts. Therefore, most of the structural

members, comprising the front and rear end structures, will be subject to mixed modes comprised of axial collapse and bending. Higher order, more complex modes, which include torsion, are more likely to occur in the structural beam elements comprising the passenger compartment and the structural interface, which support the energy-absorbing structures. In a well-designed and executed energy-absorbing structure, the mixed modes will be avoided to assure predictable performance during crash. The sheet metal closure/shear and outer skin panels are likely to collapse by predominantly irregular folding or crumpling. The degree of folding regularity will depend on the panel's size-to-thickness ratio and its

Fig. 2.4.1.1.1 **Axial mode of collapse**

geometric stiffness, that is, its curvature. The greater the curvature (greater geometric stiffness), the more regular the folding pattern.
Axial folding crush mode is considered to be the most effective mechanism for energy absorption. It is also, perhaps, the most difficult one to achieve in real structures because of the instability problems associated with it. This will be discussed in Section 2.4.1.2 – Axial Collapse. Figure 2.4.1.1.1 shows a typical stable axial mode of collapse of a square column. In this case, the mode is composed of symmetrically alternating folds.

The bending mode, which involves formation of local hinge mechanisms and linkage-type kinematics, is a lower energy mode. A front-end structure will always have a tendency to collapse in this type of mode. Even a structure designed for axial collapse will fail this way, unless very specific rules are followed to enhance its stability and resistance to off-angle loading. A typical bending mode of collapse of a thin wall beam-type structural component is shown in Figure 2.4.1.1.2.

2.4.1.2 Axial Collapse

2.4.1.2.1 Mathematical Models

The approaches taken by different investigators to model the axial folding process of thin wall columns, and the associated characteristics (strength properties), has varied over the years from the purely analytical to strictly experimental. In early

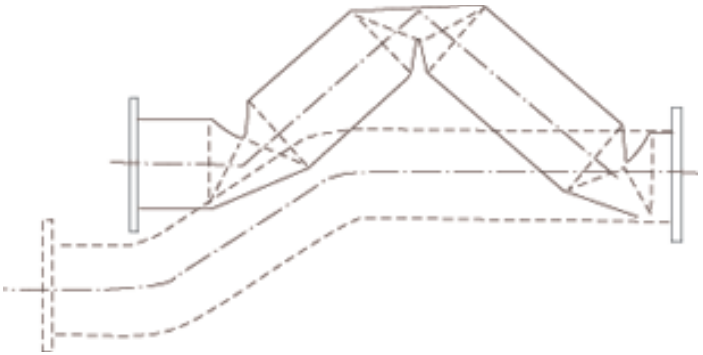

Fig. 2.4.1.1.2 **Bending mode of collapse**

analytical works by Ohokubu et al [32], Johnson et al [33], Wierzbicki and Akerstrom [27], Alexander [34] and others, the investigators began by modeling the mechanics and kinematics of the folding process and then derived from the model the desired crush characteristics in the form of relatively simple relationships involving component geometry and material properties. Some simplifying assumptions were made to accommodate the different types of problems, such as the assumptions of purely inextensional (middle/neutral surface neither stretches nor shrinks) deformation modes for the box type columns, or predominantly extensional deformation modes for rotationally symmetrical tubular columns. These assumptions limited the predictive capabilities of these earlier formulations and, thus, their value as design aids. In more recent work, Wierzbicki and Abramowicz [25] combined the approaches, and, using kinematics plasticity, developed a theory of crushing behavior of thin wall, plate-type columns. The expression for the average or mean crush load is derived from the energy balance by equating the external work done by the crush load with energies dissipated in different types of deformation mechanisms as they occur in a folding process.

$$P_m = 38.27\, M_o\, C^{1/3}\, t^{-1/3} \qquad (2.4.1.2.1.1)$$

where P_m is the mean/average crush force, $M_o = \sigma_o\, t^2 / 4$,the fully plastic moment, σ_o, is the average flow stress (σ_o = *(0.9 to 0.95)* σ_u), σ_u is the ultimate tensile strength of the material, $C = 1/2\,(b+d)$ with b and d being the sides of a rectangular box column, and t its wall thickness. For a square tube, for which $C = d = b$, Eq. 2.4.1.2.1.1 simplifies to:

$$P_m = 9.56\, \sigma_o\, t^{5/3}\, b^{1/3} \qquad (2.4.1.2.1.2)$$

On the other side of the modeling spectrum are purely experimental approaches, notably the work of Magee and Thornton [35]. Using data from crush tests of columns (steels ranging in tensile strength from 40 to 190 ksi, aluminum alloys and composites) of several different section geometries provided a relationship between structural effectiveness η of the section and relative density ϕ. The structural effectiveness η is defined as the ratio of specific energy (maximum energy that can be dissipated, divided by specimen weight) to the specific ultimate strength (ultimate tensile strength divided by material density). Also, the relative density ϕ is defined as the ratio of material volume to the volume enclosed by the structural section. They then derived, by way of curve fitting, a relationship between these two parameters. Figure 2.4.1.2.1.1, taken from [35], shows such a plot for square and rectangular thin wall columns. The relationships for other

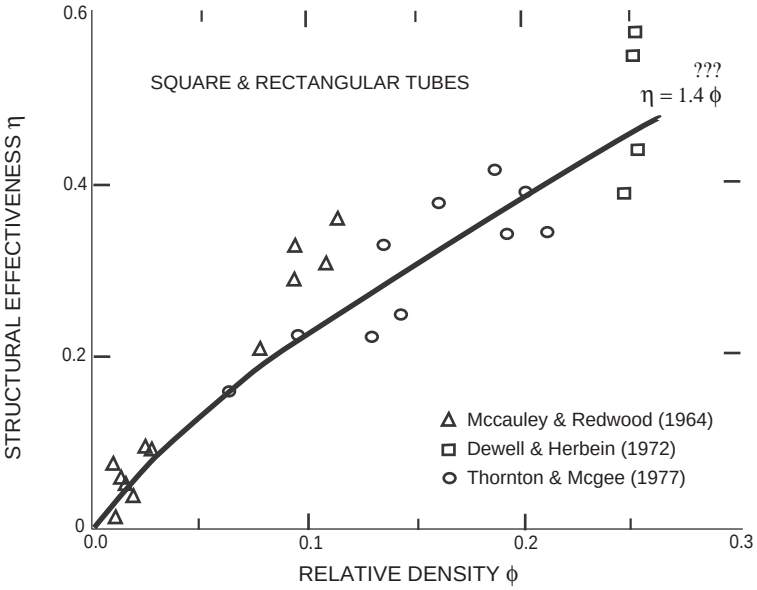

Fig. 2.4.1.2.1.1 **Variation of structural effectiveness [35]**

TABLE 2.4.1.2.1.1 **Empirical relationship between η and f for the collapse of various structures**

Structure	$\eta = (\phi)$	ϕ
Cylindrical Tubes	$2\phi^{0.7}$	4t/D
Square and Rectangular Tubes	$1.4\phi^{0.8}$	4t/S
Honeycomb	$5\phi^{0.9}$	8t/3S
Foam	$0.7\phi - 4\phi$	ρ_f / ρ_m

where t is wall thickness, D outside diameter, S length of side, ρ_f foam density and ρ_m matrix density.

basic configurations can be found in Table 2.4.1.2.1.1, taken from the same reference.

The expression for mean crush load is obtained from the expression for specific energy ($E_s = P_m / \rho \phi A_o$) and is of the form:

$$P_m = \eta \, \sigma_u \, \phi \, A_o \tag{2.4.1.2.1.3}$$

ρ being the density and A_o the overall area of the section as defined by its outer circumference. For a square section $\eta = 1.4 \, \phi^{0.8}$ and the mean/average crush load becomes:

$$P_m = 17 \, t^{1.8} \, b^{0.2} \, \sigma_u \tag{2.4.1.2.1.4}$$

where b is the width of the side and t is the wall thickness.

One of the drawbacks of the formulations given by Eqs. 2.3.2.3.4 and 2.4.1.2.1.3 is that the elasticity of the material does not come into play. Thus, for the same ultimate strength, materials like steel and aluminum would exhibit the same mean crush strength (P_m). This has been shown by Mahmood and Paluszny [36] to be

Fig. 2.4.1.2.1.2 **Folding pattern of thin-walled box with very small thickness/width ratio**

contrary to test findings, which do show a considerable difference in the crush characteristics for these two materials.

Mahmood and Paluszny [9] developed a quasi-analytical approach that overcomes some of these drawbacks. They start with a premise that thin-walled box columns, composed of plate elements and subjected to axial compression, will buckle locally when critical stress is reached. Local buckling initiates the processes that lead to the eventual collapse of the section and a subsequent folding of the column. The collapse strength of the section is related to its thickness/width (*t/b*) ratio and material properties. For very small *t/b* ratios (*t/b=0.0085-0.016*), representing the so called "non-compact" sections, the mode of collapse of a section will be influenced predominantly by the geometry, since its local buckling strength is considerably below the material yield strength. As shown in Figure 2.4.1.2.1.2, the mode of collapse of "non-compact" sections is characterized by large irregular folds reminiscent of crumpling, which give rise to a bending type (global buckling) instability that is induced by fold irregularities. For larger *t/b* ratios, typifying the "compact" sections in which the elastic buckling strength exceeds material yield strength, the material strength properties are expected to govern the mode of collapse and, consequently, the post-buckling stability. The collapse mode in this case, as shown in Figure 2.4.1.2.1.3, will appear very stable even in the presence of considerable geometry or loading imperfections. Since the "compactness" of an axially compressed column affects

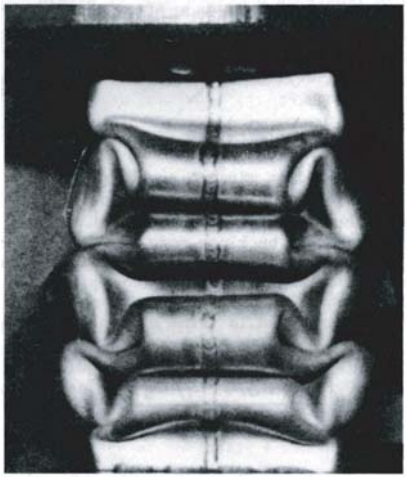

Fig. 2.4.1.2.1.3 **Folding pattern of thin-walled box with large thickness/width ratios**

the stability of collapse, it is important to define when a section becomes "non-compact" and fails in a crumbling mode. According to Mahmood and Paluszny [37] the threshold $(t/b)^*$ ratio is given as:

$$(t/b)^* < 0.48 \left[\sigma_y (1-\nu^2)/E \right]^{1/2} \qquad (2.4.1.2.1.5)$$

where E is the Young's modulus of elasticity and ν the Poisson's ratio.

Figure 2.4.1.2.1.4 shows a sketch of an axially compressed rectangular column with a typical pattern of buckles (local buckling) that will appear when the elastic critical local buckling stress is reached.

$$\sigma_{cr} = k \pi^2 E(t/b)^2 / 12(1 - \nu^2) \qquad (2.4.1.2.1.6)$$

$$k = (b/\lambda)^2 + p + q(\lambda/b)^2 \qquad (2.4.1.2.1.7)$$

where λ is the elastic half wave length and p and q are factors that depend on the degree of restraint of its longitudinal edges or, in the case of a box column like the one shown in Figure 2.4.1.2.1.4, on the section aspect ratio (d/b). The plate with a smaller (t/b) ratio is regarded as a buckling plate and the other as the restraining plate.

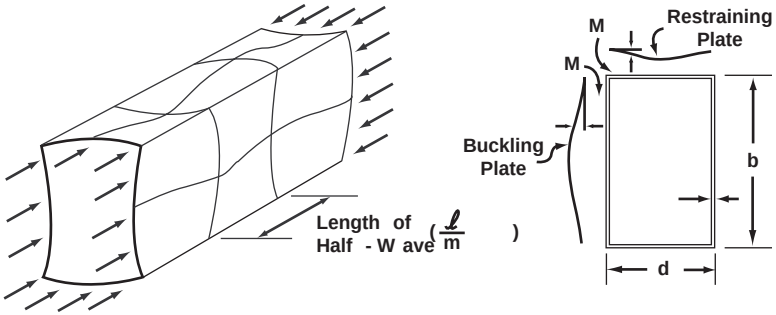

Fig. 2.4.1.2.1.4 **Locally buckled rectangular box column**

In general, the average maximum crush strength (S_{max}) and the collapse of plate type columns will be controlled by a combination of geometry and material properties.

$$S_{max} = [k_p E(t/b)^{1/2}]^n [(1 - \nu^2) \beta \sigma_y]^{-n} \sigma_y \qquad (2.4.1.2.1.8)$$

where the crippling coefficient k_p is a function of the degree of restraint at the longitudinal edges, such as provided by the neighboring plates, and is usually expressed in terms of the aspect ratio as shown in Figure 2.4.1.2.1.5, taken from [9], the exponent n is influenced by the degree of warping and lateral bending of the unloaded edges (corners), E is the Young's modulus of elasticity and σ_y the yield strength of material. For box-type columns, n has been determined experimentally to be 0.43. β is the material strain hardening factor.

For thin-walled sections of $t/b \leq 0.08$, $\beta = 1$. β could reach the ratio σ_u / σ_y for a very thick walled section, [36]. The expression for the maximum load carrying capacity is obtained by multiplying Eq. 2.4.1.2.1.4 by the area of cross-section. Thus, for instance, the maximum crippling load of a rectangular section of uniform thickness t and sides b and ($Area = 2t(b=d) = 2tb(1+\alpha)$)

$$P_{max} = 2[k_p E/\beta (1- \nu^2)]^{0.43} t^{1.86} b^{0.14} (1+\alpha) \sigma_y^{0.57} \qquad (2.4.1.2.1.9)$$

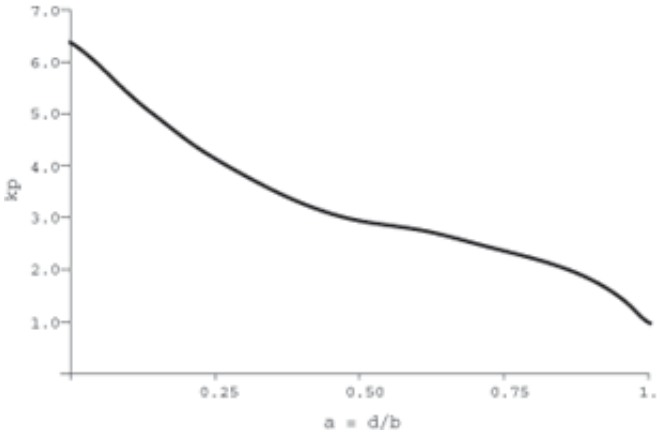

Fig. 2.4.1.2.1.5 **Crippling plate coefficient [9]**

where $\alpha = d/b$ is the aspect ratio of the section for which the appropriate crippling coefficient can be obtained from Figure 2.4.1.2.1.5

For a square steel column ($\alpha = 1$, $k_p = 2.11$ (Figure 2.4.1.2.1.5), $\nu = 0.3$ and $E = 30 \times 10^6$ *psi*) Eq. 2.4.1.2.1.9 reduces to:

$$P_{max} = 9430\, t^{1.86}\, b^{0.14}\, \beta^{-0.43}\, \sigma_y^{0.57} \qquad (2.4.1.2.1.10)$$

In a similar manner, an expression is obtained for the average mean crush strength S_m of a plate column restrained at both unloaded edges, by substituting the crippling coefficient k_p with k_m, which, too, is dependent on the degree of restraint, that is, the plate aspect ratio α.

$$S_m = [k_m\, E(t/b)^2 / \beta(1-\nu^2)]^{0.43}\, \sigma_y^{0.57} \qquad (2.4.1.2.1.11)$$

For a square column ($\alpha = 1$) k_m has been determined experimentally to be approximately 0.18. Multiplying Eq. 2.4.1.2.1.7 by the area (*Area* = $4tb$), an expression for the mean crush load of a square box section is obtained.

$$P_m = 3270\, t^{1.86}\, b^{0.14}\, \beta^{-0.43}\, \sigma_y^{0.57} \qquad (2.4.1.2.1.12)$$

To get a feel for the relative accuracy of the three methods described, Eqs. 2.4.1.2.1.2 and 2.4.1.2.1.4 were normalized with area A and plotted along with Eq. 2.4.1.2.1.11

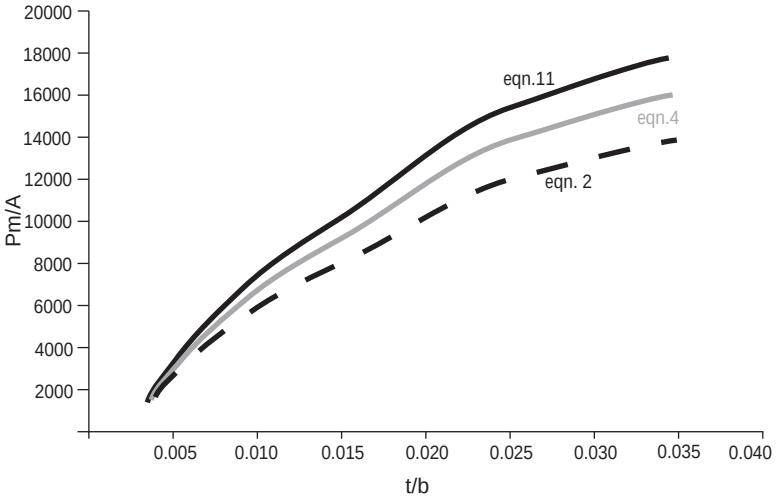

Fig. 2.4.1.2.1.6 **Comparison: design formulations for mean crush strength**

in Figure 2.4.1.2.1.6 against the test results obtained by Mahmood and Paluszny on steel columns (σ_y = 43 ksi and σ_u = 60 ksi) [37].

A typical crush signature, that is, the load-deformation characteristics of an axially collapsing square steel column, is shown in Figure 2.4.1.2.1.7 side-by-side with its idealized representation, on which all characteristics relevant to design have been identified. The high load peak, representing the maximum crippling load P_{max}, can be effectively attenuated by appropriately designed imperfections and triggers to minimize the load transferred to the downstream structures.

Eqs. 2.4.1.2.1.8 and 2.4.1.2.1.11 are quite general, with simple modifications that apply to plate-type box columns having section configurations commonly found in automotive structures. This provides the structural designer with very simple, yet practical and fairly reliable tools. These tools allow rapid sizing of the structural elements for energy absorption and are of a form that is very convenient for use in parametric studies.

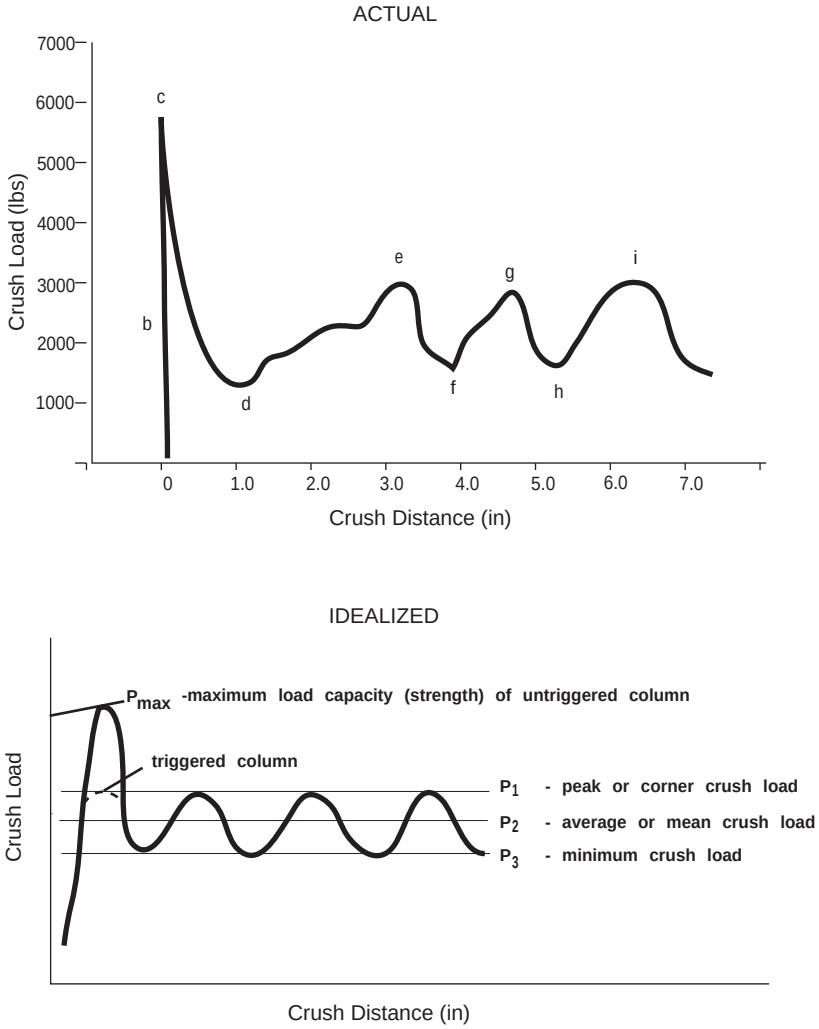

Fig. 2.4.1.2.1.7 **Load-deformation characteristics of an axially collapsing square steel**

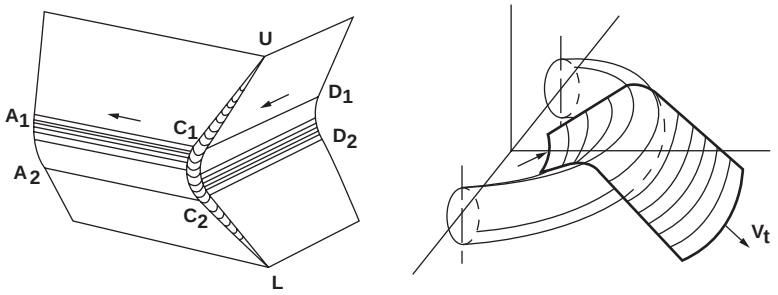

Fig. 2.4.1.2.2.1.1 **Moving plastic hinge and basic folding collapse mechanism**

2.4.1.2.2 Folding Mechanism of Box Column During Axial Collapse

2.4.1.2.2.1. Mechanism of Folding

The plate element of a box column loaded axially in compression buckles locally as shown in Figure 2.4.1.2.1.4. The local buckling mode in these plate elements provides a base for localized plastic deformation as the crushing progresses. Within the deformed buckle geometry, the purely compressive state changes into bending and the folding process is initiated. The formation of the fold can be described using the concept of a moving plastic hinge [25,39-41] where the material bends and unbends in a collapse mechanism (Figure 2.4.1.2.2.1.1) that consists of:

- Four plane trapezoidal elements moving as rigid bodies.
- A section of a toroidal surface that produces extension in the circum-ferential directions and one principal curvature that continuously changes from a positive value to a similar negative one.
- Two sections of a cylindrical surface with moving hinge lines.
- Two sections of a cylindrical surface in which material is bent to a small radius and rebent again by inclined hinge lines.

The simplest geometry of a folding element is the intersection (corner) of two flat plate elements found in all box-type sections referred to here as an angle-folding element, shown schematically in Figure 2.4.1.2.2.1.2. After the initial collapse, the corner in the middle of the buckle (point C) begins to roll (bends and unbends while traveling) in a direction perpendicular to the bisector of the included angle (ψ) between the two sides. The fold is formed by way of travel of the plastic hinge line (UCL) at which $A A_o = D D_o$ = half of the fold length.

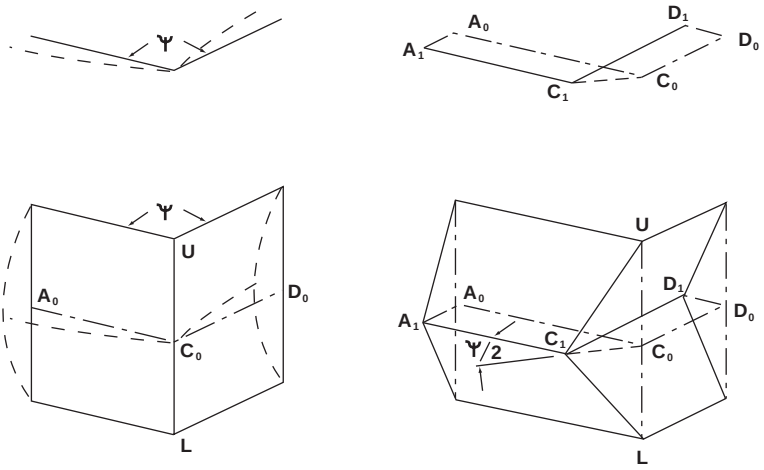

Fig. 2.4.1.2.2.1.2 **Angle**

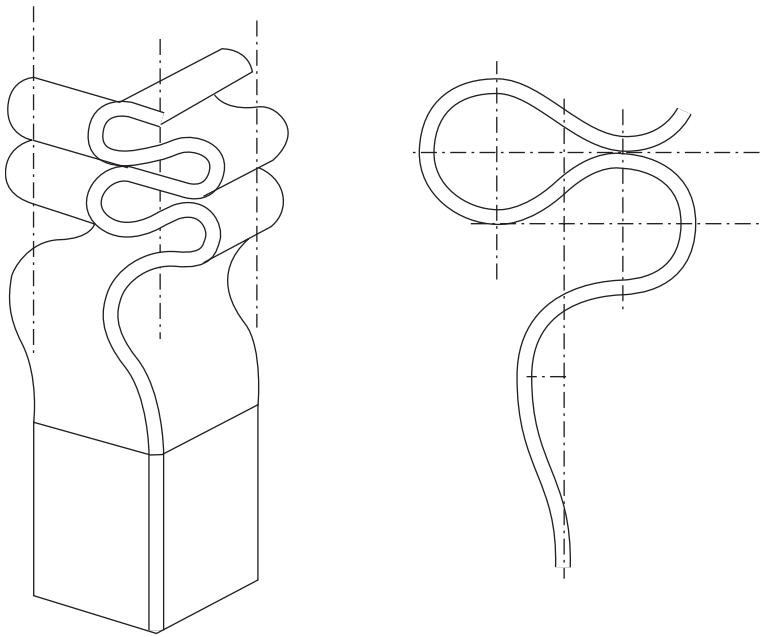

Fig. 2.4.1.2.2.1.3 **Progressive folding in a stable crush**

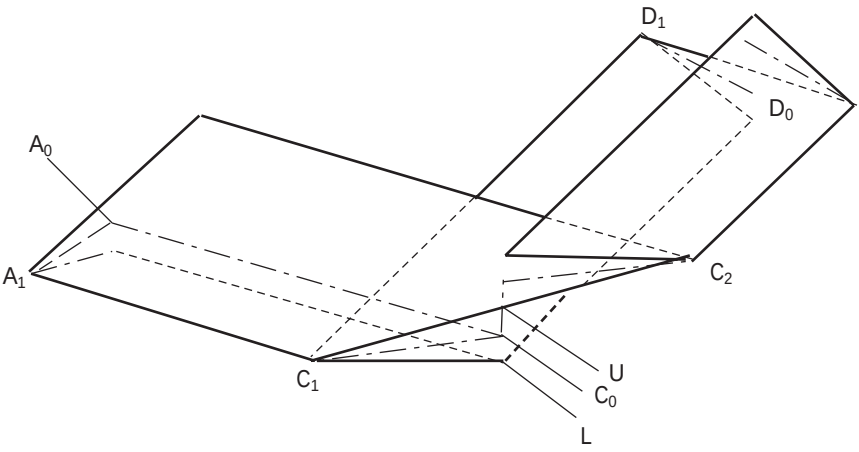

Fig. 2.4.1.2.2.1.4 **Second fold in an angle-folding element**

For most stable structures, the completed fold initiates (triggers) the formation of a subsequent fold in the longitudinal direction. This behavior is described in [39], (also observed during component crush tests) and is shown in Figure 2.4.1.2.2.1.3. The formation of the second fold is represented schematically, for design purposes, in Figure 2.4.1.2.2.1.4 for the angle-folding element.

In automotive-type structures, some cross-sections are designed with more than two flat plate elements intersecting at one corner. Examples are the flanged box sections and the interconnection between two or more box sections. The folding mechanism for the case of four plates intersecting at one corner (2 angle elements), such as T- or Y-intersections, which are referred to here as T- or Y-folding elements (Figure 2.4.1.2.2.1.5) is determined using the angle folding element described earlier. Two of the three branches are assumed to be single plates and the third branch is made of two plates spot-welded at a distance from the branches' intersection. Welding of the three branches at the intersection will prevent folding and result in an irregular collapse mode. The collapse in this case is possible only if the free edges of the three branches can move unrestrained in and out of their planes.

For shell-type structures, the initial curvature becomes flat after buckling and the perimeter of the buckle forms hinge lines which travel to form the fold [42], (Figure 2.4.1.2.2.1.6).

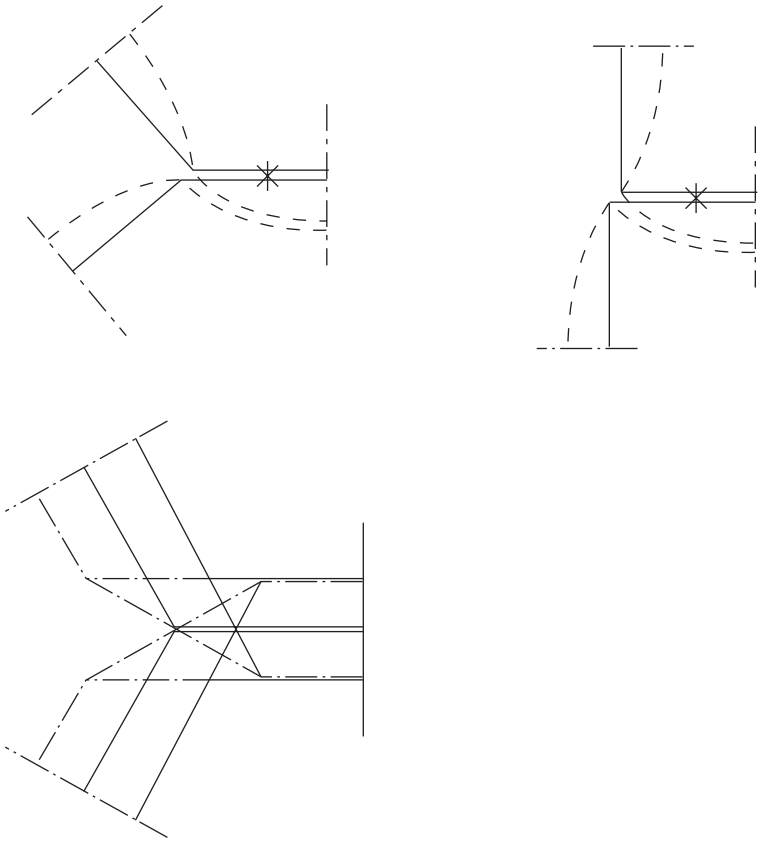

Fig. 2.4.1.2.2.1.5 **T- and Y-folding elements**

The simplified model of the folding mechanism described above, supplemented with the knowledge of the buckling mode of the elements in an assembly, can be used to qualitatively investigate the admissibility of a folding mode in structures of increased complexity. Experience shows that a structure composed of several collapsible elements will crush by progressive folding if it successively develops at least three fairly uniform folds in a longitudinal direction. A given cross-section is divided into the basic folding elements where the buckled and folded geometries are determined then assembled and checked for:

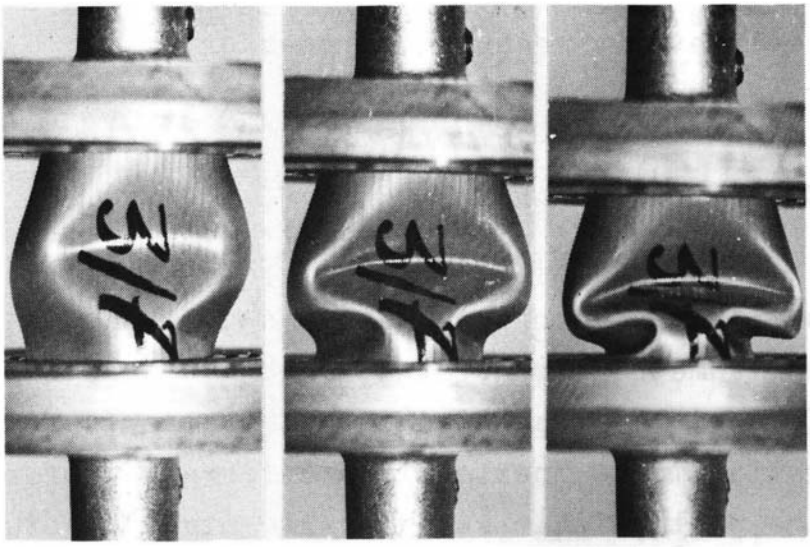

Fig. 2.4.1.2.2.1.6 **Traveling hinge in shell structures**

- continuity of the fold geometry across the perimeter of the section,
- compatibility of the folding in the longitudinal direction, and
- excessive distortion (warpage) of the original shape, which prevents formation of successive folds. In cases where no prior experience exists, experimental verification may be required.

As mentioned earlier in this section, one of the requirements to achieve a regular folding mode, Figure 2.4.1.2.1.3, is to design the flat plate elements of box section members for buckling in the inelastic range of the material. Small *t/b* ratio (corresponds to an early elastic buckling) results in an irregular folding mode, Figure 2.4.1.2.1.2 [40], therefore these ratios should be avoided.

Examples are given next for cross-sections made of angle folding elements and T- or Y-folding elements. The fold size is assumed to be known. The half-fold length in the longitudinal direction l_x for these elements can be approximately determined from the buckling half-wave length equations given in [9].

A square section is the simplest form of a cross-section made of four angle folding elements with included angle $\psi = 90°$ and sides of equal width. Schematics

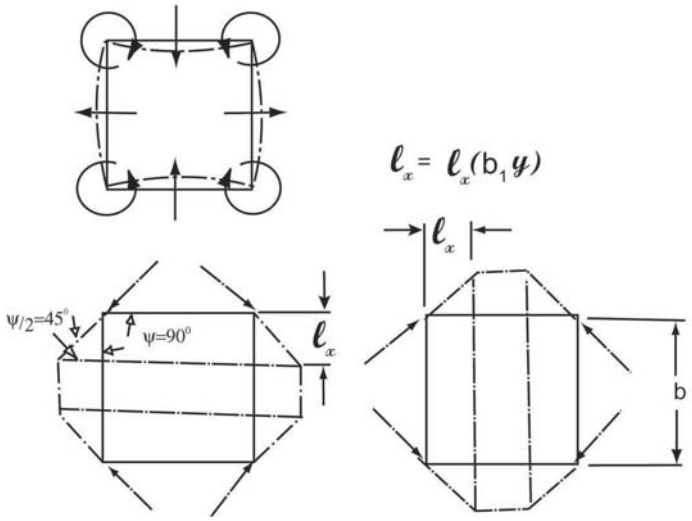

Fig. 2.4.1.2.2.1.7 **Folding mode of square section**

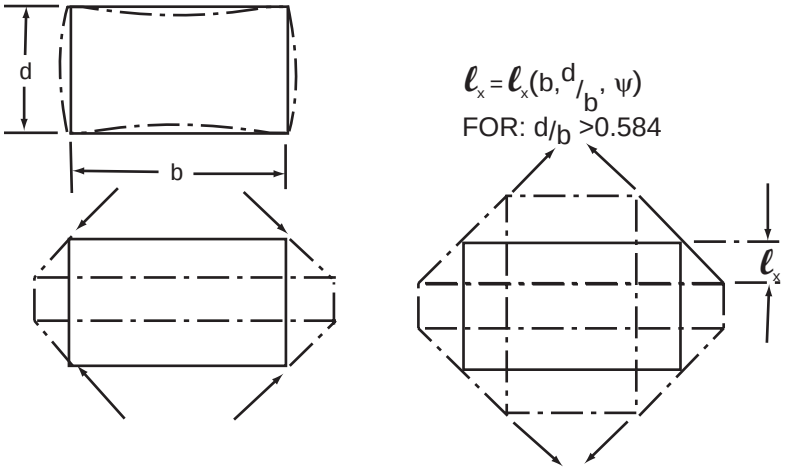

Fig. 2.4.1.2.2.1.8 **Folding mode of rectangle section**

of the buckling mode, first fold and second fold (Figure 2.4.1.2.2.1.7) indicate that this cross section admits the formation of folding.

A rectangular cross-section (Figure 2.4.1.2.2.1.8), $\psi = 90°$, sides of widths b and d and ratio $d/b < 1$. The longitudinal wave length $l_x = (b, d/b, \psi)$ becomes smaller as d/b ratio decreases. At a critical ratio of $d/b = .584$ [40], the sides of the fold contact and hinder the travel of the plastic hinges, thus causing bending instability. Therefore, the rectangular cross-section admits the formation of folding only for $d/b > .584$.

Cross-sections composed of angle folding elements with included angle ψ varying between 90° and 120° (hexagonal tubes, corrugations) have been shown in tests to allow formation of folds and to crush by progressive stable folding. Configurations with angles exceeding 120° (130° to 135°) were also found to fold. However, the folding was irregular and generally led to unstable crush behavior. Reference [43] shows that in a multi-sided cross-section with included angle (ψ) greater than 163.6°, the corners snap inward during buckling, which indicates that folding is inadmissible for these angles. For included angles less than 90°, an investigation is required to determine the lower limit on angle for admissibility of folding. Therefore, when designing for a folding mode, it is recommended, to stay within the range $90° \leq \psi \leq 120°$.

For an angle cross-section with free edges, the deformation assumes an asymmetric buckling mode (Figure 2.4.1.2.2.1.9). When the member length equals the width of the flange, one fold is formed. In longer members multiple folding may occur if properly triggered; however, a mixed mode involving global instability and folding is more likely.

2.4.1.2.2.2 Size and Shape of Folds for Box Columns

The size and shape of folds while crushing thin-wall components can be calculated using two different methods. One method is based on the length of the wave of a buckled plate element under compression load and then extended to the folding through adjustment coefficients

$$\lambda = 0.8\, b\, q^{-0.25} \qquad (2.4.1.2.2.2.1)$$

where q is dependent on the degree of restraint of the plate elements making the box section.

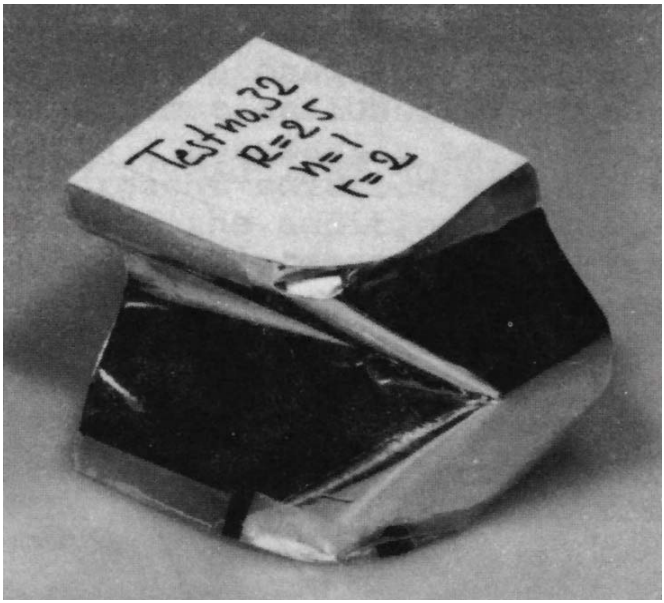

Fig. 2.4.1.2.2.1.9 **Collapse mode of an angle cross section**

$$q = \begin{cases} 1.0 \text{ for simply supported square column, } \lambda = .8b \\ 5.0 \text{ for a very narrow rectangula r column} \\ \quad \text{or plate with fixed unloaded edge, } \lambda = .67b \end{cases}$$

Irregular crumpling of the column instead of the regular folding occurs when the ratio "*t/b*" is small, that is, the buckling strength of the plate elements is low.

2.4.1.2.3 Stability of the Axial Collapse (Folding) Process

As mentioned earlier, all compressively-loaded structural elements may be subjected to instability. In an axially collapsing column, this manifests in a premature bending/global buckling of the column and, in most cases, results in a loss of energy absorption capacity. Since a premature loss of energy absorption capacity may completely alter the crash behavior of the system, often in a very unpredictable way, it is very important to understand the underlying causes and mechanisms that trigger these instabilities so that appropriate design countermeasures can be taken to avoid them.

Published literature on the subject of stability of the axial collapse process is very scarce, in spite of it being of great concern in the design of energy-absorbing structures. The reason is that the subject of collapse stability is complex and involves many underlying causes, each of which needs to be studied and understood. Some limited studies in this area, [44,45], have shown the loss of stability to be attributable to the sharply reduced bending stiffness of the collapsed portion of the column, which buckles in a global mode when a certain critical collapsed length is reached. Mahmood and Paluszny [37] elaborated on this concept and showed that fairly good correlation with experimental observations is achieved if the reduced flexural stiffness of the collapsed section is used in determining the critical length, which is calculated using Eqs. 2.4.1.2.3.1 and 2.4.1.2.3.2.

The critical (stability threshold) slenderness ratio for the collapsed length of the column is obtained by equating its buckling strength, using reduced/collapsed section properties, to the maximum axial load that the column will see during the collapse process, that is, the crippling corner load [9]

$$(l_c/p')_{cr} = [\pi^2 E_t/(\sigma_y)^2]^{0.5}[(1-\nu^2)\beta/K_1 E(t/b)^2]^{0.215} \qquad (2.4.1.2.3.1)$$

and the critical length for an axially collapsing column, that is, the threshold length at which the collapse process becomes unstable and the column will buckle globally when fully crushed

$$l_{cr} = (l_c)_{cr} / (1-\eta) \qquad (2.4.1.2.3.2)$$

where l_c is the collapsed length (see Figure 2.4.1.2.3.1), $(l_c)_{cr}$ its critical length, K_1 the corner crippling coefficient (function of (d/b) ratio [9]) and η the collapse efficiency, defined as ratio of axial crush to the original length of the column.

Mahmood and Paluszney [37] identify two other causes or mechanisms of crush instability. One, mentioned in Section 2.4.1.2.1 – Mathematical Models, is related to the "compactness" of the section. The other is related to the stability of rectangular box columns, in which the reduction in flexural stiffness of the collapsed section is much more pronounced and may be reduced almost to zero if the fold width exceeds half width of the section. Figure 2.4.1.2.3.2 shows examples of these three different types of instabilities. Interested readers are referred to [37] for more information.

The studies referred to are far from being exhaustive. More elaborate models are needed to explain the effects of the end boundaries and constraints, as well as load and geometric imperfections. The subject of stability of the axial collapse

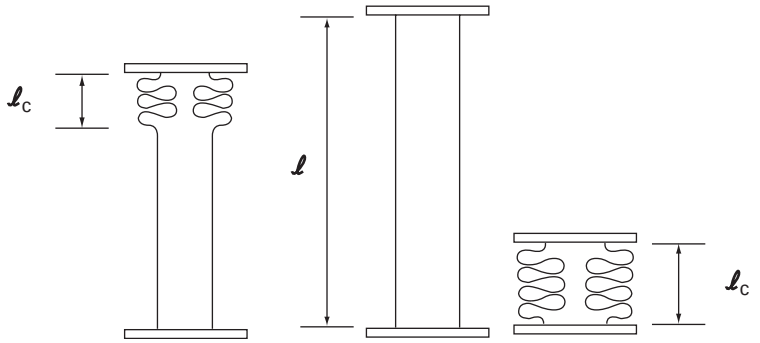

Fig. 2.4.1.2.3.1 **Collapsed length of axially compressed column**

process has been addressed in detail by Wierzbicki and Abramowicz [46] under the auspices of the Massachusetts Institute of Technology-Industry Crashworthiness Consortium.

2.4.1.3 Bending Collapse Mathematical Models

Although the bending mode of collapse is the predominant mechanism of structural collapse of beam type structural elements of today's vehicles, it has drawn considerably less attention than the axial collapse. This predominance of the bending mode is the result not only of the current design practice but also of natural tendency of structures to collapse in a mode that requires the least expenditure of energy; which in the case of thin-walled beam elements is bending. Pure bending failures are extremely rare in vehicle structures. In most collision scenarios except, perhaps, for side impact, mixed modes involving axial compression and bending or sometimes even torsion, will prevail. In these situations, component failure will be triggered at the location where compressive stress reaches critical value, causing the side or flange of the section to buckle locally, which initiates formation of a plastic hinge-type mechanism. Since the bending moment at the newly-created "plastic hinge" cannot increase any more, the moment distribution changes and a further increase of the external load creates additional hinges, until eventually, the number and the distribution of hinges is such that they turn the structure into a kinematically movable, linkage-type collapse mechanism. Thus, the overall collapse mechanism is controlled by hinge location and is dependent on the instantaneous strength (load capacity) distribution, which is a function of the loading state. Once the collapse mechanism has been developed, the extent of final deformation will depend on the energy

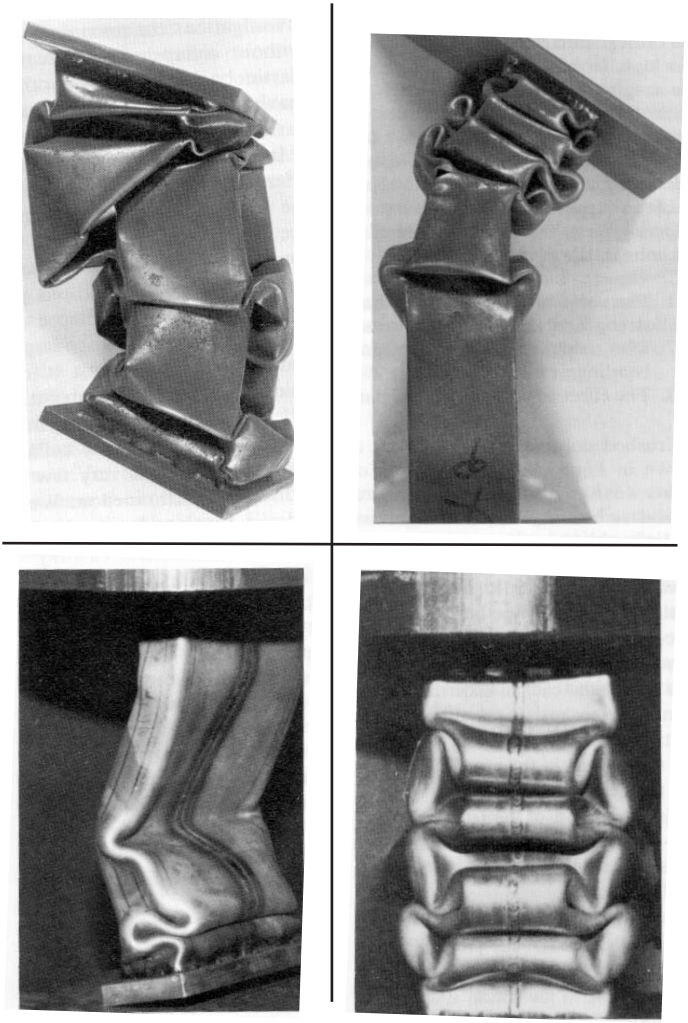

Fig. 2.4.1.2.3.2 **Samples of various modes of collapse**

absorbing capacity of the "plastic hinges". It is, therefore, important that the analytical models allow for both the local and the global (linkage kinematics) effects.

There are three different types of collapse modes observed in box-type beams subjected to bending. The first mode is associated with the collapse of a

compressively-loaded flange of a compact section that is identified by a uniform hinge mechanism composed of straight yield lines. The second mode is initiated by the flange collapse of non-compact sections, identified by non-uniform hinge mechanisms composed of curved yield lines. The third mode is initiated by the web collapse of narrow or stiffened flange beams. This mode is identified by a collapse mechanism similar to the fold forming mechanism encountered in axially collapsing columns.

An excellent treatise on bending collapse is found in Kecman's doctoral thesis [47]. The author starts with the premise, postulated above, that bending collapse is initiated by local buckling of the compressively-loaded flange and, using the concept of "effective flange width", develops expressions for the maximum bending strength capacity of a rectangular box section. If the critical local buckling stress (σ_{cr}) is less than material yield stress (σ_y), the compressively-loaded flange will buckle elastically, producing a non-linear stress distribution with the middle portion carrying considerably less load than the corners. Thus, in terms of the corner stress, the effective width of the flange has been reduced

$$d_e = d(0.7\sigma_{cr} / \sigma_y + 0.3) \qquad (2.4.1.3.1)$$

where critical local buckling stress is given by

$$\sigma_{cr} = K_1 \pi^2 E(t/d)^2 /12(1-\nu^2) \qquad (2.4.1.3.2)$$

with $K_1 \approx 5.23 + 0.16\,(d/b)$ being the flange buckling coefficient and d and b the sides of the section.

Different formulations are used for the maximum moment depending on the magnitude of the critical local buckling stress relative to the material yield strength.

$$M_{\max} = \begin{cases} M'_{\max} \\ M'_p + \dfrac{(M_p - M'_p)(\sigma_{cr} - \sigma_y)}{\sigma_y} \\ M_p \end{cases} \qquad (2.4.1.3.3)$$

where

$$M'_{max} = \sigma_y\, t\, b[(2d + b + d_e\,(3a/b + 2))] /3(d + b) \qquad (2.4.1.3.4)$$

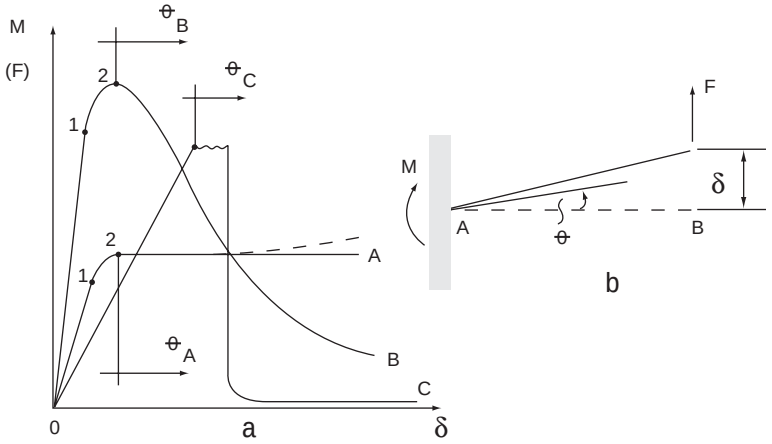

Fig. 2.4.1.3.1 **Load-deflection characteristics of a plastic hinge**

$$M'_p = \sigma_y \, t \, b(d + b/3) \tag{2.4.1.3.5}$$

$$M_p = \sigma_y \, t \, [d(b-t) + (b-2t)^2/2] \tag{2.4.1.3.6}$$

In addition to deriving expressions for the maximum bending strength, Kecman developed a comprehensive model of the "plastic hinge" mechanism and its bending collapse behavior/characteristic, achieving very good agreement with experimental results. An interesting diagram (Figure 2.4.1.3.1) reproduced from his thesis shows three different load deflection characteristics of a "plastic hinge". Curve A corresponds to the assumption of a classical "plastic hinge" where the bending strength of the hinge remains constant. This type of hinge occurs in solid sections or very thick-walled beams made of ductile material. Curve B is representative of thin-walled beams that buckle locally either before or after the maximum bending strength is reached. The drop-off in bending resistance is a function of the section "compactness", described in Section 2.4.1.2.3 – Stability of the Axial Collapse (folding) Process, the smaller the (*t/d*) ratio, the smaller (σ_{cr} / σ_y) and the steeper the drop-off. Automobile structural components generally fall into this category. Curve C corresponds to hinge collapse with material separation, which is characterized by an abrupt reduction in bending resistance. For more details on the subject of deep collapse behavior in bending the reader is referred to Kecman's thesis.

Mahmood and Paluszny [10,17], start with the same premise that bending collapse is initiated by the local buckling of a compressively-loaded plate element when the stress reaches the critical value σ_{cr} as given by Equation 11, except the buckling coefficient K_1 has been expanded to cover more general loading and geometry cases representative of vehicle structural components. In their formulation the buckling coefficient K_1 becomes a product of the crippling coefficient k_p (see Eq. 2.4.1.2.1.4), which is a function of aspect ratio α (Figure 2.4.1.2.1.5) or in other words section geometry, and a stress coefficient k_s, which is a function of the applied stress. Thus the expanded buckling coefficient k_e becomes

$$k_e = k_p\, k_s \tag{2.4.1.3.7}$$

Again, as in the Kecman model, the concept of "effective flange/web width" is employed to account for the non-linear stress distribution that results with the onset of elastic buckling. Their expression for the effective width varies from Kecman's and for a square box beam takes the form

$$b_{e/b} = 1.46[E(t/b)^2 / \beta\sigma_y]^{0.43} \tag{2.4.1.3.8}$$

Using some simplifying assumptions, which are explained in [48], a stiffness model is developed for a structural component composed of plate elements and subjected to crush loading. The whole procedure, including the axial loading, can be combined, as shown by the authors, into a simple computer program SECOLLAPSE [10], which is easily adaptable to personal computers. This procedure was applied by the authors to a B-pillar section of a compact car with excellent results (less than 3 percent error).

The use of the "effective width" method for determining the maximum strength, that is, the maximum load capacity of compressively-loaded, thin-walled structural components and/or their elements (bending), has its origin in structural engineering. The formulations used by the structural engineers differ somewhat from those developed by Mahmood and Paluszny and vary depending on the source. For instance, the formulation, recommended by American Iron and Steel Institute (AISI) [49] for the effective width of a compressively-loaded, simply-supported plate column, is of the form:

$$b_{e/b} = 1.9(t/b)\ (E/\sigma_y)^{0.5}\ [1-0.415(t/b)(E/\sigma_y)^{0.5}] \tag{2.4.1.3.9}$$

while that recommended by British Standard (B.S.) [50] is

$$b_{e/b} = [E(t/b)^2 / \sigma_y]^{0.33} \tag{2.4.1.3.10}$$

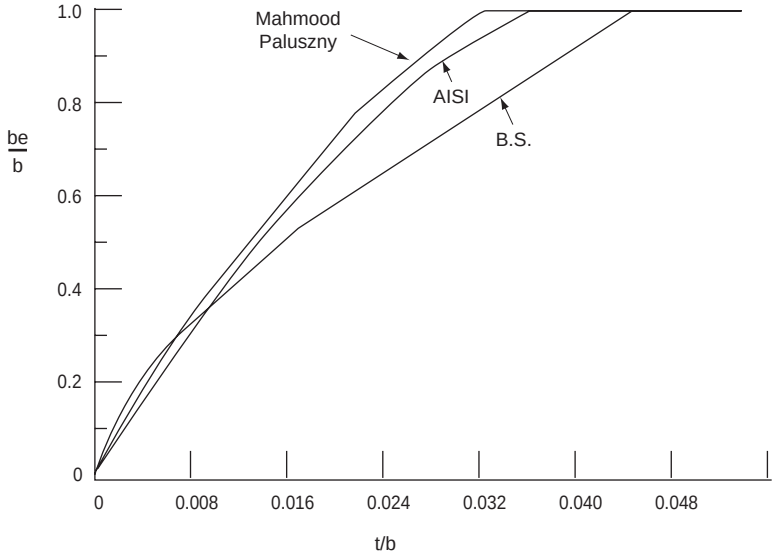

Fig. 2.4.1.3.2 **Comparison: effective width formulations for compressively loaded, simply supported plate**

Eqs. 2.4.1.3.8, 2.4.1.3.9 and 2.4.1.3.10 are plotted and compared in Figure 2.4.1.3.2 taken from [51]. As expected, both the AISI and B.S. formulations will give more conservative estimates of load capacity. This is of major concern in structural engineering where the service load, which is specified a priori, is not expected ever to reach the ultimate strength of the structure, and an underestimate of the structure's strength will result in a safer design. In crash energy management, the design criteria are different. The structure's configuration, its mode of collapse and its resistance to crush (its crush strength), dictate the load magnitude corresponding to that particular mode of collapse. Thus, an underestimate of peak crush load, generated by a collapsing structure, may trigger a premature failure of its support structure, which is designed to carry the peak load. This could result in an undesirable mode of collapse. Therefore, a very accurate estimate of the maximum crush load is imperative if predictable crash performance and lightweight designs are to be achieved.

The above work was extended by Mahmood and Paluszny [48] to deep-bending collapse behavior and crush characteristics of automotive-type structures subject to bending and mixed axial-bending loading states. Two methods have been

developed for modeling deep collapse of thin-walled sections: a force method or strength approach and a displacement method or energy approach. The component is divided into individual sub-elemental plates and its cross section is identified by nodes that coincide with the plate. In the force method, the component crush characteristic is determined as functions of the sub-element boundary conditions, geometry and the applied stress distribution, which, in the case of

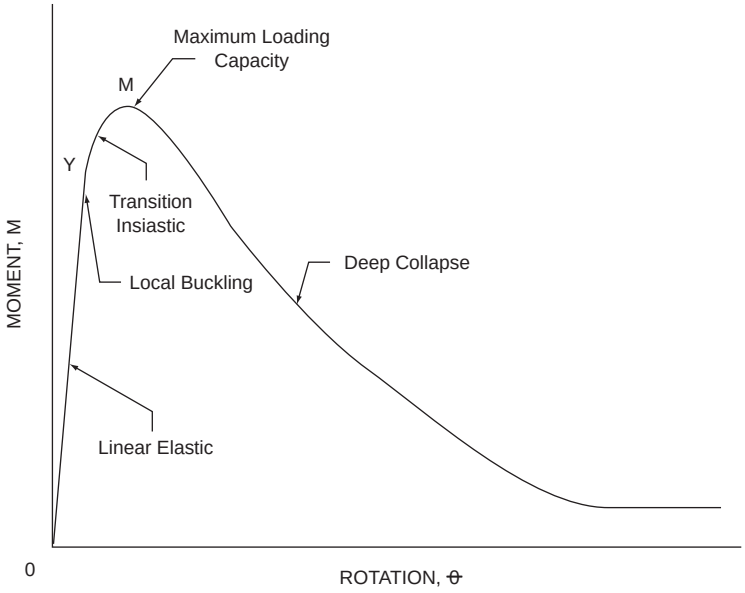

Fig. 2.4.1.3.3 **Moment-rotation characteristics of thin-walled beam**

bending collapse, is expressed as moment-rotation (M-θ) such as shown in Figure 2.4.1.3.3, taken from [48]. In the displacement method, the collapse mode and failure mechanism of each sub-element is assumed from the nodal stress distribution. This latter method was adopted in [48]. The following briefly summarizes the pertinent material from [48] to acquaint the reader more closely with the mechanics of bending collapse.

In designing the vehicle structure for crash energy management, the designer is concerned with its maximum strength (load capacity), its mode of collapse, the energy absorbed and the residual strength. When a thin-walled structural

component is subjected to a gradually increasing bending load, localized elastic buckling initiates the collapse and the energy absorption processes (Point Y in Figure 2.4.1.3.3). With the increasing moment capacity (Point M) and starts to collapse. In the plastic (deep collapse) region, the moment capacity decays exponentially with the collapse (increasing angle θ), which take the form of localized failure sites that constitute the "plastic hinge". The energy absorbed is proportional to the area under the M-θ curve. The initial portion of the curve from zero to the point of maximum bending capacity (segment O-M) usually can be neglected, since there is very little energy absorbed in that initial deformation. Most of the collision energy is converted into the plastic deformation energy of the hinge, which corresponds to the area under the tail segment of the M-θ curve, that is, after the maximum bending capacity has been reached.

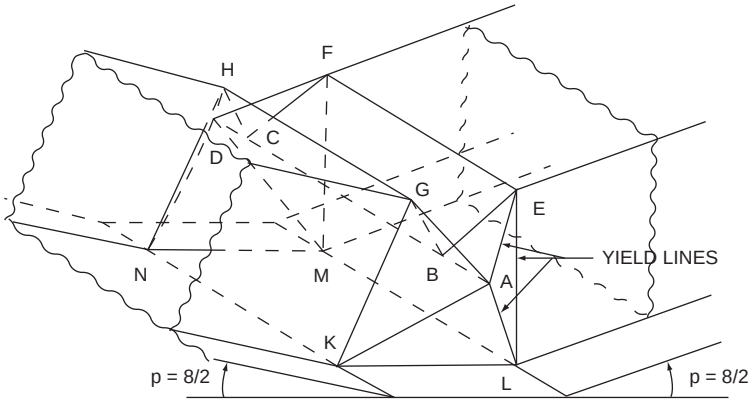

Fig. 2.4.1.3.4 **Hiinge mechanism of a uniaxial bend ing of a hat**

The shape and geometry of the collapsed mechanism plays a significant role in determining the amount of energy absorbed. Although the collapse mechanism appears to be complex, on closer examination, distinct deformation mechanisms such as bending about stationary hinge/yield lines and rolling along specific yield lines can still be identified. Figures 2.4.1.3.4 and 2.4.1.3.5 show schematically two such mechanisms of bending collapse: a uniaxial bending collapse of a hat

section and a combined bending (bending about non-principal axis) of a rectangular section.

Assuming that hinge deformation involves an inextensional process, that is, the neutral surface does not stretch during bending, and employing the plastic limit analysis techniques, the deformation energy dissipated in the bending and rolling mechanisms can be calculated. The work dissipated in bending

$$W_b = M_p L \psi \tag{2.4.1.3.11}$$

where $M_p = \sigma_y t^2/4$ is fully plastic moment per unit length of the yield line, σ_y the yield stress, t the thickness, L the length of the yield line and ψ the angle of relative rotation between the two surfaces adjoining the yield line. The energy absorbed in a rolling yield line of length L is

$$W_r = 2M_p A_r/r \tag{2.4.1.3.12}$$

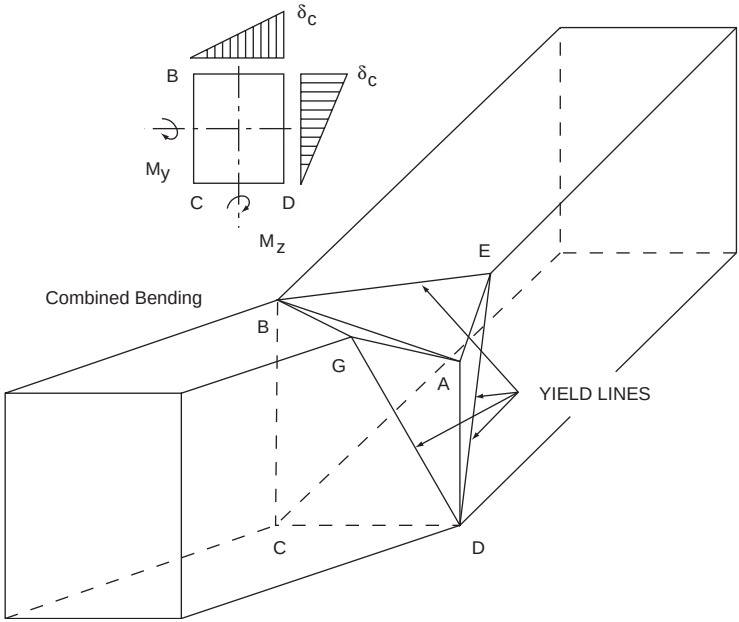

Fig. 2.4.1.3.5 **Hinge mechanism of a rectangular box section: combined bending**

where A_r is the area swept by the yield line during rolling deformation and r is the radius of rolling curvature. Again, the above procedure can be computerized. A flowchart for the computer program DEEPCOLLAPSE, developed by the authors, is included in the paper. Figures 2.4.1.3.6 and 2.4.1.3.7, taken from the paper, compare the results of the DEEPCOLLAPSE program with the experimental data obtained from the Cranfield Institute of Technology on bending collapse behavior of a slender rectangular hat section. As can be seen from Figures 2.4.1.3.6 and 2.4.1.3.7, very good agreement with test results is achievable with relatively simply models, providing the designer with a fairly reliable, yet simple and practical design aid.

The following are some additional thoughts on bending collapse of thin-walled structures. The energy absorption capacity of beam-type components can be enhanced by strategically placed reinforcements core filling, discussed earlier and involving structural foams. A word of caution: in order to be effective, the reinforcement must deform "in harmony" with the basic section. If the reinforcement is too "soft" it may be ineffective, while if it is too "hard" it may shift the point of failure to an undesirable location or may tear the section apart and reduce its crush performance/characteristic even below that of the "virgin" section. The superiority of beams over sheets in terms of the energy absorbing capacity in bending is best demonstrated by bending a sheet of paper and comparing its resistance to that of a cylinder made of the same sheet. However, this comparison does not hold to the same extent if the sheet is subject to stretching or "rolling" deformation. The relative contribution of sheets to the energy absorption also increases with the length of the yield line along which plastic deformation takes place. It should be noted that sheet cladding/shear panels may have significant effect on the internal load distribution in structural frameworks, and hence, on hinge location and the overall collapse mechanism. Once the collapse mechanism has started, however, most of the energy absorption will take place in the beam-type structural elements.

2.4.1.4 Combined Loading

As noted in the Section 2.4.1.3 – Bending Collapse Mathematical Models, the collapse mode resulting from combined loading states are the dominant failure modes found in the load bearing structural components of today's automobiles during impacts. These modes occur as biaxial bending, axial-bending (both uniaxial and biaxial) and the axial-bending-torsion modes, which are the most complex insofar as analytical modeling is concerned.

Biaxial bending occurs when the bending moment axis is at an angle to the principal axis. In biaxial bending, the plastic neutral axes (in thin-walled sections) are,

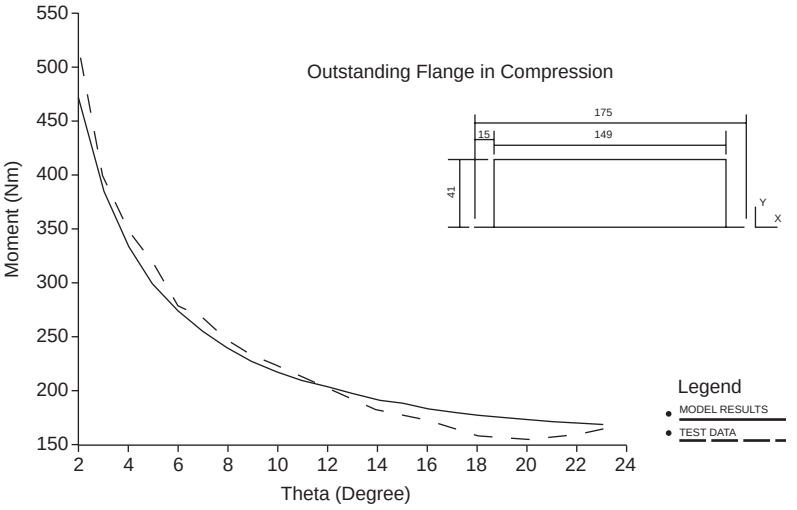

Fig. 2.4.1.3.6 **Bending collapse characteristic of hat section: outstanding flange in compression**

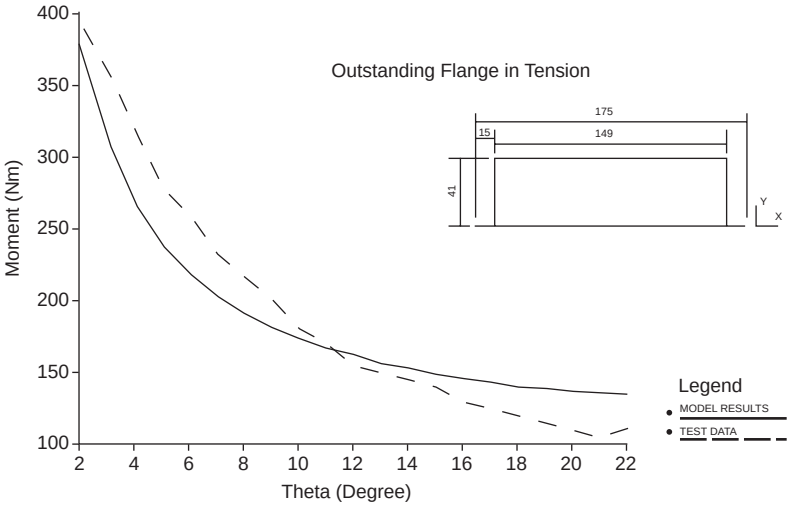

Fig. 2.4.1.3.7 **Bending collapse characteristic of hat section: outstanding flange in tension**

generally, inclined either to the bending moment axis or the elastic axes of the section. The analytical modeling process used in this case is identical to the process used in the case of uniaxial bending, which was described in Section 2.4.1.3 – Bending Collapse

Mathematical Models. The computation process developed by Mahmood and Paluszny [17] and incorporated in the SECOLLAPSE computer program (also described in Section 2.4.1.3), is applicable to combined loading cases involving both the biaxial bending and axial-bending collapse modes. The difficulty normally encountered in the literature on combined loading cases is that different components and different loading cases require different failure surfaces, which determine the mode of failure. As shown in [17], the SECOLLAPSE program eliminates this difficulty in a very elegant and simple way. The strength of each sub-element of a component section is related to the total applied stress. When one of the sub-elements reaches its maximum (crippling) strength, the geometry of the section is distorted in such a way that the collapse of the sub-element induces the collapse of the whole component. Thus, SECOLLAPSE automatically generates a failure surface appropriate to the component and the loading case investigated. Figure 2.4.1.4.1 shows a failure surface obtained for a plate-type steel section (σ_y = 43 ksi and σ_u = 50 ksi) subjected to bending moments about Z- and Y-axes.

Verification of analytical models is normally done in well-controlled laboratory tests. Although seemingly simple, the bending collapse/crush tests are, in reality, extremely difficult to execute with reasonable accuracy, particularly the biaxial bending of thin wall sections involving large deformations (rotations).

These tests are usually of a built-in cantilever type. The difficulties arise from the freedom of lateral movement of the tip of the cantilever, which is controlled by the effective rotation axis of the buckled hinge. Thus, extreme care must be exercised in the mounting of the test sample, load alignments and measurements. Biaxial bending tests are conducted mainly to investigate the component behavior and to check the possibilities of predicting the multi-axial collapse behavior on the bases of uniaxial data. Figure 2.4.1.4.2 shows two basic test arrangements used in biaxial bending tests of thin walled beams. These tests were developed by Cranfield Impact Center [52].

In the restrained mode, the cantilever tip is restrained in the lateral direction by cables whose pivots lay on a straight line passing though the hinge. The hinge is forced to collapse about a specified axis, and the moment causing the collapse is measured by load cells located in the sidestays BD and BG and the main load

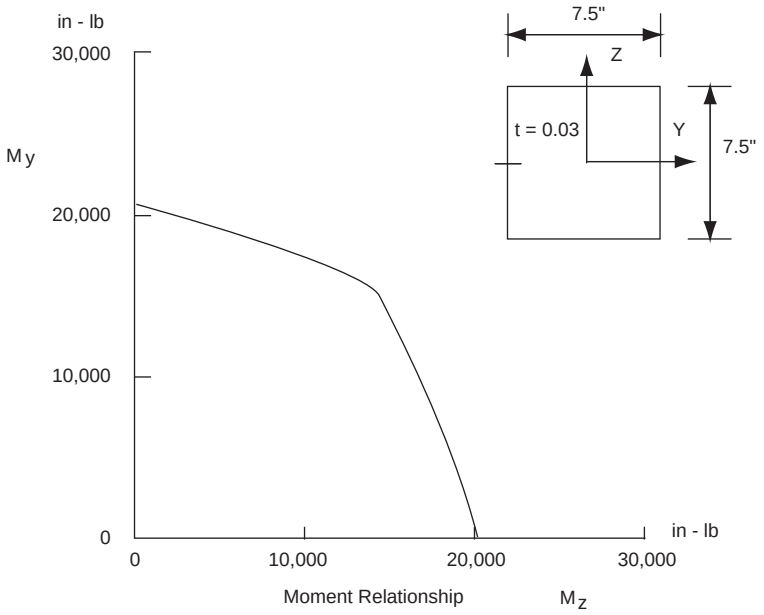

Fig. 2.4.1.4.1 **Failure surface of thin-walled square box section**

link BJ. During deep collapse, the hinge rotation angle is calculated in a similar way as in uniaxial bending.
In the free mode, the axis of bending is constant and the cantilever tip is free to move in any direction. The displacements of the tip are measured in two directions, and the load link BC is kept parallel to its original direction by moving the support C along the beam DE. The resultant moment has a constant axis parallel with the Z-axis of the rig. In deep collapse, since the hinge axis is not known in advance and may be moving during collapse, the instantaneous direction of hinge rotation is calculated incrementally from the displacement traces.

The mechanics of the more complex modes of collapse of thin-walled beam sections, such as those resulting from combined loading states that involve axial compression, bending and torsion, are still not well understood and, as yet, no analytical models exist. In most cases, the effects of torsion are likely to be negligible and can be safely neglected in arriving at a satisfactory design

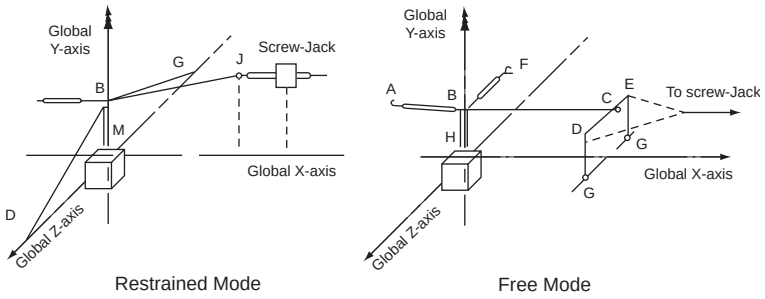

Fig. 2.4.1.4.2 **Test arrangements for biaxial bending**

configuration. In rare cases, where these modes are unavoidable, recourse must be taken to FE modeling. The FE model, when correctly executed, should provide adequate information for making the design decisions. The other opinion, is testing, which, as described above for biaxial bending loading case, is cumbersome and requires great care in its execution. The development of "simpler" design-oriented models, of the types developed for the biaxial bending and axial-bending collapse modes, hinges simply on the question of economics of need versus cost.

2.4.1.5 Structural Joints

Structural joints define the end conditions and constraints for structural load-carrying elements such as beams and columns. Thus, they have a profound effect on the response (deformation/rotation under load) of these elements and, consequently, their load carrying capacity and stability when compressively loaded. In other words, the structural joints control, to a considerable degree, the stiffness of the vehicle structural systems. This has been found to be true in the dynamic (NVH) studies of vehicle structures [26, 53, 54] and applies equally well in crash energy management. The joints are some of the more critical elements in structures composed of beam and column type components.

Structural joints are complex, 3-dimensional structures which are subjected, in crash situations, to equally complex loading states usually composed of several loading components: axial, bending and torsion. Because of these complexities, no "simple" models, of the kind discussed in the previous sections, have, as yet, been developed. Current crash analysis of beam-type structural systems [55] relies heavily on experience and available data banks. Cranfield Impact Center and Ford of Europe pioneered deep collapse tests of structural joints and

developed an extensive library of crash characteristics (load-deformation and mode/s) of existing structural joints. It should be understood, however, that most of these joint developments evolved over the years to satisfy dynamic (NVH), fatigue/durability and manufacturing considerations. Crash energy management requirements are much more demanding, particularly if weight savings are to be achieved. They may, very likely, require development of new joint concepts, possibly involving use of foam fillers and/or reinforcements, to enhance structural integrity during various collision modes. The tools most likely to be used in their design and development rely on non-linear FE plate and shell analysis, supported with appropriate tests. From these studies, a library of basic joint configurations and associated load-deformation characteristics could be developed for future designs and/or modification of existing structures for NVH and crash performance.

2.4.2 Design of Substructures

After designing a component for energy absorption and crush loads through a given amount of axial crush, it becomes necessary to check the function of that component as a part of the structural frames or substructure to which it belongs. An example is the behavior of the rail when assembled with the subframe, shock-tower, apron and shotgun, or the behavior of the rail when attached to the back-up structure (see Figure 2.4.2.1.)

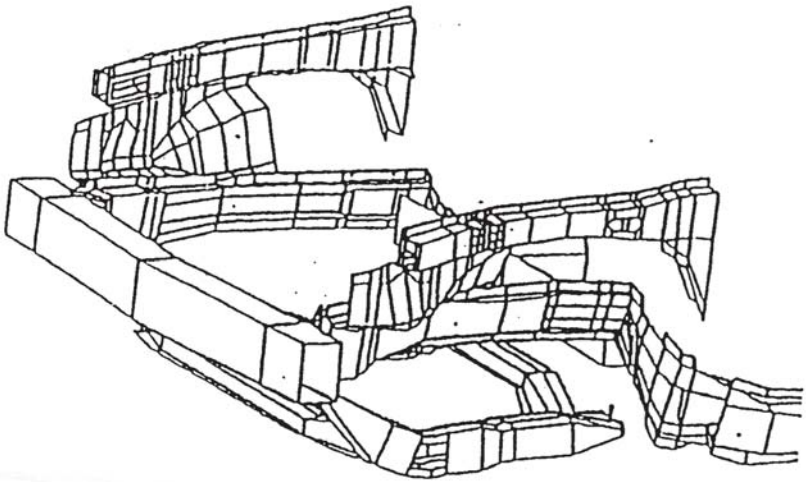

Fig. 2.4.2.1 **3-D front crash model**

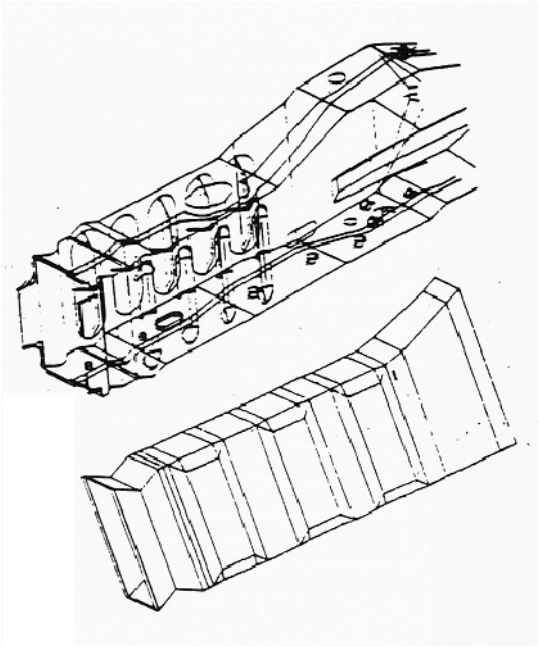

Fig. 2.4.2.2 **Two convolution design concepts**

To illustrate this point, Figure 2.4.2.2 shows a vehicle front rail that was designed to absorb energy by providing convolutions as a way to make the section fold, rather than bend, while crushing. To ensure that the rail also folds when crushed as a part of the frame, the substructure, shown in Figure 2.4.2.3, was analyzed. One complete side rail was tested and the results, shown in Figure 2.4.2.4, correlated very well with the test. That proved that the folding mode could be maintained while the structure is being crushed as part of the vehicle.

2.4.2.1 General Analysis Methods

The analysis methods for the design and analysis of these substructures are simplified finite elements with collapsible-type beams such as VCRUSH, described in [17,53]. Other computer programs use the hybrid methods approach was KRASH, of Cranfield. Also, LS-DYNA introduced a beam element that handles collapse by bending using the plastic hinge concept, as shown in Figure 2.4.2.1.1 [15]. It is obvious that the crushable beam element technology is fundamental to the development of a "super collapsible beam element". Because of its importance

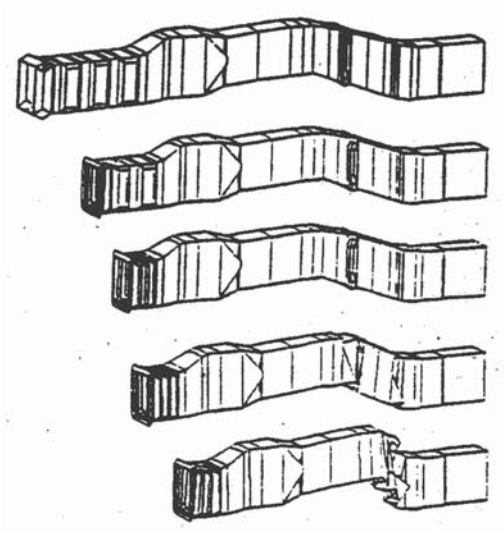

Fig. 2.4.2.3 **Collapse sequence in a convoluted design**

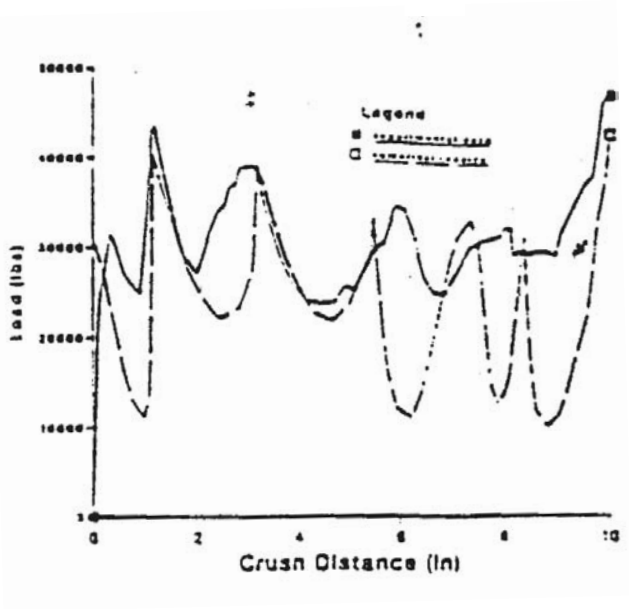

Fig. 2.4.2.4 **Performance of one rail**

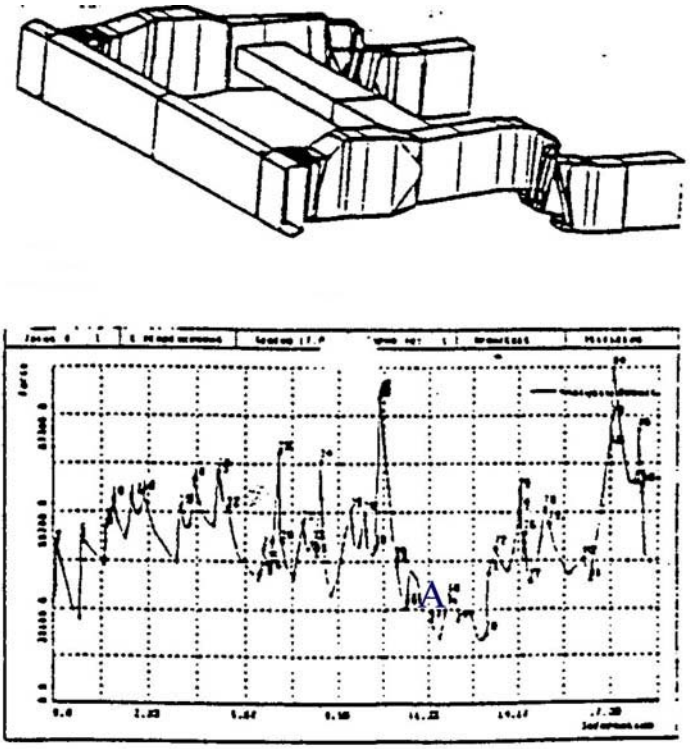

Fig. 2.4.2.1.1 **Performance of a full front end frame, simulation vs. test**

as a design tool, further description of that development is presented in Section 2.4.2.2 – Super-collapsible Beam.

2.4.2.2 Super-Collapsible Beam

The finite beam element theory is very well documented in the literature [56]. Automotive components are generally made of thin-walled sheet metal that can be divided into many sub-elements. A sub-element is a four-node plate or shell supported by the adjacent sub-element. The mode of collapse and strength characteristic of the sub-element is well presented in [10]. Mahmood et al [10] indicate that the failure process can be divided into four stages:

1. elastic: $\sigma < \sigma_{cr}$
2. buckled: $\sigma_{cr} \leq \sigma < \sigma_{max}$

3. crippling: $\sigma_{max} \geq \sigma \geq \sigma_{min}$
4. folding: $\sigma_{cor} \geq \sigma \geq \sigma_{min}$

where σ is the applied stress and σ_{cr}, σ_{max}, σ_{min} and σ_{cor} are the buckling, maximum, minimum and corner crush stresses of the plate. These stresses can be calculated by the thin-walled plate buckling theory and the details are given by Mahmood et al [10].

In the elastic stage, the entire plate is effective in stiffness contribution to the section. In the buckled stage, the middle portion deforms out of plane and the

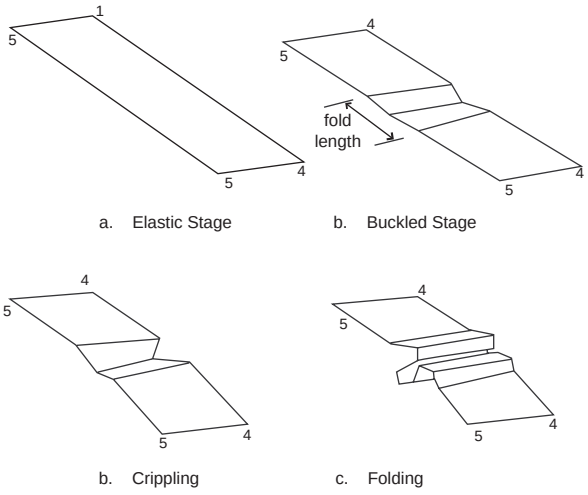

Fig. 2.4.2.2.1 **Sub-element deformation**

effective area is the linear interpolation between the full area when $\sigma = \sigma_{cr}$ and the zero area when $\sigma = \sigma_{max}$, depending on the stress level. In the crippling and folding stages, the plane section-remain-plane assumption is no longer valid because of the large distortion. The effective section stiffness is formulated for the whole section, as will be discussed in the Section 2.4.2.3 – Thin-walled Finite Beam Element. The deformation of the sub-element in the four stages can be idealized as illustrated in Figure 2.4.2.2.1.

For moderate thin-walled sub-elements it is possible that:

$$\sigma_{cr} > \sigma_y$$

where σ_y is the yield stress. In this case, yielding occurs earlier than buckling and the second stage should be yielding stage.

2.4.2.3 Thin-Walled Finite Beam Element

Although the beam element is the combination of sub-elements, it can be treated as classical beam in structural analysis. The emphasis of this section is placed on the failure mode of the beam element due to the crippling of the thin plates and the element stiffness formulation after sub-element buckling. The failure mode of a general thin-walled section component can be very complicated due the combined axial force and bending moments. Extensive test observations, however, give indications that failure modes usually follow certain rules, and these rules make the failure mode predictable. The rules, after simplification and idealization, are summarized as follows:

- The first crippled sub-element buckles inboard and the adjacent ones buckle outboard.
- The fold length of the first crippled sub-element controls the length of the hinge.
- Deformation pattern is approximately proportional to the stress pattern at crippling.

Plane-sections-remain-plane assumption is used, which could cause some error locally but should model the element deformation fairly well before crippling when the deformation is small. With the above rules the failure mode of the element in Figure 2.4.2.3.1 can be predicted as shown in Figure 2.4.2.3.2. For each fold, the axial deformation at section C.G. and the rotation can be calculated as:

$$\varepsilon = d_1/d_2\varepsilon_n \tag{2.4.2.3.1}$$

$$\theta = artg(\varepsilon_n/d_2) \tag{2.4.2.3.2}$$

where ε_n is the fold length at first crushed node, d_1, is the distance from the C.G. to the neutral axis and d_2 is the distance from the first crushed node to the neutral axis.

As with the sub-elements, the beam element also fails in four stages. The axial force-deformation (P-δ) and bending moment-rotation (M-θ) relationships can be

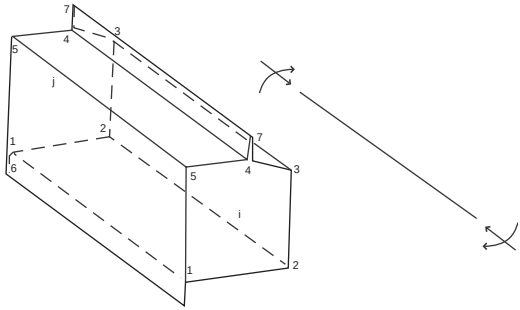

Fig. 2.4.2.3.1 **Typical thin-walled component**

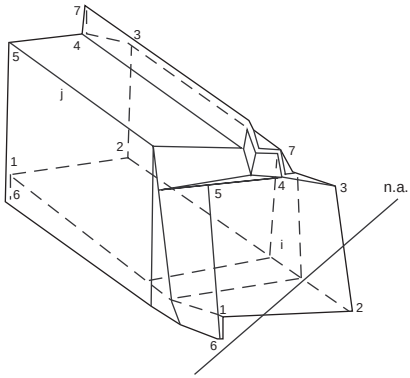

Fig. 2.4.2.3.2 **Section failure mode**

divided into the four stages. The idealization of extensive experiment and analysis results gives the simple P-δ and M-θ curves shown in Figure 2.4.2.3.3.
The four stages and some critical points can easily be identified on the curves. Each cycle represents a fold process and e, q represent the axial, bending deformation for each cycle. P_{cr}, P_{max}, P_{min} and P_{cor} represent the axial forces at the buckling, crippling, minimum and corner crushing, which can be calculated from plate stability theory. The same is true for M_{cr}, M_{max}, M_{min} and M_{cor}. Therefore, the critical point on the curves in Figures 2.4.2.3.3 and 2.4.2.3.4 can be pre-determined. Although the fitted curve between the critical points may not exactly represent the real curves, the energy dissipation of the element crushing is well managed.

2.4.2.4 Structural Programming

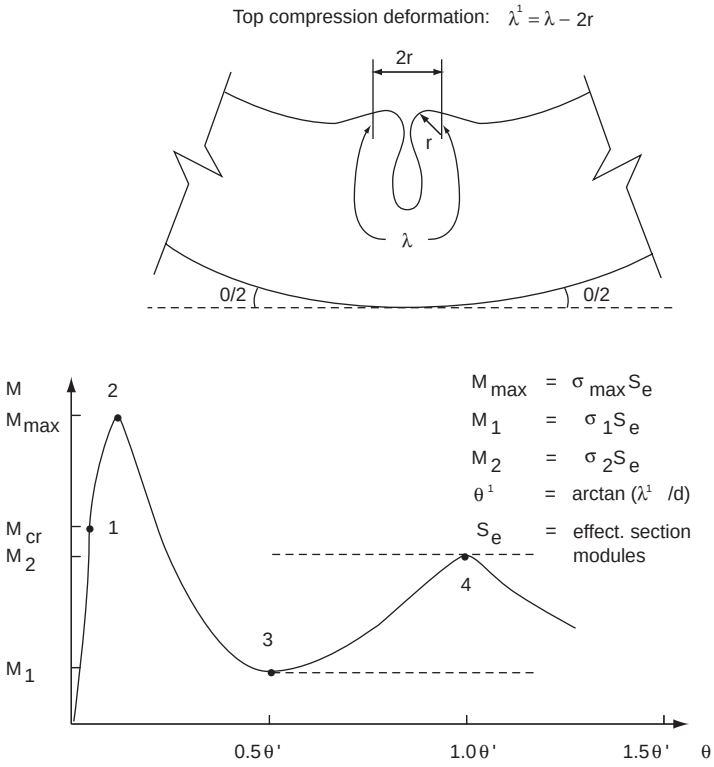

Fig. 2.4.2.3.3 **Bending crash mode**

To make the element realistically capable of modeling and analyzing crush/crash of automotive structures, it is important to consider other important factors in finite element programming, such as large-deformation, tapered beam element, contact and strain-rate effect.

The buckling-crippling-folding process usually involves severely large deformation and the element stiffness formulation should consider this effect. A simple and realistic way to follow is starting from the assumption on the basic strain variables in 2-D coordinates:

$$\varepsilon_r = y'' \qquad (2.4.2.4.1)$$

$$\varepsilon_a = x/(1+{}^1/_2 y') \qquad (2.4.2.4.2)$$

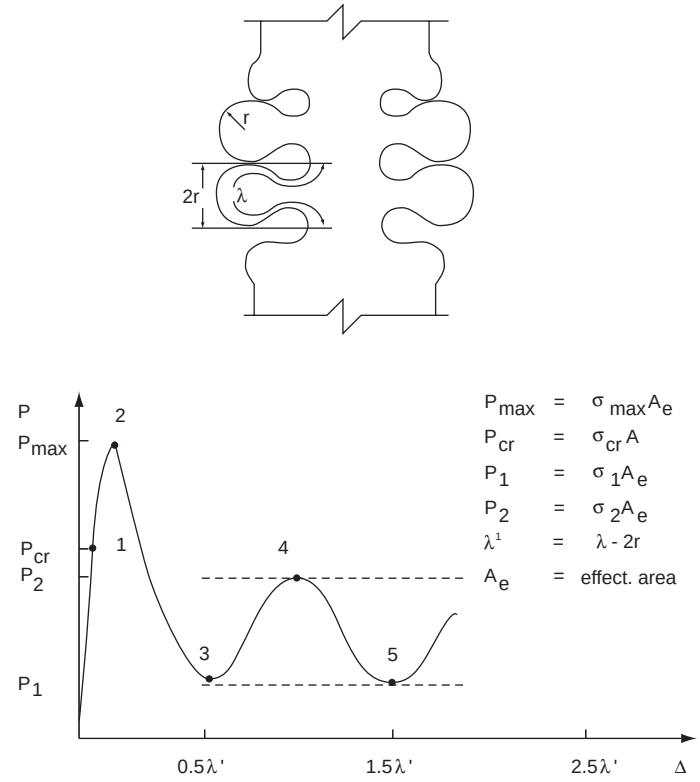

Fig. 2.4.2.3.4 **Axial crash mode**

where ε_r and ε_a, are the rotational and axial strains, x is the axial deformation and y' and y'' are the first and second order derivatives of the vertical displacement y. The above expressions are the same as those of small deformation except the term $^1/_2 y'$. The resultant stiffness can be derived as:

$$[K] = [K_e] + [K_a] + [K_b] + [K_g] \qquad (2.4.2.4.3)$$

where $[K_e]$ is the small deformation stiffness, $[K_a]$ and $[K_b]$ are the axial and bending stiffness due to large deformation and $[K_g]$ is the bending stiffness due to axial force, usually called geometric stiffness. $[K_a]$ and $[K_b]$ are the functions of displacement y and $[K_g]$ is function of axial force.

The complexity of automotive structures often requires the element to have different section shapes at the two ends. Therefore, it is necessary to modify the

local buckling theory for tapered sub-elements. It is also necessary to consider the tapered element effect in stiffness formulation.

2.5 Vehicle Front Structure Design for Different Impact Modes

Assessment of vehicle structural crashworthiness performance originated in the United States before World War II. This included rollover tests and vehicle-to-barrier tests as well. During the 1950's, similar tests started in Europe. Currently in the U.S., frontal impact testing with a rigid barrier (full overlap) at speeds up to 35 mph is the primary mode for evaluating front structure performance. In Europe, however, the corresponding test is an offset (40% overlap) test with a deformable barrier at 37.5 mph. The offset test arguably is a closer representation of field vehicle-to-vehicle crash [57]. Recently, U.S. manufacturers adopted offset impact testing with a deformable barrier similar to the Insurance Institute for Highway Safety (IIHS) test. This test is conducted at 40 mph, otherwise is similar to the European test.

As a result of these practices, the vehicle structure, along with its restraint system, is designed to provide optimum protection to its occupants with no regard to occupant's safety of the colliding vehicle. Research published in the last five years [58-60] pointed out that severe injuries occur in incompatible vehicle-to-vehicle crashes.

Currently, research is being conducted by the National Highway Traffic Safety Administration (NHTSA) to evaluate vehicle deformations and the potential for occupant protection in car-to-truck and car-to-SUV situations during various types of frontal collisions such as head-on, offset head-on or oblique frontal. [61-63]. Similar research is also being conducted by General Motors and Ford to develop vehicle front structures with countermeasures for occupant protection in "incompatible" vehicles. Researchers from NHTSA and the automobile industry have been exchanging information that should ultimately yield an appropriate test (or tests) for crashworthiness assessment of vehicle front structures. Due to the difference in vehicle mix between Europe and the U.S., research in Europe [64] is focusing on large-to-small car frontal collisions. The ultimate goal of this research in both the U.S. and in Europe is to develop a test procedure that ensures occupants' safety in their own vehicles as well as those in partner vehicles in the event of a collision. These, however, should not ignore the significant number of real-world collisions involving single vehicles striking objects such as trees, bridge abutments, roadside structures and buildings.

Some automobile manufacturers have already started designing their vehicles with the protection of other vehicles' occupants in mind in offset frontal car-to-car testing. For example, Renault designed its super mini-car (Twingo) for compatibility with their mid-size car Laguna, which is 1.45 times heavier than the Twingo [65]. Also, Audi developed the A8 car for compatibility with heavier cars [66]. Another example is Daimler Benz, which developed the MCC car for compatibility with the heavier E-class car [67].

In light of this trend, the vehicle front structure may soon have to be designed to manage the energy and protect its occupants as well as its partner vehicles' occupants. The implication of all these crash test requirements is additional complexity in designing the front structure, particularly when constraints on weight, space, and cost are considered.

In this section, the effect of designing vehicles' front end for NCAP and offset testing with deformable barrier is discussed. Then, some of the published research on compatibility of vehicles in frontal crashes will be reviewed including the mechanics of collision. This is followed by an examination of the challenge of designing vehicle's front structure for vehicle-to-vehicle frontal crashes, and identifying strategies of solutions that are balanced with the safety of occupants in the barrier-impact modes. Finally, some of the analytical tools that can be used in evaluating design of vehicles for these modes are assessed.

2.5.1 Vehicle Front Structure Design for Current Standards

2.5.1.1 FMVSS 208

All passenger vehicles sold in the U.S. are required to comply with Federal Motor Vehicle Safety (FMVSS) 208. The standard sets performance requirements for occupant protection in frontal crash, which are measured using anthropomorphic test devices (dummies) located in the front seat. Either a passive restraint (air bag) or a combination of air bag and lap/shoulder belt system may restrain the dummies. Testing or analysis demonstrates compliance with FMVSS 208. Typically, it is achieved by testing, where a full-scale vehicle is launched to impact a rigid barrier from 30 mph at 90 degrees to the barrier surface. In 1999, FMVSS was amended to allow for a reduction in air bag power to reduce the potential harm for vehicle occupants sitting close to the air bag. Although not required by regulations, some auto manufacturers conduct frontal crashes with narrow objects, such as poles, rigid offset barriers and objects simulating impact with animals.

2.5.1.2 NCAP Test

The New Car Assessment Performance (NCAP) test was initiated by NHTSA in the early 1980's. It is identical to FMVSS 208, except for increasing the impact speed to 35 mph and restraining the front dummies by lap/shoulder belts in addition to the passive air bag. When designing a vehicle's front structure for NCAP, the vehicle deceleration-time history and the maximum crush distance are selected to protect the occupants of that vehicle. For both the heavy (large) and light (small) vehicles, the maximum deformation is dictated by the state of technology of the restraint system. Thus, regardless of the vehicle mass, the decelerations of these vehicles during crash are approximately the same. Figure 2.5.1.2.1, showing the deceleration versus crush in an NCAP test of a medium-size vehicle that weighs 3190 lbs. and a full-size vehicle that weighs 4250 lbs. illustrates the point. However, the dynamic crash loads (on average) on the front structure in the light car are less than the corresponding loads in the heavy car. In other words, designing vehicles for NCAP testing promotes the stiffness of the structure to be proportional to the mass of the vehicle. The heavier the vehicle, the stiffer its front structure will be.

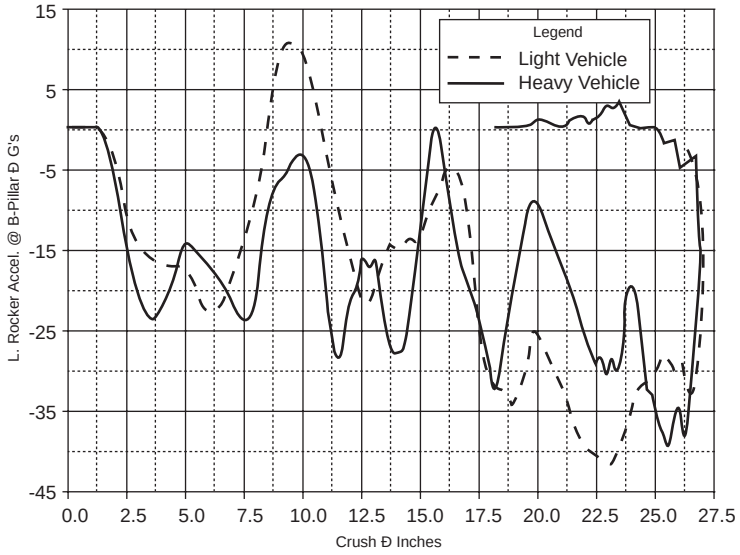

Fig. 2.5.1.2.1 **Deceleration of light and heavy vehicles: NCAP testing**

When two vehicles designed for NCAP testing are involved in a frontal collision, the deformation in the heavier vehicle is expected to be more than that in the lighter vehicle, and equals the deformation of the small car times the square root of the mass ratio (M_{small} / M_{large}) [68]. But, that doesn't happen in actual crashes, since the deformation zone in the heavy vehicle can't be activated. As a result, the small car likely sustains more crush with potential for intrusion into the passenger compartment [68].

2.5.1.3 IIHS Test

When designing vehicle front structure for offset impact with deformable barrier, both the light and heavy vehicles cause bottoming of the barrier material. The energy absorbed by the barrier constitutes a very small percentage of the total energy absorbed by the structure of the heavy vehicle. On the other hand, the

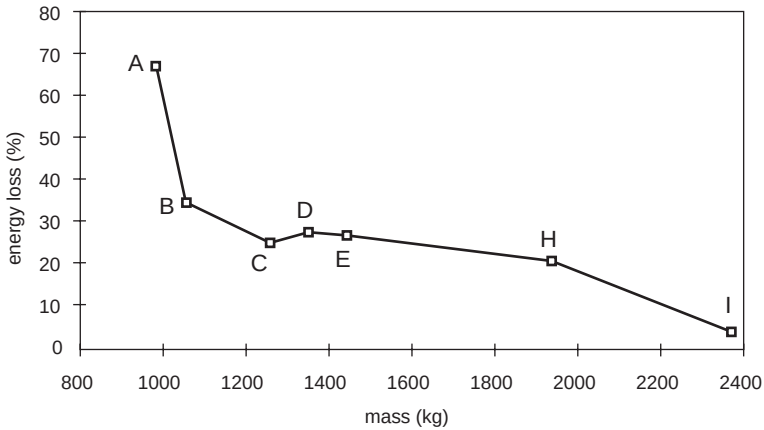

Fig. 2.5.1.3.1 **Energy loss in frontal offset deformable crash test**

energy absorbed by the barrier represents a higher percentage of the lighter vehicle's kinetic energy. Test data [69] supports this observation, showing energy loss in the deformable barrier vs. car mass (Figure 2.5.1.3.1). Furthermore, a similar conclusion was reported by Ragland [62], and also by Ingo Kallina [68]. Consequently, both the light and heavy vehicles don't experience the same crash

severity in this type of test. In fact, the impact testing with deformable barrier is more severe on the heavier vehicle, a condition that promotes a stiffer front structure to compensate for that severity [68,70].

2.5.2 Vehicle-to-Vehicle Frontal Collisions

Vehicle-to-vehicle collisions include many types of impact modes. In this chapter, only frontal collision are considered, and only the case of head-on impact between two vehicles, as shown in Figure 2.5.2.1, are presented. Even after narrowing the scope to this impact mode, the issue of designing vehicles to be compatible with others in frontal collision is very complex. This is because vehicles on the roads

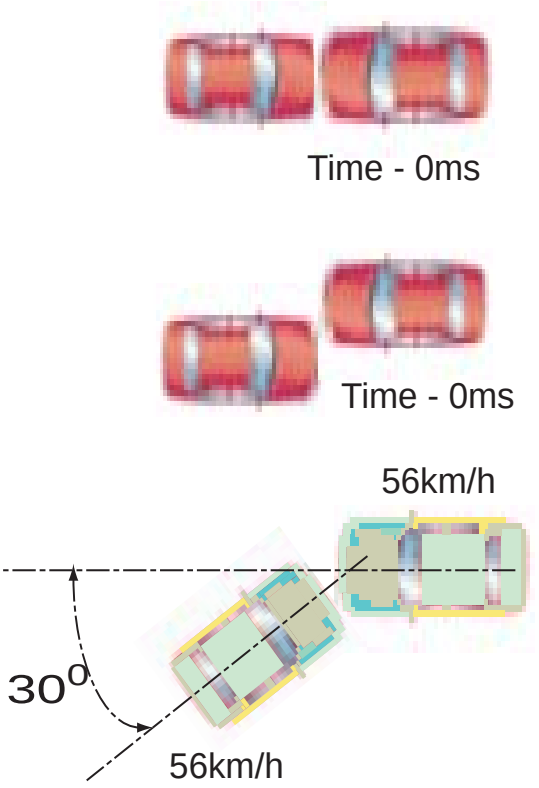

Fig. 2.5.2.1 **Types of vehicle-to-vehicle frontal crashes**

have different masses, geometries, and stiffness. In fact, in most crashes between two vehicles, it is generally the lighter vehicle that is damaged more extensively and whose occupants are subjected to higher loads. Thus, it may be beneficial to first review some preliminary relationships on collisions, such as the laws of conservation of momentum and energy as well as methods of computing distribution of energy and deformation in this type of collision. This is reviewed in Section 2.5.2.1 – Preliminary Relationships in Head-on Frontal Collision. In Section 2.5.2.2 – Strategies for Designing Front Structures for Head-on Impact, the possibilities of finding design solutions are discussed, and alternative design strategies are described. Finally, in Section 2.5.3 – Assessment of Analytical Tools, the analytical tools that help in designing vehicles' front end for vehicle-to-vehicle crashes are examined.

2.5.2.1 Preliminary Relationships in Head-on Frontal Collision

2.5.2.1.1 Conservation of Momentum

Applying the law of conservation of momentum to the head-on collision of two vehicles gives very useful kinematic relations. Of course, this idealized impact between two vehicles assumes that the collision is perfectly plastic, and the masses move as one rigid body after collision [71-73]. In other words, the dynamic equations given below are only valid until the time at which both vehicles have the same speed. It is also assumed during collision that no plastic unloading or reloading occurs during the crushing process.

Thus, if v_1 and m_1 are the velocity and mass of the heavier vehicle and v_2 & m_2 are the velocity and mass of the lighter vehicle, and the velocity after the crash is assumed to be the same for both vehicles V_f, then:

$$V_f = (m_1 v_1 + m_2 v_2) / (m_1+m_2) \qquad (2.5.2.1.1.1)$$

$$= m_2 V_c / (m_1+m_2) \qquad = m_1 V_c / (m_1+m_2)$$

Knowing (V_f) helps to calculate the change of vehicle velocity during impact, which is a good indicator of the severity of impact on each vehicle, from the following:

$$\Delta v_1 = V_f - v_1 \qquad \text{and,} \qquad \Delta v_2 = V_f - v_2 \qquad (2.5.2.1.1.2)$$

Eq. 2.5.2.1.1.2 gives an expression of the Δv's ratio in terms of $\mu = (m_1 / m_2) > 1$, the mass ratio of the two vehicles:

$$(\Delta v_2 / \Delta v_1) = (m_1 /(m_2) = \mu \qquad (2.5.2.1.1.3)$$

Thus, the lighter car goes through higher change in velocity than the heavier car. As a result, it will undergo more deformation than the rigid or deformable barrier cases.

For the special case where $v_2 = - v_1 = v_0$, the expression for the velocity after impact, Eq. 2.5.2.1.1.1 becomes

$$V_f = [(m_1 - m_2)/(m_1 + m_2)] v_0 \qquad (2.5.2.1.1.4)$$

which means when $m_1 = m_2$, $V_f = 0$. But, when $m_1 \neq m_2$, i.e. $\mu = (m_1 / m_2) > 1$, and defining V_c as pre-impact closing velocity between the two vehicles, that is, $V_c = v_1 - v_2$, the above equations may be written as follows:

$$V_f = [(\mu - 1)/(\mu + 1)] v_0$$
$$\Delta v_1 = V_c /(\mu + 1)$$

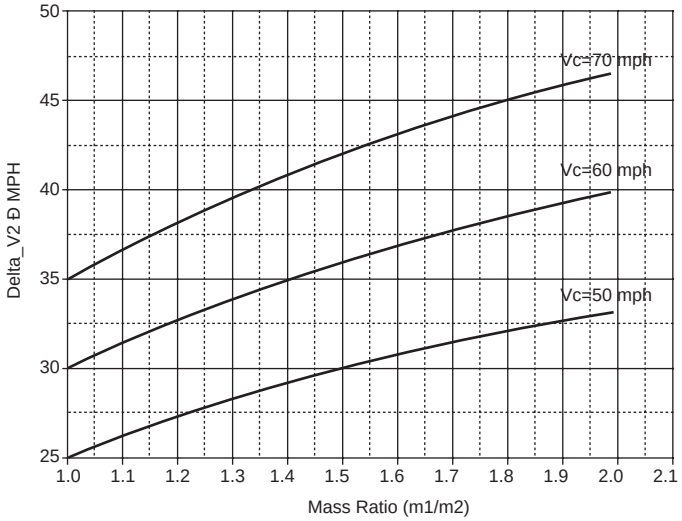

Fig. 2.5.2.1.1.1 **Delta V2 for mass ratios and closing velocities**

$$\Delta v_2 = [(\mu)/(\mu + 1)] V_c \qquad (2.5.2.1.1.5)$$

Eq. 2.5.2.1.1.5 is very interesting because it gives the change of velocity for the light vehicle versus the closing speed before impact, and it is plotted in Figure 2.5.2.1.1.1. The figure shows that for vehicles designed for NCAP testing, V_c=70 mph is too severe of a case to handle, regardless of the mass ratios of the vehicles involved. However, in theory, a V_c=50 mph is manageable for up to approximately μ = 2.1. But a V_c= 60 mph, the critical mass ratio at which Δv_2 is 35 mph is 1.4.

2.5.2.1.2 Conservation of Energy

Furthermore, by applying conservation of energy theorem, the total energy absorbed by both vehicles (through deformation) during crash can be computed from the following equation [71-72]:

$$E_{def.} = ½ [(m_1 m_2)/(m_1+m_2)] (V_c^2) \qquad (2.5.2.1.2.1)$$

that is, the deformation energy depends on the two masses and the closing velocity V_c of the two colliding vehicles.

Eq. 2.5.2.1.2.1 may be written in terms of (μ) and (m_2), the mass of the lighter vehicle as:

$$E_{def.} = ½ [(m_2) (\mu) / (1+(\mu)] (V_c^2) \qquad (2.5.2.1.2.2)$$

Eq. 2.5.2.1.2.2 was used in calculating the energy absorbed by two vehicle in head-on collision for m_2=3000 lbs , V_c = 60, 70 mph, and at different mass ratios. The results are shown in Figure 2.5.2.1.2.1. On the same figure, the energy absorbed during vehicle-to-vehicle collision was compared with sum of energies absorbed by similar vehicle during NCAP tests. The comparison confirms the conclusion stated in [73], that when two vehicles are individually designed to absorb the energy during frontal rigid barrier impact at speed of V_B (for example the case of NCAP test), and these vehicles are involved in head-on collision at closing velocity ($V_c \leq 2V_B$), which is $V_c \leq$ 70 mph for the NCAP case, they are capable of absorbing the energy of that crash. Furthermore, the analysis is valid regardless of the mass ratio of the two vehicles. This finding shows that the design of compatible structures is possible, and over-crush of the light vehicle can be avoided.

2.5.2.1.3 Distribution of Energy and Deformation

The energy absorbed by each vehicle in vehicle-to-vehicle crashes is dependent on the way crush is activated in that vehicle, which is dependent on the stiffness of each vehicle front end. But since a lighter vehicle is generally softer than a heavier vehicle, as discussed in Section 2.5.2.1.1 – Conservation of Energy, the

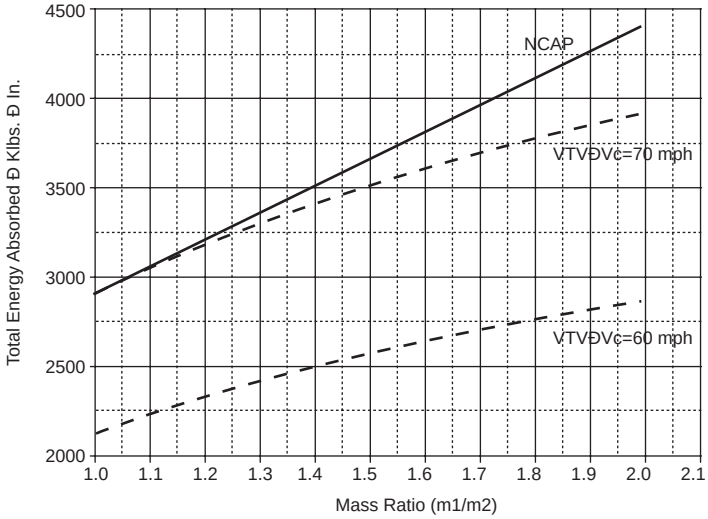

Fig. 2.5.2.1.2.1 **Total energy absorbed in head-on collision**

lighter vehicle will have a significant amount of crush before deformation starts in the heavier vehicle.

Unfortunately, Eqs. 2.5.2.1.12.1 and 2.5.2.1.2.2 are limited to calculation of the sum of energy absorbed by the two vehicles, and they do not help in determining the way that total energy is shared by the individual vehicle. Therefore, some assumptions are made to help calculate that distribution by a simple method.

Many researchers [71,74-76] used a linearization technique to approximate the dynamic crushing characteristics of the vehicle during rigid barrier crashes. Figure 2.5.2.1.3.1 is taken from [74] as an example. With an additional condition that the forces at the contact interface between the two vehicles, and assuming the vehicle's load characteristics in rigid barrier impact remain the same in a head-on collision, an estimate can be made of the distribution of crush and energy between the two cars. For example, in Figure 2.5.2.1.3.2 taken from [75], the crush distances of the heavy and light cars in rigid barrier impact are assumed 850 mm and 550 mm. Yet in a head-on collision, by virtue of equal forces at the interface, the heavier car crush decreases to 620 mm while the lighter car crush increases to 870 mm.

Although many authors used the linear approximation technique, this author's experience with this approach was not very positive. The approximation was

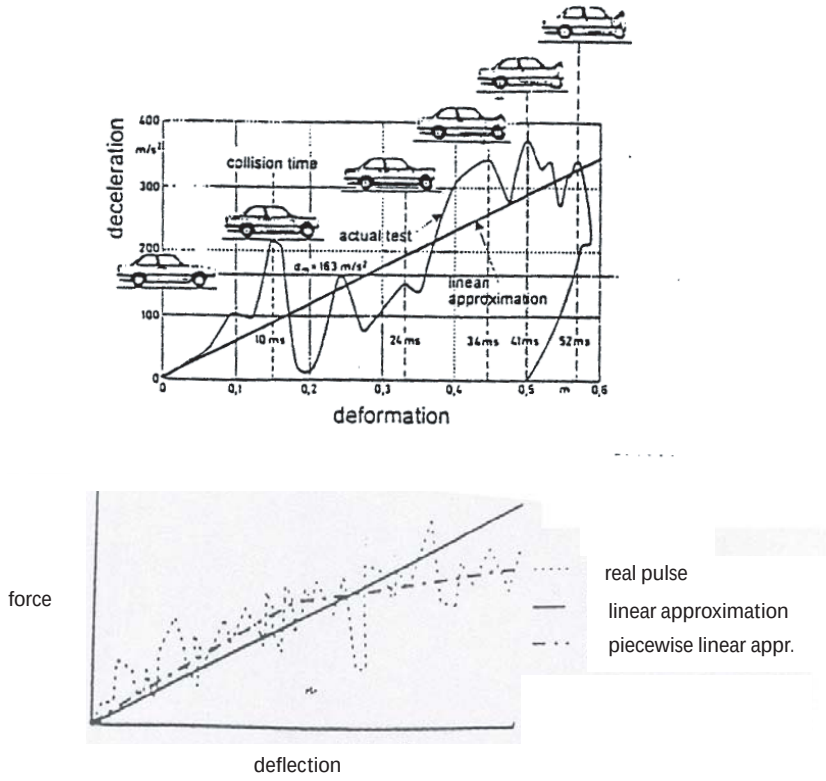

Fig. 2.5.2.1.3.1 **Linear approximation of vehicle deceleration vs. crush [74, 71]**

found to be very crude and can be misleading. In examining some typical acceleration-displacement characteristics of different types of vehicles, a nonzero-acceleration was required at a zero crush (Figure 2.5.2.1.3.3). A better approximation is the stepped-type (mostly a 2-step pulse) approximation, which can be easily implemented in any of the simple computer models discussed later in this report under the heading of analytical tools.

2.5.2.2 Strategies for Designing Front Structures for Head-on Impact

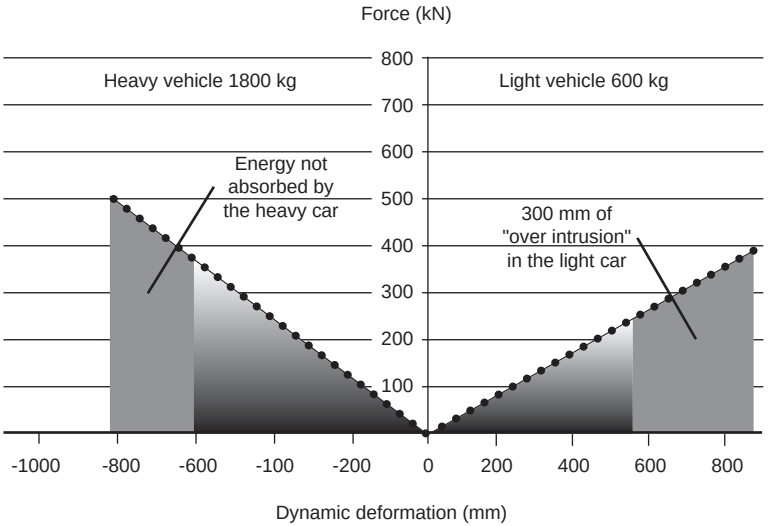

Fig. 2.5.2.1.3.2 **Comparison: head-on collision and rigid wall impact [75]**

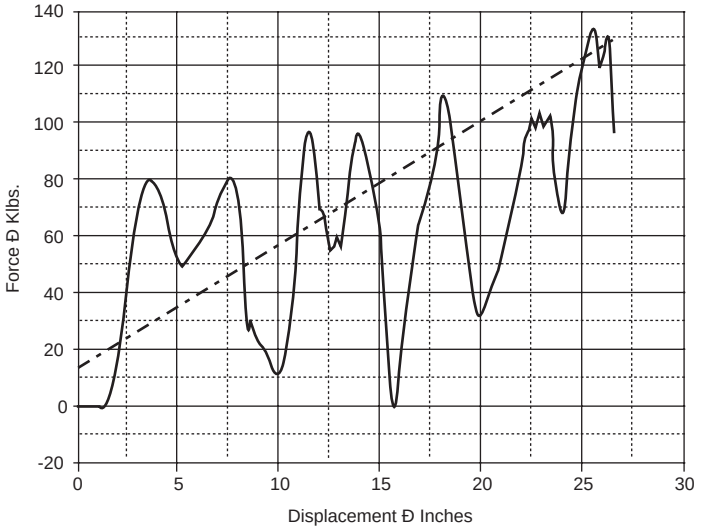

Fig. 2.5.2.1.3.3 **Linear approximation of crash pulse unsuitable for simplified analysis**

Designing front structures that ensure fairness in sharing the energy and crush during head-on impact among the variety of vehicles on the road may be difficult to handle and very complex to manage. Numerous publications are written by government agencies and industry experts. Although as yet, there is no clear answer or direction as to what the requirements might be, there are some ideas emerging from the research on the design of vehicle front ends. These ideas may be viewed as goals that can help in developing designs that embody a balance between meeting requirements for the current NCAP and IIHS testing, while avoiding undesirable performance during vehicle-to-vehicle crash.

The difference in the stiffness of the impacting vehicles is the factor highlighted by many researchers as the reason for the discrepancy in energy absorption between vehicles. Since vehicle stiffness is generally associated with other important design parameters, such as vehicle mass, it is important to include other factors when discussing design solutions for head-on impact.

2.5.2.2.1. The Mass Ratio (μ) & Closing Speed (v_c)

Since the effect of the mass can't be avoided, a decision must be made on the range of mass ratios of vehicles to be protected in that design. In Europe, approximately 90 percent of all vehicle-to-vehicle accidents have a mass-ratio less than 1.6 [73]. On the mass ratios of vehicles involved in accidents, [75] shows that 90 percent of head-on collisions had a mass ratio of 1.4. According to [76], two-thirds of accidents were between vehicles of equal masses.

On the other hand, the mass ratios of vehicles involved in accidents in the U.S. are not well established. Additionally, in the U.S., when SUV's and LTV's crash into cars, the issue of having front structure designs of different heights come into play. This issue referred to as geometric mismatch. This situation complicates the head-on collision design problem, and it is not addressed here. However, an estimate of the average mass ratio between a car and LTV was calculated from published data [77] to be 1.31. From [77], the median mass of U.S. cars is 1400 kg, while the median mass of the U.S. LTV fleet is 1830 kg. In vehicle-to-vehicle tests conducted by NHTSA (Ford Explorer to Honda Accord) [78], the mass ratio was 1.36. Therefore, for the purpose of designing vehicles for head on collisions, mass ratios within the range of 1.3-1.6 may be assumed. This range is expected to represent vehicles in a high percentage of accidents in the U.S. and Europe.

As for the closing speed, 60 mph to 70 mph appears to be the accepted range where tests are conducted in both Europe and U.S. With this high speed, and considering impact of vehicles with a high-mass ratio, the condition may be too severe or unrepresentative in accidents for designing vehicle front structures.

For example, accident data [75] show that in 90 percent of accidents, the mass ratios of the vehicles involved were less than 1.4, and the difference between the equivalent energy speeds (EES) is less than 6.2 mph (10 kph). The difference in delta-*v*'s of the light and heavy vehicles for different mass ratios and closing speeds of 60 mph and 70 mph are calculated from the momentum equations and

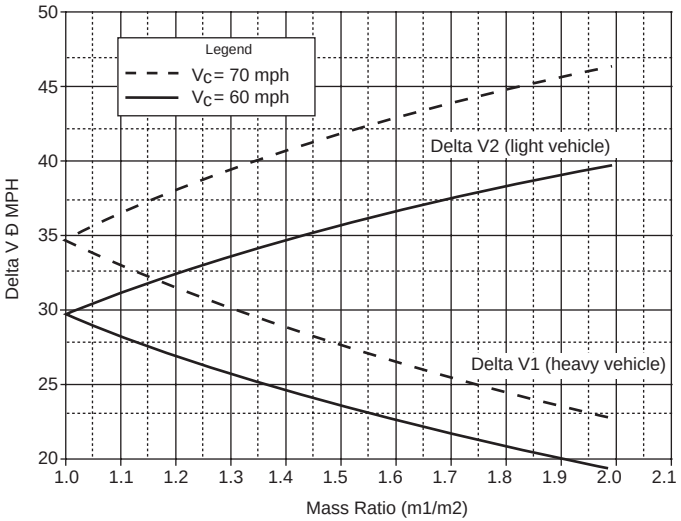

Fig. 2.5.2.2.1.1 **Delta V's for different mass ratios during head-on impact**

plotted in Figure 2.5.2.2.1.1. The figure shows that the mass ratio that corresponds to the difference in EES of 6.2 mph (10 kph) is approximately 1.2, regardless of V_c.

This underscores the importance of qualifying a front-end design for the mass ratio and closing speed capabilities.

2.5.2.2.2 Energy and crush distribution targets

Many researchers express the opinion that during head-on collision, each of the vehicles involved should absorb an amount of energy that is proportional to its mass, that is,

For the heavy vehicle of mass m_1, E_1 should be:

$$E_1 = m_1 E_{def} / (m_1 + m_2) \qquad (2.5.2.2.2.1)$$

and for the light vehicle of mass m_2, the energy would be E_2

$$E_2 = m_2 E_{def} / (m_1 + m_2) \quad (2.5.2.2.2.2)$$

Using a numerical example to illustrate the idea, the approach of [75] was applied. Assume two vehicles, the heavy vehicle weighs 4800 lbs, and a light vehicle weights 3000 lbs. Mass ratio is 1.6, and pre-crash closing speed is V_c=70 mph.

The total energy absorbed by both vehicles using the above two equations, E_{def}= 3680 klbs-inch. By Equation 45, 61.5 percent of this energy should be absorbed by the heavy vehicle m_1, or 2263.2 klbs.-in, which represents an EES of 34.33 mph. The variation of the heavier vehicle speed from Equation 35 is only 26.6 mph. Also, 38.5 percent of the total energy should be absorbed by the light vehicle m_2, or 1416.8 klbs-in, which represents an EES of 34.36 mph. The variation in the speed of the lighter vehicle is 43.0 mph.

The way to achieve this type of energy absorption distribution is to design the stiffness and load deflection characteristics of the light and heavy cars as follows.

For the light (small) car, a strategy that gained some acceptance in Europe was to increase the strength of the passenger compartment of the light vehicle to a level called the compatibility force [75]. The same idea, proposed in [73], was called the bulkhead concept, where the back-up structure and the passenger compartment frame of the light vehicle are designed to be stiffer than their current levels. An appropriate design target for the peak force is determined based on restraint system limits to produce acceptable dummy response during NCAP test. Moreover, an energy absorbing structure in front of the compartment would be designed such that it crushes below the compatibility force, and has enough stroke to absorb an amount of energy proportional to the mass of the car.

A peak force level for designing the passenger compartment strength was proposed in [75] as a reasonable target, since it was obtained from actual barrier loads in offset deformable barrier crash test results of many European cars. This force level ranges from 300 KN to 400KN. Another researcher, in [73], proposed the peak force might be determined by assuming the highest deceleration level that can be applied to the passenger compartment structure while still passing the requirements of rigid barrier impact within the current technology of the restraint system. This deceleration level was proposed to be 30 g's.

As for the heavy (large) car, some design changes must be made in order to have a design that is compatible (effective in vehicle-to-vehicle crashes) with that

proposed for the light vehicle. That is, the heavy vehicle's structure must be designed to be softer than its current design stiffness. However, the corresponding increase in the crush distance must be affordable, particularly for the case of impact with rigid barrier at 35 mph (NCAP).

The idea of having equal equivalent energy speed (EES) for designing the two vehicles was shown to be feasible [75]. Furthermore, by using the simplified design models described in Section 2.5.3 – Assessment of Analytical Tools, alternative effective designs can be created.

2.5.3 Assessment of Analytical Tools

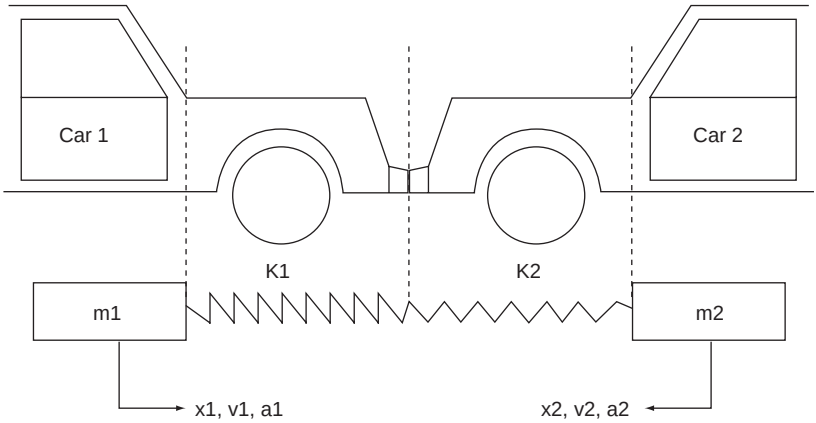

Fig. 2.5.3.1 **Mass-spring model of two colliding cars [71]**

Many modeling techniques and simplifications have been used to identify critical design and performance parameters in head-on collisions. The most simplistic model was the use of two rigid masses and two linear springs to model the complete system impact as shown in Figure 2.5.3.1 [71]. Others modeled the powertrain of both vehicles to capture their interface and how it might influence the behavior, as shown in Figure 2.5.3.2 [79].

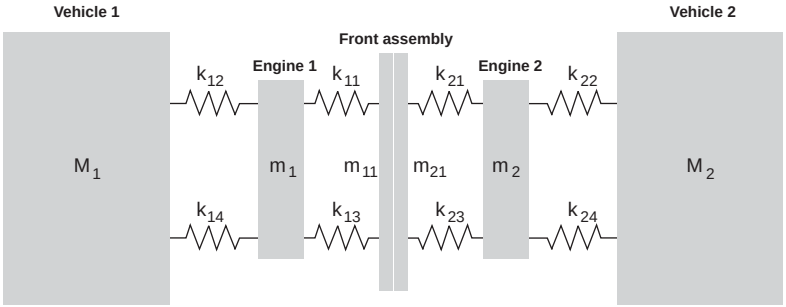

Fig. 2.5.3.2 **Schematic model of crush system [79]**

Simulation of head-on impact of two cars had been conducted with 1-D lumped spring mass approach as early as the 1970s [80]. The model is shown in Figure 2.5.3.3. It proved to be very useful in understanding the fundamental mechanics of collision and the factors which influence the behavior such as closing speed, mass ratio and structural stiffness of each vehicle. Also, responses such as vehicle deceleration-time history, energy absorption by each vehicle and the amount of crush that occurs are easily computed.

However, this modeling has limitations because it models only the behavior in the longitudinal direction (one-dimensional). For example, a behavior due to mismatch or non-alignment of the structure in the vertical plane or a horizontal plane cannot be captured. Also, with one-dimensional modeling, two-dimensional impact problems such as offset impact or angular impact cannot be simulated. As such, the ability to accurately compute or acquire the model spring characteristics is one of the primary limitations with this modeling approach.

Again, to manage the vehicle-to-vehicle offset impact and possibly the mismatch in geometry of the colliding vehicles, the three-dimensional lumped masses and springs with MADYMO have been used [81,] as shown in Figure 2.5.3.4.

Another three-dimensional simplified modeling technique, which implemented advanced beam elements, has been used [38] for studying the factors influencing compatibility between vehicles. Beam elements combined with shell elements and other rigid body masses, hybrid modeling, is shown in Figure 2.5.3.5.

The above models are invaluable in helping to design vehicles front structures for vehicle to-vehicle crashes because of their simplicity. They are needed to

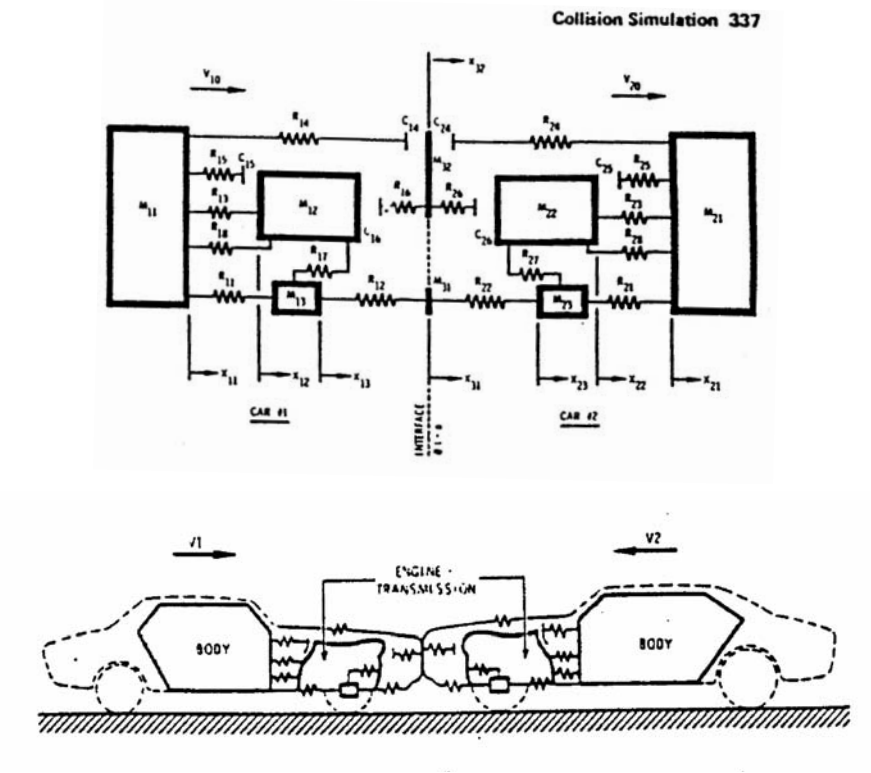

Fig. 2.5.3.3 **Application of 1-D LMS models for head-on impact simulation [80]**

evaluate impact severity regarding the car deformation, compartment intrusion, and vehicle acceleration relative to rigid barrier and offset barrier crashes.

On the other hand, detailed modeling of the two impacting vehicles using shell finite elements is being developed to evaluate crashes using the explicit crash codes. This technique is used as an evaluation tool by NHTSA [78] and the automotive industry [65,82] to reduce the testing involved in these crashes.

2.5.4 Conclusion

A test to check occupants' safety in vehicle-to-vehicle collision will inevitably emerge. In fact, some vehicle manufacturers have already provided plans to check their designs for this impact mode in their product development process. Current design standards (the rigid barrier and offset deformable barrier tests) promote

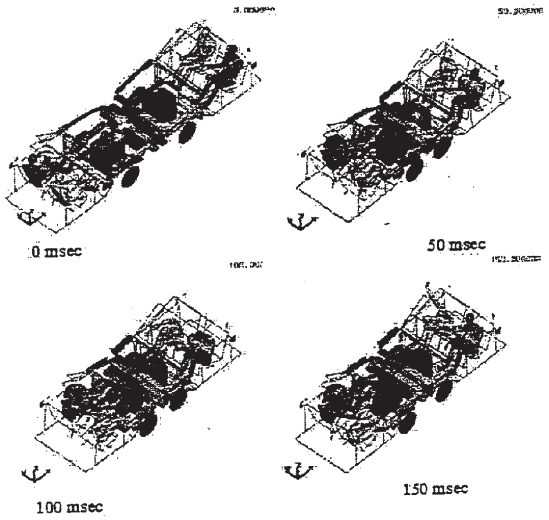

Fig. 2.5.3.4 **Car-to-car full frontal impact [81]**

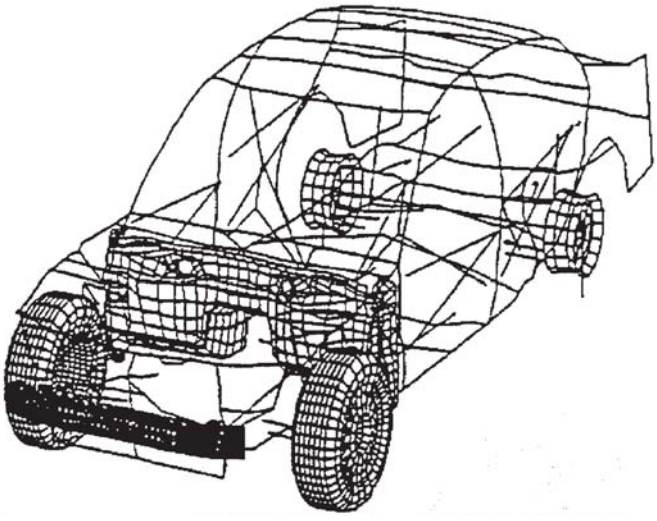

undesirable stiff front-end structure designs for the heavier vehicles, which are

Fig. 2.5.3.5 **Beam element model of body structure**

not readily crushable in a head-on collision.

Several simplified models are used, but the hybrid technique may be the most promising, since it combines features that are suitable and easy to apply by engineers. It also overcomes the oversimplification in 1-D modeling that may not be correct for vehicle-to-vehicle simulation.

Designing the back-up and compartment structures of a small light vehicle for approximately 30 g's average force in a two-level crash pulse would significantly improve its safety in head-on collision with a heavier full-size vehicle with closing velocity of 60 mph and mass ratio of 1.33.

2.6 References

1. Kamal, M. M., "Analysis and Simulation of Vehicle to Barrier Impact," SAE Paper No. 700414, 1970.

2. Magee, C. L. - Keynote Address, "Design for Crash Energy Management - Present and Future Developments," The Seventh International Conference on Vehicle Structural Mechanics, April 1988.

3. Lim, G. G., and Paluszny A., "Side Impact Research," XXII Fisita Congress - SAE Publication P-211, Paper No. 885055, Sept. 1988.

4. Green, J. E., "Computer Simulation of Car-To-Car Collisions," SAE Paper No. 770015, February-March 1977.

5. Cheva, W., Yasuki, T., Gupta, V., and Mendis, K., "Vehicle Development for Frontal/Offset Crash Using Lumped Parameter Modeling," SAE Paper No. 960437, 1996.

6. Kim, O-S, Kim, S-T, Jung, S-B, and Kim, D-S, "Sub-Structure Vehicle Test and Analysis to Predict the Frontal Crash Performances of Full-Scale Vehicle," SAE International Congress and Exposition, Detroit, Paper No. 1999-01-0076, 1999.

7. Hahm, S-J, Won, Y-H, and Kim, D-S, "Frontal Crash Feasibility Study Using MADYMO 3D frame Model," SAE International Congress and Exposition, Detroit, Paper No. 1999-01-0072, 1999.

8. Deshpande, B., Gunasekar, T. J., Morris, R., Parida, S., Rashidy, M., and Summers, S., "Methodology Development for Simulating Full Frontal and Offset Frontal Impacts Using Full Vehicle MADYMO Models," Crashworthiness, Occupant Protection, and Biomechanics in Transportation Systems, ASME Mechanical Engineering Congress and Exposition, pp. 19-37, 1999.

9. Mahmood H. F., and Paluszny, A., "Design of Thin Wall Columns for Crash Energy Management - Their Strength and Mode of Collapse," SAE Fourth International Conference on Vehicle Structural Mechanics, Nov. 1981, Paper No.811302.

10. Mahmood, H. F., Saha, N. K., and Paluszny, A., "Stiffness and Crash Strength Characteristics of Thin Walled Plate Components," Computers in Engineering 1985, Vol. 1, pp. 501-507, ASME Publication.

11. McIvor, I. K., "Modeling and Simulation as Applied to Vehicle Structures and Interiors," Vehicle Safety Research Integration Symposium, U.S. Department of Transportation, May 1973.

12. Liaw, J. C., Walten, A. C., Brown, J. C., "Structural Impact Simulation using Program KRASH," SAE Technical Paper Number 900466 published in SP-820, Engineering Technologies in Vehicle CAE & Structural Mechanics, February 1990.

13. Hagiwara, I., et al., "Vehicle Crash Simulation Using Hybrid Model," SAE Technical Paper Number 810476, International Congress and Exposition, February 23-27, 1981, Detroit, Michigan.

14. Abe, K., et al., "Collapse of Thin-Walled Curved Beam with Closed-Hat Section-Part 2: Simulation by Plane Plastic Hinge Model," SAE Technical Paper Number 900461 published in SP-820, Engineering Technologies in Vehicle CAE & Structural Mechanics, February 1990.

15. Vignjevic, Kecman, D., and Sadeghi, M., "The Improved Compound Beam Element with Nonlinear Moment-Rotation Curves for the Car Side Impact and Roof Crush Analysis Using DYNA3D Program," ASME Proceedings on Crashworthiness and Occupant Protection in Transportation Systems, AMD-Vol. 169, BED-Vol. 25, 1993

16. Drazetic, P., et al., "Serial Mounting of Kinematic Models in Compression and Flexion," report received from Engineering System International,

January 1994.

17. Mahmood, H. F., and Paluszny, A., "Analytical Technique for Simulating Crash Response of Vehicle Structures Composed of Beam Elements," Sixth International Conference on Vehicle Structural Mechanics, Detroit, 1986, SAE Paper No.860820.

18. Mahmood H. F., Paluszny, A., and Tang, X. D., "A 3D Computer Program for Crashworthiness Analysis of Vehicle Structures Composed of Thin-Wall Beam Components," ASME Publication No. AMD-Vol.79.

19. Prasad, P., and Padgaonkar, A. J., "Static to Dynamic Amplification Factors for Use in Lumped Mass Vehicle Crash Models," SAE Paper No. 810475, Feb. 1981.

20. Davis, R. G., and Magee, C. L., "The Effect of Strain Rate Upon the Tensile Deformation of Materials," Journal of Engineering Materials and Technology, April 1975, pp.151-155.

21. Davis, R. G., and Magee, C. L., "The Effect of Strain Rate Upon the Bending Behavior of Materials," Journal of Engineering Materials and Technology, January 1977, pp.47-51.

22. Kassar, M., and Yu, W-W., "Design of Automotive Structural Components Using High Strength Sheet Steel - The Effect of Strain Rate on Mechanical Properties of Sheet Steels," Civil Engineering Study 89-2, Structural Series, Eleventh Project Report, Department of Civil Engineering, University of Missouri-Rolla, Rolla, Missouri, Jan. 1989.

23. Thornton, P. H., "Static and Dynamic Collapse Characteristics of Scale Model Corrugated Tubular Sections," ASME Journal of Engineering Materials and Technology, Paper No. 75-Mat-G, 1975.

24. Abramowicz, W., and Jones, N., "Dynamic Crushing of Square Tubes," International Journal of Impact Engineering Vol. 2, No. 2, pp. 179-208, 1984.

25. Wierzbicki, T., and Abramowicz, W., "On The Crushing Mechanics of Thin-Walled Structures," Journal of Applied Mechanics, Vol. 50, pp. 727-734, Dec. 1983.

26. Chang, D. C., "Effects of Flexible Connections on Body Structural Response," SAE Paper No. 740041, 1974.

27. Wierzbicki, T., and Akerstrom, T., "Dynamic Crushing of Strain Rate Sensitive Box Columns," SAE Paper No. 770592, Proceedings of the 2nd International Conference on Vehicle Structural Mechanics, April 18-20, 1977.

28. Fileta, B., and Liu, X., "Simplified System Modeling and 3D Simulation Methods for Frontal Offset Crash," presented at Vehicle Structural Mechanics Conference, April 1997, Troy, Michigan.

29. Chang, D. C., and Rohde, S. M.," The Role of Synthesis, Analysis & Simulation in Engineering a Complex System: The Automotive Vehicle," Proceedings of Engineering Systems DSC-VOL. 60, ASME 1996.

30. Wang, H., et al, "A Methodology for Early Front End Structural Design to Meet Safety Requirements Using CAE Tools," ASME 1997.

31. Walker, B. D., Miles, J. C., and Keer, T. J., "Vehicle Crashworthiness from Lumped Parameter to Continuum Models," Proceedings on Crashworthiness, Occupant Protection and Biomechanics in Transportation Systems, AMD-Vol. 169/BED-Vol. 25, ASME 1993.

32. Ohokubo, Y., Akamatsu, T., and Shirasawa, K., "Mean Crushing Strength of Closed-Hat Section Members," SAE Paper No. 740040, Feb. 1974.

33. Johnson, W., Soden, P. D. and Al-Hassani, S. T. S., "Inextensional Collapse of Thin-Walled Tubes Under Axial Compression," Journal of Strain Analysis, Vol.12, 1977, pp. 317-330.

34. Alexander, J. M., "An Approximate Analysis of the Collapse of Thin Cylindrical Shells Under Axial Load," Quarterly Journal of Mechanics and Mathematics, 1960.

35. Magee, C. L., and Thornton, P. H., "Design Consideration in Energy Absorption by Structural Collapse," SAE Paper No. 780434, Feb. 1978.

36. Mahmood, H. F., and Paluszny, A., "Axial Collapse of Thin Wall Cylindrical Column," Fifth International Conference on Vehicular Structural Mechanics, Detroit, 1984, SAE Paper No. 840727.

37. Mahmood, H. F., and Paluszny, A., "Stability of Plate Type Box Columns Under Crush Loading," Computational Methods in Ground Transportation Vehicles, AMD-Vol. 50, pp. 17-33, 1982 Winter Annual Meeting of ASME, Phoenix.

38. Makino, K., et al., "A Simulation Study on the Major Factors in Compatibility," Paper Number 98-S3-O-03, Proceedings of the 16th International Technical Conference on the Enhanced Safety of Vehicles, May 31 to June 4, 1998.

39. Wierzbicki, T., "Crushing Analysis of Plate Intersections," Structural Crashworthiness, edited by Jones, N., and Wierzbicki, T., Butterworth Press, 1983.

40. Mahmood, H. F., and Paluszny, A., "Stability of Plate Type Box Columns Under Crush Loading," Proceeding of the ASME Winter Sessions on Computational Methods in Ground Transportation Vehicles, Phoenix, Nov. 14, 1982.

41. Johnson, W., Soden, P. D., and Al-Hassani, S. T. S., "Inextensional Collapse of Thin-Walled Tubes Under AxL-d Compression," Journal of Strain Analysis, Vol. 12, 1977, pp. 317-330.

42. Wierzbicki, T., and Abramowicz, W., "A Kinematic Approach to Crushing of Shell Structures," Proceedings of the 3rd International Conference on Vehicle Structural Mechanics, Troy, Michigan, Oct. 10-12, 1979.

43. Bulsen, P. S., "The Strength of Thin-Walled Tubes Formed from Flat Elements," International Science, Vol. 11, pp. 613-620, 1969.

44. Wimmer, A., "Einfluss der Belastungsgeschwindigkeit auf das Festigkeits und Verforinungsverhalten von Blechkonstruktionen am Beispiel von Kraftverzeugen," ATZ 77, No. 10, 1975.

45. Wierzbicki, T., "Stability Effects in Dynamic Crushing of Sheet Metal Column," Proceedings of HOPE International JSME Symposium, Tokyo, od. 3 1, Nov. 1977.

46. Wierzbicki, T,. and Abramowicz, W., "Stability of Progressive Collapse," Manual of Crashworthiness Engineering, Vol. III, Center For Transportation Studies, Massachusetts Institute of Technology, June 1988.

47. Kocman, D., "Bending Collapse of Rectangular Section Tubes in Relation to the Bus Roll Over Problem," Ph,D. Dissertation, Cranfield Institute of Technology, Cranfield, England, 1979.

48. Mahmood, H. F., Paluszny, A., and Lin, Y. S., "Bending Collapse of Automotive type Components," XXEI Fisita Congress, Technical Papers Vol. 1, pp. 1.220-1.342, Fisita '88, Dearborn, Michigan, 1988.

49. American Iron and Steel Institute, "Cold Formed Steel Design Manual," 1968 Edition, (1977 Publication).

50. B.S. 449:1959, "Specification for the Use of Cold Formed Steel Sections in Building," (Edition No. 1, 1961), British Standards Institution.

51. Mahmood, H. F., and Magee, C. L., "Computer Aided Design of Thin Wall Structural Elements for Crash Energy Management," Proceedings International Symposium on Automotive Technology and Automation, Sept. 1982.

52. Brown, J. C., and Tidbury, G. H., "An Investigation of the Collapse of Thin-Walled Rectangular Beams in Biaxial Bending," International Journal of Mechanical Sciences, Vol. 25, No. 9-10, pp. 733 - 746, 1983.

53. Rao, M. D., Zebrowski, M. P., and Crabb, H. C., "Automotive Body Joint Analysis for Improved Vehicle Response," ISATA 1983.

54. Kamada, N., and Sakurai, T., "Vehicle Structure of Thin Wall Steel Plate Joint Stiffness Analysis," Society of Automotive of Japan, Conference Publication 872, pp. 691-696, 1987.

55. Ng, P., and Tidbury, G.H., "The Development of a Vehicle Angled Side Collision Computer Simulation Program," SAE Proceedings of the 6th International Conference on Vehicle Structural Mechanics, April 1986, Paper No. 860822.

56. Zienkiewicz, O. C., "The Finite Element Method," third edition, McGraw-Hill Book Company Ltd., London, 1977.

57. Hobbs, C. A., "The Rationale and Development of the Offset Deformable Frontal Impact Test Procedure," SAE Technical Paper Number 950501, (SP-1072).

58. Vehicle Aggressivity & Compatibility in Automotive Crashes, 1999 SAE publication Number SP-1442.

59. Vehicle Aggressivity & Compatibility in Automotive Crashes, 2000 SAE publication Number SP-1525.

60. Proceedings of the 16th International Technical Conference on the Enhanced Safety of Vehicles, held at Windsor, Canada, May 31 to June 4, 1998.

61. Gabler, H. C., and Hollowell, W. T., "NHTSA's Vehicle Aggressivity and Compatibility Research Program," Paper Number 98-S3-O-01, Proceedings of the16th International Technical Conference on the Enhanced Safety of Vehicles, May 31 to June 4, 1998.

62. Ragland, C. L., "Offset Test Procedure Development and Comparison," Paper Number 96-S4-O-01, the Proceedings of the 15th International Technical Conference on the Enhanced Safety Of Vehicles, May 13-16, 1996. pg. 576.

63. Hollowell, W. T., and Gabler, H. C., "NHTSA's Vehicle Aggressivity and Compatibility Research Program," Paper Number 98-S3-O-01, Proceedings of the 16th International Technical Conference on the Enhanced Safety of Vehicles, May 31 to June 4, 1998.

64. Friedel, B., "EEVC Status Report," Proceedings of the 16th International Technical Conference on the Enhanced Safety of Vehicles, May 31 to June 4, 1998.

65. Steyer, C., Delhommmeau, M., and Delannoy, P., "Proposal to Improve Compatibility in Head On Collisions," Paper Number 98-S3-O-05, Proceedings of the 16th International Technical Conference on the Enhanced Safety of Vehicles, May 31 to June 4, 1998.

66. Schoeneburg, R., and Pankalla, H., "Implementation and Assessment of Measures for Compatible Crash Behavior Using the Aluminum Vehicle as an Example," Paper Number 98-S3-O-07, Proceedings of the 16th

International Technical Conference on the Enhanced Safety of Vehicles, May 31 to June 4, 1998.

67. Zeidler, F., Knochelmann, F., and Scheunert, D., "Possibilities and Limits in the Design of Compatible Cars for Real World Accidents," SAE Paper 1999-01-0068, 1999.

68. Kallina, I., "Crashworthiness," Published as Technical Briefs, Vehicle Aggressivity and Compatibility in Automotive Crashes 2000, SAE publication Number SP-1525, pg. 88-88.

69. Bloch, J-A, and Chevalier, M-C, "In Depth Analysis Offset Frontal Crash Tests In View Of Aggressivity Criteria," Paper Number 96-S4-O-07, the Proceedings of the 15th International Technical Conference on the Enhanced Safety of Vehicles, May 13-16, 19996. pg. 634.

70. Klanner, W., Felsch, B., and Van west, F., "Evaluation of Occupant Protection and Compatibility Out of Frontal Crash Tests Against the Deformable Barrier," Paper Number 98-S3-O-06, Proceedings of the 16th International Technical Conference on the Enhanced Safety of Vehicles, May 31 to June 4, 1998.

71. Mooi, H. G., and Huibers, J., "Simple and Effective Lumped Mass Models for Determining Kinetics and Dynamics of Car-to-Car Crashes," IJCRASH '98, Conference Proceedings, Dearborn, Michigan, September 9-11, 1998.

72. Kossar, J. M., "Big and Little Car Compatibility," Fifth International Technical Conference on Experimental Safety Vehicles, London, June 4-7, 1974.

73. Zobel R., "Accident Analysis & Measures to Establish Compatibility," SAE Paper 1999-01-0065, 1999, pp. 2-6.

74. Abramowicz, W., "Compatibility of Energy Absorbing Structures," IJCRASH'98, Conference Proceedings, Dearborn, Michigan, September 9-11, 1998.

75. Steyer, C., and Dubos, A., "Renault's Proposal to Improve Compatibility," Proceedings of the International Body Engineering Conference IBEC '97, Germany, September 30-October 2, 1997.

76. Zeidler, F., Knochelmann, F., and Scheunert, D., "Possibilities and Limits in the Design of Compatible Cars for Real World Accidents," SAE Technical Paper Number 1999-01-0068, 1999.

77. Gabler, C., and Fides, B., "Car Crash Compatibility: The Prospects for International Harmonization," SAE Technical Paper Number 1999-01-0069 (SP-1442).

78. Summers, S., Prasad, A., and Hollowell, T. W., "NHTSA's Vehicle Compatibility Research Program," SAE Technical Paper Number 1999-01-0071 (SP-1442).

79. Jawad, S. A., "Compatibility Analysis of Vehicle to Vehicle in Head on Collisions," 6th International Mechanical Engineering Congress & Exposition, Dallas, November 1997.

80. Lin, K., Kamal, M., and Justusson, J. W., "Effect of Vehicle Mix on Two-car Head-on Impact," SAE Technical Paper Number 750117.

81. Deshpande, B., Gunasekar, T.J., Morris, R., Parida, S., Rashidy, M., and Summers, S., "Methodology Development for Simulating Full Frontal and Offset Frontal Impacts Using Full Vehicle MADYMO Models," Proceedings on Crashworthiness, Occupant Protection and Biomechanics in Transportation Systems, AMD-Vol. 237/BED-Vol. 45, ASME 1999.

82. Puppini, R., et al, "Proposal for a New Frontal Crash Test Procedure to Meet Self Protection and Compatibility Needs," SAE Tech. Paper Number 2000-01-1373 (SP-1525).

Finite Element Analytical Techniques and Applications to Structural Design

Tawfik Khalil and Paul Du Bois

Analytical simulation of vehicle crashworthiness has evolved over the past 30 years. Three types of models are used to simulate vehicle structures - Lumped Parameter (LP) models, hybrid models, and Finite Element (FE) models. The FE models can be divided into two groups: heuristic beam models and continuum mechanics-based models which use beam, solid and shell elements. The progression of these models over the years followed a pattern of increasing geometric details since it was realized that a simple analytical model of the crash event, developed and tuned to fit one or more parameters from a specific test, does not ensure accurate prediction for all impact conditions. In fact, the most detailed models (LP or FE) developed to date should be considered approximations of a highly complex non-linear system that is often subject to large and unstable elastic-plastic deformations. Obviously, advances in understanding complex system performance such as crashworthiness can be achieved by increasingly including more details that capture realistic vehicle kinematics and loads encountered in general crash conditions.

This chapter provides an overview of the FE techniques used in vehicle body structural development to satisfy the design constraints necessary for the vehicle to meet myriad safety requirements expected of the vehicle structure and to assure vehicle crashworthiness. The analytical tools used to assess occupant response in crash and human tolerance to impact is addressed in another chapter. For completeness, recent models that integrate the occupant, restraint systems, and vehicle structure in a single analysis will be discussed in this chapter.

3.1 Historical Background

The history of structural crashworthiness analysis can best be characterized by two periods of historical development: an early period, extending from 1970 to

about 1985; and a second period beginning in the mid-1980s with the introduction of supercomputers and vectorized explicit finite element codes.

The first period was essentially one of genesis and growth, a period of trial, of attempting to develop some understanding of an extremely complex structural mechanics problem. A variety of numerical techniques were applied to simulate the deformations, including folding and buckling of a car structure during the decisive first 50 to 100 ms of a crash test. Approximate solutions were obtained by spring-mass modeling of the vehicle [1,2], an approach originated in the aerospace industry. Alternatively, solutions were obtained by using beam element models in conjunction with nonlinear joint formulations [3,4,5] that proved very successful on numerous occasions, but required a relatively high degree of skill and experience from the analyst.

There were also attempts to obtain solutions based on first principles by modeling the car body as a continuum, and thus, automating the task of attributing discretized stiffness values to the structural components. Some of this work was based on quasi-static beam element formulation [6], implicit FE techniques [7,8,9], finite difference methods [10], implicit/explicit FE formulations [11] and, explicit FE time integration [12].

It appears that the first crash model [13] simulated a head-on collision of a vehicle front structure with a rigid wall, using the computer code DYCAST with an implicit solver [8]. In this model, the left half of the vehicle was represented by 504 membrane triangular, beam, bar, and spring elements. Haug [11] discussed the development of an implicit-explicit integration FE PAM-CRASH code, which was then applied to analyze the response of an A-pillar, and next to the right front quarter of a unit-body passenger vehicle structure. The quasi-static analysis was accomplished by an iterative incremental force/displacement analysis. The theoretical background for implicit FE formulation and an associated code for crash analysis were presented by Argyris et al [9]. The developed code was applied to calculate the impact response of a vehicle front structure, devoid of engine, transmission and driveline, when it impacted a rigid barrier from an initial velocity of 13.4 m/s. The solution accounted for material strain hardening and rate effects, and provided structural deformations. Other than the three examples mentioned above, the application of implicit FE solvers to crash analysis did not proceed beyond that point, primarily due to its inability to account for contact and folding of thin sheet metal structures and due to excessive demands on computer hardware storage and speed.

Some of these developments already contained the essential features that make up the core of any crash analysis software today. They combined time integration

with shell elements, node-to-segment contact force transmissions, and plane stress elasto-plasticity. Since these are still the basic algorithms used in today's analysis environment, it is not surprising that as early as 1973, very good analytical results were obtained on vehicle substructures. The continuum approach, however, remained mainly in the province of research, since the goal of full-vehicle simulation could not be achieved with sufficient accuracy due to the limited number of shell elements that could be handled by state-of-the-art computers before the mid-1980s. The resulting coarse meshes did not allow a representation of the global buckling modes in a full-vehicle model. Due to the high degree of interaction between the different panels of an automobile structure, it is necessary to consider the full vehicle in a single model to predict the energy absorption of the individual parts during a crash. The inability to fulfill this requirement brought the continuum approach and thus, the finite element approach, to automotive crash simulations to a standstill in the late 1970s and early 1980s.

The second period of development began in 1985 and continues to the present. It can be characterized as a period of rapid growth in both explicit finite element technology development and applications to progressively more complex vehicle structures. The breakthrough of finite element methods in this field and their consequent implementation in the design process of vehicles happened in the mid-1980s [14-17]. During these years, vectorized supercomputers were introduced to the industry, allowing explicit finite element technology to establish itself as the leading numerical technique for crashworthiness calculations of vehicle structures. These few crucial years paved the way for the rapid and dramatic evolution in the following decade, when analytical tools evolved from the research environment to an integrated and essential part of the vehicle design process.

Although similar processes occurred roughly simultaneously in Japan [18], the United States [19], and Europe [20], the first writing about application of explicit FE technology to crashworthiness of actual vehicle structure was published by ESI in 1985 [21]. ESI modeled the front vehicle structure of a VW POLO impact into a rigid barrier, from an initial velocity of 13.4 m/s. The FE model simulated the structure by 2,272 shell and 106 beam elements. An elastic-plastic constitutive model with strain hardening was used to describe the sheet metal behavior. The analysis provided vehicle kinematics and barrier force-time pulse. Subsequent to this simulation, automotive manufacturers have attempted many crashworthiness calculations. This chapter focuses on the efforts of the German automotive industry to develop an analytical capability, primarily due to one of the authors' involvement in these developments.

The genesis of the VW POLO model can be traced back to the Forschungsgemeinschaft-Automobiltechnik (FAT) committee of Germany. The

TABLE 3.1.1 **Computer runtime**

Hardware platform / software	Runtime for 80ms crash simulationon the Volkswagen Polo model
VAX-750/PAM CRASH	2000 hours
Cray-1 (scalar code)	100 hours
Cray-1 (vectorized code)	24 hours
Cray-1 (optimized code)	12 hours

FAT is a joint research committee of the German automotive industry, formed in 1983 as a working group. This group included all seven German automotive assemblers: Mercedes-Benz, Porsche, BMW, Audi, Volkswagen, Opel and Ford of Germany. The objective was to investigate the potential of the finite element method to predict the buckling behavior of an automotive car body during an overnight computer simulation. It is important at this point to note that two goals were set: accuracy and efficiency. Accuracy, and thus, the sufficiently realistic prediction of the vehicle's deformation mode, was not considered a complete result by itself. It was clearly realized that the industrial use of this methodology would depend mainly upon efficiency; that is, the ability of the analyst to provide a result within reasonable deadlines. Two projects commissioned by the FAT committee were executed concurrently during the next 2 to 3 years. The two contractors were IABG of Munich and ESI of Paris and Eschborn. They built finite element models of the BMW 300 and VW Polo respectively. Both models were based on quadrilateral shell elements and very similar in size as well as in concept. The model sizes of 6,000 to 7,000 shell elements were minimal compared to today's standards.

After a number of initial iterations, the research in both companies converged toward the use of explicit finite element methods due to the high convergence of problems observed when using implicit integration techniques to solve these highly nonlinear problems. Using explicit element-by-element techniques showed that the problem could be solved, at least in principle, although the computer runtimes involved were initially prohibitively high. Table 3.1.1 illustrates the dramatic changes that took place in the engineering hardware environment in the course of this project:

Two thousand hours represents roughly three months of continuous computation. This would obviously render all results obsolete in any modern design process, even before the results were obtained. Additionally, it is unrealistic to expect three months of continuous functioning of any hardware, due to hardware and software maintenance requirements. The performance of such a simulation thus required substantial effort by the analyst for management of results, restart data and other factors.

Although the transfer of the problem to the Cray supercomputer brought a spectacular improvement, runtimes of nearly one week could not be considered satisfactory, and had to be improved by other means. Vectorization of the software (PAMCRASH and CRASHMAS for ESI and IABG, respectively) and consequent optimization with respect to the particular features of the Cray-1 hardware ultimately allowed for runtimes that satisfied the original FAT overnight performance criterion.

Both projects were successful, resulting in a number of publications [22-24] which boosted the use of explicit finite element techniques in crashworthiness engineering in Germany and worldwide. Other European car companies had started working along the same lines independent of the FAT effort [25], contributing to the remarkable initial success of this methodology.

Since 1986, the development of simulation technology for crashworthiness has been spectacular, but industrial rather than technological in nature. It is instructive to compare the role of numerical simulation (based on explicit finite element methods) concerning crashworthiness engineering in an automotive company today to what it was in the mid-1980s. In the late 1980s, numerical simulation was almost exclusively a research activity involving very few engineers, and hardly affecting the design cycle. These simulations focused on frontal car-to-barrier crashes.

Today, car manufacturers are faced with numerous restraints dictated by different governments, in-house safety criteria, due care issues, and consumer-driven requirements that must be met before a new car is introduced to the world market. Corresponding to a variety of collision scenarios, 15 to 20 full-scale vehicle tests may be performed on a prototype. For example, to meet frontal crash requirements, a world vehicle's performance is assessed in a 30 mph crash into a full rigid barrier at 0 degree, +30 degrees, and -30 degrees. A similar test at 0 degrees from 35 mph into a full overlap rigid wall is run to assess NCAP performance. In addition, offset tests where the vehicle is run into partial overlap, deformable or rigid

barriers are conducted. These tests are in addition to air-bag deployment and immunity tests.

In addition to frontal impact performance, the industry must consider U.S. side impact, European side impact, rear impact, and rollover protection requirements. In short, the regulatory environment has mushroomed in the last decade. Added to this list are the competitive pressures to shorten the development cycle. In view of all this, it is obvious that the testing capacity with the automotive assemblers (and their suppliers) had to answer to a considerable growth in demand during this constantly reduced development cycle.

Numerical simulations have taken up a substantial part of the increased workload of crashworthiness engineers. The potential of simulations due to the constant and spectacular development of hardware and software as well as the accumulated experience of a rapidly growing number of analysts has evolved quickly enough in order to enable analysis groups to become fully integrated in the vehicle design cycle. Indeed, it would be difficult to conceive of vehicle design with today's constraints of regulations and safety on one hand, and competitive pressure on the other hand, without any simulation at all.

It is important to note that numerical simulations have not lowered the normal workload of the test laboratories in the least if this workload is considered as the verification and certification of vehicle prototypes. The contribution of simulation lies in that it complements a testing facility by preventing unnecessary work from being done. The strength of simulation lies in rapidly performing important simulations in the form of parametric studies that allow quick elimination from prototyping those designs which have a high probability of not satisfying the testing criteria. The ideal picture is indeed one of a design, heavily supported by analysis, resulting in building of only those prototypes that are almost certain to pass all final verification testing. This type of mainstream use of numerical simulation as a direct support for the design team requires the rapid development of full vehicle FE models at the very early stages of the design. In fact, FE crashworthiness models are, in today's design environment, the very first numerical models of a prototype to be completed. It is the building of these models that constitutes the most important bottleneck in the analyst's work plan.

Although it is generally believed that the usefulness of simulations for car design decreases rapidly as the design stage becomes more advanced and the type of design changes that influence safety become increasingly expensive, there is a role for simulations in later, and even ultimate, design stages.

When a safety-related problem appears in a prototype during a test, it is simulation that allows for diagnosis of the cause of the problem and selection of an appropriate structural modification in a minimal amount of time.

Finally, it must be mentioned that numerical simulations have found their way into each aspect of traffic safety-related engineering, although the above-mentioned design support work is certainly its main function. In addition to structural analysis, occupant simulation is increasingly performed using finite element models [26]. Simulations are used extensively by legislative bodies to support the development of new regulations [27] and for the improved design of roadside hardware [28].

From the previous discussion, it is clear that numerical simulations enabled the car companies to comply with an otherwise impossible escalation of the regulatory environment. Only the extensive use of numerical simulation has enabled the motor vehicle industry to introduce increasingly safer cars and trucks in less time without a corresponding increase in test facilities.

3.2 Overview of Explicit FE Technology

FE crashworthiness analysis of transportation vehicles in general, and of ground vehicles in particular, is among the most challenging nonlinear problems in structural mechanics. Vehicle structures are typically manufactured from many stamped thin shell parts and subsequently assembled by various welding and fastening techniques. The body-in-white may contain steel of various strength grades, aluminum and/or composite materials. During a crash incident, the structure experiences high impact loads which produce localized plastic hinges and buckling. This can ultimately lead to large deformations and rotations with contact and stacking among the various components. The deformations initially involve wave effects, associated with high stresses. Once these stresses exceed the yield strength of the material and/or its critical buckling load, localized structural deformations occur during a few wave transits in the structure. This is followed by inertial effects, which dominate the subsequent transient response. Of particular interest here are structural integrity and associated kinematics and stacking of components, forces transmitted through the various members, stresses, strains, and energy absorption. In addition, the crash event may be considered as a low- to medium-dynamic event (5-100 mph), in comparison with ballistic impact, persisting for a short duration of 100-200 ms. Closed-form analytical solutions for this class of problems in structural mechanics present a formidable

challenge to the analyst. Numerical techniques, at this time, appear to be the practical option.

The FE method of structural dynamics solves numerically a set of nonlinear partial differential equations of motion in the space-time domain, coupled with material stress-strain relations along with definition of appropriate initial and boundary conditions. The solution first discretizes the equations in space by formulating the problem in a weak variational form and assuming an admissible displacement field. This yields a set of second order differential equations in time. Next, the system of equations is solved by discretization in the time domain. The discretization is accomplished by the classical Newmark-Beta method [29]. The technique is labeled implicit if the selected integration parameters render the equations coupled, and in this case the solution is unconditionally stable. If the integration parameters are selected to decouple the equations, then the solution is labeled explicit, and it is conditionally stable. Earlier developments in nonlinear FE technology used primarily implicit solutions [30]. FE simulation for structural crashworthiness by explicit solvers appears to be first introduced by Belytschko [11]. Later, Hughes et al [31] discussed the development of mixed explicit-implicit solutions.

The explicit FE technique solves a set of hyperbolic wave equations in the zone of influence of the wave front, and accordingly does not require coupling of large numbers of equations. On the other hand, the unconditionally stable implicit solvers provide a solution for all coupled equations of motion, which require assembly of a global stiffness matrix. The time step for implicit solvers is about two to three orders of magnitude of the explicit time step. For crash simulations involving extensive use of contact, multiple material models and a combination of non-traditional elements, it turned out that explicit solvers are more robust and computationally more efficient than implicit solvers.

3.2.1 Formulation

The discretized equations of motion for explicit FE formulation can be written as:

$$\underline{M}\,\ddot{\underline{x}} = \underline{f}^{(ext)} - \underline{f}^{(\mathrm{int})} \tag{3.2.1.1}$$

where $\underline{M}$ is the inertia matrix of the structure, $\ddot{\underline{x}}$ is the nodal acceleration vector, $f^{(ext)}$ is the external force vector and $f^{(\mathrm{int})}$ is the internal nodal force vector.

Time integration of equations (3.2.1.1) are obtained by a central difference wtechnique (explicit integration) as follows:

$$
\begin{aligned}
&\ddot{\underline{x}}^{(n)} = \underline{M}^{-1}\left(\underline{f}^{(ext)(n)} - \underline{f}^{(\mathrm{int})(n)}\right)\\
&\dot{\underline{x}}^{0.5(n+1)} = \dot{\underline{x}}^{0.5(n-1)} + \ddot{\underline{x}}^{(n)}\,\Delta t^{(n)}\\
&\underline{x}^{(n+1)} = \underline{x}^{(n)} + \dot{\underline{x}}^{0.5(n+1)}\,\Delta t^{0.5(n+1)}\\
&\Delta t^{0.5(n+1)} = 0.5(\Delta t^{(n)} + \Delta t^{(n+1)})
\end{aligned}
\qquad (3.2.1.2)
$$

where *n* is the integration step, Δt is the time step, $\dot{\underline{x}}$ and $\underline{x}$ are nodal velocity and displacement vectors , respectively.

Using the initial conditions, the nodal kinematics can be computed. Next, compute the strain rate, spin and Jaumann stress rate for each element:

StrainRate :

$$\dot{\underline{\varepsilon}}^{(n)} = 0.5\left(\underline{\nabla} \dot{x}^{(n)} + \underline{\nabla} \dot{x}^{(n)T}\right)$$

Spin:

$$\underline{\omega}^{(n)} = 0.5\left(\underline{\nabla} \dot{x}^{(n)} - \underline{\nabla} \dot{x}^{(n)T}\right) \qquad (3.2.1.3)$$

Jauman Stress Rate:

$$\nabla \underline{t} = \underline{C}\,\dot{\underline{\varepsilon}}$$

then, update the Cauchy stress for each element:

$$t_{ij}(t+\Delta t)=t_{ij}(t)+\dot{t}_{ij}(t)$$
$$Where\ \dot{t}_{ij}=\nabla t_{ij}+t_{ik}\omega_{kj}+t_{jk}\omega_{ki} \qquad (3.2.1.4)$$

then the solution proceeds to the next time increment and so on until the desired solution time is reached.

3.2.2 Explicit Integration

As can be seen, the explicit integration method stands for a numerical technique to integrate a system of ordinary differential equations that usually results from the spatial discretization of a continuum. "Explicit" refers to a specific technique whereby the equilibrium is expressed at a moment in time where the displacements of all spatial points are already known. Accelerations are determined from the equilibrium, and a central differencing technique allows the analyst to determine the displacements at the next timestep and repeat the process. The technique's attractiveness is that since the displacements are known at the time for which the dynamic equilibrium of the system is solved, this process requires the only inversion of the mass matrix, *M*.

Clearly, if a lumped-mass approach is used, the mass matrix is diagonal and no matrix inversion is necessary. This results in a very fast algorithm, since a system of uncoupled equations is all that needs to be treated. In all practical implementations, the internal forces are calculated using an element-by-element approach, thus avoiding the assembly of a global stiffness matrix and resulting in an algorithm with minimal central memory ('core') requirements. If carefully implemented, explicit integration is second order accurate. It is the element-by-element nature of the explicit algorithm that allows for the best characterization of this solution technique. Since stresses are calculated in each element separately from the corresponding nodal displacements and/or velocities, each timestep simulates the effect of the loads on one side of the element upon the opposing sides, thus representing the stress wave propagation through the element. The only drawbacks of the explicit algorithm are the conditional stability and the clear inability of the methodology to treat static problems. The conditional stability of

the explicit integration algorithm means that the integration timestep must be smaller then or equal to an upper bound value given as the Courant condition:

$$\Delta t \leq \frac{l_c}{c} \tag{3.2.2.1}$$

saying that the analysis timestep should not exceed the smallest of all element timesteps determined by dividing the element characteristic length through the acoustic wave speed through the material of which the element is made. The requirement is equivalent to saying that the numerical timestep of the analysis must be smaller than, or equal to, the time needed for the physical stress wave to cross the element. For typical automotive applications using mild steel elements (c= 5000 m/s) with a characteristic length of 5 mm, this results in an analysis time step of 1 microsecond. Due to this restriction, it is clear that explicit methods are best suited to treat problems of short duration and thus, high loading velocity and problems of a highly nonlinear nature that require small timesteps for accuracy reasons. It is again the rapid hardware development in the mid-1980s that has propelled automotive crash, a 100 ms phenomenon, in the realm of explicit analysis.

3.2.3 Shell Element

The shell element that has been, and still remains, the basis of all crashworthiness simulations is the 4-noded Belytschko and Tsay shell. [32-34]. Because this is a bilinearly interpolated isoparametric element, the lowest order of interpolation functions available is used. The element is underintegrated in the plane: there is a single integration point in the center of the element. Treatment of elasto-plastic bending problems is made possible by the definition of a user-defined number of integration points through the thickness of the element, all placed along the element normal in the element center. For computation, the use of an underintegrated formulation is very efficient. In most cases, it is faster to compute four underintegrated elements than it is to treat a single fully integrated element with four integration points. This is due to certain symmetries in the strain-displacement matrix that arise in the case of underintegrated finite elements.

The use of low order interpolation functions and a single in-plane integration point are the main reasons for the remarkable computational efficiency of the Belytschko and Tsay shell element. The drawback of the underintegration is that a number of zero-energy or hourglass modes exist in the element. Due to the simplifications in the evaluation of the element strain-displacement matrix, certain deformation modes result in a zero-strain calculation, and consequently, no stresses and nodal forces are calculated. This means that the nodal velocities can easily and rapidly diverge towards infinity as long as they remain parallel to the hourglass

modes of deformation of which there are six in the Belytschko and Tsay element. Hourglass instability is the major drawback with the Belytschko and Tsay shell element, or any other underintegrated element.

Hourglass instabilities are prevented mainly by the use of perturbation hourglass resistance techniques [35, 36]. This consists of detecting the presence of the hourglass mode in the element deformation pattern, and consequently, applying an external force field to ensure that the corresponding velocities and/or displacements remain bounded. It cannot be stressed enough that the hourglass forces result from an artificial external force field and do not form equilibrium with stresses in the material, consequently they tend to remove kinetic energy from the structure in a non-physical way.

The element formulation and integration techniques are chosen in a way to optimize computational efficiency, thereby compromising the material stiffness in the hourglass modes and the continuity of the out-of-plane displacement across the element boundaries.

Two additional features add to the amazing performance of this element. First, a co-rotational local system is used to ensure objectivity. All element strains and stresses are calculated in a local reference system that follows the element normal and the element 1-2 side. This ensures objectivity in the sense that no spurious strains and stresses are calculated if the element is subjected to large rigid body rotational motions. However, the position of the element local reference system depends upon the nodal numbering of the element, since it explicitly follows the element 1-2 side. This limits the validity of the formulation to problems involving small shear deformations. In practice, this is not a problem for solving crashworthiness problems since no large membrane shear deformations occur in sheet metal. It may cause hourglass modes to appear due to exaggerated rotations of the stress tensor.

Secondly, the element formulation is based on a strict uncoupling of membrane and bending effects. The membrane strains and stresses are calculated as resulting from the loads parallel to the local x-y plane exactly as in a plane stress element. The formulation is usually limited to small bending strains since no thickness changes of the element are considered. Again, this is not a problem when dealing with the simulation of sheet metal deformations. Bending stresses result from loading along the local z-axis and bending moments around the local x and y-axes. The bending strains in all integration points away from the element midplane are calculated using the Reissner-Mindlin equations and thus the assumption is made implicitly that the element is flat. In other words, all four nodes are in the same plane and a single normal is valid for the entire surface of the element. The

Belytschko and Tsay shell element is thus the sum of a plane stress membrane element and a Reissner-Mindlin plate element. Clearly, this is not valid if the element is warped. In a warped element, loads parallel to the local x-y plane cause bending strains and these strains are missed by the current element formulation. Consequently, warped Belytschko and Tsay elements severely underestimate the structure's bending stiffness. This is why this element fails the twisted beam test often cited in the literature.

In spite of a number of choices that clearly include a loss of generality and tradeoff for numerical robustness and computational efficiency, the results obtained using the Belytschko and Tsay element in thousands of crashworthiness simulations during more then a decade have been good enough to establish its usefulness to the industry. This can be explained in part by the particular nature of automotive crash events. Essentially, plastic hinges develop very rapidly over the full section of the thin (roughly 1 mm) sheet metal followed by large rigid body rotations of the parts between the hinges. Objectivity of the element is thus the primary requirement, and this is fulfilled in the element formulation. As long as the time for the development of the individual plastic hinges is small compared to the duration of the global event, the bending stiffness plays a less important role. Also, the small membrane deformation behavior and buckling behavior of the sheet metal is in line with the assumptions of the Belytschko and Tsay shell. Triangular elements were obtained by arbitrarily collapsing two nodes of a four-node shell element. This can result in a very inaccurate element, depending upon the shape of the triangle.

3.2.4 Plasticity

The plane stress plasticity at the individual integration points of the element is based on the membrane components of the stress tensor only. The yield condition is then written as follows for each integration point:

$$\sigma_{xx}^2 + \sigma_{yy}^2 - \sigma_{xx}\sigma_{yy} + 3\sigma_{xy}^2 \leq \sigma_y^2 \qquad (3.2.4.1)$$

where the yield stress is a function of the equivalent plastic strain and the strain rate in one way or another. After performance of an elastic stress update the yield condition is checked, and if it is not fulfilled, the stresses must be scaled back to the yield surface. Here, care must be taken to account for the nature of the plastic deformation and thus a flow of the material at constant volume must be simulated. Usually, a Newton iteration technique involving the unknown through-the-thickness strain in the element is performed. A non-iterative, radial return approach will lead to a deformation pattern involving a non-zero volumetric plastic strain. In fact, the apparent Poisson coefficient of the material during plastic deformation

will be equal to the elastic Poisson coefficient. Still, this computer-time-saving approach has been implemented in most explicit finite element codes and the approximation does not seem to have a very negative effect upon results of crashworthiness simulations, a further indication for the generally small deformation nature of the problem.

3.2.5 Contact Treatment

Finally, the code must provide for a means to simulate the transmission of forces between the individual body parts through contact. This is done by making contact interaction definitions part of the model or part of the spatial discretization. All early contact algorithm implementations were node-to-segment contacts: a well-defined set of nodes is not allowed to penetrate an equally well-defined set of segments (defined as either shell elements or sides of brick elements). If the nodes and segments are on different physical surfaces, a so-called master-slave contact definition exists. If they are on the same physical surface, a so-called single surface contact definition exists where the nodes of the surface are not permitted to penetrate the shell elements that they define. As previously stated, the contact definitions are an indispensable part of the spatial discretization of the structure. The definitions consist of a number of "contact springs" or spring elements that are generated in the model as soon as a penetration is detected and automatically deleted from the model as soon as that very penetration has been annihilated. The stiffness of this contact spring is given a default value by the software, but ultimately controlled by the user, who multiplies this default value with a penalty factor.

Clearly, users tend to increase the penalty factor in order to avoid deep penetrations and, consequently, unrealistic simulation results. However, an upper bound to the contact stiffness must always be considered since otherwise, the conditional stability of the explicit integration algorithm could be violated and instabilities could result. The default values of contact spring stiffnesses have been selected such that they operate just under the stability limit for a contact between two surfaces with identical (elastic) material properties and equal mesh densities. A contact spring operating at the stability limit will stop penetration of the slave node through the master segment in a single timestep. The penetration in a typical crash analysis where nodal velocities are of the order of 10 m/s is:

$$10*0.000001=0.000010m=0.01mm \tag{3.2.5.1}$$

showing that a safety factor of 10 with respect to the stability limit should not cause any appreciable loss of accuracy due to penetrations intrinsically allowed by the nature of the contact algorithm.

The main problems in contact algorithms originate in the node-to-segment nature of the model definition, as well as in the search algorithms that define which nodes are in contact with which segments. In particular, treating node-to-segment conditions only leads to a systematic failure of detecting edge-to-edge or edge-to-segment penetrations. Early search algorithms detected a nearest master node for each slave node and selected a single nearest master segment from all segments connected to the nearest master node. This is an algorithm that works very well for the simulation of the contact of two smooth convex surfaces, but fails in many situations that occur in the high curvature failure modes of an automotive structure. In particular, multiple impacts may occur simultaneously, and high curvatures in the mesh, as well as irregular meshes, may easily lead to the detection of a wrong neighbor segment, allowing numerous penetrations to remain undetected. Additionally, the search of the nearest neighbor node remained the most inefficient and time consuming part of the explicit solvers for many years, even after the introduction of the bucket sort algorithms.

3.3 Models Development Between 1987 and 1997

Between 1987 and 1997, the state-of-the-art model size for a full vehicle crashworthiness model has grown by a factor of 15, from 10,000 to 150,000 elements. The vast majority of this high number of elements are in the model of the vehicle body-in-white. All other car components are usually represented in much less detail, since their energy absorption is considered less important. It is generally thought that in the future, homogeneous models will be built in order to cover all load cases for frontal, side and rear impact simulations by a single model, saving roughly half of the expense of model development. The mesh size for this uniform and multi-load case model is between 5 and 10 mm. Mesh sizes larger than 10 mm do not provide enough accuracy, which mesh sizes below 5 mm make the element size smaller than the spot weld connections, in which case, another approach (brick element modeling) would make more sense. If the total sheet metal surface of a body-in-white is about 25 square meters, it is expected that model sizes between 250,000 and 500,000 elements for a full body-in-white would be the limit that should sensibly be used with shell elements. Each element represents between 0.5 and 1 gram of steel.

A further impression of the nature of this spectacular evolution can be obtained from Table 3.3.1 provided by Dr. Hannes Moeller of DaimlerChrysler Corporation:

TABLE 3.3.1 **Evolutuon of modelsize and CPU from 1988 to 1998**

Year	Typical model size	Hardware platform	Single processor CPU-time
1988	8-10000	XMP	5-10
1990	15-20000	YMP	10-20
1992	30-40000	YMP	20-30
1994	60-80000	C90	30-40
1996	100-120000	T90	40-50
1998	140-160000	T90	50-60

The search for higher reliability of the numerical results is the reason behind this ever-increasing model size. The first requirement would be that the mesh is able to smoothly represent the deformed shape of the car body, including all the highly-curved buckles in the crashed sheet metal. As a first order requirement, five elements (half a wavelength) are necessary to represent the width of a buckle in order to enable representation of the deformed geometry. The simulation result, however, remains mesh-dependent, and the predicted accelerations and energy absorption will continue to change until mesh convergence is reached. This point lies between 10 and 16 elements per buckle depending upon the section size, section shape, sheet thickness and material properties.

But model size is only the first half of the story. In over a decade of gained experience, it has become clear that mesh and element quality are of utmost importance for the reliability of the result of a crashworthiness simulation. The evolution in this field has, upon close inspection, been more spectacular than the increase in mesh size. From a coarse and rough approximation of the car body geometry (containing many conscious violations of elementary finite element theory) as was the state of the art in the mid-eighties, it has evolved toward a highly precise and a rigorous approach. Indeed, it is possible to say that meshing for crashworthiness has become a profession in its own right.

Normally, every sheet metal component in the car body is meshed separately using CAD surface data. In order to become a precise model of the sheet in the midplane, offsets of the surface data are carefully performed. The sheet is then meshed in a regular way using meshlines that are as much as possible parallel and orthogonal to the incoming pressure wave and using triangles only where necessary. Triangles are thus found in areas of mesh transition or areas of high double curvature (warpage) only. At the assembly of the individual sheets, further offsets may be necessary in order to guarantee a minimum gap between all parts so that no initial penetrations are generated. These gaps are also necessary to ensure a good performance of the contact algorithms and avoid deep penetrations through the midplane of the opposing part.

Once this task of generating the geometrical model has been performed, connections (spot welds) must be generated without deforming the geometry of the flanges on the individual sheet metal parts. This task can be completed in a number of ways and currently no clearly superior method can be distinguished. Several automatic procedures to generate spot weld elements of different kinds are currently being developed by software vendors as well as by automotive companies. Some fundamental problems remain, however. One is the real rotational stiffness of the spot weld, which will be discussed in a subsequent paragraph. Another problem lies in the desire to make the spot weld element location independent of the finite element mesh on both flanges. Since flanges are currently meshed with two elements over the width, automatic generation of a regular pattern for the spot weld elements proves a rather elusive goal. Still, it should be appreciated that in a modern vehicle model, between 3,000 and 5,000 spot welds are modeled individually and roughly in their exact locations.

Although the car body model accounts for approximately 75 percent of the entire model, more and more care is been given to modeling of the many other vehicle components. First to be mentioned are structural parts such as the subframe, doors, hood and wings, which use roughly the same modeling rules as the car body.

Particular care must be given to the connections between car body and subframe, which are often realized by bolts containing rubber bushings. Whereas the modeling of the rubber parts would require a prohibitively fine mesh in the context of a full vehicle simulation, it is still necessary to correctly account for the relative rotations between the body-in-white and subframe which can severely influence the acceleration response calculated in the passenger compartment. Therefore, a rigid body connection as well as a spring element connection will both lead to erroneous results. It is necessary to correctly simulate the motion of the bolt in

the bushing using contacts between surfaces that simulate the presence of the incompressible part of the rubber.

The powertrain model contains models for the engine, transmission, driveshaft and engine mounts, including their rubber bushings. The goal of this submodel is the correct simulation of the engine and driveshaft kinematics in order to account for the possible contacts with structural parts later on in the crash event. To achieve correct kinematics, it is necessary to accurately model the mass, rotational inertia and center of gravity position of the engine and transmission block. Furthermore, the engine mounts must be modeled in a similar way to the subframe mounts. This has proven to be the decisive factor in determining the relative rotation between powertrain and body-in-white. A cylindrical shell model with 5 or 6 elements over the circumference is typically used to model driveshafts in order to simulate potential contacts with brackets in the car body. Spherical joints connect the driveshafts to the wheel knuckles and to the transmission block. In order to avoid small timesteps, rigid body definitions are usually superimposed on the powertrain subsystem models. In order to obtain smooth contact forces between engine block and structure, the external geometry of the engine block must be accurately modeled using elements of a size not much larger then the ones used for the car body.

All the main parts of the front axle are also modeled using shell elements starting from CAD surface or line data. For a typical McPherson front axle, this subsystem will contain detailed modeling of the wheel knuckle, suspension strut, lower control arm and stabilizer bar. The same remarks made in the description of the powertrain system remain valid here. A detailed shell model is necessary to ensure that all potential contacts with structural parts can occur in the model. This means that the stabilizer bar is modeled as a cylindrical bar with 5 or 6 shells over the circumference. If these elements have a very small dimension, mass scaling or other techniques can be used in order to prevent a dramatic decrease in the calculated stable timestep. Usually the rubber bushings in the chassis model are not modeled in detail, as is done for the subframe and engine mounts. Rather, a series of revolute, cylindrical and spherical joints provide the correct hinges in the connections between the chassis parts as well as between chassis and car body structure. Obviously, a similar strategy is employed to model the rear axle parts in the case of rear impact simulations.

The wheels are connected to the axle models. The wheels consist of detailed geometrical models for wheel rim, brake disk and outer tire. The wheel rim and the brake disk are usually rigidly connected to the wheel rim, thus preventing the wheel from rotating. This must obviously be improved if mishandling simulations are performed, but is acceptable for crash simulations. A detailed model is

necessary to account for the correct inertial response of the wheel. The wheel can become a major load path in offset or oblique frontal crash events. Therefore, the tire stiffness must be accurately simulated. The air in the tire is simulated using the airbag algorithms of the explicit codes, yielding the pressure of a constant amount of air in the tire as a function of the compressed volume, assuming isothermal or isentropic conditions. A remaining problem is in the material model of the tires themselves. Existing tire models are far too complex to be incorporated in full vehicle crash models, and research is needed to generate reasonable and efficient approximations.

The third primary system to be modeled for a full vehicle simulation is the steering system including the steering rack, steering column and steering wheel. For the steering rack and its connections to the wheel knuckle, the same remarks are valid as for the modeling of the front and rear axles. A correct modeling of outer contours releasing the correct degrees of freedom in the connections using joint and/or spring elements is usually considered sufficient. Rarely, a detailed model is built that couples the translational motion of the steering rack to the rotation of the wheels. This can be of importance in the study of frontal offset and oblique impacts. Very often, a steering rack model that is fixed to the subframe structure is used, thus effectively blocking the wheel rotation. The steering column is usually modeled as a set of cylindrical tubes sliding in each other. It is this sliding motion that simulates the telescopic deformation of the steering column as the dummy hits the steering wheel.

To simulate the Cardan joints in the steering column, the exact geometry of the device is usually modeled with contact algorithms automatically accounting for the so-called stop-angles.

Observation has shown that engine motion is crucial for the dummy response in the passenger compartment during a frontal impact. Engine motion, in turn, is at least partly determined by contacts with the structure and other components located under the hood. Consequently, these components must be modeled carefully and with mesh sizes that are not very different from the engine block mesh size. These components include the battery, radiator, air conditioning unit, automatic braking system unit, ventilators and electro-engines at the radiator, radiator bracket and light brackets. Some of these are mild steel structures and can be modeled as such. Others are hard points and little care must be given to the determination of their stiffness as long as the resulting strength is considerably higher than that of the surrounding structural parts. An exception is the radiator model, which must crush under the impact of the engine block and somewhat damp its acceleration response. Equivalent models based on force-displacement

curves determined in a drop test are usually used, since a detailed modeling of the radiator structure is again prohibitive.

Whereas a structural model of the doors is largely sufficient for the simulation of frontal and rear crashes, this is not true for the simulation of side impact load cases. In this case, the door inner components must be carefully modeled. Hinges and locks must be modeled in such a way that the correct rotational degrees of freedom are released between the door model and the model of the body-in-white. Door structures are mostly quite weak with respect to bending. The inner components such as guide rails for the window, electrical motors, loudspeakers and the window glass provide the flexural stiffness of the entire component, and thus, determine the critical timing of the impact between door and occupant. The inertial response of the door structure is important in determining the velocity of impact with the dummy. The mass of the door as well as the masses of its individual components should be carefully checked.

For completeness, the following modeled components for different load cases are mentioned. Windshield and bumper are modeled in frontal impact, whereas the fuel tank and spare wheel and tire are typically present in rear impact models. The instrument panel may be required for the simulation of frontal and side impact and the front seats are essential in all models. At this point, roughly 50 to 60 percent of the total vehicle mass is modeled and a careful mass check is typically performed at this stage. The remaining masses are traced and locally added to the model as density increases and/or nodal added masses.

The modeling technology has expanded beyond the actual vehicle models with finite element approximations of deformable barrier structures, crash dummies and different impactor devices.

3.4 Software Development Between 1987 and 1997

Modeling technology has evolved towards ever larger and more detailed numerical models of the vehicle in a quest for more accuracy and more reliability in the results. Software development has primarily fought a battle of trying to run and manage these models with continuously increasing size, using essentially the same basic technology. A first important focus point of development was on animation packages for rapid post-processing of the simulations. These packages allowed for visualization of the simulated crash event and the deformation modes of the car body and for display of plastic strain, stresses and energy densities over the individual parts. This allowed the engineer to immediately identify those components that absorb more or less energy. Similarly high emphasis was placed

on the interactive pre-processing software of the models. The main goal was to quickly incorporate structural changes in an existing numerical model.

The main programming effort has been to increase the efficiency of the solvers themselves. Explicit finite element codes have been optimized to the point that they run in a 99 percent vectorized mode. Although it must be said that the element-by-element nature of the codes lends itself particularly well for vectorized processing, this was certainly a remarkable achievement considering the nodal force assembly, and the search algorithms in the contact-impact routines. A similar, even more important effort is continuously displayed in the parallelization of the codes achieving ever better scaling performance on both shared memory and distributed memory machines. A major advance was the replacement of node-based contact search algorithms by so-called segment-based search algorithms. The old algorithms based on the search of a nearest master node for every slave node are always computer-time consuming even if bucket sorting improves this situation. With the new segment-based search methods, an algorithm was introduced that is not only computationally much more efficient, but also improves on many of the shortcomings of older algorithms.

Finally, a number of techniques were developed in order to allow explicit simulations to run with a constant timestep value. This at first seems a non-trivial matter since the stable time step of the analysis is linearly dependent upon the shortest mesh dimension in the model. As deformation changes (reduces) this dimension, a drop of the timestep seems mathematically unavoidable. Indeed it is not possible to keep a constant timestep during a crash simulation with highly deforming shell elements without changing the physics of the problem. Several methods were developed to achieve this. They vary from the so-called small strain formulations where the influence of the change in geometry upon the element stiffness is ignored from a certain point on (or during the entire analysis), to a controlled reduction of the material's elastic modulus as it plastically deforms. The most widely used method is mass scaling. As an element dimension decreases, the corresponding material density or nodal masses are increased in such a way that the resulting time step remains constant.

These options render crashworthiness simulations feasible and useful in about 75 percent of all cases. Although the physics of the problem are locally modified, this is not a major objection if one considers that the local stress distributions must have been wrong before mass scaling (or any of the other constant timestep options) was applied. Since a vehicle crash is by nature a small strain event, no large membrane strains should really occur in the shell elements that represent the car body. Consequently, the mesh dimensions should not change and the timestep should ideally be constant.

This is true only if the mesh is sufficiently fine in order to give a smooth representation of the deformed (crashed) vehicle geometry, including all high curvatures that may occur. This will in practice rarely be the case. Mostly, the mesh is at least locally too coarse, and large strains occur at the element level, resulting in a drop of the timestep. Apart from a non-realistic stress distribution, large deformations also violate the basic assumptions of the Belytschko and Tsay element and will mostly result in a locally unstable behavior or in the development of hourglass modes. It can then be said that the application of mass scaling has little or no influence on the resulting accuracy of the global simulation result.

The basic technology of explicit finite element codes as applied to crashworthiness problems remained largely the same during the last decade. One of the major improvements in accuracy was the replacement of degenerated quadrilateral elements by a true C0 triangle element as proposed by Belytschko [35]. This element is free of hourglass modes and has a bending response equivalent to the flat quadrilateral Belytschko and Tsay element. It constitutes a major improvement with respect to a degenerated quad but still must be used with care and in limited numbers mainly because of the in-plane shear stiffness that can be too high in certain cases, depending on mesh size and shape.

It must also be noted that a large number of special purpose options were added to the codes in order to fulfill crash-specific functions in the models. Such as rigid bodies, but spring elements, spot weld elements, joint elements and occupant simulation oriented options such as seatbelt, and airbag models. These mainly improve the application scope of the codes. It seems that the simulations have arrived at a crossover point where the factor limiting the accuracy of the simulation is no longer the mesh, but rather, the numerical algorithms that are used in the explicit finite element codes. Consequently, a clear trend can be observed towards the use of more sophisticated algorithms as will be explained in the Section 3.5 – Limitations of Current Technology.

3.5 Limitations of Current Technology

In the late 1980s, a leading engineer in the German automotive industry referred to crashworthiness simulations as “numerical adventure,” and it must be said that he was not wrong. To claim that early simulation work in this field was more of an art then a science is almost an understatement.

Any finite element simulation activity can be seen as a chain with two links. The first link is the numerical model, essentially a hyper-complicated mass-spring system whose dynamic behavior is an approximation of the continuum (the car) that is to be modeled. The second link is the software or the numerical algorithm that has to perform a numerical time integration of the system of ordinary differential equations that govern the behavior of the model. Again, the solution obtained on the computer is an approximation of the correct (analytical) solution.

The main problem with early simulation work was clearly the coarseness of the shell element mesh representing the car body. This resulted in simulation of the low curvature (high wavelength) buckling modes only, and thus constantly overestimated the energy absorption in the structure since high curvature modes were precluded from the simulation by the outlay of the mesh. Too coarse meshes generally resulted in too stiff behavior of the energy absorbing, highly deforming structural parts. The weak link in the chain was clearly the mode, and any additional loss of accuracy due to the use of very simple algorithms was almost welcome.

Some of the algorithmic deficiencies tended to compensate for the errors due to the coarseness of the finite element mesh. Penetrations allowed due to failing contact algorithms and zero energy modes in underintegrated shell elements would all weaken the structural response and thus improve correlation between the numerical and measured results.

Today, this situation has been reversed. Greater potential for improvement in the near future lies in the use of more accurate algorithms rather than in further refinement of the models. This is due to the continuous increase in mesh size and mesh quality and better representation of the real vehicle by the model through detailed modeling of multiple components. In other words, the algorithms have become the weak link in the chain. Improved algorithms for shells and contacts have been available in explicit codes for quite a while, but have not been used extensively for a variety of reasons, including increased computer time and lack of numerical robustness.

In the near to mid-future, current model sizes of roughly 150,000 elements for a single class of load cases (frontal, side or rear) and a homogeneous mesh of roughly 350,000 elements for all load cases could be a reasonable model size for all crashworthiness engineering purposes. This assumes that improved contact algorithms with edge-to-edge capability are used in conjunction with fully-integrated, or at least physically stabilized, shell elements. The required computer time is estimated to be three to four times more than current technology requires.

Approximately half of all numerical problems in modern crashworthiness analysis work are caused by edge-to-edge penetrations. In early explicit simulations (for example in the defense industry), this was never a problem since contacts between convex surfaces with low curvature were considered and consequently node-to-segment contact algorithms have more than sufficient generality to detect all occurring penetrations. This is no longer the case for automotive structures. The complex surfaces with high double curvature are discretized by somewhat too-large finite elements, resulting in a polygonal surface with lots of kinks and edges. Edge-to-edge penetrations can go undetected since they cause no nodal penetrations through any of the segments. This by itself should cause no further problems, except for making the model less stiff than the actual structure where no penetrations can occur. However, consequent movements of the penetrated segments can easily lead to so-called impacts of nodes on segments 'from the wrong side.' These contacts in tangled structures will lead to extremely high local contact forces since entire structural parts may be hung up upon a single node. Suanomalies in the models will lead to local instabilities, hourglassing due to the extreme out-of-plane loads and potentially abort the simulation prematurely. The only way out provided by classical contact algorithms is to set the tangled nodes free and allow penetration without any further checks resulting in a further loss of realism. Edge-to-edge algorithms are currently being introduced into all commercial explicit finite element codes.

A second improvement is the efficient neutralization of the zero-energy or hourglass modes in the shell elements. As explained in Section 3.2.3 – Shell Element, zero-energy modes exist in underintegrated shell elements and correspond to zero-element stiffness with respect to certain deformation modes, such as in-plane bending. The loss of stiffness caused by this approach was clearly offset by the gain in efficiency due to underintegration, and in any case, was not seen as a great burden as long as the use of coarse meshes resulted in a behavior of the model that is generally too stiff.

The use of increasingly finer models allows for detection of the influence of the zero-energy modes and the corresponding perturbation hourglass forces in the numerical models. The perturbation hourglass forces are nodal forces introduced numerically in order to prevent the hourglass velocity components in the element from becoming unbounded. Although these forces are supposed to make up for the missing element stiffness, they do not correspond to a stress in the element, and thus constitute an external force field of rather arbitrary magnitude controlled by user-defined coefficients. Due to the introduction of this force field, a perturbation-stabilized underintegrated element may behave both too weak or too stiff compared to reality.

A first possibility to cope with the problem seems to be full integration using four-Gauss integration points in the element of the bilinearly interpolated element. Unfortunately, this rather straightforward solution does not work. Fully underintegrated elements with uniform bilinear interpolation suffer from another drawback called shear locking. Shear locking occurs when non-zero out-of-plane shear strains are predicted by the element in conditions of pure bending resulting in an overly-stiff element response. This problem is caused by uniform interpolation: if out-of-plane deflections are interpolated with higher order rather then bilinear functions, formulations that exhibit no shear locking are possible. However, this dramatically increases the complexity of the implementation and decreases the element performance. Development of a fully-integrated element that avoids all shear locking and maintains the simplicity of uniform bilinear interpolation has proven to be a challenging task.

Several solutions exist to neutralize hourglass modes using uniform bilinear interpolation while avoiding shear locking. A first possibility is the selective-reduced-integration (SRI) elements. [37,38]. This solution consists of performing a full integration for the membrane and bending strains combined with a reduced integration for the out-of-plane shear strains. These elements effectively avoid shear locking for rectangular elements but some problems still occur in irregular meshes.

A second solution corresponds to the assumed-natural-coordinate-strain (ANS) elements. Here, the isoparametric coordinate field is no longer differentiated, but improved estimates of the out-of-plane shear strain field are used directly. This approach leads to a formulation without shear locking independently of the quadrature rule used and both reduced integration and full integration implementations exist in most commercial explicit finite element codes. Obviously, a reduced integration ANS element does not solve the original hourglass problem and would not suffer from shear locking. The advantage of the ANS approach for these elements lies in the improved accuracy obtained in irregular meshes. In particular, the ANS element passes the Kichhoff patch test, whereas elements with classical quadrature of the shear strains always fail this rather elementary requirement. A very efficient fully-integrated ANS element exists in the LS-DYNA code, which overcomes all hourglassing and shear locking problems at a cost of roughly three times the original Belytschko and Tsay shell element.

If full integration is still perceived as not efficient enough to allow parametric studies on large-scale crashworthiness models of vehicles, a more economical approach may be given by physical stabilization [39]. Here, underintegrated versions (preferably of the ANS element) are used and an approximate analytical integration is performed over the element of the non-constant part of the strain.

The constitutive law is invoked in order to estimate hourglass stresses resulting in a set of nodal forces that are supposed to correct missing stiffness components of the element rather exactly. This approach is much more efficient than full- or reduced-selective integration and requires only about 30 percent more computer time then the original Belytschko and Tsay element. The element also passes the Kichhoff patch test.

Next to the existence of zero-energy modes, a second potential problem with the highly efficient Belytschko and Tsay shell element is its limitation to flat geometries. This results from the use of the Mindlin plate theory where the fiber direction is assumed to coincide with the normal to the plate surface. If this assumption is used in warped elements, the bending strain can be underestimated for two reasons. First rotations normal to the element will not cause any curvature to be calculated although these rotations may not be parallel to the nodal drill degrees of freedom (fiber direction) in all nodes of the element. Second, force loads in the element plane should also cause bending strains in a warped element and will fail to do so when the unmodified Belytschko and Tsay element is used. Those effects will lead to the failure of the so-called twisted beam test by this element. An efficient coupling of membrane and bending deformation is advocated in [39]. These formulations allow accurate modeling of surfaces with double curvature using warped elements with warp angles up to 15 to 20 degrees.

It should be emphasized strongly that none of the improvements described above affect the original assumption that only small deformations exist within a single shell element. These improvements are merely meant to correct some deficiencies of the element formulations within this framework. Thus, the use of more sophisticated elements does not allow the use of coarser meshes. All rules developed earlier to determine mesh density of a crashworthiness model still apply. A good crashworthiness simulation can only be obtained if the mesh is able to smoothly represent the deformed geometry of the car body. In fact, this condition may have become stronger then before since large element deformations may lead to numerical problems and generate instabilities that were almost never the case with the numerically ultra-robust Belytschko and Tsay element.

3.6 Applications

This section presents a summary of typical FE models used in frontal crashworthiness analysis.

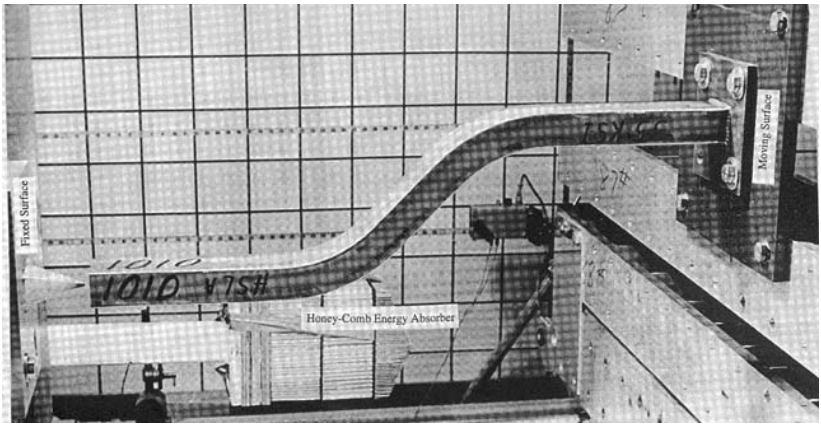

Fig. 3.6.1.1 **Rail test set-up**

3.6.1 Component Models

Component models can be grouped into generic components such as S-rails and rectangular tubes, and actual isolated components such as upper rails, lower rails and hoods. These components are typically tested in both quasi-static and dynamic modes to identify their crush performance. In dynamic testing, a drop-silo or a sled is used. In drop-silo testing, the component is fixed to the ground on a load cell and loading is typically applied from the gravitational fall of a rigid mass onto the free end of the component. In sled testing of components, the component is mounted horizontally onto the sled (Figure 3.6.1.1) which subsequently is launched to impact a rigid or deformable surface with the component making first contact. Figure 3.6.1.2 shows the S-rail final deformations corresponding to initial impact speeds of 2, 4.5 and 8.2 m/s into a rigid wall. The rail deformations exhibited two plastic hinges at the rail curvatures, rotation at the free end and plastic hinge at the fixed end. The measured peak force increased with impact speed from about 50 to 60 kPa, due to strain rate effects of the material used. The FE simulation corresponding to 8.2 m/s impact agreed quite well with the test result when the strain rate effects were included in the simulation. Increasing the number of shell elements from 2,000 to 3,000 showed minor influence on the overall response.

The deformed mid-rail shapes of an actual passenger car mid-rail are shown in Figure 3.6.1.3, corresponding to test speeds of 2.2, 4.4 and 6.7 m/s, respectively [40]. In Figure 3.6.1.4 the FE predictions of the force-time pulse show good a

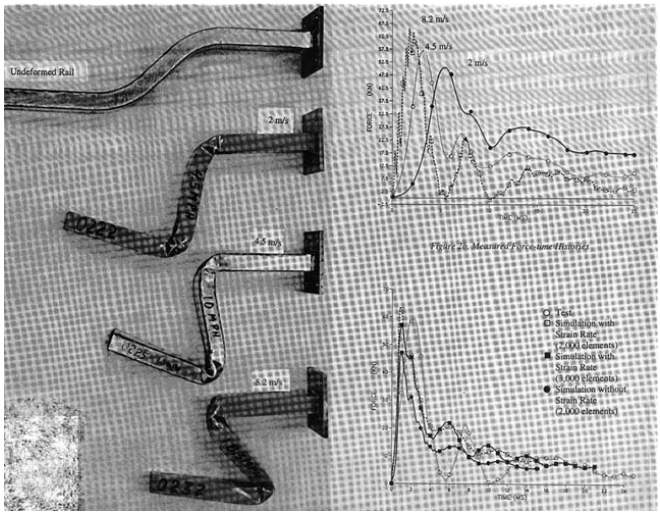

Fig. 3.6.1.2 **Rail response**

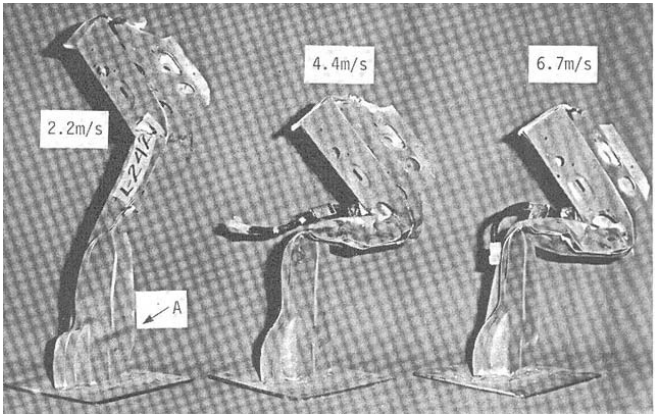

Fig. 3.6.1.3 **Vehicle component deformations**

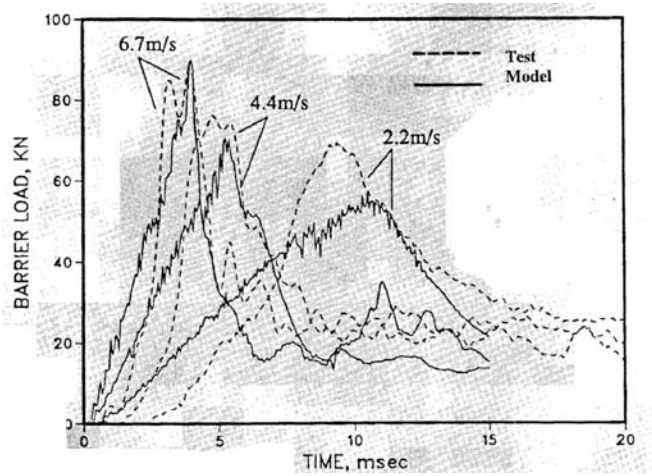

Fig. 3.6.1.4 **Measured and FE-calculated forces**

agreement with the test data. Like the S-rail response, the peak force increased with increasing the impact speed due to strain rate effects.

3.6.2 Substructure Models

A vehicle front structure subassembly finite element model is presented in Figure 3.6.2.1. Figure 3.6.2.2 shows a comparison between the predicted and measured force pulse from impact of a front structure subassembly into a rigid wall [41]. In this case, the impact speed was 13.4 m/s. In this simulation, no strain rate effects were included in the analysis since themid-rails were manufactured from high strength steel, which typically exhibits little strain rate effects.

3.6.3 Full-scale vehicle structure models

As indicated earlier, FE models of frontal crashworthiness have been evolving since the early 1980s. Table 3.6.3.1 provides a summary of representative front structure models, available in the open literature. These models simulated vehicle crash into a rigid wall. They clearly indicate the evolution of the models in size and complexity. It may also be observed that detail modeling of vehicle structures has become an integral step in the vehicle design process. Other frontal impact models include oblique (+/-30 degree) impacts with a rigid barrier, offset impact

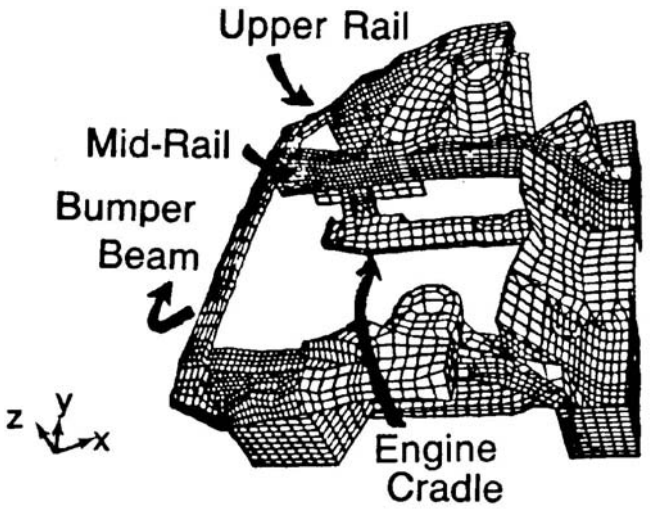

Fig. 3.6.2.1 **Vehicle front structure subassembly**

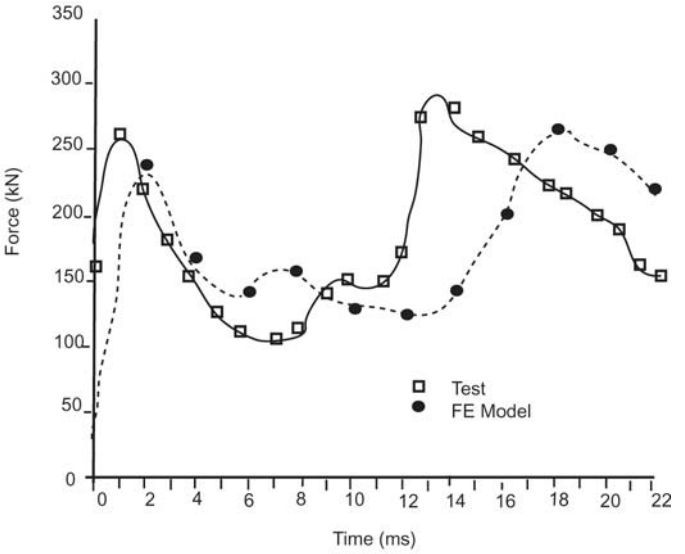

Fig. 3.6.2.2 **Force-time history**

Table 3.6.3.1 **Summary of typical frontal impact models**

Year/Ref	Mfr.	Elements	Sim.time (ms)	Analysis Code	CPU hours/ platform
1986 [42]	BMW	2,800	90	CRASHMAS	89/
1986 [19]	Suzuki	3,439	60	DYNA3D	24/Cray-XMP
1986 [43]	VW Polo	5,661	60	PAM-CRASH	4/Cray1
1986 [24]	Citroen (BX)	7,900	80	PAM-CRASH	12/Cray/XMP
1986 [25]	Opel (Vectra)	7,991	80	PAM-CRASH	16/Cray-1S
1987 [44]	GM (GM 80)	9,500	80	PAM-CRASH	12/Cray-XMP
1987 [18]	Isuzu (750 Coupe)	10,000	70	PAM-CRASH	14/Cray-XMP
1989 [20]	Saab (900)	7,500	80	DYNA3D	22/Cray-XM-P28
1989 [45]	Mazda	18,000	80	PAM-CRASH	18/Cray-XMP
1989 [46]	Nissan	12,000	120	PAM-CRASH	20/Cray-XMP
1989 [47]	GM (W Coupe)	17,000	80	DYNA3D	20/Cray-XMP
1992 [48]	GM	17,000	80	DYNA3D	9/Cray-YMP4
1994 [49]	Opel (Omega)	16,000	100	RADIOSS	—/Cray-YM-P4
1994 [50]	Ford (Windstar)	60,000	100	RADIOSS	12/Cray-C90-16
1996 [51]	GM (G Sedan)	62,235	100	DYNA3D	45/Cray YMP8E

models with rigid or deformable barriers with 40 to 50 percent overlap, vehicle-to-vehicle impact with full or partial overlap, and central or off-center impacts with a rigid pole.

The following example illustrates the development of a frontal crash model of a four-door passenger car. It simulates the primary load carrying components of the vehicle in frontal impact with a rigid barrier. Particular attention was paid to the FE mesh of the mid-rails, lateral rails, front tie bar, and dash panel. All sheet metal components were modeled and fastened together by spot welds corresponding to the actual hardware. Approximately 10 mm x 10 mm shell elements were used in the front structure where plastic hinges and buckling were anticipated. Coarser mesh was used for the structure behind the dash panel where limited deformations were expected. The model included a bumper system with appropriate connectivity to the mid-rails. The radiator was modeled using solid elements, with material properties corresponding to honeycomb behavior in compression. The engine and transmission were simulated by rigid shell elements, which represented the mass and moments of inertia at the engine's CG location. The engine mounts between the engine and the supporting structure were modeled by appropriate joints. The tires and wheels were modeled by a combination of shell and solid elements to represent the compliance and load transmission characteristics of these components. Two front door models were included with appropriate hinge properties. The rear doors were excluded, as their influence on frontal crash performance was assumed negligible. An instrument panel was also included along with appropriate structures for knee restraint. Finally, the inertial characteristics of the whole vehicle model were checked against the actual vehicle and concentrated masses were added to ensure agreement between the model's inertia and the corresponding hardware.

3.6.3.1 Model Statistics:

- 61,500 shell elements
- 500 solid elements
- 25 beam elements
- 1,200 spot welds
- 15 joints
- 40 concentrated nodal masses
- 10 springs
- 200 parts
- 66,000 nodes

3.6.3.2 Contact Definitions

A rigid wall was defined in front of the vehicle with stick condition. Automatic contact surfaces were defined in six zones as follows:

- Front-left corner (up to front body hinge pillar)
- Front-right corner (up to front body hinge pillar)
- Front-center (include up to the middle of the engine)
- Rear-center (from middle of the engine to the fire wall)
- Driver side center-pillar to door
- Passenger side center-pillar to door

3.6.3.3 Initial Condition

An initial velocity of 13.4 m/s was defined for the entire vehicle structure which impacted a rigid wall.

3.6.3.4 Results

The model response was calculated on a CRAY Y-MP8E system. The time step was approximately 0.7 ¼s. A 100 ms simulation was completed in about 45 hours on one processor. In this run, it was necessary to refine the radiator model since severe hourglassing was observed. The initial (at time 0) and final (at 100 ms) vehicle deformed shapes are shown in Figure 3.6.3.4.1. Intermediate vehicle configurations (not shown here) exhibited realistic sequential deformations as seen in high-speed film analysis of barrier crashes. The time histories of the global energy balance, velocity at the front rocker, and barrier force provided very reasonable results, comparable to test data [51].

In addition to frontal crash models, other models have been developed to simulate side impact with a deformable barrier [52], rear impact, and roof crush models, respectively [53]. Also, car-to-car crash models have been simulated [54].

3.6.4 Integrated Vehicle-Occupant-Restraints Model

Traditionally, frontal crashworthiness analysis has focused on sequential simulations of vehicle structures and occupants, with the occupant simulation being driven by the vehicle (calculated or measured) deceleration pulse. Consequently, analysis techniques and associated tools have been developed to meet the needs of the two communities. This process has many shortcomings, including real-time interactions between the occupant and vehicle structure during the crash event are not simulated, the analyst must learn and use two analysis

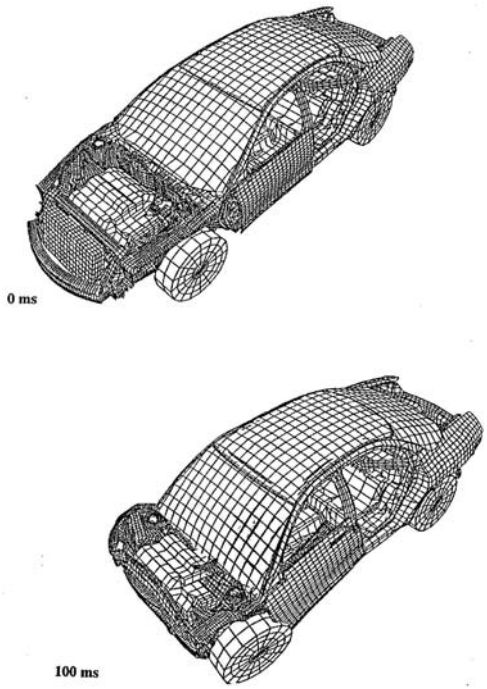

Fig. 3.6.3.4.1 **Initial and final vehicle deformations**

techniques which is an inefficient use of human and hardware resources. To remedy this situation, attempts have been made to couple occupant and structural codes [55]. This process allowed for real-time interactions between the vehicle and occupant, but left the analysis community to deal with two analytical tools.

It has always been, and still remains, the desire of safety analysts to simulate the crash event in one model that can predict occupant response associated with the crash event in real time. Conceptually, all FE codes can accomplish this task, since rigid body equations of motion are a special case of the FE formulation. The only missing components were dummy and restraint models. Once these are developed, crashworthiness simulations that include structures, occupants and restraint systems in one model become a reality. The development of a subsystem model of the Hybrid III thoracic dummy model interactions with a steering wheel using a single code has been demonstrated [56]. The Ove-Arup group discussed the advantages of using a single code in safety analysis, and presented graphics depicting dummy models and an integrated vehicle-dummy model [57].

Schelkle and Remensperger [58] discussed the development of an integrated model of a passenger compartment and occupant using a single FE code. The model simulated a sled test by 8,700 elements in frontal crash, and included an unfolded air bag, steering system, knee bolster and seat. A 100 ms simulation required 13 CPU hours on a CRAY-2 computer. Although the model exhibited reasonable kinematics, the authors indicated that the contact algorithms were not sufficiently robust to account for interactions between the dummy arms and the deploying air bag.

Khalil and Sheh [51] developed an integrated model for frontal crash. This model integrated the following components/subsystems into one FE model. These are the primary components of the model:

- vehicle including a body-in-white structure of a four-door passenger sedan,
- engine, transmission, etc., weighing 1,750 kg,
- bucket car seat structure with the seat cushion,
- nergy absorbing steering column with a steering wheel and folded air bag,
- instrument panel, including a driver side knee bolster,
- door structure, and
- Hybrid III dummy

Model statistics:

- 70,000 shell elements
- 9,000 solid elements
- 300 beam elements
- 1,300 spot welds
- 300 parts
- 91,000 nodes
- 20 contact segments

Figure 3.6.4.1 shows the integrated model at time 0 and a deformed configuration at 100 ms. The model kinematics, showing vehicle deformations, air bag deployment and forward motion of the dummy and subsequent interactions with the air bag and knee bolster are qualitatively similar to a barrier test (Figure 3.6.4.2). Figure 3.6.4.3 shows the energy balance for a typical run. It can be observed that the total energy remained approximately constant throughout the 100 ms duration, and the rise in internal energy and the decay in kinetic energy are smooth. This attests to very little interpenetrating among the contacted segments. The vehicle velocity response in time, at the rear rocker, is shown in Figure 3.6.4.4, along with experimental data from one test. The velocity trace agreed quite well with test data, particularly at the point where the vehicle velocity crosses the zero line.

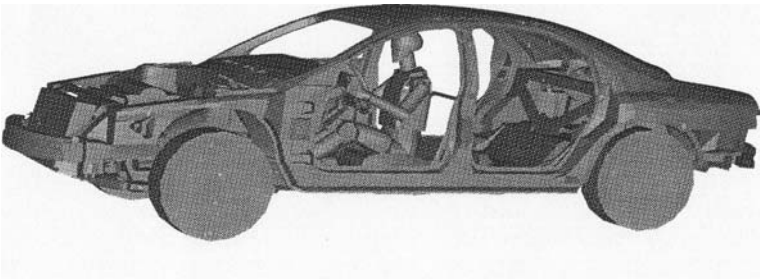

Fig. 3.6.4.1 **Integrated model**

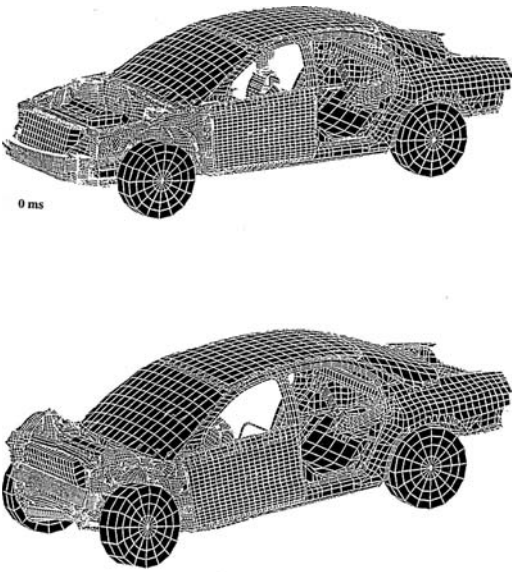

Fig. 3.6.4.2 **Integrated model deformations**

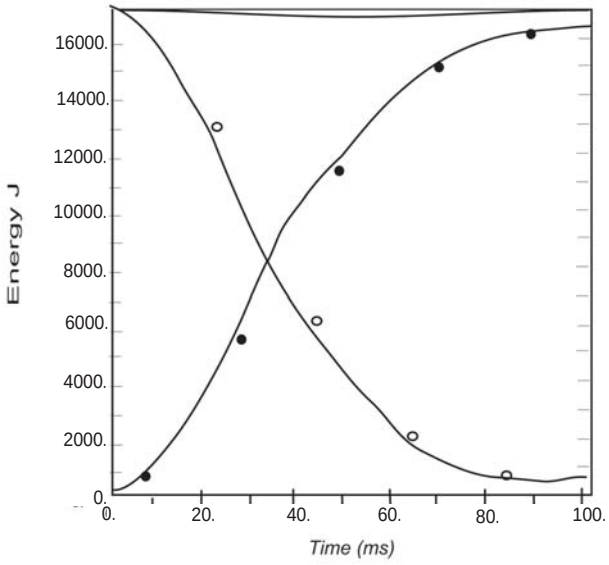

Fig. 3.6.4.3 **Energy balance of integrated model simulation**

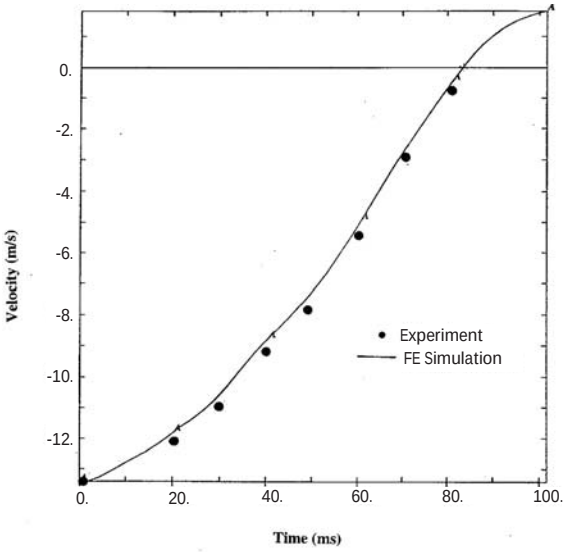

Fig. 3.6.4.4 **Rear rocker velocity**

This is of interest as it indicates that the model captured the overall stiffness of the deforming vehicle structure.

Figure 3.6.4.5 shows the barrier unfiltered force-time pulse. The pulse shape with its two peaks and the times at which they occurred is consistent with experimental data.

The first peak force almost coincided with the results obtained from one test. However, the second peak was only 60 percent of the test value. This may be due to inexact modeling of the engine-to-dash panel interactions.

Subsequent to development of the integrated model, to illustrate its robustness it was exercised to simulate an NCAP test. Figure 3.6.4.6 shows the model deformations at 100 ms corresponding to impact with a full rigid barrier from an initial speed of 35 mph.

Next, the model was exercised to simulate vehicle frontal impact with a rigid pole. The initial impact speed was 30 mph. Figure 3.6.4.7 shows the initial model set-up and the deformed configuration at 100 ms.

Finally, the model was tested to simulate vehicle impact with an offset rigid barrier. The initial vehicle speed was 30 mph. The vehicle impact was on the left side with 50 percent barrier overlap. The initial model configuration and deformed configuration at 100 ms is shown in Figure 3.6.4.8. A comparison of frontal vehicle deformations in time is shown in Figure 3.6.4.9, which clearly demonstrate the difference in frontal deformations corres-ponding to the previous four impact scenarios.

3.7 Summary

Although the FE technology for structural mechanics was introduced in the early sixties, it took about 25 years of additional development to apply it successfully to crashworthiness simulation of automobile structures. The developments were mainly in nonlinear problem formulation of shell elements, reduced spatial integration, explicit time integration, plasticity, and contact-impact treatments. The role of super computers and code vectorization was indeed indispensable for the development of full-scale vehicle models.

The mid-eighties to the mid-nineties time span can be characterized as the renaissance period of FE crashworthiness models. Generic and actual components of vehicle structures as well as full-scale vehicle models were developed to simulate

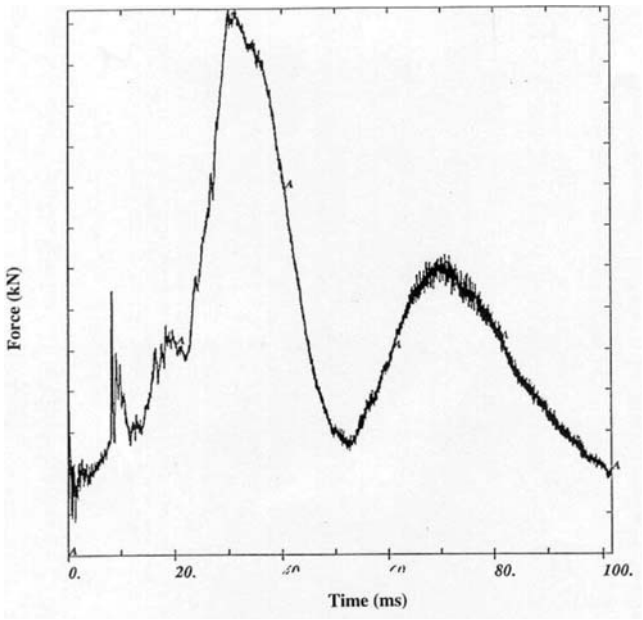

Fig. 3.6.4.5 **Force pulse of integrated model simulation**

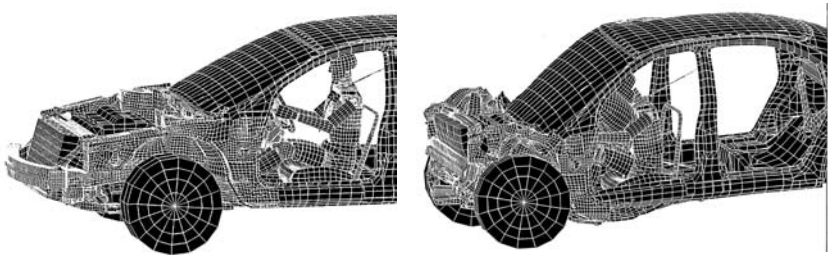

Fig. 3.6.4.6 **Initial and final model configurations for NCAP test (35 mph)**

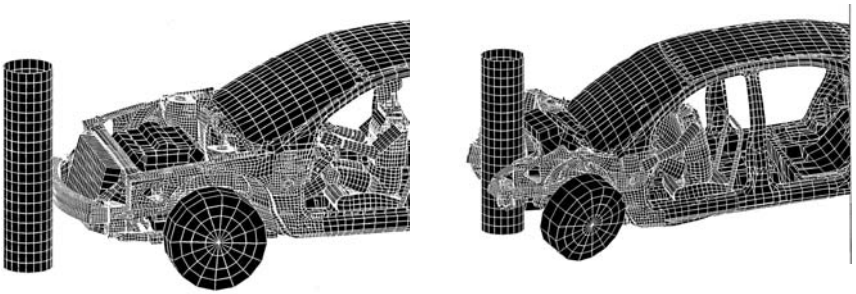

Fig. 3.6.4.7 **Initial and final model configurations for pole impact test (30 mph)**

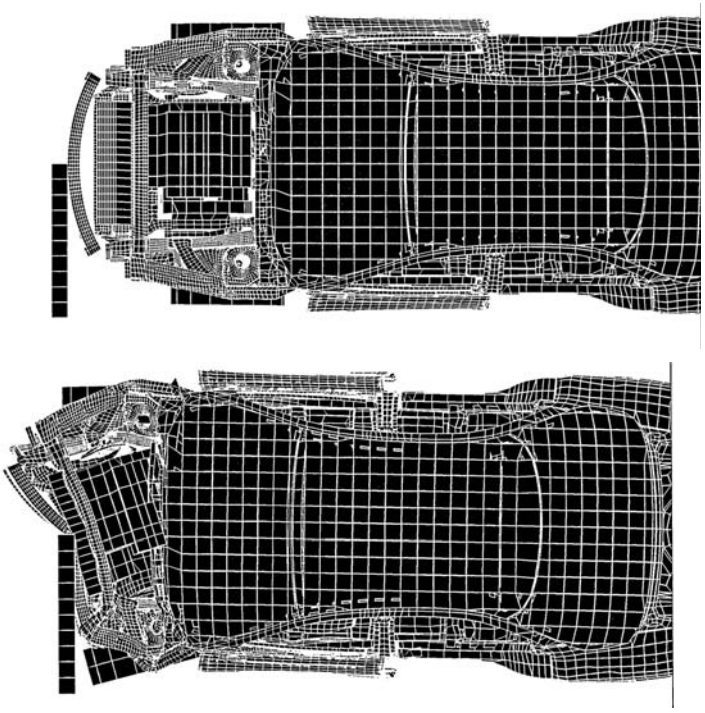

Fig. 3.6.4.8 **Initial and final model configurations for offset test 30 mph)**

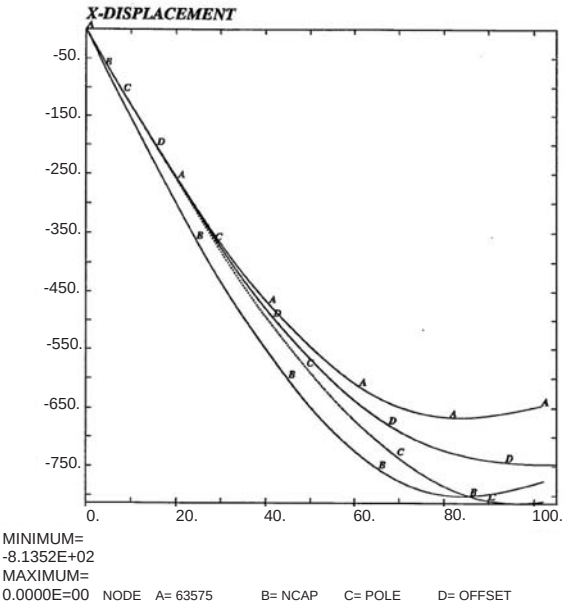

Fig. 3.6.4.9 **Frontal vehicle deformations for 30 mph, NCAP**

frontal, side, rear vehicle impact with barriers. Vehicle-to-vehicle collisions were also developed and analyzed. In addition to vehicle structural modeling, dummy and air bag models were created and their responses were validated against experimental data.

In 1995 [51], a process was established to integrate vehicle structure, instrument panel, steering assembly, driver air bag and Hybrid III dummy models in a single FE model. This process centered on integrating existing components and subsystem models and clearly demonstrated that explicit FE technology can simulate both structural and restrained occupant response resulting from a vehicle crash in a single integrated model, although the results are preliminary.

3.8 References

1. Rapin, M.P., (1970) Vehicle Structural Crashworthiness in Proceedings of 1970 International Automobile Safety Conference Compendium, Detroit, Michigan, pp. 927-940.

2. Kamal, M.M. (1970) Analysis and Simulation of vehicle to Barrier Impact, *Society of Automotive Engineers*, SAE Paper No. 700414.

3. Wang, H.C. and Merdith, D., (1983) The Crush Analysis of Vehicle Structures, International Journal of Impact Engineering, Vol. 1, No. 3, pp. 199-225.

4. Chang, D.C. (1977) A Design-Analysis Method for the Front Crush Strength of Body Structures, SAE Paper No. 770593.

5. McIvor, I.K. (1973) Modeling and Simulation as Applied to Vehicle Structures and Exteriors, Proceedings of Vehicle Safety Research Integration Symposium, DOT HS-820-306.

6. Mahmood H.F. and Paluzeny A. (1986) Analytical Technique for Simulating Crash Response of Vehicle Structures Composed of Beam Elements, *6th International Conference on Vehicle Structural Mechanics*, SAE Publisher.

7. Gamon, M.A., (1978) General Aviation Airplane Structural Crashworthiness User's Manual, Vol.1, Program KRASH Theory, FAA Report No. FAA-RD 77-18.

8. Pifko, A.B. and Winter, R. (1981) Theory and Applications of Finite Element Analysis to Structural Crash, in *Structural and Nonlinear Solid Mechanics*, A.K. Noor and H.G. McComb (eds.), Pergamon Press, Oxford.

9. Argyris, J., Balmer, H.A., ST. Doltsinis, J. and Kruz, A. (1986) Computer Simulation of Crash Phenomena, Int. J. for Numerical Methods in Engineering, 22, pp. 497-519.

10. Ni, C.M. (1981) A General Purpose Technique for Nonlinear Dynamic Response of Integrated Structures, 4th International Conference on Vehicle Structural Mechanics, SAE Publisher.

11. Haug, E., Arnadeau, F., Dubois, J. and De Rouvray A. (1983) Static and Dynamic Finite Element Analysis of Structural Crashworthiness in the Automotive and Aerospace Industries, in *Structural Crashworthiness*, N. Jones and T. Wierzbicki (eds.), Butterworths Publisher, pp. 175-218.

12. Belytschko, T.B. and Hsieh, B.J. (1974) Nonlinear Transient Analysis of Shells and Solids of Revolutio by Convected Elements, *AIAA Journal*, 12, pp. 1031-1039.

13. Winter, R., Mantus, M. and Pifko A.B. (1981) Finite Element Crash Analysis of a Rear Engine Automobile, 4th International Conference on Vehicle Structural Mechanics, SAE Publisher, pp. 55- 61.

14. Haug, E., Scharnhorst, DuBois, P. (1986) FEM-Crash: Berechnung eines Fahrzeugfrontalaufpralls VDI-Tagung, Wuerzburg.

15. Bretz, Jarzab, Raasch, (1986) Berechnung eines Frontalen Crashvorganges bei einer heckangetriebenen Limousine, VDI-Tagung, Wuerzburg.

16. Hieronimus, Nalepa, (1986) Introduction and Use of a Supercomputer at Opel, e.g. for Crash Simulation, International Conference on Supercomputer Applications in the Automotive Industry, Zurich.

17. Gonard, Germain-Lacour, Azais, (1986) International Conference on Supercomputer Applications in the Automotive Industry, Zurich.

18. Isuzu Motors Limited, (1987) Crash Analysis of 760 Coupe, Body Engineering Department, Personal Communication.

19. Benson, D.J. and Hallquist, J.O. (1986) The Application of DYNA3D in Large Scale Crashworthiness Calculations, Lawrence Livermore National Laboratory, *Report No. UCRL*-94028.

20. Nilsson, L. (1989) Computational Crash Analysis at the Saab Car Division, *12th International Technical Conference on Experimental Safety Vehicles*, Goteborg, Sweden.

21. Haug, E., Scharnhorst, T. and Du Bois, P. (1986) FEM-Crash Simulation of a Frontal Impact (VW-POLO), Translated From German, VDI Report 613, pp. 479-505.

22. Bertz, G., Jarzab, W. and Raasch, I. (1986) Computation of a Frontal Impact of a Rear Wheel Drive Car, Translated From German, *VDI Report* 613, pp. 507-525.

23. Scharnhorst, T. I., Rassch, I. and E. Schelke, E. (1986) Conclusiveness of Math Methods for Crash Behavior Simulation of Cars, Translated from German, *VDI Report,* 613.

24. Chedmail, J.F., et al, (1986) Numerical Techniques, Experimental Validation and Industrial Applications of Structural Impact and Crashworthiness Analysis with Supercomputers for the Automotive Industry, International Conference on Supercomputing, Zurich, Switzerland.

25. Nalepa, E. (1989) Crashworthiness Simulation of the Opel Vectra Using the Explicit FE Method, International. Journal of Vehicle Design, IAVD Congress on Vehicle Design and Components, pp. 191-201.

26. Khalil, T.B. and Lin, T.C. (1994) Simulation of the Hybrid III Dummy Response to Impact by Nonlinear Finite Element Analysis, in Proceedings of 38th. Stapp Car Crash Conference, SAE Publisher, pp. 325-345.

27. Zouk, A.K., Marzougui, D. and Bedewi, N. E. (1998) Development of a detailed Vehicle Finite Element Model Part I: Methodolgy, International Crashworthiness Conference, Dearborn, Michigan, Woodhead Publishing Limited, pp. 184-195.

28. Cofie, E. (1994) Finite Element Model of a small Automobile Impacting a Rigid Pole, Office of Safety and Traffic Operations Research and Development, Federal Highway Administration, Final Report, Contract No. NHI GFR Project # 93-31.

29. Newmark, N.M. (1959) A Method of Computation for Structural Dynamics, *J.* Engineering Mechanics Division, ASCE, 67, 67-94.

30. Farhoomand, I. (1972) Nonlinear Dynamic Stress Analysis of Two-dimensional Solids, *Ph.D. Thesis*, University of California, Berkeley, Graduate Division.

31. Hughes, T.J.R., Pister, K.S., and Taylor, R.L. (1979) Implicit-Explicit Finite Elements in Nonlinear Transient Analysis, Computer Methods in Applied Mechanics and Engineering, 17/18, 159.

32. Belytschko, T.B, and Tsay, C.S. (1981) Explicit Algorithms for Nonlinear Dynamics of Shells, AMD, Vol.48, ASME, pp. 209-231.

33. Belytschko, T.B., Lin, J.I., and Tsay, C.S., (1984) Explicit Algorithm for the Nonlinear Dynamics of Shells, Comp. Methods. in Applied Mechanics and Engineering, Vol. 43, pp. 251-276.

34. Belytschko, T.B. Stolarski, H., and Carpenter, N., (1984) A Triangular Plate Element with One-Point Quadrature, International J. of Numerical Methods in Engineering, Vol. 20, pp. 787-802.

35. Flanagan, D.P., and Belytschko, T., (1981) A Uniform Strain Hexahedron and Quadrilateral and Orthogonal Hourglass Control, International Journal of Numerical Methods in Engineering, Vol. 17, pp. 679-706.

36. Belytschko, T.B., and Tsay, C.S. (1983) A Stabilization Procedure for the Quadrilateral Plate Element with One-Point Quadrature, International Journal of Numerical Methods in Engineering, Vol. 19, pp. 405-419.

37. Hughes, T.J.R. and Liu, Y.K., (1981) Nonlinear Finite Element Analysis of Shells: Part II Two Dimensional Shells, Computer Methods in Applied Mechanics, Vol. 27, pp. 331-362.

38. Hughes, T.J.R. and Liu, Y.K., (1981) Nonlinear Finite Element Analysis of Shells: Part I Three Dimensional Shells, Computer Methods in Applied Mechanics, Vol. 27, pp. 167-181.

39. Belytschko, T.B., Wong, B.L., and Chiang, H.Y., (1992) Advances in one-point Quaderature Shell Elements, Computer Methods in Applied Mechanics and Engineering.

40. Sheh, M.Y. and Khalil, T.B. (1991) The Impact Response of a Vehicle Structural Rail by Experiments and Finite Element Analysis in *Symposium on Crashworthiness and Occupant Protection in Transportation Systems,* T.B. Khalil, H.F. Mahmood, C.M. Ni and A.I. King (eds.), ASME Publication, AMD-Vol. 126/BED-Vol. 19, pp. 195-207.

41. Khalil, T.B. and Vander Lugt, D.A. (1989) Identification of Vehicle Front Structure Crashworthiness by Experiments and Finite Element in Symposium on Crashworthiness and Occupant Protection in Transportation Systems, T.B. Khalil, and A.I. King, (eds.), ASME Publisher, AMD-Vol. 106 and BED-Vol. 13, pp. 41-53.

42. Bertz, G., Jarzab W. and Raasch I. (1986) Computation of a Frontal Impact of a Rear Wheel Drive Car, Translated From German, VDI Report ,613, pp. 507-525.

43. Scharnhorst, T. I. Rassch, I. and Schelke, E. (1986) Conclusivness of Math Methods for Crash Behavior Simulation of Cars, Translated from German, VDI Report, 613.

44. Vander Lugt, D.A. et. al. (1987) Passenger Car Frontal Barrier Simulation Using Nonlinear Finite Element Method, SAE Passenger Car Meeting and Exposition, Dearborn, Michigan, Paper No. 871958.

45. Kurimoto, K. et.al. (1989) Simulation of Crashworthiness and its Application, 12th. International Technical Conference on Experimental Safety Vehicles, Goteborg, Sweden.

46. Futamata, T. et. al. 1989) Crash Simulation Methods for Vehicle Development at Nissan, 12th International Technical Conference on Experimental Safety Vehicles, Goteborg, Sweden.

47. Johnson, J.P. and Skynar, M.J. (1989) Automotive Crash Analysis Using the Explicit Integration Finite Element Method, in *Proceedings of Crashworthiness and Occupant Protection in Transportation Systems*, T.B. Khalil, and A.I. King, (eds.), ASME Publisher, AMD-Vol. 106 and BED-Vol. 13, pp. 27-33.

48. Sheh, M.Y. et. al. (1992) Vehicle Crashworthiness Analysis Using Numerical Methods and Experiments, 8th International Conference on Vehicle Structural Mechanics and CAE, Traverse City, Michigan, SAE Publisher, pp. 119-128.

49. Kohlhoff, St et.al. (1994) A Computational Approach to an Investigation of Frontal Car-To-Car Collision for the Development of Barrier Test, Numerical Analysis in Automobile Engineering, VDI Conference Wurzburg, Germany, pp. 467-484.

50. Cheng, J.C. and Doong, J. (1994) Numerical Analysis of Vehicle Crashworthiness in Various Configurations*, Cray Channels,* Vol. 16, No. 2, pp. 8-11

51. Khalil, T.B. and Sheh, M.Y. (1997) Vehicle Crashworthiness and Occupant Protection in Frontal Impact by FE Analysis – An Integrated Approach, in *Proceedings of Crashworthiness of Transportation Systems: Impact and Occupant Protection, Kluwer Academic Publisher, pp. 363-399.*

52. Steyer, C., Diet, S. and Du Bois, P. (1989) Numerical Simulation of the Proposed Side Impact Procedure, in *Proceedings of Crashworthiness and Occupant Protection in Transportation Systems*, AMD-Vol. 106 and BED-Vol. 13, T.B. Khalil, and A.I. King, (eds.), ASME Publisher, pp 53-95.

53. Kaiser, A. (1992) Some Examples on Numerical Simulation in Vehicle Safety Development, 8th International Conference on Vehicle Structural Mechanics and CAE, Traverse City, Michigan, SAE Publisher, pp. 119-128.

54. Calso, S.M. et. al. (1993) Simulation of Offset and In-line car to Car Rear Impact", in *Proceedings of Crashworthiness and Occupant Protection in Transportation Systems*, AMD-Vol. 169 and BED-Vol. 25, J. Reid, and K. Yang (eds.), ASME Publication, pp. 149-161.

55. *PAM-CVS User's Manual*, Version 1.0 (1990), Engineering Systems International, Paris, France.

56. Khalil, T.B. and Lin, K.H. (1991) Hybrid III Thoracic Impact on Self-Aligning Steering Wheel by Finite Element Analysis and Mini-Sled Experiments, in *Proceedings of 35th Stapp Car Crash Conference,* SAE Publisher, pp. 73-85.

57. Ove Arup & Partners International, (1992) An Integrated Approach To Vehicle Crashworthiness and Occupant Protection, Report, Issue 1, London, England.

58. Schelkle, E. and Remensperger, R. (1991) Integrated Occupant-Car Crash Simulation with the Finite Element Method: The Porsche Hybrid III-Dummy and Airbag Model, in Frontal Crash Safety Technologies for the 90's, SAE paper No. 910654.

Fundamental Principles for Vehicle/Occupant Systems Analysis

Clifford C. Chou

4.1 Introduction

Restraint systems are safety devices that are designed to assist in restraining the occupant in the seating position, and help reduce the risk of occupant contact with the vehicle interior, thus helping reduce the risk of injury in a vehicular crash event. This chapter describes fundamental dynamics principles for occupant restraint systems analysis. These principles are essential and are the established basis on which restraint systems are designed and analyzed for the problems involved in automotive safety.

At its simplest, automotive safety is a matter of reducing the relative velocity between the occupants and the vehicle interior to help reduce the risk of injury to the occupant during a collision. Newton's Laws indicate that a change in an occupant's velocity requires a force to be applied to the occupant. To reduce the risk of injury to the occupant, safety engineers analyze the maximum force that can be applied to the driver or passenger without injury. Consequently, it is necessary to quantify the injury parameters in a manner that permits them to be used as performance numbers in safer designs. Since automobile manufacturers must design their products to comply with certain Federal Motor Vehicle Safety Standards (FMVSS) for occupant protection, the injury criteria specified in these standards must be met. Standards pertaining to occupant protection are FMVSS 208 for frontal impact protection and FMVSS 214 for side impact protection, which will be described later.

All new cars to be sold in the United States are also required to meet a range of federal safety standards that meet the need for motor vehicle safety features such as windshields that resist penetration and steering wheel assemblies designed to absorb crash energy and help cushion the occupants upon impact. The most familiar safety restraint features required by federal standard are safety belts and supplemental air bag restraint systems. Other non-regulated restraint systems

include energy- absorbing E-A (or collapsible) steering column and E-A knee bolsters.

There is abundant literature dealing with the effectiveness of restraint systems such as belts and supplemental airbags in providing occupant protection in automobile crashes. Statistics indicate that mandatory seat belt usage and airbags have significantly reduced occupant fatality and injury (see Chapter 7 - Anthropomorphic Test Devices). In addition, each vehicle design must comply with FMVSS 208 and 214 for frontal and side impact occupant protection, respectively. The requirements of the FMVSS 208 standard include a 30 mph (48 k/hr) impact to a non-movable rigid barrier. New FMVSS 208 requires also the offset impact and the rigid barrier impact at different velocities. This chapter addresses only the rigid barrier impact tests in which the potential injury to the occupant is assessed by using Hybrid III anthropomorphic dummies (refer to Chapter 7 – Anthropomorphic Test Devices for details). Hybrid III, the most advanced test dummy for frontal impact, possesses human-like impact response in critical body regions such as the head, neck and thorax. Injury severity indices measured from Hybrid III in barrier tests include the Head Injury Criterion (HIC), chest G, chest deflection, femur load and neck loads and moments. The requirements of FMVSS 214 are assessed using a moving deformable barrier (MDB) impacting the driver side of a target vehicle. Potential injury includes peak pelvic acceleration and TTI (Thoracic Trauma Index). If any of these injury severity indices exceeds the dummy performance number limits specified by the standards, the vehicle design must be modified until the requirements are met. However, relying exclusively on crash tests for design improvement is very inefficient. Furthermore, in the early stage of design, not all hardware has been fabricated, yet competing design concepts must be evaluated.

With rapid advancement in digital computer technology and CAE methodology, simulation has become an essential and useful tool in the design stage. Mathematical models can provide quick assessment of various design concepts and explore new design directions. A review of mathematical models widely used by the automotive industry for occupant simulations is given by Prasad and Chou [1]. Detailed occupant modeling technology for restraint systems is also presented in Chapter 5 – Design Tools: Human Body Modeling.

To design an effective restraint system that stops the occupant within the vehicle compartment without injuring the occupant, it is essential to know the required stopping distance. An example: consider the stopping distance required by the chest if the tolerance level of 60 g's is not to be exceeded. Note that a "g" is usually used in the automotive safety field to indicate a force being applied to an occupant, as will be described later. First, the optimum or minimum stopping

distance would be achieved with a square wave (uniform) deceleration pulse, a.k.a. Equivalent Square Wave (ESW). This would require a 6-in stopping distance from 30 mph, or a 24-in stopping distance from 60 mph. These values are optimum and will never be reached in practice. A more reasonable stopping pulse shape is a half-sine deceleration pulse, which requires 9.7 in from 30 mph and 37.7 in from 60 mph without exceeding 60 g's. Thus, it is obvious that larger distances are required to stop from high velocities at sub-injury levels. Studies of stopping distance under various ideal pulses are given by Patrick [2], and Chou and Nyquest [3].

Now considering the vehicle, available distances can be determined. In a 30-mph barrier collision, a typical full-size car can have up to 28 in of front-end crush. The National Highway Transportation Safety Administration (NHTSA) has conducted numerous New Car Assessment Programs (NCAP) on cars produced by automobile manufacturers, and maintains a crash database with a range of dynamic crush information and occupant response data. In addition, there is about 15 in between the occupant and the interior, and during impact perhaps as much as 6 in deformation of the interior compartment, for a total of about 49 in. Referring back to the 60 g's half-sine wave example, it appears that occupants should be able to survive a 60 mph collision, which requires a stopping distance of 37.7 in with the assumed half-sine pulse shape. In a barrier collision such as a car striking a bridge abutment or some other immovable object (which is extremely rare in the real world), the vehicle stops before an unrestrained occupant hits the interior. In this case, the front-end crush and the interior space are of no value. The occupant continues forward at the original vehicle velocity until striking the stopped interior with only the assumed 6 in of stopping distance available.

It is obvious that to survive high-speed collisions, it is essential to use the front-end crush and available distance between the occupant and the interior. This is accomplished when a restraint is used. The air bag, energy absorbing steering column and safety belts are all restraint systems that slow the occupant shortly after the vehicle starts to decelerate. The front-end crush and interior distance are both useful to some extent. Part of the distance is lost in a harness by slack and belt stretch. The distance between the driver and the steering wheel is lost in the case of the energy-absorbing column restraint, and the distance of the front-end crush and occupant space traversed during the sensing and deployment time for the air bag are lost. However, the remaining useful distance does increase the survival velocity appreciably. Occupant kinematics under a given restraint system will be described later using simple models. Details of a barrier crash will now be considered to show the temporal requirements of the restraint systems. Dynamic side impact test procedure used in FMVSS 214 and side impact analysis is given in Section 4.4 – Application of Concepts to Vehicle/Occupant Analysis.

4.2 Barrier Collision

Analysis of a vehicle in a frontal crash event, in general, consists of studies of the vehicle response and the occupant response. Basically, there are two stages in a vehicle frontal impact with a fixed barrier: the primary and the secondary impacts. The primary impact is the collision between the vehicle front-end structure and the fixed barrier. During this impact mode, the major portion of the crash energy is absorbed by way of structural deformation that produces a crash pulse transmitted to the occupant compartment. The compartment intrusion is largely affected by the extent of the vehicle front-end deformation which is, in turn, influenced by vehicle design parameters such as the strength of the structural members, the available package space, the stack-up of non-crushable powertrain components, the vehicle mass, and the test speed. The secondary impact is between the occupant and the restraint system and/or the vehicle interior. The occupant responses are measured by parameters such as the HIC, chest g's, chest deflection, and femur loads. These are affected by the vehicle crash pulse, the extent of the intrusion and the intrusion rate into the occupant compartment, the restraint system, the vehicle interior profile/stiffness, and the dummy construction/instrumentation.

Traditional design methodology requires full vehicle crash testing to determine responses of an occupant, restrained or unrestrained, when contacting vehicle interiors with or without compartment intrusion. Integrated structural and occupant simulation modeling offers several potential advantages over the traditional full-vehicle crash testing. These include early design guidance, shorter vehicle design and development time, optimization of structural and package efficiency, evaluation of design alternatives and reduced prototype test requirements.

Since the frontal rigid barrier collision is considered to be the most severe and perhaps the most easily reproduced, it was used as the basis for comparing performance of safety systems in the past. FMVSS 208 adopts this test mode as a standard to evaluate the vehicle crashworthiness for occupant protection. This standard specifies performance requirements for the protection of vehicle occupants in crashes. The purpose of establishment of the standard is to reduce the number of deaths of vehicle occupants and the severity of injuries on the roads. This is accomplished by specifying vehicle crashworthiness requirements in terms of force and deceleration measurements on a 50^{th}-percentile Hybrid III dummy as a human surrogate in crash tests, and by specifying active and passive restraint requirements. Descriptions of the development and biofedelity of various

anthropomorphic test dummies are given in Chapter 7 – Anthropomorphic Test Devices.

To meet the requirements of FMVSS 208, vehicles impacting a fixed barrier either perpendicular or at a 30 degree angle at a speed of 30 mph must provide protection for the front-seated Hydrid III dummy occupants as follows:

a) Head Injury Criterion (HIC) - The resultant acceleration at the center of gravity of the dummy head must be such that the expression:

$$HIC = \left[\frac{1}{t_2 - t_1} \int_{t_1}^{t_2} a dt \right]^{2.5} \left(t_2 - t_1 \right) \qquad (4.2.1)$$

does not exceed 700 where *a* is the resultant acceleration expressed as a multiple of g, and t_1 and t_2 are any two points in time during the crash of the vehicle which are within a 15 ms time interval.

b) Chest Injury (CLIP) - The resultant acceleration at the center of gravity of the dummy chest shall not exceed 60 g's, except for the intervals whose cumulative duration is not more than 3 ms.

c) Femur Loads - The compressive force transmitted axially through each dummy upper leg shall not exceed 2,250 lbs.

d) Chest Deflection - The chest deflection shall not exceed 76.2 mm.

Barrier test vehicles are instrumented to provide vehicle acceleration/deceleration data that are representative of an acceleration experienced in the passenger compartment. Generally, two triaxial accelerometers are mounted to the rocker panels at the base of the B-pillar for such measurements. In the analysis of frontal barrier or rear impacts, it is customary to use the vehicle longitudinal component of acceleration from underneath the B-pillar, located in an undeformed area of the vehicle occupant compartment. In general, the deceleration-time history is a superposition of a spectrum of frequencies representing the instrumentation noises, elastic-plastic vibrations, structural collapse, and engine/accessories interactions as they impact one another. An unfiltered or raw deceleration-time history provides little information of value. In order to utilize crash data, techniques for characterizing the deceleration pulse with various degrees of approximations have been developed. Several techniques have been developed to characterize the vehicle compartment deceleration pulse, along with the

associated vehicle structural configuration for identifying significant structural behavior of the vehicle in a frontal barrier crash. Huang et al [4] and Chou and Lim [5] have presented and summarized these techniques. Equivalent Square Wave (ESW), mentioned in the Introduction section, is a specific type of this characterization, and will be discussed later.

The barrier collision is the most severe type of collision. A 30 mph barrier collision, for example, is approximately equal to a head-on collision in which two identical cars are both traveling at 30 mph. Another illustration of its severity is shown by a front-end collision in which the bullet or the striking car traveling 60 mph strikes a stationary vehicle, resulting in about the same severity of collision as the 30 mph barrier collision.

A collision sequence can best be explained by referring to the events during the collision and the record of the collision. A mid-sized car crashed into a 120,000-lb reinforced concrete barrier at 32.2 mph, shown in Figure 4.2.1. The driver was an unbelted 50th-percentile Hybrid III dummy protected by the steering assembly airbag. The right front passenger was an identical dummy restrained by a three-point restraint system design.

In addition to vehicle instrumentation, both the driver and right front passenger 50^{th}-percentile Hybrid III dummies are instrumented with triaxial accelerometers at the centers of gravities of the head and chest, and load cells at the femur. The recorded data are processed according to SAE J211 specification as shown in Table 4.2.1. The filtered data are then analyzed for calculating injury performance numbers mentioned above, and used further for assessing dummy performance in compliance with FMVSS 208.

4.3 Basic Laws and Concepts of Motion

Basic laws and concepts of motion are covered in Mechanics, which is the physical science concerned with the motion and deformation of bodies under the action of forces. It is the basic science underlying much of engineering analysis and will be applied to understanding of the vehicle and occupant under the influence of forces and the operation of occupant restraint systems in automobiles.

The four fundamental elements of mechanics are force (F), mass (M), length (L) and time (T). However, only three independent dimensions are needed, namely, *MLT* or *FLT*, but the concept of force is not truly defined by saying that its dimension is ML/T^2. Some of the characteristics of forces and mass are discussed below.

Fig. 4.2.1 **Mid sized vehicle crash against a full rigid barrier**

Force is a push or a pull exerted on a body. In Newton's formulation, it was the "action of one body to another body." It may be exerted by actual contact or at a distance as in case of gravitational forces and magnetic forces. It is often convenient, however, to think of the force as being exerted by a force field on a body, without inquiring too closely into what bodies are responsible for the presence of the field. This is especially useful for the force on a charged particle in an electrical or magnetic field whose form may be known either from a theoretical

Table 4.2.1 **Data filtering requirements**

	Data Type	Filter Class
Head	acceleration	SAE 1000
Chest	acceleration	SAE 180
	deflection	SAE 180
Femur	load	SAE 60

calculation or by an experimental mapping of the field. Force is a vector quantity and possesses the following characteristics:

- magnitude
- direction
- point of application (or line of action in rigid-body mechanics)

The magnitude of a force measures how large or intense it is, and is often represented graphically by the length of an arrow (as in a vector sense) along the line of action. The direction of a force is defined by the line of action and the sense of the force as indicated by an arrow.

In rigid-body mechanics, the point of application does not matter, since the force will have the same effect no matter where it is applied on its line of action. This is sometimes called the principle of transmissibility. The effects of a force acting on a body are of two kinds:

- external effects (rigid body)
  - acceleration of the body if it is unconstrained (change of motion)
  - bringing into action other forces (support reaction) if it is constrained
- internal effects (deformable body)
  - deformation (changing in shape and size)

The distinction is artificial but useful. A rigid body is an idealization, but if the deformations of a body are small enough, the external and internal effects may frequently be analyzed separately. This Chapter will not discuss internal effects, which are a principal concern of strength of materials. The two kinds of effects furnish two methods by which force magnitudes may be measured: stretching a calibrated spring balance, and observing the acceleration imparted to a standard mass.

Mass is a scalar quantity of matter in a body, measuring the inertia of a body with respect to its tendency to resist being accelerated when acted upon by a given unbalanced force. But if the force in question is gravitational force, the magnitude of the force is also proportional to the mass of the body on which it acts. Mass and weight are not the same thing. Weight is the gravitational force acting. It varies inversely as the square of the distance from the center of the earth (as does the free-fall acceleration g), while the mass of a body is the same in all positions in Newtonian mechanics. In addition, mass is also the measure of the quantity of energy contained in a body.

Energy is another concept that governs motion, and will be discussed in Section 4.3.6 – Energy and Work.

4.3.1 Basic Principles of Postulates

Six postulates are usually stated as the basis of this science of Newtonian mechanics of particles and rigid bodies: Newton's Three Laws of Motion, The Parallelogram Law for Adding Forces, The Principle of Transmissibility, and Newton's Law of Gravitation. Only Newton's Second Law and the Parallelogram Law are needed to predict the motion of a particle (or a body) under given forces. Newton's Law of Gravitation and Newton's Third Law deal with interactions between two particles. The other two postulates, Newton's First Law of Motion and the Principle of Transmissibility, are sometimes omitted. Newton's First Law is redundant, since it is merely a special case of the Second Law. The Principle of Transmissibility begins to matter only when dealing with a rigid body of finite extent instead of with idealized mass point particles. It can be derived from the other postulates, if Newton's Third Law is assumed to apply to the interaction forces in the system of particles forming the rigid body.

4.3.2 Particle Under Given Forces

The Parallelogram Law postulates that if two forces act at a point, their combined effect is the same as that of a single force acting at the same point and equal to the vector sum of the two forces.

Newton's Second Law postulates that the time rate of change of the momentum of a body (a particle or a system of particles) is proportional to the vector sum of all the forces acting on the body:

$$\sum \vec{F} = k \frac{d}{dt}(m\vec{v}) \qquad (4.3.2.1)$$

where m is the mass of the body and mv is the momentum. If units are chosen so that $k = 1$, and m is considered constant, this leads to a more familiar form:

$$F = ma = mdv/dt \qquad (4.3.2.2)$$

where $a = dv/dt$ is the acceleration, and F now denotes the total force (or net force) on the body. Eq. 4.3.2.2 therefore defines the relationship between the force applied to a body and acceleration or the rate of change in velocity the body will experience. From Eq. 4.3.2.2, one can rewrite

$$a = F/m. \qquad (4.3.2.3)$$

This means that the acceleration of a body is directly proportional to the net force acting on the body and inversely proportional to the mass of the body, and is always in the direction of the net force.

The Second Law has meaning only if some reference system is given relative to which the velocity and acceleration are measured. It holds in an inertial reference system and for all engineering problems to date, the so-called fixed stars may be considered an inertial system. Indeed, for most ordinary engineering work, the earth may be considered an inertial reference, and this chapter often refers to "fixed axes," meaning fixed to the earth.

4.3.3 Interactions

Newton's Third Law postulates that if one body exerts a force on a second body, then the second body exerts on the first body a force equal in magnitude, opposite in direction and collinear with the first force. This is the meaning concealed by the words, "action equals reaction." Newton's Third Law deals with interaction forces between two bodies, which may contact or push each other. Note that both bodies may be in accelerated motion. It should be further noted that the Third Law has nothing at all to do with equilibrium, which is described for one body only.

If the two interacting bodies were subject to no other external forces, then the Second Law and Third Law together would imply that the rate of change of momentum of one body is equal and opposite to the rate of change of momentum of other one, so that the total momentum of the system (vector sum) would be constant. Thus, the interaction forces are such as to conserve the momentum of the system of the two bodies. The conservation of momentum might be taken as the basic postulate and the Third Law derived from it, a procedure particularly attractive for some electromagnetic interactions, where the Third Law fails to hold but where conservation of momentum is still satisfied, if the momentum carried by the electromagnetic field is included in the total momentum.

Newton's Law of Gravitation postulates that any two particles are attracted toward each other by a force whose magnitude is inversely proportional to the square of

the distance between them, $F=Km_1m_2/r^2$. By the Third Law, body one experiences a force equal and opposite to the force experienced by body two.

4.3.4 Two Additional Postulates

Newton's First Law postulates that a body under the action of no forces would continue to travel in a straight line with constant velocity. This is merely a special case of the Second Law.

The Principle of Transmissibility postulates that the external effects of a force acting on a rigid body are independent of the point of application of the force on its line of action. Force is thus a "sliding vector," which may be considered to act anywhere along a certain line of action. This evidently does not apply to the internal effects, since a different deformation of a body is produced by pulling forward on the front of it than by pushing forward on the back of it. Many deductive treatments of the science of mechanics derive this principle as a conclusion from the other postulates by considering the rigid body as a collection of particles.

4.3.5 Idealizations

In Newtonian mechanics, some idealizations are made in the analyses. The object in motion is considered a "particle," which is assumed to be a rigid body under the action of concentrated forces.

4.3.6 Energy and Work

Two additional concepts that govern motion apply to vehicle and occupant kinematics as well as occupant restraint systems. These are: Energy, which is the property (or capacity) of a body or a system that enables it to do work and overcome resistance, and Work, which is the transference of energy from one body to the other. Energy is an abstract concept, which cannot be seen, felt, tasted or smelled. The only time energy becomes evident is when it changes. Energy appears in many forms including thermal (heat), solar (light), electrical (electricity), and mechanical energies. The most commonly known energies are kinetic energy (*K.E.*) and potential energy (*P.E.*). In mechanical systems, a force does work on a body provided that the point where the force is applied has a component of displacement in the direction of force. The work done, or energy transferred to or from the body, is then equal to the magnitude of the force times the distance over which it acts. The kinetic energy, which is the energy of motion

of a body, is equal to half its mass multiplied by its velocity squared as expressed by the following relationship:

$$K.E. = (m.v^2)/2 \quad (4.3.6.1)$$

where m is the mass of the body and v is the velocity. Potential energy is a stored energy within a body or a system because of its position with respect to other bodies. When energy is in the stored state, a body or a system has the potential for doing work.

4.3.7 Conservation of Energy

The Law of Conservation of Energy states that energy within a body or a system cannot be created or destroyed, and it may be transferred from one form into another, but the total amount of energy never changes. When considering mechanical systems, such as the occupant restraint systems in this chapter, the work output of a system cannot exceed the work input. Energy transmitted to a system is equal to the work done by forces externally to the system, which is equal to the product of the force (F) exerted and the distance (d) through which the force moves:

$$Work = Fd. \quad (4.3.7.1)$$

Ideally, all of the work input should be transformed to work output. In practice, this does not happen, although one can simplify the assumption. Inefficiency exists whenever energy is transformed from one form to another. Efficiency is defined as the percent of the work put into a system that is converted into useful work output, and can be expressed by the ratio:

$$\text{Efficiency} = \text{work done} / \text{energy used} \quad (4.3.7.2)$$

4.4 Application of Concepts to Vehicle/Occupant Analysis

4.4.1 Background

Elemental dynamics shows that the force required to change a velocity is proportional to acceleration. In order to simplify the explanation of automotive safety, complicating factors such as relative motion that produces injury when the head rotates or extends rearward, causing the so-called whiplash injury, will not be considered. Emphasis will be placed on the fundamentals of elementary

dynamics with the understanding that there are other complicating factors and specifications that must be considered in the final design. The parameter that causes injury is force, which can be measured with a force transducer (or load cell) or inferred from the acceleration of the body. Further simplification is made by assuming that rigid body dynamics apply, understanding that the human body is not a rigid body. Human tolerance (or injury criteria) to impact is usually given in terms of g's. A "g" as generally used by biomechanics engineers and automotive researchers is the acceleration of gravity. The fundamental expression derived from Newton's Second Law as given in Eq. 4.3.2.2 is used in automotive safety analysis:

$$F = ma. \tag{4.4.1.1}$$

This equation can be rewritten as:

$$F = W/g\ (ng) \tag{4.4.1.2}$$

where n denotes the acceleration in multiples of acceleration of gravity. Canceling the g in the denominator with the g in the numerator, the above expression results in the form:

$$F = Wn \tag{4.4.1.3}$$

Therefore, the force acting on a body is equal to the multiples of acceleration multiplied by the weight of that body. For example, if the human head can stand about 80 g's for several milliseconds without injury, then multiplying the 80 g's by the weight of the head (15 lbs) arrives at a force of about 1200 lbs without head injury. Of course, this requires that the force be distributed over the head so there is no localized deformation or skull fracture at the point of impact. The chest can stand about 60 g's if the force is distributed.

The advantage of establishing the tolerance in g units is that the stopping distance required without exceeding the tolerance can be calculated by the basic laws and concepts of motion presented in Section 4.3 – Basic Laws and Concepts of Motion.

To apply these basic laws and concepts to the study of occupant kinematics with automotive restraint systems, it is noted that Newton's First Law implies that both the vehicle and occupant engaged in the deceleration process must be acted upon by forces. Newton's Second Law states that the velocity acquired by the vehicle and/or the occupant, either increasing (positive) or decreasing (negative), is proportional to the product of the applied force and the duration for which it is applied and inversely proportional to their respective mass. When

designing an automotive safety device for occupant protection, safety engineers would like to achieve as long a duration as possible. But some physical package limitations may preclude this. If the time available for a particular velocity change cannot be accomplished within a long duration, but in a shorter one, a very large force must be exerted to achieve the required velocity change in accordance with Newton's Second Law. If the force applied to the occupant exceeds the human tolerance level, it generates conditions that could become hazardous to passengers within the vehicle.

Discussions to this point implicitly assume that the bodies under the influence of forces are rigid bodies that are non-deformable during the course of motion. In the real world, both the vehicle and the occupant are actually deformable bodies. This capacity to deform, which is an internal effect of a force acting on bodies through changing its shape and the associated state of stresses, does not invalidate the laws of motion but does introduce an interesting aspect to the concept of strain energy.

4.4.2 Vehicle Response

A vehicle that initially travels at 30 mph can decrease its velocity to zero via different processes. This vehicle can be stopped by various means including

- coasting (gradually slow down);
- normal stop;
- panic stop;
- crashing into a barrier.

In the first three cases, gradually coasting the vehicle or applying the brakes to the vehicle generate so-called friction forces of varying magnitudes between the tires and road surface. In coasting, vehicle deceleration only approaches 1 g, while in panic stopping, the vehicle can generate higher friction forces. These friction forces at the tire/road interface will act on the vehicle due to action and reaction, and eventually bring the vehicle to stop. These tire forces, acting in the opposite direction of the motion, will bring the vehicle to a stop. Among these three cases, the work done, which is equal to the initial energy, will be identical, and equal to the initial kinetic energy. Since different magnitudes of the friction forces are generated for these three cases, their respective stopping distances vary accordingly. Generally, the smaller the friction force, the larger the stopping distance, thus, the longer the vehicle will take to stop under an identical initial condition for a given velocity.

In the case where a vehicle crashes into a rigid fixed barrier, less stopping distance is required than the aforementioned cases. The vehicle loses all of its kinetic energy in a fraction of a second through front-end structural deformations. The amount of deformation is equal to the stopping distance of the vehicle. Since the stopping distance of a vehicle in the barrier crash is normally short, a much higher force is generated at the barrier interface.

Although the vehicle stops in all these cases, several differences among them are worth noting:

a) Since the vehicle in four cases undergoes the same velocity change, the product *F.dt* from Eq. 4.3.2.2 is the same. Therefore, the vehicle experiences small forces for a longer time in the first three cases, and a larger force for a short time in a crash environment as in the fourth case.

b) As noted in the coasting, normal and panicking situations, the braking force performs work, thus removing energy from the vehicle. In the case of barrier impact, the force at the barrier that arrests the motion of the vehicle does not move; therefore, does not transfer any energy away from the vehicle. The kinetic energy is converted into a potential energy stored within the vehicle by means of front-end structural deformation. The amount of this structural deformation is called the dynamic crush of a vehicle. In other words, the total kinetic energy is absorbed by the crushing of the front-end of the vehicle since the energy must be conserved.

c) The stopping distances vary in all cases. In coasting situation, the vehicle requires a long stopping distance, while in barrier crashes, the vehicle stops at a distance of approximately 30 in. in a 30 mph barrier impact. The average force that can be determined by the *K.E.* divided by the stopping distance from Eq. 4.3.7.1 affects significantly the occupant response within the vehicle compartment.

As pointed out earlier, design of a vehicle whose performance meets the safety requirements can be tested using prototype and production vehicles. The vehicle stopping distance (or dynamic crush) in barrier tests largely depends on crash pulses. These pulses are in fact signals representing vehicle deceleration time histories measured by accelerometers mounted at the non-crash zone of the occupant compartment (i.e. rocker at the "B"-pillar or seat cross members). The dynamic crush can be determined by double integration of the vehicle crash pulse with known initial impact velocity. Figure 4.4.2.1 – Longitudinal Vehicle Deceleration at Rocker/B-Pillar shows a typical deceleration time (G_v-T) history of a mid-size vehicle during a fixed barrier impact test at 30 mph. Integration of the deceleration yields a velocity change as a function of time (V_v-T) as shown in

Figure 4.4.2.2 – Longitudinal Vehicle Velocity. Further integration of the V_v-T curve gives the vehicle displacement time (D_v-T) history shown in Figure 4.4.2.3 – Longitudinal Vehicle Displacement. The vehicle stopping distance occurred at the maximum displacement, which in this particular case shown in Figure 4.4.2.3 is 23.2 in. This is referred to as the vehicle dynamic crush or vehicle dynamic crush length, X_v. The relationship between the crash pulse and the restraint system performance in a vehicle will be addressed in regard to the occupant restraint system designs. Furthermore, the deceleration and displacement time histories with time as a common parameter can be cross-plotted to obtain a deceleration vs. displacement, shown in Figure 4.4.2.4. Assuming the frictional forces are negligible, it is noted that the area under the deceleration vs. displacement curve (or G_v vs. D_v) in Figure 4.4.2.4 is equal to the initial kinetic energy of the vehicle, that is:

$$\frac{1}{2}mv^2 = \int_0^{V_x} mG_V dx \qquad (4.4.2.1)$$

In Figure 4.4.2.4, the deceleration vs. displacement curve can be circumscribed with a "square-wave or rectangular pulse" whose height and width are the peak deceleration and the maximum dynamic crush, respectively. This can then be used to determine the efficiency of a crash pulse and demonstrate the concept of an "Equivalent Square Wave."

4.4.3 Pulse Waveform Efficiency (η)

The efficient utilization of the vehicle available package space in front-end structure, which depends on the pulse waveform efficiency, is of vital importance. It is defined as:

$$\eta = \frac{Area\ under\ the\ curve\ of\ \ Deceleration\ vs.\ Displacement}{Area\ enclosed\ by\ the\ circumscribing\ \ square\ wave\ or\ rectangular\ \ pulse} \qquad (4.4.3.1)$$

$$\eta = \frac{\frac{1}{2}mv^2}{mX_v A_p} \qquad (4.4.3.2)$$

If v is in mph, A_p in g's and X_v in inches, then:

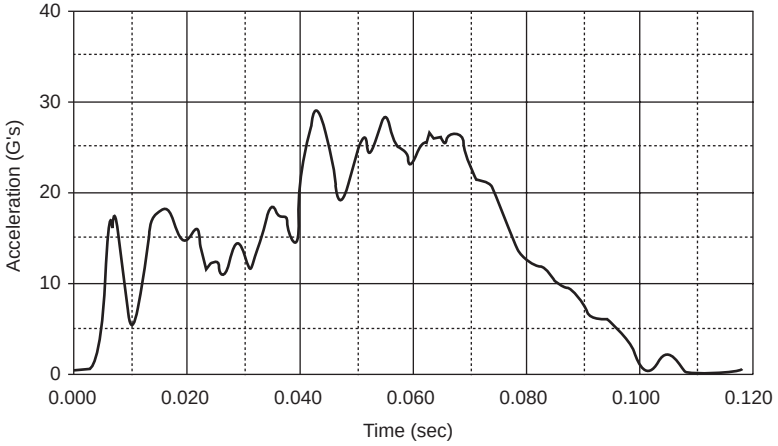

Fig. 4.4.2.1 **Longitudinal vehicle deceleration at rocker/ B-pillar**

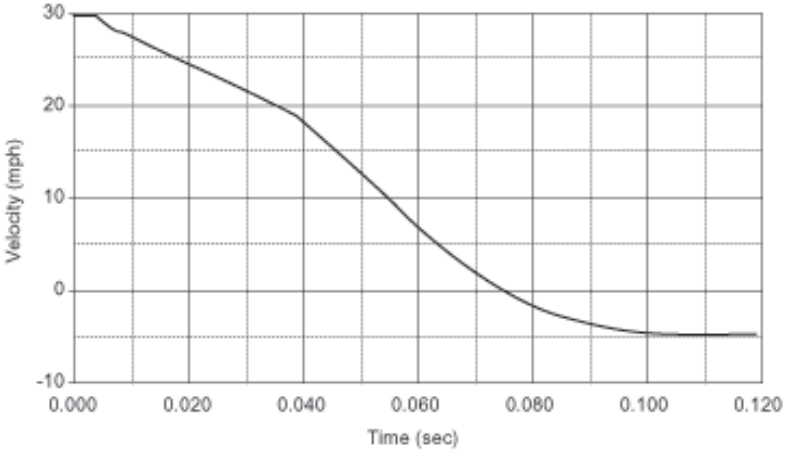

Fig. 4.4.2.2 **Longitudinal vehicle velocity (1st integration of longitudinal deceleration)**

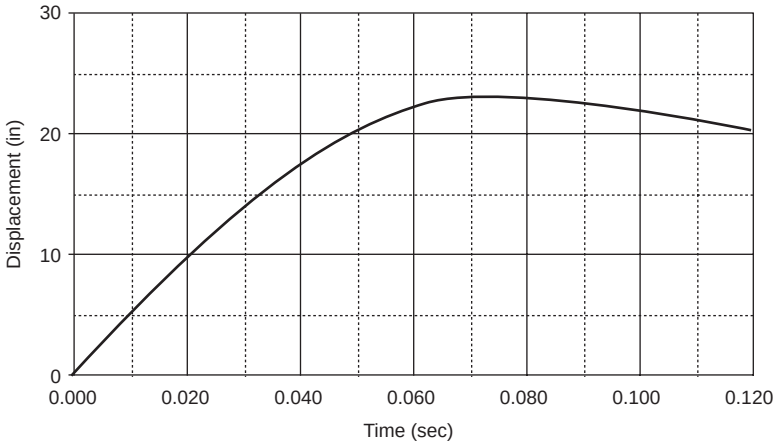

Fig. 4.4.2.3 **Longitudinal vehicle displacement (2nd integration of longitudinal deceleration)**

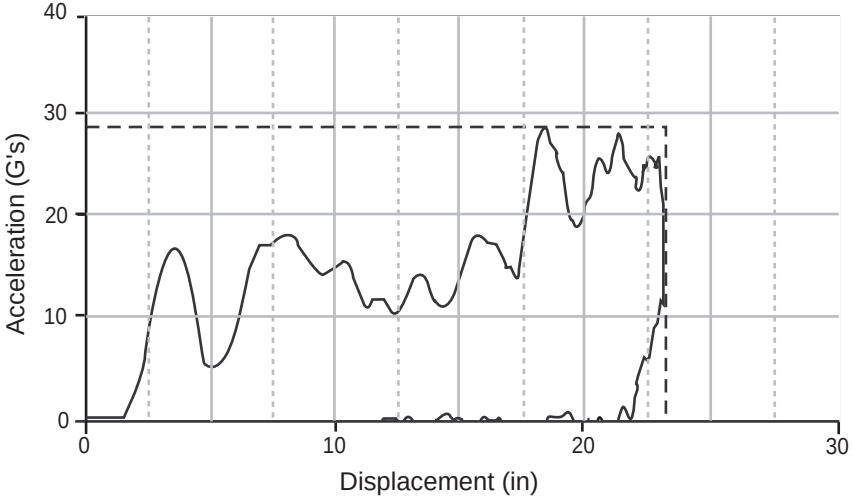

Fig. 4.4.2.4 **Vehicle deceleration versus displacement**

$$\eta = \frac{0.4008 v^2}{X_v A_p} \tag{4.4.3.3}$$

4.4.4 Equivalent Square Wave (*ESW*):

Square wave is an idealized pulse that is used in many crash-related analyses. The concept to determine its equivalent rectangular shaped pulse of constant g-level from any arbitrary shaped pulse is an Equivalent Square Wave (*ESW*). To obtain an *ESW*, an average force F_{avg} acting on the vehicle from the barrier is calculated from the following expression:

$$F_{avg} = \frac{1}{2}\left(\frac{mv^2}{X_v}\right) \tag{4.4.4.1}$$

An *ESW*, expressed in terms of g's, is calculated by dividing F_{avg} by the weight of the vehicle, which is *mg*:

$$ESW = \frac{F_{avg}}{mg} = \frac{1}{2g}\left(\frac{v^2}{X_v}\right) \tag{4.4.4.2}$$

Using mph for *v*, inches for X_v and $g = 32.2$ ft/s^2, the above equation becomes:

$$ESW = 0.4008\left(\frac{v^2}{X_v}\right) \tag{4.4.4.3}$$

Therefore, an *ESW* can be computed by knowing the initial velocity and the maximum vehicle crush, both of which are design parameters for the vehicle and restraint systems. Other hypothetical pulses such as half-sine, haversine, cosine and triangular waveforms used for basic analysis of occupant as well as vehicle kinematics are presented by Patrick [2], and Chou and Nyquest [3].

4.4.5 Effect of Pulse Shape

Consider two idealized pulse shapes, namely, a square and a triangular waveform. The waveform efficiency of a square pulse is 100 percent, while the efficiency of the triangular waveform is 50 percent. For a 3,000 lb vehicle impacted with a fixed barrier at 35 mph, assuming the same maximum crush (or deformation) of 30 in.,

the force-deformation curves are shown in Figures 4.4.5.1 – Force as Function of Dynamic Crush/Square Pulse, and 4.4.5.2 – Force as a Function of Dynamic Crush/ Triangular Pulse. It is seen that the vehicle structure in the triangular pulse case experiences a higher force, and that of the square pulse experiences a lower force. The G_V vs. D_V curves are shown in Figures 4.4.5.3 – Acceleration as a Function of Dynamic Crush/Square Pulse, and 4.4.5.4 – Acceleration as a Function of Dynamic Crush/Triangular Pulse, exhibiting that the vehicle with the triangular pulse case experiences a higher "peak" deceleration force than the square pulse. The crash pulses are generally considered as "forcing functions" acting on the vehicle to affect the occupant's movement within its compartment. Therefore, a higher force will be exerted on the occupant in case of a triangular pulse than in a square one, and, in order to stop the occupant inside the occupant compartment requires a greater demand on the restraint system, as summarized in Table 4.4.5.1.--Force required on occupant restraint system.

How a front-end crushes is as important as how much it is crushed. Ideally, the force-displacement (or deceleration/acceleration vs. time) curve should approach a square pulse, an optimal waveform. While in reality, design of a vehicle structure to behave like a square wave is not possible, an *ESW* concept is useful in establishing a basic requirement for a vehicle to meet regulatory requirements. Today's front-end structures of passenger vehicles are designed to be more crashworthy by managing crash energy through effective use of available crush space. Sled tests and occupant model simulations indicated that crash pulses over *ESW* of 20 g make it difficult to meet FMVSS 208 dummy performance criteria. Theoretically, when a square wave of 20 g is used, a crush distance of 24 in is required for a 35 mph frontal impact with a fixed barrier. However, a square wave cannot be achieved with today's technology, and a vehicle is required to provide an extra 20 to 25 percent deformation or 29 to 30 in overall for a better crash energy management. Vehicle structure design methodologies are presented in Chapter 2 – Design of Vehicle Structures for Crash Energy Management.

4.4.6 Occupant Response

The processes of force application and associated energy transfers that occur to the occupants within the vehicle are very similar to the cases discussed previously in the Section 4.4.2 – Vehicle Response. Two extreme cases, namely, a coasting and a crashing vehicle, will be used for demonstrating occupant response in this section. The principles presented here are applicable equally well to the normal and panic braking situations. During the deceleration, various types of forces, such as friction forces generated between the occupant and the seat, foot/toe-board and hands-to-steering-wheel interaction forces will act on the unrestrained

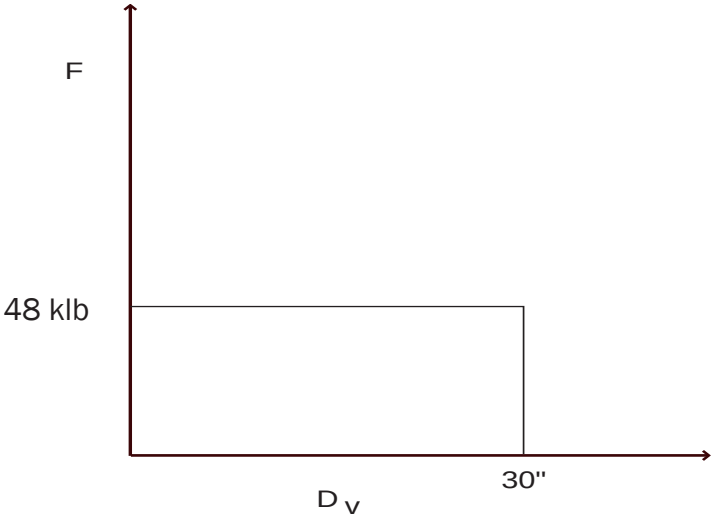

Fig. 4.4.5.1 **Force as function of dynamic crush – square pulse**

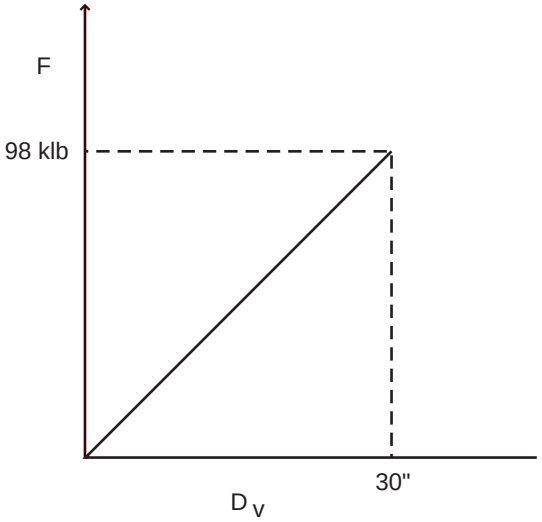

Fig. 4.4.5.2 **Force as function ofdynamic crush - triangular pulse**

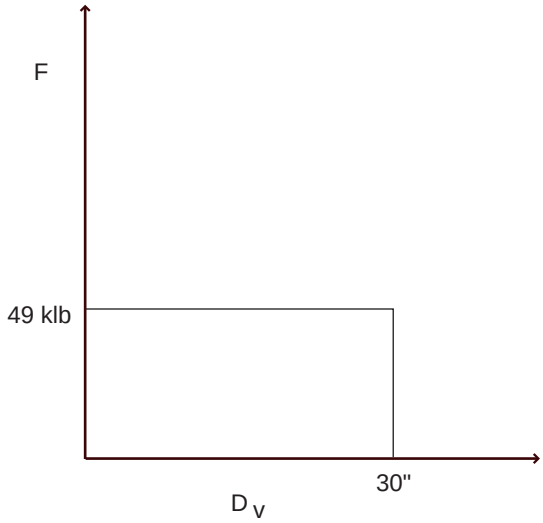

Fig. 4.4.5.3 **Acceleration as a function of dynamic crush**

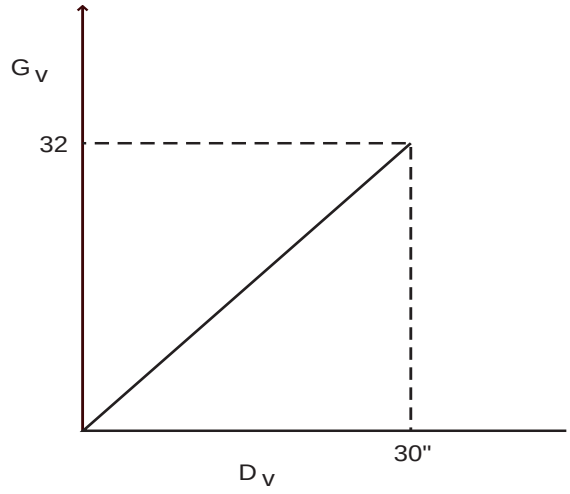

Fig. 4.4.5.4 **Acceleration as a function of dynamic crush – triangular pulse**

Table 4.4.5.1 **Force required on occupant restraint system**

	Triangular Pulse*	Square Pulse
Structure	Higher force	Lower force
Passenger Compartment	Higher acceleration	Lower acceleration
Occupant	Higher force	Lower force
Restraint System	Greater demand	Lesser demand

*Based on same vehicle crush as square pulse

occupant of the coasting vehicle. These forces will slow the occupant down within the vehicle and remove kinetic energy from the occupant. The unrestrained occupant inside the crashing vehicle; however, will experience different kinematics. Since the crashing car stops so quickly – within 0.1s – the occupant continues to move forward at the same initial velocity within the compartment until impact with the surfaces of vehicle interior structural components such as the steering assembly, instrument panel, knee bolster or windshield, which are now stopped. The contact forces generated from occupant interaction with these component surfaces will apply to the occupant, thus reducing the occupant's velocity to zero. Depending on the characteristics of these components, very large forces may be generated if the components are too stiff and do not absorb much energy. The occupant's kinetic energy, therefore, must be transformed to other forms of energy that remain within the occupant's body. This transformed energy causes injuries to the occupant, which constitute the subject of many impact biomechanics research studies.

In order to reduce the impact injury to the occupant, various restraint systems have been designed, exist, and will be continuously improved for occupant protection during a vehicular crash event. Examples show how significantly the introduction of an occupant restraint system into the above scenarios change the kinematics of the occupant. In order to examine and illustrate the differences between the unrestrained occupant in a braking vehicle and a crashing vehicle, and a restrained occupant in a crashing car, the velocity time (V_v- T) histories are needed. In Figure 4.4.6.1 – Velocity-Time Histories/Vehicle and Occupant, the

velocities of the occupant and the vehicle over the ground are plotted as a function of time, and differences between the various scenarios discussed above can be easily explained. The advantage of using the V_v-T diagram is that many important parameters are discernible from this diagram, including:

- the acceleration of the vehicle and/or the occupant is directly related to the slope of the velocity-time curve at any time t;
- the difference, at any time t, between the occupant and the vehicle velocity time curves represents the relative velocity (D v) between them; and
- the displacement of the vehicle and occupant over the ground is represented by the area under their respective velocity-time curves with respect to the time axis, and the relative displacement of the occupant with respect to the vehicle is the area between their respective velocity-time curves.

Figure 4.4.6.2 – Velocity-Time Diagram of Braking Vehicle and Occupant shows the velocity-time history for the braking vehicle. It is reasonable to assume that

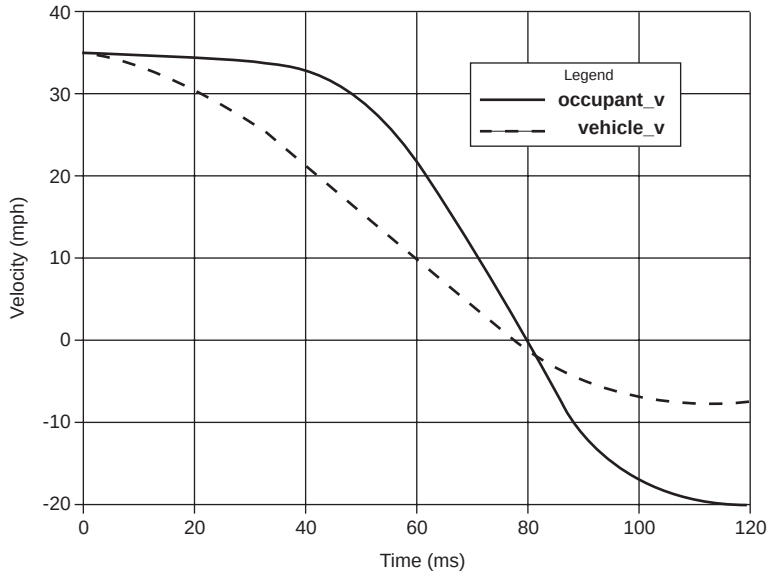

Fig. 4.4.6.1 **Velocity-time histories/ vehicle and occupant**

the vehicle is under a 0.7 g deceleration rate. This means that the braking force, when applied, generates an amplitude such that the vehicle decreases in velocity by 22.54 ft/sec per second. At this rate, the vehicle comes to a stop in 1.95 s. During this deceleration period, the vehicle displaces 43 ft over the ground, which is represented by the shaded area under the velocity-time curve shown in Figure 4.4.6.2. For an unrestrained occupant, the various forces acting on the occupant through the seat and floor pan are instantaneously applied, and the occupant's velocity will be reduced in the same manner as the vehicle. However, if the same forces (0.7 g's) were applied, but their onset was delayed by 0.01 s, the occupant's velocity-time history is shown in the figure. The occupant's displacement over the ground, again represented by the area under the occupant's velocity curve, will now be 43.4 ft. Therefore, the delay of force application has caused the occupant to travel 5.3 in inside the compartment, which is represented by the area between the occupant's velocity curve and that of the vehicle in Figure 4.4.6.2.

Figure 4.4.6.3 – Velocity-Time Diagram of Crashing Vehicle and Unrestrained Occupant illustrates a 30 mph barrier impact case, assuming that the front-end of the vehicle is crushed 24 ins and the compartment also moves that amount over the ground without taking intrusion into consideration. The shaded area under this velocity curve represents the 24 in of vehicle crush, which is equal to the distance the vehicle travels over the ground. The unrestrained occupant will continue to move at the initial velocity of 30 mph, according to the First Law of Motion under no influence of applied forces, until the moment of contact with the

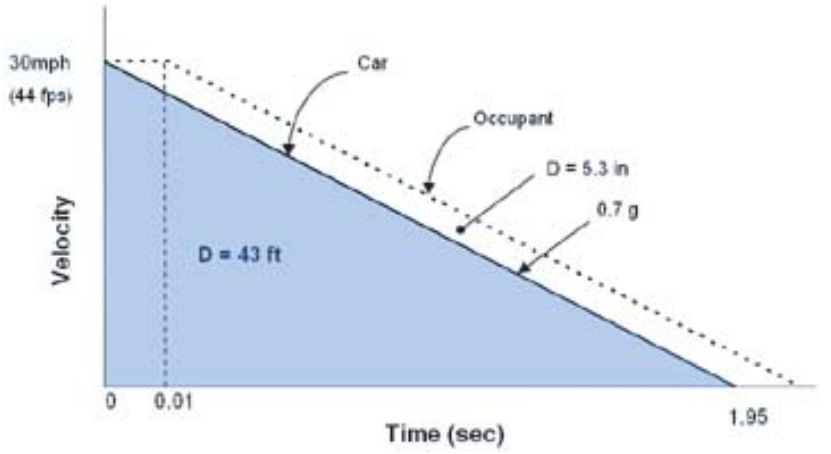

Fig. 4.4.6.2 **Velocity-time diagram of braking**

vehicle interior components, such as the instrument panel. If the initial clearance between the occupant and the panel is 24 in and if the occupant contacts the panel just as the vehicle has stopped, the occupant will have translated 48 in with respect to the ground. If the deflection of the panel allows only additional 3 in of motion, the occupant will come to rest 11 ms later at a constant deceleration of 120 g, which is obtained from $a=v^2/2s$, where v = 30 mph and s= 3 in. The occupant deceleration can be further reduced if the panel can deform more to absorb the occupant's kinetic energy. For the unrestrained occupant in this case, the speed of impact to the interior is equal to the speed change of the vehicle, since the occupant contacts the interior after the vehicle is completely stopped. The relative

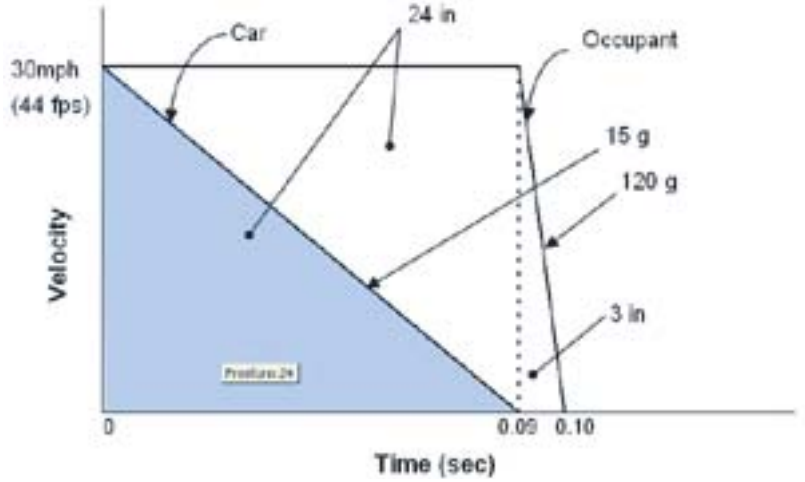

Fig. 4.4.6.3 **Velocity-time diagram of crashing vehicle and unrestrained occupant**

speed of occupant impact with the interior is typically attributed to occupant potential injuries. The speed at which the occupant hits the interior components may be different from the speed change of the vehicle if the occupant is restrained with various restraint systems.

Figure 4.4.6.4 – Velocity-Time Diagram of Crashing Vehicle and Restrained Driver illustrates the velocity-time histories for the same vehicle and a restrained occupant. Since a restraint system has a "slack," and cannot apply restraining force to the occupant immediately, an effectiveness time of 0.030 s is assumed.

During this time, the occupant will continue at an initial velocity of 30 mph and will travel 15.8 in within the compartment as shown in the velocity-time curve. If the occupant comes to rest at the same time as the vehicle, the restraint force needs to be applied to decelerate the occupant at 22.4 g in the next 0.061 s. During this period of restraint, the occupant will move another 5.4 in within the compartment. The occupant's total displacement over the ground is then 32 in, which is comprised of 24 in of vehicle crush and 8 in of relative motion within the compartment. Note that, in this case, the time required to reduce the occupant's initial velocity to zero has been increased by six times as compared to the unrestrained occupant case, 0.061 s in the restrained case vs. 0.01 s in the unrestrained case. From the above examples, the occupant's deceleration is 22.4 g and 120 g in restrained and unrestrained condition, respectively. From Newton's Second Law, the magnitude of the forces applied to the restrained occupant will

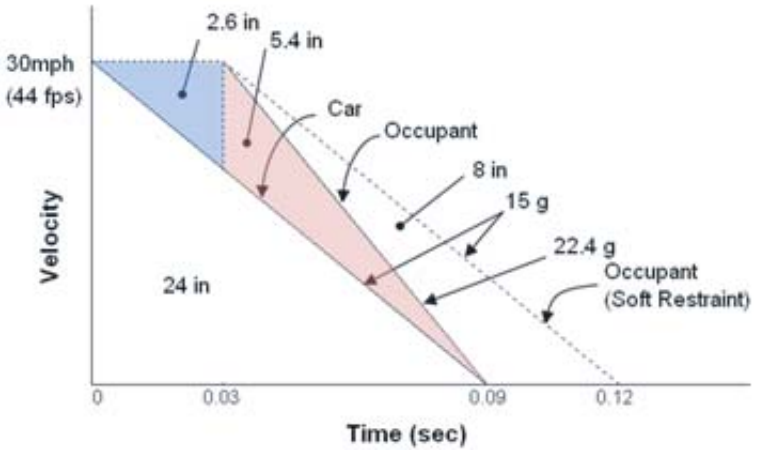

Fig. 4.4.6.4 **Velocity-time diagram of crashing vehicle and restrained driver**

therefore be reduced to one-sixth the magnitude of the forces applied to the unrestrained occupant (22.4 g vs. 120 g). The benefit of a restraint system thus can be realized.

If the instrument panel is 18 inches in front of the occupant as in the previous example, and because the occupant traveled only 8 in in the compartment, the occupant will have missed the panel by 10 in. If the applied restraint forces were modified such that the occupant uses the entire 18 in of interior space to arrest his

motion, then the occupant's velocity-time curve will be as shown by the dashed line in Figure 4.4.6.4. This indicates that the time to reduce the occupant's velocity to zero can be extended from 60 to 98 ms. Newton's Second Law indicates that the restraining forces will also be half as large as the previous case and one-eighth of the hypothetical unrestrained case.

4.5 Axioms for Good Occupant Restraint Performance and Design

The basic concept discussed in Section 4.3 - Basic Laws and Concepts of Motion, allows establishment of:

- the relationship between the acceleration, velocity and displacement in time.
- the relationships between forces and motions of a system; and
- energy of system(s) such as occupant and vehicle.

Using an ESW concept, the following relationships hold:

$$A_s = \frac{V_0^2}{2X_v} \tag{4.5.1}$$

and

$$T_s = \frac{V_0}{A_s} \tag{4.5.2}$$

where A_s is the deceleration of the equivalent square wave, V_0 the initial velocity, and X_v the maximum vehicle crush or the maximum stopping distance. It should be noted that T_s is different from the crash duration, T, of an actual pulse. The crash duration, in general, is not a design objective, because it is beyond designers' control.

Combining the above relationships with considerations of general structural energy management for impact with controlled collapse mechanisms, human anatomy and injury mechanisms and biomechanic tolerance level, Eppinger [6] and Patrick [2] suggested certain guidelines that help designers and engineers estimate design requirements of a given restraint system, evaluate their restraint system performance, and apply the results to the design of an optimal restraint system in meeting or exceeding safety performance requirements.

These guidelines are cited here for reference:

1) From Eq. 4.3.2.2, maximize the time over which restraint forces are applied to minimize the magnitude of the forces applied to an occupant. According to Eq 4.3.2.2, this, in turn, will minimize the "g"-level, which should be below human tolerance levels. The total time is very difficult to control or design. However, the effectiveness of the belt (to be discussed in Section 4.7 – Compatibility between Restraint System and Vehicle Front Structure) can be a parameter in a restraint system design.

2) Maximize the distance of the occupant's travel over the ground by utilizing the vehicle crush and the available space within the occupant compartment. Therefore, a restraint system should be designed to provide sufficient cushioning (or the necessary distance) for decelerating the occupant.

3) Minimize the effectiveness time of a restraint system by applying as great a restraint force as soon as possible during the impact event. This force should not exceed the established tolerance level in terms of dummy performance numbers as specified in FMVSS requirements.

4) Minimize body articulations, local deformations and rate of deformations, and local inertial accelerations during the restraint event. Minimize excessive relative motion between body segments and body-to-vehicle interiors.

5) Minimize concentrated forces on sharp edges and hard surfaces. Distribute forces over the greatest possible area. Distributed forces are preferable to concentrated forces in design of occupant protection systems. Structures generally deform less with distributed loads and therefore, deformation-based injuries are reduced. This reduces local surface pressures applied to a body region that have also been related to structural failure.

6) Use energy-absorbing materials designed to crush at forces below human tolerance levels and extract energy from the occupant by maximizing the energy absorption during crush or deformation. Force-distributing padding is preferred over major energy-absorbing structures such as steering hub, knee contact area, instrument panel and interior components.

7) Maximize the efficiency of a restraint system by designing as closely as possible to a square waveform. This is most effective in terms of utilizing a minimum package space requirement.

8) Maintain compartment integrity and minimize structural intrusions in both magnitudes and relative velocities.

4.6 Vehicle/Occupant Velocity Profiles

Vehicle/occupant velocity-time histories obtained from barrier tests will be discussed in this section. Examples of a braking vehicle vs. a crashing vehicle using velocity profiles will be demonstrated. This may include applications to side and car-to-car impacts.

4.6.1 Frontal Impact Analysis

A frontal crash is a two-impact event. In the first (primary) impact, the vehicle strikes a barrier, causing the front-end to crush. Kinetic energy of the vehicle is expended in deforming the vehicle's front structure. The design of the front-end, rear, or side to crumple in a collision and absorb crash energy is called crash energy management or crashworthiness.

The second (secondary) impact occurs when the occupant continues to move forward as a free-flight mass and strikes the vehicle interior or interacts with or loads the restraint system. Some of the kinetic energy is expended in deforming the vehicle interior or the restraint system, and in compressing the occupant's torso. The remaining kinetic energy is dissipated as the occupant decelerates with the vehicle.

During the secondary impact, injury may occur while the occupant is loading the interior or the restraint system, if the impact loading or severity exceeds the injury threshold level. The kinetic energy of the occupant's torso should be dissipated gradually for the impact to be non-injurious. If there is a large differential velocity between the occupant and the interior, much of the kinetic energy must be dissipated during the impact of the occupant with the interior or the restraint system. If the second impact is of a very short duration, the resulting force on the occupant can exceed human tolerance levels. The kinetic energy dissipated during the second impact is a function of the occupant's mass and of the differential velocity of the occupant to the interior.

Energy-absorbing (EA) materials on the interior, and devices such as EA steering columns, belts and air bags provide two important synergistic benefits. First, these enhance "ride-down" for the occupant within the vehicle compartment. Second, these absorb some of the energy of the second impact.

"Ride-down" can be described as managing the occupant's energy by taking advantage of the gradual deceleration of the vehicle measured at rocker at B-pillar or at any non-deformed location in the vehicle, such as seat cross members. At the onset of a frontal crash, the unbelted free-flight occupant and the decelerating vehicle interior have the same initial velocity. The vehicle interior slows down while decelerating as the front-end structure of the vehicle crushes. The occupant travels at the initial speed until the occupant contacts the interior. Vehicle interior components such as instrument panels in current production vehicles are padded with EA materials that allow crushing to produce an earlier coupling (engagement) of the occupant with the gradually decelerating interior. The forces required to decelerate the occupant during ride-down should be kept below human tolerance levels. The earlier contact also results in a smaller differential (relative) velocity between the occupant and the interior, thus reducing the portion of the occupant kinetic energy that must be dissipated in the second impact. Some mathematical treatment of this ride-down phenomenon is presented in Section 4.9 – Ride-Down Concept and Application.

EA materials can be designed through selection of appropriate characteristics to crush at forces below human tolerance levels. EA materials absorb energy while being crushed, and because of this crush, the occupant's differential velocity with the interior in the second impact is reduced over a longer period of time than that from impacting with a rigid surface. This produces lower deceleration forces on the occupant.

4.6.2 Side Impact Analysis

Theories outlined in Section 4.4 – Application of Concepts to Vehicle/Occupant Analysis, can be used in side impact analysis [7]. Use of velocity-time history for analysis of a typical FMVSS 214 (NHTSA-type) side impact test can be demonstrated to study the effects of structural upgrading vs. occupant cushioning countermeasure.

4.6.2.1 Baseline Analysis

The significant crash event in a typical NHTSA-type side impact test is explained by analyzing the velocity profiles of Figure 4.6.2.1.1 – Typical Velocity Profile in Side Impact. The profiles are obtained by the numerical integration of accelerometer data taken from the following locations:

- Center of gravity (CG) of the moving deformable barrier (MDB)

- Non-impacted left-hand rocker of the target vehicle
- Door inner panel at the armrest
- Side Impact Dummy (SID) pelvis

The following momenta exchanges are taking place:

- the primary momentum exchange taking place between the MDB and the target vehicle. During this event, the rigid body motion of the target vehicle increases while the MDB velocity decreases until at some point in time, both the MDB and the target vehicle achieve a common velocity.
- the momentum exchange taking place between the MDB and the door. The door quickly attains the high velocity of the MDB.
- finally, the momentum exchange taking place as the intruding door comes into contact with the stationary SID. The dummy pelvis, hit by a fast-intruding door, is quickly accelerated in the lateral direction.

Door-to-dummy interaction forces can be reviewed by looking at the door and the dummy "free-body" diagram of Figure 4.6.2.1.2 – Door and SID "Free-body" Diagrams. The forces acting on the door are:

- F_{MDB} is the punch-through force of the MDB acting on the door.

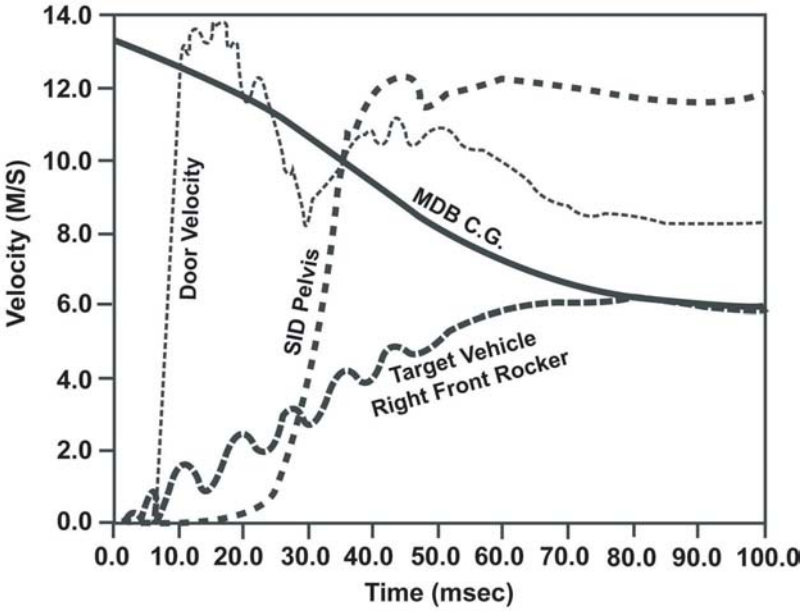

Fig. 4.6.2.1.1 **Typical velocity profile in side impact**

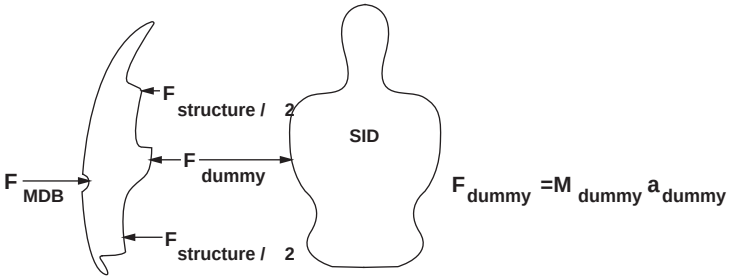

Fig. 4.6.2.1.2 **Door and SID "free-body" diagrams**

- $F_{structure}$ is the body side structural resistance of the target vehicle that resists door intrusion. This structural resistance is provided by door support frame (consisting of the hinge pillar, door hinges, A-pillar, roof side rail, B-pillar, latch/striker, and the rocker), the door anti-intrusion beam, the floor pan/cross members, instrument panel (I/P), I/P cross car beam, cowl, header, and the roof skin/bow). This force is the integral of the door support frame reaction pressures acting on the door peripheral areas and is shown in Figure 4.6.2.1.2 as one-half of its concentrated load in two locations to facilitate explanation.
- F_{dummy} is the door-to-dummy interaction force, which also is the reaction force acting on the dummy.

Using Newton's Second Law, which states that the rate of change in the door linear momentum is equal to the summation of forces acting on the door free-body diagram,

$$\frac{d}{dt}[M_{door} v_{door}] = \sum F = F_{MDB} - F_{structure} - F_{dummy} \qquad (4.6.2.1)$$

and solving for F_{dummy}, one obtains the following:

$$F_{dummy} = F_{MDB} + \frac{d}{dt}[M_{door} v_{door}] - F_{structure} \qquad (4.6.2.2)$$

Thus, it is noted that:

- decreasing the MDB punch-through force (F_{MDB}) would decrease the force

acting on the dummy (F_{dummy}).
- decreasing the rate of change in the linear momentum of the door by making the door lighter or decreasing the door intrusion velocity would decrease the force acting on the dummy.
- increasing the struck vehicle body side structural resistance ($F_{structure}$) would also decrease the force acting on the dummy.

Referring to the free-body diagram of SID as shown in Figure 4.6.2.1.2 and using Newton's Second Law, the mass of the SID (M_{dummy}) represents that of a 50th-percentile male, which is difficult to change. Because the federal government regulates the maximum allowable dummy acceleration (a_{dummy}), the only recourse for the automobile manufacturers is to limit the force acting on the dummy (F_{dummy}) so as not to exceed the allowable dummy acceleration limits. This simple analysis provides some insight into the important parameters that affect dummy responses during side impact and allow for development of countermeasure strategies.

Countermeasures for limiting the force on the dummy during side impact include:

- reducing the door intrusion velocity and hence, its rate of change in linear momentum via structural upgrading of the body side. This would reduce the severity of the subsequent momentum exchange between the door and the dummy.
- limiting the peak forces acting on the dummy (F_{dummy}) using a foam cushion with a nearly constant force-crush characteristic or a deployable side airbag. This would reduce the MDB punch-through force (F_{MDB}) while also making the door inner sheet metal and trim more compliant for occupant cushioning, thereby further reducing F_{dummy}.
- optimizing the specific stiffness by maximizing the structural stiffness/unit material usage of the vehicle body side structure via efficient structural design and use of an airbag or foam cushion. This strategy is an optimum combination of the first two strategies.

4.6.2.2 Effects of Structural Ugrading

Figure 4.6.2.2.1 – Effects of a Hypothetical Structural Upgrade shows the effects of structural upgrading based on hypothetical simulation and the results of an upgraded experimental vehicle. These curves reflect general trends as summarized below:

The crash event between the MDB and the target vehicle is shortened. The MDB slows at a faster rate while the struck vehicle rigid body motion speeds up at a higher rate. The door intrusion and intrusion velocity are reduced. The reduction can be significant, depending on the extent of structural upgrade. The dummy pelvis, hit by a slower intruding door, is subjected to a milder acceleration as evident by the slope the dummy pelvis velocity curve. Therefore, the momentum exchange between the door and the dummy pelvis is reduced accordingly. However, the structural upgrade weight penalty to achieve this effect is enormous. The weight penalty is estimated at more than 18 kg (40 lbs) for a 2-door compact vehicle, since the structural stiffness is needed upfront at the early stage of the crash event prior to the door developing significant intrusion and intrusion velocity. Furthermore, Transportation Research Laboratory [8] has shown that certain structural upgrading of the vehicle body side structure could lead to an undesirable intrusion profile of B-pillar/door by tilting inboard at the "waistline" and concentrating the impact load on the occupant in the thorax region. A more desirable crush pattern for the B-pillar/door is to remain upright during side impact for a more evenly distributed impact loading on the occupant.

4.6.2.3 Effects of Cushioning

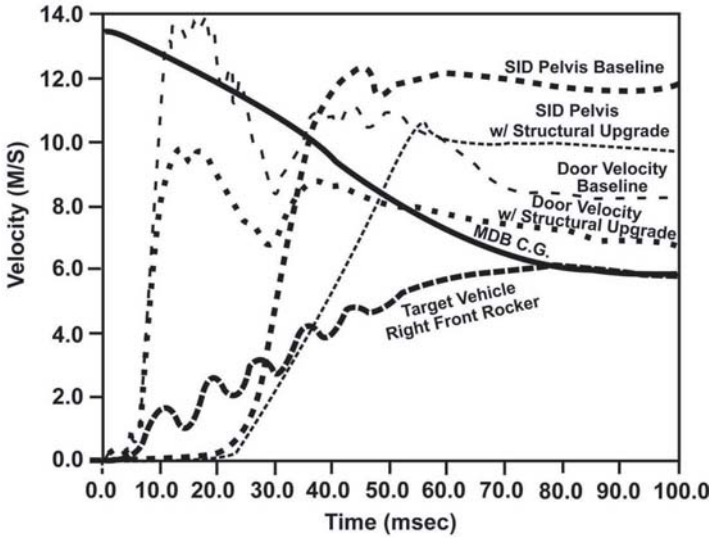

Fig. 4.6.2.2.1 **Effects of a hypothetical structural upgrade**

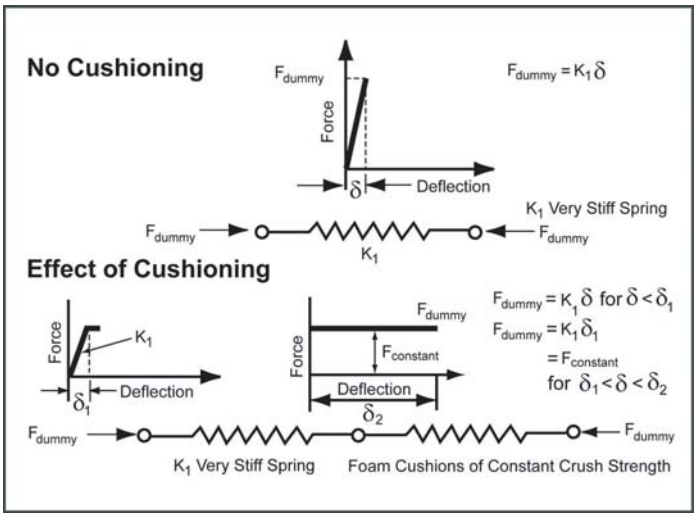

Fig. 4.6.2.3.1 **Effects of load-limiting cushioning**

Figure 4.6.2.3.1 – Effects of Load-limiting Cushioning illustrates the effects of load-limiting constant force-crush cushioning. In the case of no cushioning, the reaction force of a stiff door panel, represented in Figure 4.6.2.3.1 by a stiff linear spring constant (K_1), increases in direct proportion to the panel deflection (δ) as the dummy leans heavily against the door during side impact. The force (F_{dummy}) acting on the dummy pelvis, which is equal to $K_{1\delta}$ causes the pelvis acceleration (in the $M_{pelvis}a_{pelvis}$ term) to exceed the federal limits. Figure 4.6.2.3.1 also illustrates the condition in which a load-limiting constant force-crush spring is connected in series with the same stiff spring of the door inner panel. Initially, when the dummy is hit by the intruding door and as the reaction force (F_{dummy}) begins to rise but is less than $F_{constant}$, the stiff spring K_1 will deflect up to δ_1 until $F_{dummy} = F_{constant}$. At this point onward, the load-limiting spring will begin to crush (δ) at a constant force ($F_{constant}$). The dummy pelvis, subjected to an appropriate level of this constant reaction force from the door, will accelerate at a constant level without exceeding the federal requirement as long as the cushion does not bottom out.

Figure 4.6.2.3.2 – The Deployable Door Trim System, shows the design concept of a deployable door trim system. A pusher foam is bonded to the inner surface of the door outer panel. A polyurethane foam cushion is stowed in the space between the glass plane and the door trim panel, thus maximizing the amount of protective foam without decreasing the interior space of the occupant compartment. During a side impact, the cushioning of the door by the impacting

vehicle causes the foam cushions to be deployed toward the occupant. The load-limiting foam cushion pushes the occupant away from the intruding door at a controlled acceleration rate, thus providing lowered dummy injury indicators.

Figure 4.6.2.3.3 – Effects of a hypothetical Door with Deployable Foam Cushion, uses a hypothetical test to illustrate:

- the crush duration between the MDB and the target vehicle will remain unchanged from the baseline (Figure 4.6.2.1.1. Typical Velocity Profile in Side Impact)
- the door velocity profile will remain unchanged from Figure 4.6.2.1.1
- the deploying load-limiting foam cushion contacts the dummy pelvis early in the crash event and accelerates it away from the intruding door sooner than that of the baseline
- consequently, the dummy pelvis will experience a milder acceleration as evident from the slope of its velocity history
- thus, the strategy is to use a deploying door trim with the load-limiting foam cushion behind it to quickly push the stationary SID away from the intruding door steel at a controlled rate.

4.7 Compatibility Between Restraint System and Vehicle Front Structure

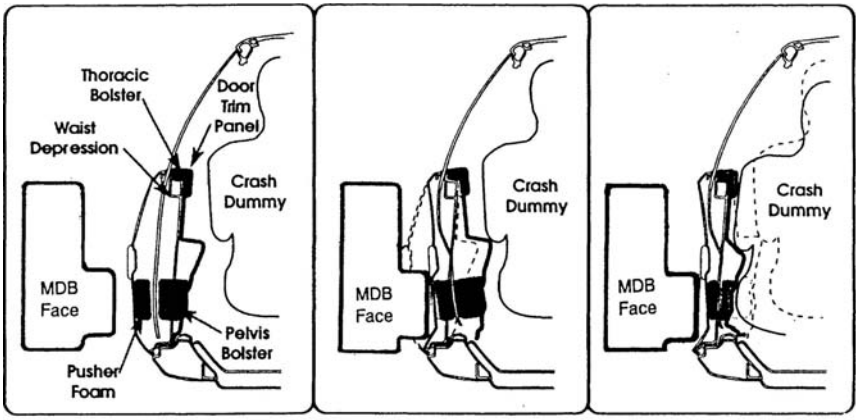

Fig. 4.6.2.3.2 **The deployable door trim system**

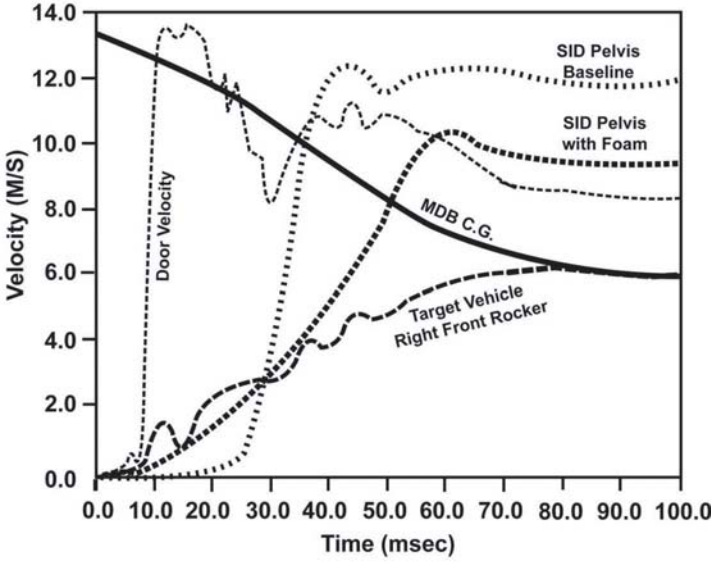

Fig. 4.6.2.3.3 **Effects of a hypothetical Door with Deployable Foam Cushion**

A fundamental requirement in the design of a vehicle front structure is that its crush characteristic be compatible with the restraint system characteristics as previously mentioned. To establish the compatibility relationship between these two systems, the following parameters must be taken into consideration:

- vehicle dynamic crush length (d_v);
- total occupant travel distance or stopping distance with respect to ground (d_p);
- occupant deceleration (a_p).

Mathematically, the compatibility condition requires that:

$$\delta_v + \delta_{p/v} > \delta_p \tag{4.7.1}$$

where $\delta_{p/v}$ is the occupant displacement with respect to the compartment, and must not exceed the interior available distance to prevent the "secondary impact" with the vehicle interior components.

Total occupant displacement can be established using a simple idealized model describing the restraint system performance, which is a function of system characteristics that are specified to comply with the established injury criteria. In Figure 4.7.1 — Idealized Model, the occupant kinematics are characterized by three parameters: the restraint system effectiveness time t_e, deceleration onset rate α, and the maximum deceleration A_p. Total occupant travel distance with respect to ground is the sum of the distances the occupant travels during the constant speed phase, the constant onset phase and the constant deceleration phase. It can be expressed in terms of t_e, α, and A_p by:

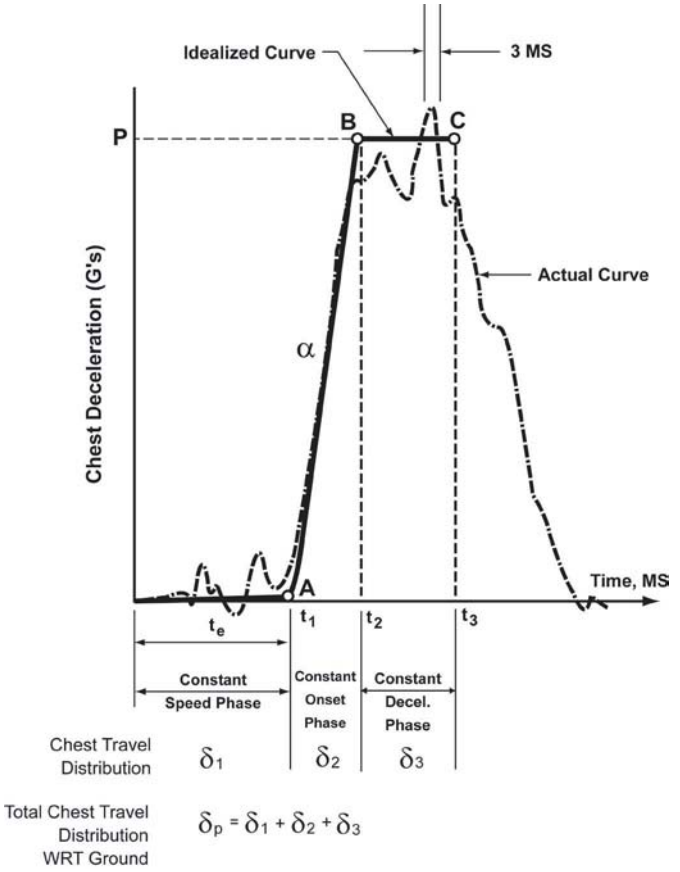

Fig. 4.7.1 **Idealized model**

$$\delta_p = 12\,V_0[t_e + A_p/2\alpha] + 12\,V_0^2/64.4\,A_p - 16.104\,A_p^3/\alpha^2 \quad (4.7.2)$$

where

- $d\eth_p$ is in inches;
- V_0: ft/sec
- t_e: sec
- A_p : g's
- $a\eth$: g/s

More detailed derivation of equations are given in Section 4.8 - Restrained Occupant Model (Analytical Approach)..

Physical interpretation of the occupant travel distances during each phase, as previously mentioned, is presented schematically in Figure 4.7.2 –Occupant Movement in a Barrier Impact. For a given set of parameters t_e, A_p, and α , a family of curves, for example, velocity vs. time, can be obtained using Eq. (4.7.2) for various impact speeds. The area under a velocity-time history curve represents the occupant travel distance relative to ground and the slope of the velocity curve equals the acceleration levels of the occupant. Figure 4.7.3 – Chest Travel during Fixed Barrier Impact shows examples using $t_e = 0.034$ s., $A_p = 40$ g's and α = 1000 g/s for different velocities.

Let D denote the available interior distance. As previously mentioned, it is desired that:

$$\delta_{pv} < D \quad (4.7.3)$$

It then follows from Eq. (4.7.1) that

$$\delta_v > \delta_p - D \quad (4.7.4)$$

The quantity, $\delta_p - D$, in Eq. (4.7.4) sets the minimum vehicle crush distance required to satisfy the compatibility between structural and restraint characteristics.

With this background, trade-offs can be made between the required vehicle crush and the effectiveness time t_e for various impact velocities, provided that the restraint system performance parameters can be chosen so that the interior available distance is fully utilized. Variations in the effectiveness time t_e allow the analysis of potential benefits of early triggering of the passive restraint system.

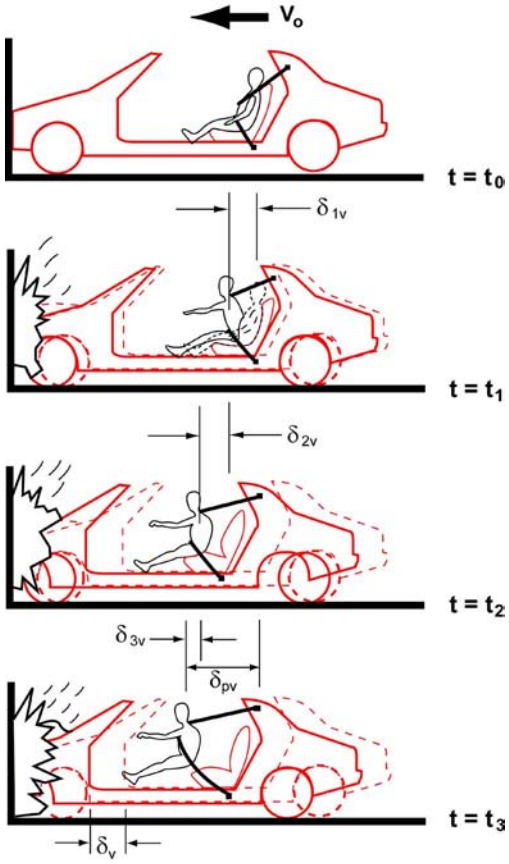

Fig. 4.7.2 **Occupant movement in a barrier impact**

4.7.1 Analysis

The hypothetical analysis presented below is carried out for the belt and the supplemental airbag restraint systems.

4.7.1.1 Belt Restraint System

Baseline parameters selected for 30 mph, 35 mph, and 40mph analyses are listed in Table 4.7.1.1.1 using D = 18 in.

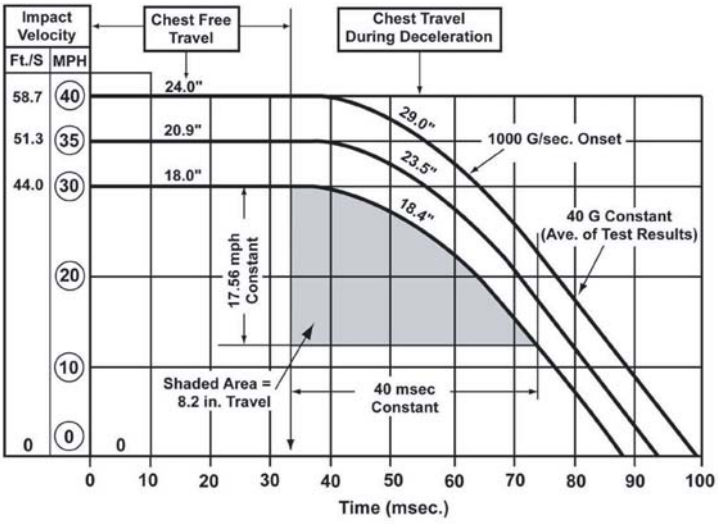

Note: Area of 240 mm^2 equals 1.0 In. of travel

Case	Barrier Impact Velocity (mph)	Chest Onset (G/sec.)	MAX. Const. Decel. (G)	Effectiveness Time (msec)	Total Chest Travel (inches)
1	30	1000	40	34	36.4
2	35	1000	40	34	44.4
3	40	1000	40	34	53.0

Fig. 4.7.3 **Chest Travel During Fixed Barrier Impact**

Substituting the above parametric values into Eq. (4.7.2) and using Eq. (4.7.4), a vehicle crush distance of 22 in is obtained for the 30 mph case. This value

Table 4.7.1.1.1 **Values of baseline parameters**

	30 mph	35 mph	40 mph
Effectiveness time t_e	0.034 s	0.034 s	0.034 s
Onset rate α	700 g/s	800 g/s	1000 g/s
Constant Decel. A_p	40 g	40 g	40 g

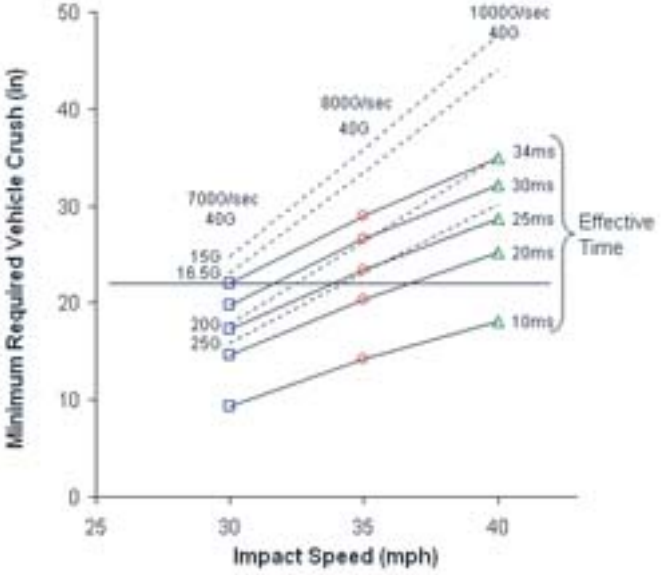

Fig. 4.7.1.1.1 **Minimum required vehicle crush versus impact speed for various belt restraint system parameters**

represents dynamic vehicle crush of a current small-sized vehicle at 30 mph barrier crash. Dynamic crush for the 35 mph and 40 mph cases are found to be 29 in and 35 in, respectively, based on these hypothetical values.

Parametric studies can be conducted by varying the effectiveness time t_e from 0.034 s (baseline) to 0.030 s, 0.025 s., 0.020 s, and 0.010 s. Results are shown in Figure 4.7.1.1.1 – Minimum Required Vehicle Crush, where the minimum required vehicle crush is plotted as a function of impact speed. Two remarks are worth making in view of Figure 4.7.1.1.1.

First, the minimum required vehicle crush decreases as the effectiveness time decreases. A certain amount of reduction in vehicle length can then be realized and benefit from application of a pre-crash sensor in early triggering restraint system.

Second, theoretically, using early triggering restraint system, the 35 mph impact could also be achieved with no increase in vehicle length using the 30 mph

baseline structure. This would result in a vehicle deceleration of 22.5 g's.

4.7.1.2 Supplemental Airbag Restraint System (SARS)

Supplemental airbag restraint system is the best-known passive restraint system introduced for occupant protection in frontal impacts. The SARS is automatically deployed after a certain crash severity is reached. Two distinct locations, the steering wheel and the instrument panel, are currently used for the air bag installation to protect the driver and the right front seat passenger, respectively, during frontal impacts. Additional locations sometimes include the rear seat, door side panel, the roof and the knee bolster area. For each location, design parameters such as bag size, bag pressure and deployment time are different, depending on the human body regions to be protected and their respective tolerance levels.

The crash sensor is the heart of a SARS. It requires high operating reliability in determining whether a "true" collision has occurred. The sensor performance can be affected by its location on the vehicle. Different types of sensors also require various sensing times depending on sensor mechanism and crash signals. Sensor performance requires sensor calibration and algorithm development, which is beyond the scope of this chapter. Additional information on this topic is available through the Society of Automotive Engineers, SAE, which sponsors a seminar on fundamentals of crash sensing [10].

The sensing times may vary from 8 ms to 13 ms with a threshold velocity of approximately 10 to 15 mph, at which the actuators trigger. After the sensing mechanism has determined that a collision has occurred, it triggers a sequence of events that result in bag deployment. Studies show that the entire sequence of operations is completed in approximately 40 to 50 ms. A passenger bag requires a total deployment time of 50 ms, of which approximately 30 ms is elapsed for inflation. Therefore, should a sensor provide an early triggering capability, a reduction of 15 ms to 18 ms in the sensing and triggering phases can probably be realized. Following the analysis outlined in Section 4.7.1.1 – Belt Restraint System versus Impact Speed for Various Belt Restraint System Parameters, the minimum required vehicle crush distance can be determined. Assuming that the bag will not be bottomed out in protecting occupants, one may take $D = 16$ in in the analysis. Results shown in Figure 4.7.1.2.1 – Minimum Required Vehicle Crush versus Impact Speed for Various Air Bag Restraint System Parameters are the required vehicle crush length for various air bag effectiveness times, that is, 50 ms, 40 ms, 35 ms and 32 ms. Higher onset rates and constant deceleration are used since the bag would act as a non-linear "hard" spring, and the minimum

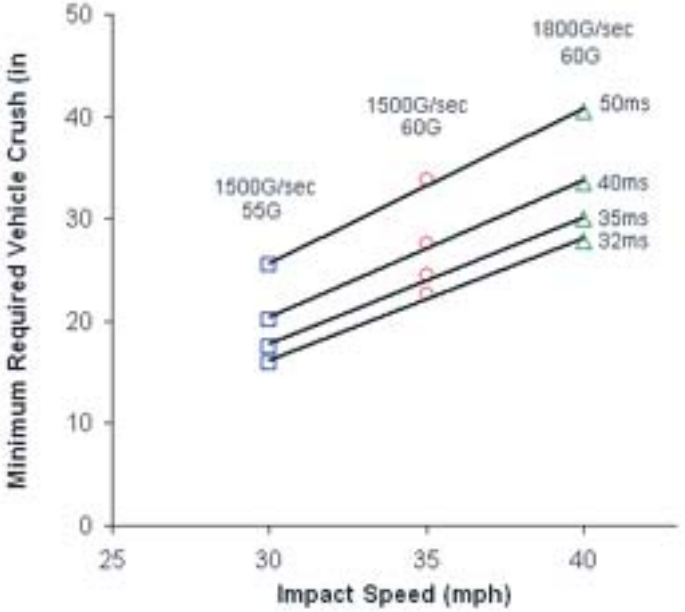

Fig. 4.7.1.2.1 **Minimum required vehicle crush versus impact speed for various air bag restraint system parameters**

required crush distance based on the supplemental airbag restraint system performance is larger than that determined for the belt restraint systems.

4.8 Restrained Occupant Models (Analytical Approach)

The simulation of a restrained occupant and vehicle front-end dynamics in a frontal collision has been demonstrated in the open literature with different models of varying degrees of complexity [1]. Two simple models [4, 9, 11] found in the literature can be used to demonstrate as a useful tool in guiding the design in the concept phase (early stage) of the vehicle development. The chest deceleration of a front passenger is idealized in two different ways. One way is to use a trilinear segment approximation to the chest deceleration as mentioned in Section 4.7 – Compatibility between Restraint System and Vehicle Front Structure (see Figure 4.7.1), while the other uses a sine-wave approximation. No provisions are made for studying driver behavior because of the steering wheel and column

interactions. The models are used to calculate the required stopping distance of the occupant relative to the ground for a given restraint system design, impact speed, and the maximum allowable chest deceleration as specified in FMVSS 208 for occupant protection. Knowing the available vehicle interior space, the required vehicle crush distance and the average vehicle deceleration can then be calculated. The two analytical models are described next.

4.8.1 The Trilinear Chest Deceleration Model for Belted Occupant Response

In this model, the response of a restrained passenger in a vehicle frontal barrier impact is idealized by dividing the time that is required to decelerate the occupant from an initial velocity V_0 to stop (a zero final velocity) into three time domains as shown in Figure 4.8.1.1 – Trilinear Belted Occupant Model.

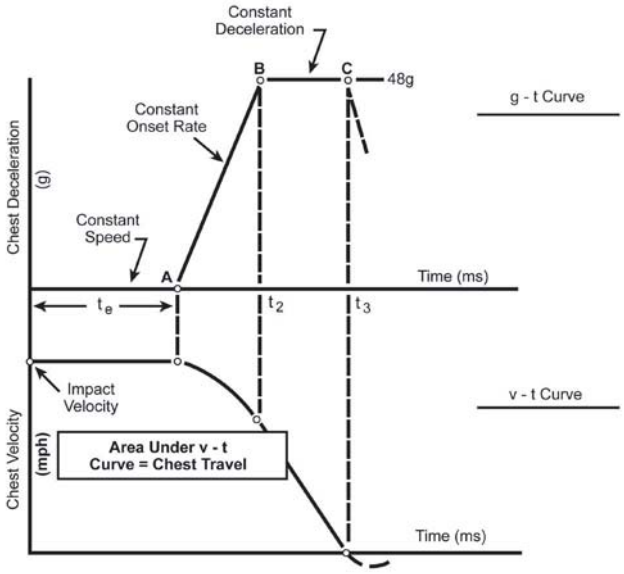

Fig. 4.8.1.1 **Trilinear belted occupant model**

In the first domain, $0 < t < t_e$, the occupant velocity is assumed to be constant, since the occupant is in a free flight because of the belt slack. The occupant continues to move at the initial velocity of the vehicle until time t_e. At $t = t_e$, the restraint system becomes effective, and therefore, it is referred to as the effectiveness time of the belt (or restraint system).

When $t_e < t < t_2$, the restraint slack has been taken up. The occupant starts interacting with the restraint at a certain relative velocity, and then begins to decelerate due to the induced belt loads until a maximum chest deceleration is reached. The occupant motion during this period is assumed to be at a constant deceleration rate (onset rate).

In the third period, $t_2 < t < t_3$, the occupant velocity continues to reduce until it vanishes. The maximum chest displacement is reached at time t_p.

The equations describing this idealized occupant response are presented for reference:

Let

V_0 = initial occupant (also vehicle) velocity in ft/s (or mph).

A_p = maximum occupant (front passenger side) chest deceleration in g's.

$\dot{\alpha}$ = occupant deceleration onset rate in g's/s.

g = gravity acceleration (32.2 ft/s^2).

$t < t_1$, the distance traveled by the occupant δ_{p1} is

$$\delta_{p1} = V_0 . t_e \qquad (4.8.1.1)$$

where t_1 = the belt effectiveness time t_e

In the second period, $t_e < t < t_2$, time of constant onset rate, t_0, is determined to be

$$t_0 = t_2 - t_e = \frac{A_p}{\dot{\alpha}} \qquad \text{for } V_2 > 0 \qquad (4.8.1.2)$$

The occupant velocity change ΔV is

$$\Delta V = V_0 - V_2 = \frac{1}{2}\dot{\alpha} g t_0^2 \qquad \text{for } V_2 > 0 \qquad (4.8.1.3)$$

The distance traveled by the occupant δ_{p2} is

$$\delta_{p2} = t_0\left(V_0 - \frac{g\dot{\alpha}}{6}t_0^2\right) \tag{4.8.1.4}$$

or $$\delta_{p2} = \frac{A_p}{\dot{\alpha}}\left(V_i - \frac{g}{6}\frac{{A_p}^2}{\dot{\alpha}}\right) \tag{4.8.1.5}$$

In the third period, $t_2 < t < t_3$; if V_2 is positive, that is, $V_2 > 0$, which implies that occupant is still in motion, the time required for the occupant to reach the final velocity $V_3 = 0$ at a constant deceleration A_p is:

$$t_c = t_3 - t_2 = \frac{V_2}{gA_p} \quad \text{for } V_2 > 0 \tag{4.8.1.6}$$

The distance traveled by the occupant during this period, δ_{p3}, can be determined from the following expression:

$$\delta_{p3} = \frac{1}{2}V_2 t_c \tag{4.8.1.7}$$

or $$\delta_{p3} = \frac{1}{2A_p}\left(V_0 - \frac{g}{2}\frac{{A_p}^2}{\dot{\alpha}}\right)^2 \tag{4.8.1.8}$$

For a given vehicle collision speed V_0 and maximum chest deceleration A_p, the Required Chest Displacement (*RCD*) relative to the ground and the total time t_p for the occupant to reach zero velocity can be obtained from Eq. (4.8.1.9) and Eq. (4.8.1.10), respectively:

$$RCD = \delta_{p1} + \delta_{p2} + \delta_{p3} \tag{4.8.1.9}$$

and

$$t_p = t_e + t_o + t_c \tag{4.8.1.10}$$

Thus, *RCD* and t_p can be defined by two parameters of the restraint system, namely, the effectiveness time t_e and the onset rate α for a given maximum chest deceleration.

Table 4.8.1.1 **Parameters for vehicle/occupant system analysis - trilinear belted case**

	Item	t_e (ms)	a (g's/s)	A_p (g's)
Case 1	3-point belt(13 - 18% elongation webbing)	34	1000	40
Case 2	3-point belt(3 -6% elongation webbing)	30	1200	40
Case 3	3-point belt(3-6% webbing with preloader)	20	1200	40

The effectiveness time t_e varies with the restraint system, and is affected by the deployment design parameters of the supplemental airbag restraint system and the slack in the belt restraint system at a given vehicle collision speed. Therefore, t_e is customarily assumed to be constant in the restraint system model analysis, although it varies with the impact velocity.

The onset rate $\dot{\alpha}$ in g's/s, varies with the relative velocity of the occupant to the vehicle, and the belt and airbag restraint loading states. For a given vehicle impact speed, the onset rate depends on the vehicle crush characteristics. Some example values of these three parameters are shown in Table 4.8.1.1 – Parameters for Vehicle/Occupant System Analysis - Trilinear Belted Case for different types of belt webbing.

The sensitivity analysis of the chest travel distance to the restraint system performance parameters is studied using this model. The results are shown in Figures 4.8.1.2 – Occupant Travel versus Effectiveness Time and 4.8.1.3 – Occupant Travel versus Chest Acceleration.

From Figure 4.8.1.2, it is evident that a more effective restraint system requires less t_e, thus reducing the chest travel distance. When t_e = 30 ms. for example, the chest travel distance during this period is 15.8 in and 18.5 in for impact velocities of 30 mph and 35 mph, respectively.

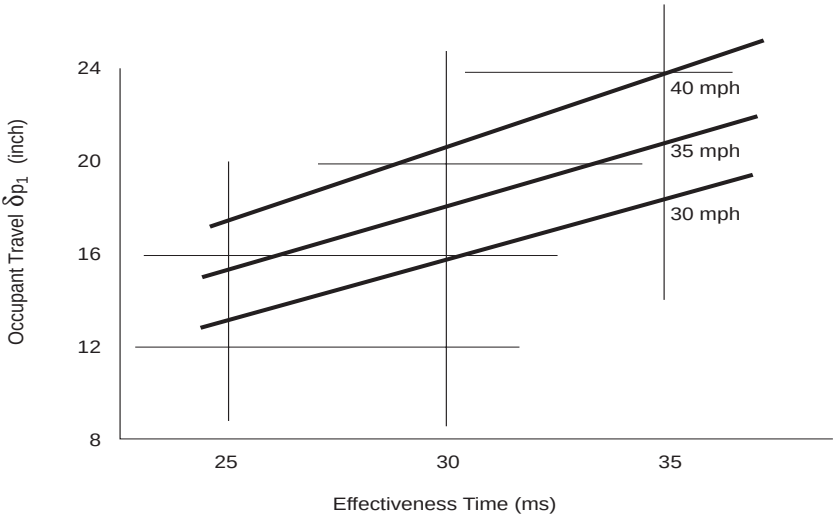

Fig. 4.8.1.2 **Occupant travel versus effectiveness time at different impact speeds**

A fundamental requirement in the design of a vehicle front-end structure is that its crush characteristics be compatible with the restraint system characteristics. Let $\delta_{p/v}$ be the vehicle dynamic crush length and $\delta_{p/v}$ be the belted occupant displacement relative to the vehicle compartment. Mathematically, the compatibility condition requires that

$$\delta_v + \delta_{p/v} = RCD \qquad (4.8.1.11)$$

where RCD is *es*tablished based on given restraint system parameters described above. To prevent the "secondary impact," $\delta_{p/v}$ must not exceed the available interior distance as previously stated. Determination of $\delta_{p/v}$, therefore, depends on a vehicle's interior design, and can be estimated using approaches described next.

The travel of a restrained right front seat occupant relative to the vehicle $\delta_{p/v}$ inside the passenger compartment is one of the important parameters for determining the required vehicle crush distance in a frontal barrier impact. The amount of $\delta_{p/v}$ depends on the details of the instrument panel design (for the driver, it depends on the steering column design), and also the design of other

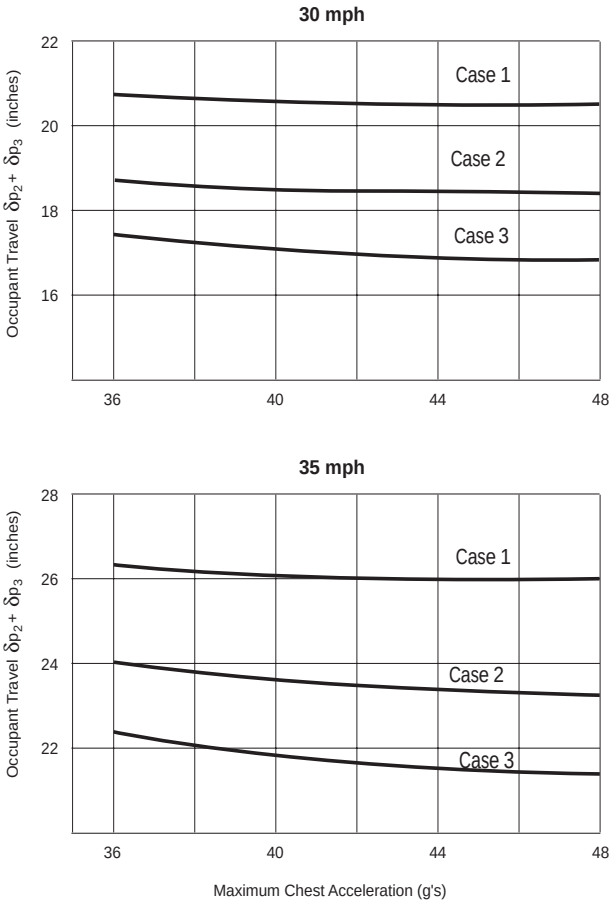

Fig. 4.8.1.3 **Occupant travel versus effectiveness time at 30 mph and 35 mph impact speeds**

components such as seat belts, anchorage and seats, which may not be available in the concept stage of design. A method for estimating $\delta_{p/v}$ *is sh*own in Figure 4.8.1.4 — $\delta_{p/v}$ from Head to Windshield Distance, based on the distance between the occupant's head and the windshield along the vehicle's longitudinal axis. However, observations of motion of a restrained dummy occupant with belt only in a frontal barrier impact show that in most cases the dummy head does not contact the windshield, but may contact the instrument panel in a combined

translational and rotational motion. In such cases, $\delta_{p/v}$ *is es*timated as shown in Figure 4.8.1.5 - $\delta_{P/V}$ from Torso CG Translation and Rotation, based on the outline of the instrument panel and the dummy torso center of gravity from its translation and rotation kinematics when the head contacts the instrument panel. For estimating $\delta_{p/v}$ for the driver, a method given by Newland et al [12] can be used.

4.8.2 Sine-Wave Chest Deceleration Model for Belted Occupant Response

In this model, the belted occupant is simulated by one mass-linear spring system subjected to a constant deceleration of magnitude equal to the vehicle ESW. The model and the parametric relationships are shown in Figure 4.8.2.1 -Sine-wave Belted Occupant Model. This model simulates only the belted right front passenger, and precludes the passenger from contact with the vehicle interior surfaces such as the glove compartment, front crash pad and windshield.

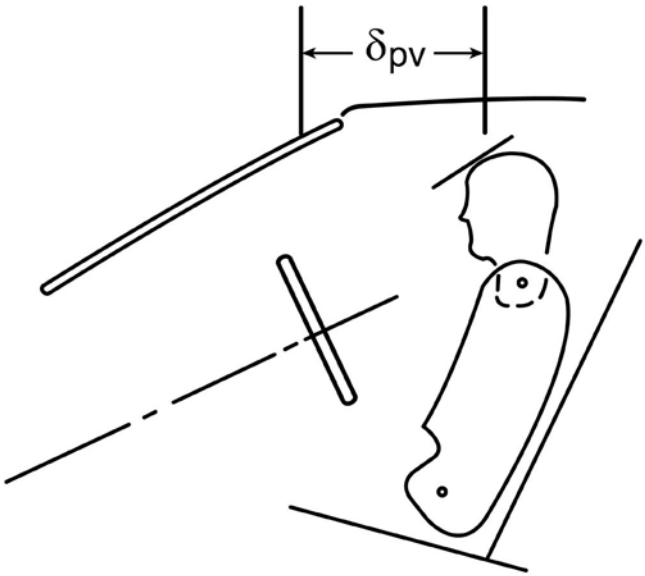

Fig. 4.8.1.4 **$\delta_{p/v}$ from head to windshield distance**

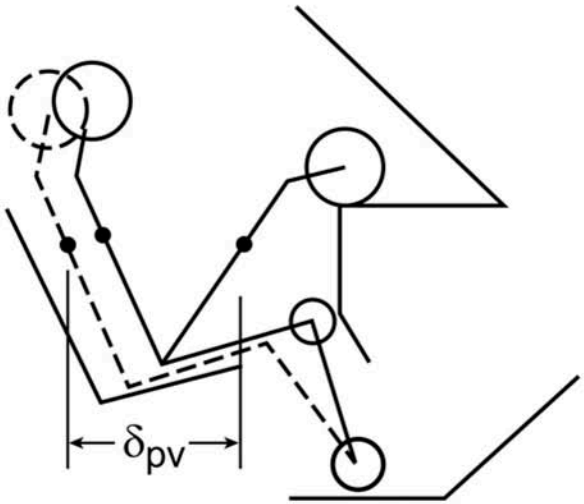

Fig. 4.8.1.5 **$\delta_{p/v}$ from torso CG translation and rotation**

Table 4.8.2.1 **Parameters for vehicle/occupant system analysis -- sine-wave belted case**

The analysis of thie vehicle/ occupant impact dynamics was carried out by Huang [11], who prescribed the equations of motion for both the vehicle and occupant. The solution to the equations of motion are given below, along with the occupant response in terms of four parameters, namely, impact velocity, ESW, and natural frequendy and slacks of the restraint system.

Equation	**Notion**
$ESW = F / W_v$	*ESW*: Equivalent square wave Vehicle deceleration level, g.
$f = 3.127\sqrt{k / W_0}$	*F*: Vehicle structure force level, lb.
$\ddot{x}_0\big\|_{t_1} = ESW$	W_v: Vehicle weight, lb.

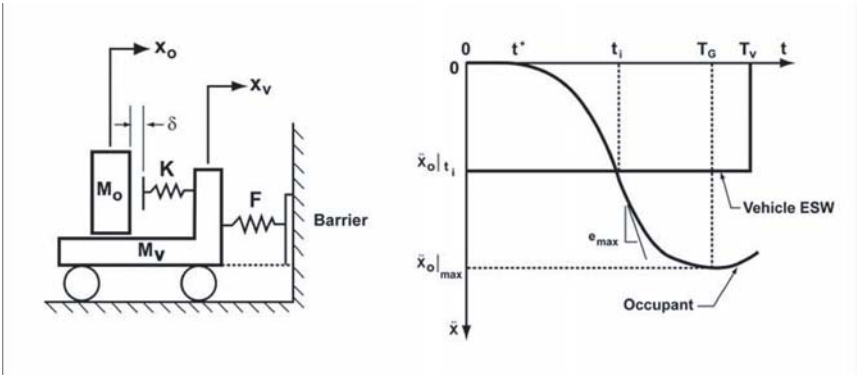

Fig. 4.8.2.1 **Sine-wave belted occupant model**

$$e_{\max} = 2\pi\left(\ddot{x}_0\big|_{\max} - ESW\right)$$

$$\ddot{x}_0\big|_{\max} = ESW\left[1+\sqrt{1+\left(2\pi f t^*\right)^2}\right]$$

$$t^* = 0.072\sqrt{\delta / ESW}$$

$$t_i = t^* + \frac{1}{2\pi f}\tan^{-1}\left(\frac{1}{2\pi f t^*}\right)$$

$$t_v = 0.0456 v_0 / ESW$$

$$\tau_G = t^* + \frac{\pi + \tan^{-1}\left(2\pi f t^*\right)}{2\pi f}$$

k: Restraint system stiffness, lb/ in.

W_o: Effective occupant weight, lb.

f: Occupant-restraint natural frequency, Hz.

$\ddot{x}_0\big|_{t_1}$: Occupant deceleration at t_i, g.

t_I: Time at which e_{max} occurs (inflection time), sec.

e_{max}: "maximum" onset rate of the occupant deceleration, g/sec.

$\ddot{x}_0\big|_{\max}$:"maximum" occupant deceleration, g.

t_e: Maximum onset rate intercept time, s.

$\dot{x}_{or}^{*} = 1.58\sqrt{\delta ESW}$

t*: Occupant-restraint contact time, sec.

$\ddot{x}_{0v}\big|_{\max} = 3..5\left((ESW)/f\right)\sqrt{1+\left(2\pi f t^{*}\right)^{2}}$

δ: restraint system slack, in.

T_v: Time at which maximum vehicle deformation occurs, sec.

$=0.556\ e_{max}/f^2$

V_o: Initial vehicle-barrier impact velocity, mph

$f = 3.127\sqrt{\ddot{x}_o\big|_{\max}\left(x_{ov}-\delta\right)}$

τ_G: Time at which occurs, sec.

$ESW = \left(\ddot{x}_o\big|_{\max}\right)^2 / \left(0.204\delta f^2 + 2\ddot{x}_o\big|_{\max}\right)$

$\dot{x}_{or}^{*}$: Occupant restraint relative contact velocity, mph.

$x_{vm} = 0.4V_o^2 / ESW$

$\ddot{x}_0\big|_{\max}$: Maximum occupant-vehicle relative velocity, mph.

$t_0 = t_i - \dfrac{ESW}{\left|e_{\max}\right|}$

x_{ov}: Occupant-vehicle interior travel, in.

x_{vm}: Maximum vehicle deformation, in.

t_o: Maximum onset rate intercept time, sec.

4.8.3 Constant Deceleration Model for Vehicle Response (ESW)

This model assumes that the vehicle deceleration remains constant during vehicle crush, namely, $A_v = constant = ESW$.

The vehicle velocity-time and crush-time histories are given by the following equations:

$$V(t) = V_0 - A_v t \tag{4.8.3.1}$$

$$X_v = V_0 t - \frac{1}{2} A_v t^2 \tag{4.8.3.2}$$

The time when the vehicle stops T_v and the maximum vehicle dynamic crush δ_v can be obtained from Eqs. (4.8.3.3) and (4.8.3.4), respectively.

$$T_v = V_0 / A_v \tag{4.8.3.3}$$

$$\delta_v = \frac{1}{2} V_0 T_v \tag{4.8.3.4}$$

Rewriting Eqs. (4.8.3.3) and (4.8.3.4) yields a useful expression:

$$A_v = 0.4 \frac{V_0^2}{\delta_v} \tag{4.8.3.5}$$

where V_0 is in mph, δ_v is in inches and A_v is in g's.

Eqs (4.8.3.3) and (4.8.3.4) are used to calculate the time T_v and the crush distances δ_v required to stop the vehicle during a frontal barrier impact from initial speeds V_0 of 30, 35, and 40 mph, assuming a constant deceleration A_v of 16 g's to 24 g's. The results are shown below: (Table 4.8.3.1)

4.9 Ride-Down Concept and Application

Ride-down, as mentioned in Section 4.6 – Vehicle/Occupant Velocity Profiles, is a mechanism whereby the occupant is in contact with the vehicle interior before the vehicle velocity approaches zero. This is advantageous for possible reduction of occupant loads by ride-down since the second collision occurs at a lesser relative velocity than that would have occurred when the vehicle is completely

Table 4.8.3.1 **Time and crush distances required to stop a vehicle for fontal impact**

A_v		30 mph		35 mph		40 mph	
g's	ft/sec^2	$T_v$ms	$\delta_v$in	$T_v$ms	$\delta_v$in	$T_v$ms	$\delta_v$in
16	515.2	85.4	22.5	99.63	30.67	113.8	40.09
18	579.6	75.91	20.04	88.56	27.28	101.23	35.63
20	644	68.32	18.04	79.71	24.55	91.10	32.07
22	708.4	62.11	16.40	72.46	22.32	82.82	29.15
24	772.8	56.94	15.03	66.42	20.46	75.92	26.72

stopped. Using the *ESW* concept, the mechanism of ride-down can be illustrated as follows:

Let A_v be an *ESW* vehicle deceleration;
V_o be the vehicle impact velocity;
δ_v be the vehicle dynamic crush or stopping distance;
V_r be the relative velocity between the occupant and vehicle interior or the ride-down velocity;
δ_{occ} be the initial spatial distance between the occupant and vehicle interior;

then, the time for vehicle to stop is:

$$t_v = \frac{V_o}{A_v} \tag{4.9.1}$$

The time of occupant contacting the interior is:

$$t_c = \sqrt{\frac{2\delta_{occ}}{A_v}} \tag{4.9.2}$$

For ride-down benefit, it is required that:

$$t_v > t_c \tag{4.9.3}$$

From the above equations, it is then required that:

(4.9.4)

Noting that $\delta_v = V_o^2/2A_v$, Eq. (4.9.4) reduces to

$$\delta_v > \delta_{occ} \tag{4.9.5}$$

Eq. (4.9.5) indicates that interior space must be less than the vehicle crush in order to achieve possible ride-down. The relative velocity of the occupant to the vehicle interior at time t_c is:

$$V_r^2 = 2A_v\delta_{occ} \tag{4.9.6}$$

Since $A_v = V_0^2/(2\delta_v)$, the relative velocity V_r can then be expressed in terms of δ_v and δ_{occ} as:

$$V_r = V_0\left(\frac{\delta_{occ}}{\delta_v}\right)^{\frac{1}{2}} \qquad \frac{V_o^2}{2A_v} > \delta_{occ} \tag{4.9.7}$$

Some interesting remarks can be made upon reviewing Eq. (4.9.7):

- If $d\delta_{occ} > d\delta_v$, the occupant impacts the vehicle interior when the vehicle is stopped or is in rebound. It is then possible that the second collision velocity may be equal to or greater than the initial impact velocity.
- The second collision velocity varies as the square root of the ratio of $d\delta_{occ}/d\delta_v$. Note that $d\delta_v$ is a function of A_v and V_r.

The above ride-down analysis is based on an *ESW* approach. More rigorous analyses of occupant ride-down are given by Maeda et al [13], Matsui [14], Huang and Loo [15] and Katoh and Nakahama [16]. In a recent publication by Huang [17], more discussions and applications can be found. The analysis is summarized below:

Let the occupant mass be m_o, the vehicle mass be m_v, the occupant position at time t be $x_o(t)$, and the vehicle position at time t be $x_v(t)$. When the occupant undergoes a deceleration of $a_o(t)$, the occupant's impact energy absorbed is:

$$E_0 = \int_0^t m_0 a_0(t) dx_0(t) \tag{4.9.8}$$

Let

$$s(t) = x_0(t) - x_v(t) \tag{4.9.9}$$

then, Eq. (4.9.8) can be rewritten as:

$$E_0 = \int_0^t m_0 a_0 ds(t) + \int_0^t m_0 a_0 dx_v(t) \tag{4.9.10}$$

where $E_0 = \frac{1}{2} m_0 v_0^2$. Note that $s(t)$ is the occupant displacement relative to the vehicle, and represents the occupant stroke into a restraint system.

In Eq. (4.9.10), the occupant energy to be dissipated can be divided into two parts: energy absorbed by the restraint system as represented by the first integral, and energy dissipated by the ride-down with the vehicle as indicated in the second term. If the restraint system can be represented as a linear spring with a stiffness k, then the first integral in Eq. (4.9.10) becomes:

$$\int_0^t m_0 a_0 ds(t) = \int_0^\delta ks ds = \frac{1}{2} k\delta^2 \tag{4.9.11}$$

where δ is the maximum stretch of the restraint system.

Let the ride-down efficiency, η_{Rd}, be defined as the ratio of the energy absorbed by the ride-down to the total kinetic energy of the occupant. Mathematically, it can be expressed as:

where v_0 is the initial vehicle velocity. Similarly, the restraint-system efficiency can be defined as:

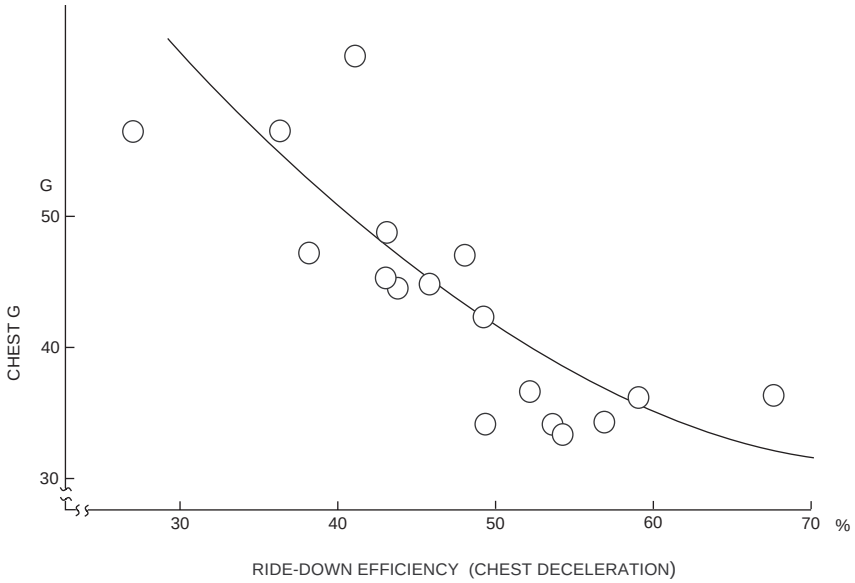

Fig. 4.9.1 **Passenger chest g and ride-down efficiency**

$$\eta_{RS} = \int_0 m a_0 \, d(st) / E_0 \qquad (4.9.13)$$

The expression given by Eq. (4.9.12) provides an indicator for relative evaluation between crashes under a combined performance of the vehicle structure and the occupant restraint system. The same ride-down efficiency may be due to a combination of different vehicle crashes and various restraint system characteristics.

Based on 35 mph collision tests in NCAP by NHTSA, Katoh and Nakahama [16] calculated the ride-down efficiency using Eq. (4.9.12) by substituting $a_o(t)$ with the A_p component of the occupant chest deceleration. These results are shown in Figure 4.9.1 – Passenger Chest g and Ride-down Efficiency. It can be seen that the occupant chest deceleration decreases as the ride-down efficiency increases.

On the basis of the ride-down mechanism described above, the ride-down efficiency is the ratio of ride-down energy to the initial occupant kinematic energy, an indicator for a combined effect of both vehicle structure and restraint system. It would be beneficial if the effect of the vehicle structure and the restraint system could be estimated and/or indicated separately. According to Katoh and Nakahama [16], the ride-down efficiency can be decomposed to one that concerns vehicle structure and the other that relates to restraint system. To accomplish this, a mathematical occupant simulation model can be used. The efficiency that concerns the vehicle structure is determined when the simulated system of the vehicle is subjected to collision with a standard restraint system (keeping δ, g_0 constant, using various harmonic reconstructed pulses). The efficiency associated with the restraint system can be obtained using the method described by Katoh and Nakahama [16].

A design chart developed by Katoh and Nakahama [16] is useful in such an analysis. One can develop a similar design chart for application by taking current restraint system performance parameters into consideration. Huang and Loo [15] also demonstrated their method in determining the ride-down efficiency using data obtained from frontal barrier crash tests on trucks and cars. They also used a simple occupant-vehicle impact model to study the ride-down efficiency of an occupant with a knee bolster system. A chart pertaining to ride-down efficiency and femur acceleration, which is related to force, are constructed as a function of vehicle dynamic crush and the stiffness of the instrumental panel (I/P.) Using these charts for practical design, an optimal I/P stiffness can be selected for a given force level and vehicle dynamic crush with a desired ride-down efficiency. Using CAE analysis, Lu et al [18] adopted this methodology to an investigation of occupant energy management by I/P structure during vehicle frontal crashes.

4.10 Design Methodology

Restraint systems designed for automotive occupant safety require the application of practical knowledge as presented in Section 4.3 – Basic Laws and Concepts of Motion, and specific design rules. Most automobile manufacturers have established their respective safety design guidelines incorporating the FMVSS standards for their product developments. Many of these guidelines are of proprietary nature and cannot be found in the open literature. However, design methodology for safety can be developed by a traditional method through trial-and-error testing or an emerging analytical approach using methodology via Computer Aided Engineering (CAE).

4.10.1 Traditional Method

In a traditional fashion, Patrick [2] outlined a generic systematic approach to a safety design, assuming a given vehicle structure, with the following steps:

- Establish the specifications for the safety design including crash modes and impact velocities.
- Establish dummy performance numbers pertaining to FMVSS to be met.
- Estimate the occupant stopping distances for the established tolerance levels based on the dummy performance numbers.
- Study the vehicle to obtain the total available stopping distance. This will include the front-end crush, side crush and roof crush if all the conditions are to be included in the design. The interior space and crush distance for the interior components must also be determined. The deceleration pulse shape for the vehicle for the collisions under consideration should be obtained from barrier crash tests and the displacement- and velocity-time curves calculated from the record. Other helpful data include the relative velocity and displacement of the occupant with respect to the vehicle in the unrestrained condition. Note that this also can be done using Restrained Occupant Response Analysis tool given in Section 4.8– Vehicle / Occupant velocity profiles (Analytical Approach).
- Compare the distance available from Step 4 with the distance from Step 3. This comparison will determine how efficient the use of the stopping distance must be, and will, in some cases, determine the type of restraint system to be incorporated. This is discussed in the compatibility between restraint system and vehicle front-end structure presented in Section 4.7 – Compatibility Between Restraint System and Vehicle Front Structure.
- Decide on the basic safety system to be incorporated into the vehicle. Depending upon the conditions, this could be EA material cushioning (or padding), a conventional belt system, belt systems with load limiter and/or pretensioner, a supplemental airbag restraint system, smart restraint systems, or even combinations of these.
- Calculate the performance requirements for each component. If the belt restraint system is to be utilized, the stiffness of the webbing and the anchor points must be determined together with the forward motion of the occupant under the loading conditions.
- Design the system based on the calculated performance requirements and the type of system chosen.
- Build a prototype restraint system for impact sled testing.
- Conduct sled tests to determine whether adequate/satisfactory performance has been achieved. Modify the prototype system as required to improve the system performance.
- Install a built prototype in a vehicle for prove-out testing.
- Conduct barrier crash tests and evaluate the results to assess whether the

prototype system meets the performance requirements. Modify, if necessary, and continue testing and modification until the system functions satisfactorily.

Again, it should be emphasized that the above design steps are generic and will vary from design to design and with guidelines established by individual manufacturers. Restraint system design engineers must modify the necessary steps to make the procedure fit their specific requirement accordingly.

The traditional method, which requires part fabrication, testing, and further refinement, is generally too cumbersome and time-consuming for providing design direction in the development stage. As an example, to meet FMVSS test requirements the concept phase of car development could include:

- 2 car lines
- 2 impact speeds: 30 mph FMVSS 208 and 35 mph NCAP (New Car Assessment Program conducted by NHTSA to provide consumers safety information on new cars);
- 3 different restraint systems (3-point belt, airbag and combination);
- 2 powertrain types;
- 2 weight conditions (the lightest and the heaviest).

This requires a total of 48 combinations of restraint systems and possible vehicle configurations to be tested for design directions. This testing will be labor intensive, time-consuming and costly. To reduce the number of tests, computer simulation technology or computer aided engineering (CAE) can be employed for rapid evaluation and iteration of designs to drive the safety design development process.

4.10.2 CAE Methods

Computer simulation provides a means of expanding the study of automotive safety-related issues. In CAE methodology development process, some test results will be used for developing vehicle structural and restraint simulation models. For example, static front-end component crush tests and non-linear finite element analysis can be used to develop lumped-mass structural models for various vehicle configurations. Results from sled tests with instrumented dummies can be used to develop dummy occupant simulation models with various restraint systems.

Computer models can simulate the structural response to a crash event. There are also computer models that can simulate the dummy occupant response to a crash event. These models separately simulate the structural crash performance from the dummy response, whereas, in actual crash event, these response occur concurrently. With a rigid body or FEA method, combined structural/occupant simulation models are now available for predicting the dummy occupant response to vehicle interior contact with or without compartment intrusion during frontal impacts. This system approach through "computer" testing becomes a more design-driven analytical tool in the design of safety restraint systems by automobile manufacturers and suppliers. More detailed analytical methods are described in Chapter 5: Design Tools: Human Body Modeling.

4.11 Conclusion

In today's quest for continued improvement in automotive safety, various restraint systems have been developed to provide occupant protection in a wide variety of crash environments under different directions and conditions. It is extremely difficult, and of course not attempted here, to present rigorous mathematical treatments to cover occupant kinematics in complicated real world situations. In this Chapter, some fundamental principles of dynamics are presented and applied to examples with primary discussions on the vehicle/occupant response in frontal impact analysis only, even though side crash events are lightly touched upon.

The performance of a restraint system depends on vehicle structural performance. The compatibility between restraint system and vehicle front structure given in Section 4.7 – Compatibility between Restraint System and Vehicle Front Structure addresses the importance of this aspect. A given restraint system that performs well with specific vehicle front-end structural characteristics may not yield an identical performance with different vehicle structures during a similar crash. The method presented in this chapter allows conceptual studies of both the restraint system and vehicle crash pulse in an ideal one-dimensional analysis of dynamics using basic principles presented in Section 4.3 – Basic Laws and Concepts of Motion. These principles can be applied to study occupant responses in nearly all directional types of impact, such as frontal, side, and rear, with respect to the magnitude of velocity change of occupant, the rate of change in velocity, and how the change in velocity is accomplished. For more complicated analysis of occupant and vehicle structural responses, mathematical models using either rigid-body-based programs (MADYMO[19], ATB[20], for example) or deformable-

body-based non-linear finite element codes (LS-DYNA[21], PAM-CRASH[22], RADIOSS[23], for example) are currently used among auto manufacturers in design of advanced/ smart restraint systems for impact safety protection of occupants.

4.12 Acknowledgments

The author would like to thank the following individuals:

Mr. B. B. Fileta for discussing occupant/restraint models
Dr. Rolf Eppinger for the use of some of his axioms in this chapter

4.13 References

1. Prasad, P. and Chou, C.C., "*A Review of Mathematical Occupant Simulation Models*," Chapter 6, Accident and Injury - Biomechanics and Prevention, edited by A. M. Nahum and J. W. Melvin, Verlag-Springer, 1993.

2. Patrick, L.M., "Human Tolerance to Impact and Its Application to Safety Design," Biomechanics and Its Application to Automotive Design, SAE Publication P-49, Jan. 1973.

3. Chou, C.C., and Nyquest, G. W., "Analytical Studies of the Head Injury Criterion (HIC), " SAE Paper No. 740082, 1974.

4. Huang, M., Lawson, G. P., Powell, B. K and Walker, J. H., "Characterization of Vehicle Deceleration Time Histories in the Analysis of Impact Dynamics," SAE Paper No. 770013, 1977.

5. Chou, C. C., and Lim, G. G., "Characterization of Vehicle Deceleration Using Harmonic Analysis," The 20th FISITA Conference, 1988.

6. Eppinger, R., "*Occupant Restraint Systems*," Chapter 8, Accident Injury - Biomechanics and Prevention, Edited by A. M. Nahum and J. W. Melvin, Springer-Verlag, 1993, pp. 186 - 197.

7. Lim, G. G., Prasad, P., Chou, C. C., Walker, L. A., Sundararajan, S., Fletcher, F. D. and Chikola, J. A., "Development of The Deployable Door Trim

System," An addendum of the proceedings, Automotive Body Interior & Safety Systems, Vol. 23, IBEC, Oct. 1-3, 1996, Detroit.

8. Hobbs, C. A., "Dispelling the Misconceptions about Side Impact Protection," SAE Paper No. 950879, 1995, Detroit.

9. Hofferberth, J. E. and Tomassoni, J. E., "A Study of Structural and Restraint Requirements for Automobile Crash Survival," Proceedings of the Third International Congress on Automotive Safety, Vol II, pp. 28-1 to 28-88, 1974.

10. Chan, C. "Fundamentals of Crash Sensing," SAE Seminar Video Tutorial, available through Professional Development Division, call (724) 772-7148.

11. Huang, M., "An Analysis of the Vehicle-Occupant Impact Dynamics and Its Application," SAE Paper No. 830977, 1983.

12. Newland, C., Scheffel, G., Armstrong, M. and Seyer, K., "A Scientific Method for Analyzing Vehicle Safety," The 16th International Technical Conference on Experimental Safety Vehicle, June 1-4, Windsor, Canada, 1998, Paper No. 98-S11-O-05.

13. Maeda, T., Irie, N. and Sato, S., "On the Occupant Crash Protection System of the Nissan ESV," SAE Paper No. 730589, 1973.

14. Matsui, S., "A Method of Estimating the Crashworthiness of Body Construction," 6th Experimental Safety Vehicles, pp. 302 - 309.

15. Huang, M. and Loo, M., "A Study on Ride-Down Efficiency and Occupant Responses in High Speed Crash Tests," SAE-SP-1077, SAE Paper No. 950656, 1995.

16. Katoh, H. and Nakahama, R., "Study on the Ride-Down Evaluation," 9th International Technical Conference on Experimental Safety Vehicles, 1982, Kyoto.

17. Huang, M., Vehicle Crash Mechanics, CRC Press, 2002, pp. 67-83.

18. Lu, D., Riley, J., Schleicher, G. and Jurosek, M., "An Investigation of Occupant Energy Management by I/P Structures During Vehicle Frontal

Crash," AMD-Vol. 210/BED-Vol. 30, Crashworthiness and Occupant Protection in Transportation Systems, ASME, 1995.

19. MADYMO User's Manual, Version 5.1, TNO Department of Injury Prevention, TNO Road-Vehicle Research Institute.

20. Fleck, J. T. and Butler, F. E., "Validation of Crash Victim Simulator: Vol. 1 - Engineering Manual - Part I: Analytical Formulation, Department of Transportation Report No. DOT-HS-806-279, Dec. 1981; Vol. 2 - Engineering Manual - Part II : Validation Effort, Department of Transportation Report No. DOT-HS-806-280, Aug. 1982.

21. Hallquist, J. O., "LS-DYNA Theoretical Manual", Livermore Software Technology Corporation, 1998.

22. PAM-Crash Reference Manual, Version 2001, PAM System International.

23. RADIOSS Input Manual, Version 3.1, 01/1996, Mecalog Sarf, France.

Additional References:

24. Strother, C. E., and Morgan, R. M., "The Efforts of the National Highway Traffic Safety Administration in the Development of Advanced Passive Protection Systems and Child Restraint Systems," Third International Conference on Occupant Protection, SAE Conference Proceedings P-53, 1974, pp. 246-267.

25. Lau, I. V., Capp, J. C. and Obermeyer, J. A., "A Comparison of Frontal and Side Impact: Crash Dynamics, Countermeasures and Subsystem Tests," The 35th Stapp Car Crash Conference, Proceedings, SAE P-251, 1991, pp. 109-124. (SAE Paper No. 912896).

26. Horsch, J. D., Viano, J. C. and Decou, J., "History Safety Research and Development on the General Motors Energy-Absorbing Steering System," The 35th Stapp Car Crash Conference Proceedings, SAE P-251, pp. 1-46. (SAE Paper No. 912890).

27. "Focus on Passive Safety," Automotive Engineer, October/November 1996, pp. 42-54.

28. Agelidis, N. and Chou, C. C., "Parametric Study of the Effect of Crash Pulse Shape on Dummy Response using MADYMO," 1991 ASME Winter Annual Meeting.

29. Prasad, P., "Side Impact Simulation Study for Door Bolster Requirements," Report prepared for Advanced Safety and Structures Technology Department, Vehicle Development Technology, March 31, 1980.

30. Suzuki, N., Sonoda, Y., Takahashi, K., Suzuki, T., Tawarayama, T. and Dokko, Y., "Optimization of Vehicle Deceleration Curves for Occupant Injury," JSAE Conference Proceedings 924, 1992-10. Paper No. 924024.

31. DuWaldt, F. A., "Matched Driver Restraint Systems," SAE Paper No. 730974.

32. Johnson, P.R. and Wiltse, W. E., "Front Structural Strength as It Affects Occupant Injury-Reduction and Survival," Proceedings of the General Motors Corp. Automotive Safety Seminars, Milford, Michigan, July 11-12, 1968.

33. Aljundi, B., Skidmore, M., Poeze, E. and Slaats, P., "Occupant Safety Simulations for Interior Design," Proceedings of the 35th Annual Symposium, SAFE Association, Phoenix, Arizona, Sept. 8-10, 1997, pp. 390-404.

34. Martin, C. E. and Kroell, C. K., "Influence of Vehicle Crush Distance, Occupant Spacing, and Interior Crush Stiffness on Severity of Occupant-Interior Impact," SAE Paper No. 670034, 1967.

Design Tools: Human Body Modeling

Jac Wismans

5.1 Introduction

In crash safety research and development, like in many other engineering disciplines, a significant increase could be observed during the last thirty years in the use of computer simulations. This is due in part to the rapid developments in computer hardware and software. In the case of automotive safety, it may be due even more to the emphasis placed on the development of reliable models describing the human body in an impact situation, as well as numerous validation studies conducted using these models. Mathematical models of the human body, in conjunction with a mathematical description of the vehicle structure and the various safety provisions and restraint systems, appear to offer a very economical and versatile method for the analyses of the crash responses of complex dynamic systems.

In the crash safety field, mathematical models can be applied in practically all areas of research and development including:

- reconstruction of actual accidents,
- computer aided design (CAD) of the crash response of vehicles, safety devices and roadside facilities, and
- human impact biomechanics studies.

Furthermore, computer simulations may be part of safety regulations, much like standard crash tests.

Depending on the nature of the problem, several types of crash analysis programs have been developed, each with its own, but often overlapping, area of applicability. Most models are of the deterministic type. That is, the outcome of the crash event is predicted based upon measured or estimated parameter values, representing characteristics of the human body, safety devices, the vehicle and its surroundings, using well-established physical laws. Statistical models are

also used in the study of crash safety. Statistical models are used in injury biomechanics research to assess the correct relationship between loading conditions and resultant injuries by means of regression type of equations (the so-called injury risk function). This chapter will concentrate on deterministic models for the human body.

Although the various deterministic models may differ in many aspects, all are dynamic models. The models account for inertial effects by deriving equations of motions for all movable parts, and solving these equations using an iterative method. The mathematical formulations used for these models can be subdivided into lumped mass models, multi-body models and finite element models. Lumped mass models are usually one- or two-dimensional, multi-body models two- or three-dimensional and finite element models are usually three-dimensional.

5.1.1 Lumped Mass Models

In a lumped mass model, a system is represented by one or more rigid elements often connected by mass-less elements like springs and dampers. An example of a lumped-mass model is shown in Figure 5.1.1.1. It is a one-dimensional model of the human thorax developed by Lobdell in 1973 [1]. This model simulates the thorax response in case of loading by an impactor. The model consists of rigid bodies with masses *m1*, *m2* and *m3* connected by springs and dampers. Mass *m1* represents the impactor mass and masses *m2* and *m3* the sternal and vertebral effective mass. Spring k_{12} represents the skin and flesh between impactor and sternum. The internal spring and dampers represent the connection between sternum and thoracic

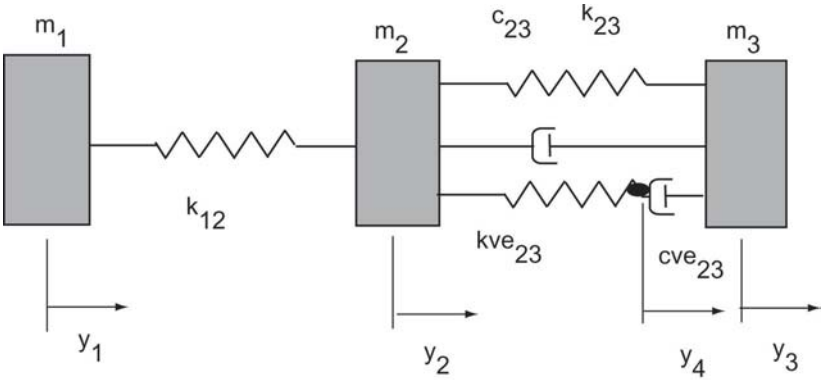

Fig. 5.1.1.1 **Example of lumped mass model: the Lobdell thorax model [1]**

spine. The response of this model was shown to correlate well with human cadaver tests.

5.1.2 Multi-Body Models

The most important difference between a lumped mass model and a multi-body model is that elements in a multi-body formulation can be connected by various joint types through which the number of degrees of freedom between the elements can be constrained. A lumped mass model can be considered a special case of the more general multi-body model formulation. The motion of the joint-connected elements in a multi-body model is caused by external forces generated by so-called force-interaction models. Examples of force-interaction models in a multi-body model for crash analyses are the models to account for an acceleration field, spring-damper elements, restraint system models and contact models. Another characteristic of lumped mass models is that in a multi-body formulation, instead of rigid bodies, flexible bodies can be specified.

The first example of a multi-body model is presented in Figure 5.1.2.1. The model was developed in 1963 by McHenry [2]. The model, which represents the human body together with restraint system and vehicle, is two-dimensional and has degrees of freedom. The human body part of the model is characterized by rigid bodies representing thorax/head, upper arms, upper legs and lower legs. Simple pin joints connect the rigid elements. The values for the parameters in the model were estimated. McHenry compared his model calculations with experimental data to demonstrate the potential of this type of calculations. He was able to show quite good agreement for quantities including hip dis-placements, chest acceleration and belt loads.

A more recent example of a multi-body model is presented in Figure 5.1.2.2. It is a three-dimensional MADYMO model of a Chrysler Neon suitable for frontal collisions. The model was developed as part of a cooperative effort between the European Community and the United States' National Highway Traffic Safety Administration (NHTSA) to study vehicle compatibility issues [3]. The vehicle part of the model has more than 200 elements and includes a description of interior, restraint system, suspension, steering wheel, bumper, engine and hood. The human body part of the model is a 32-segment model of the Hybrid III dummy. Quite realistic results were obtained when the model results were compared with a rigid wall test and offset deformable barrier tests.

5.1.3 Finite Element Models

In a finite element model, the system to be modeled is divided into a number of finite volumes, surfaces or lines representing an assembly of finite elements.

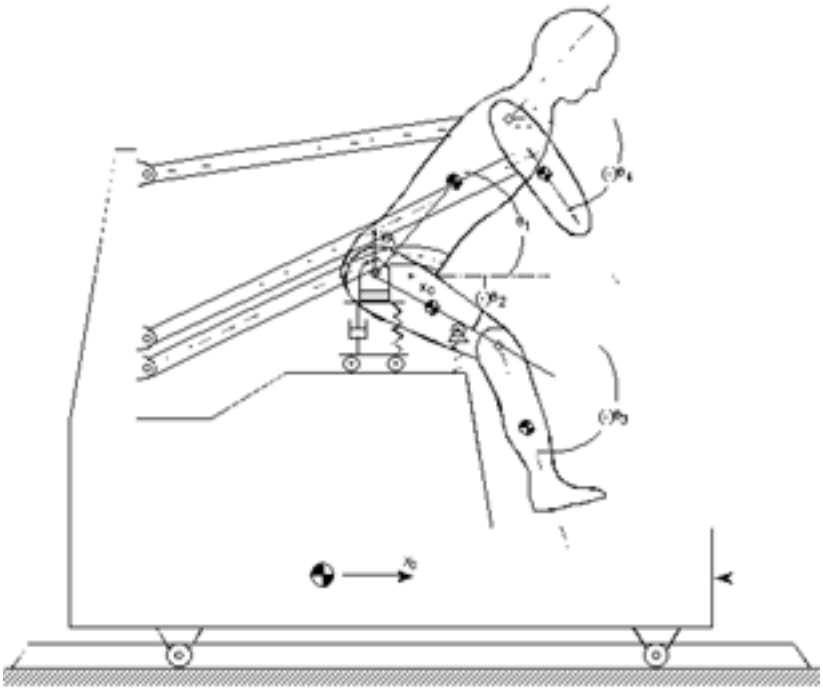

Fig. 5.1.2.1 **Example of multi-body model: 7 degrees of freedom model for frontal collisions by McHenry [2]**

These elements are assumed to be interconnected at a discrete number of points: the nodes. In the displacement-based finite element formulation, which is applied in practically all major finite element software packages, the motion of the points within each finite element is defined as a function of the motion of the nodes. The state of stress follows from the deformations and the constitutive properties of the material modeled. Figure 5.1.3.1 shows one of the earlier examples of using the finite element method for human body impact modeling: a model of the human head. The model was developed in the seventies by Shugar [4]. The model was 3-dimensional and included a representation of the skull and brain. Linear elastic and linear visco-elastic material behavior was assumed. Skull bone response and brain response from the model was compared with experimental results of head impact tests with primates.

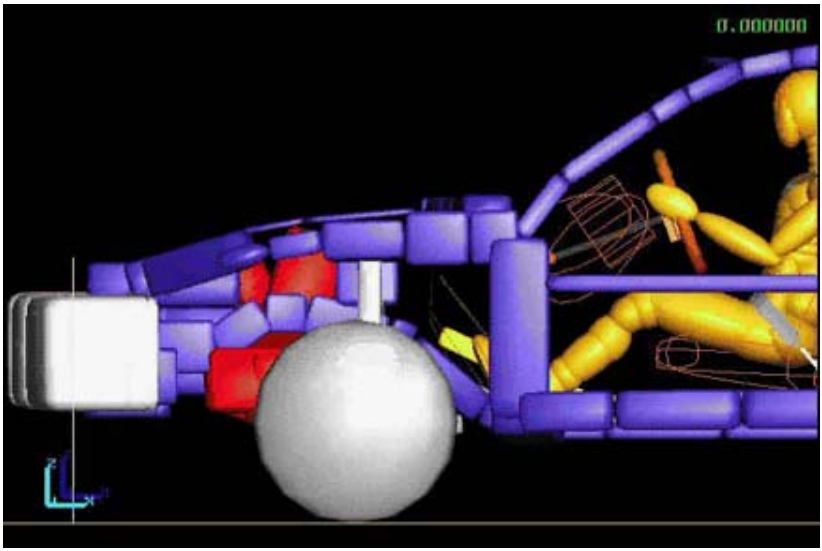

Fig. 5.1.2.2 **Example of multi-body model: 3-dimensional model for frontal collisions of Chrysler Neon with Hybrid III dummy [3]**

5.1.4 Multi-Body Models Versus Finite Element Models

Both the multi-body method and the finite element method offer specific advantages and disadvantages in case of crash analyses. The multi-body approach is particularly attractive due to its capability of simulating in a very efficient way complex kinematic connections as present in the human body and in parts of the vehicle structure like the steering assembly and the vehicle suspension system. The finite element method offers the capability of describing (local) structural deformations and stress distribution, which allows for the study of injury mechanisms in the human body parts. Usually much longer computer times are required to perform a finite element crash simulation than a multi-body crash simulation, making the finite element method less attractive for optimization studies involving many design parameters.

Figure 5.1.4.1 shows an example in which both the multi-body approach and the finite element approach are used. This integrated approach is sometimes referred to as "hybrid" approach. It is a model of a car occupant interacting with a passenger airbag developed in the eighties by Bruijs [5]. The airbag (and airbag straps) was modeled in the PISCES 3D-ELK program (now MSC-DYTRAN) using almost 2000 triangular membrane elements. The gas inside the airbag was described using the perfect gas law. The model takes into account leakage through airbag material and exhaust orifices.

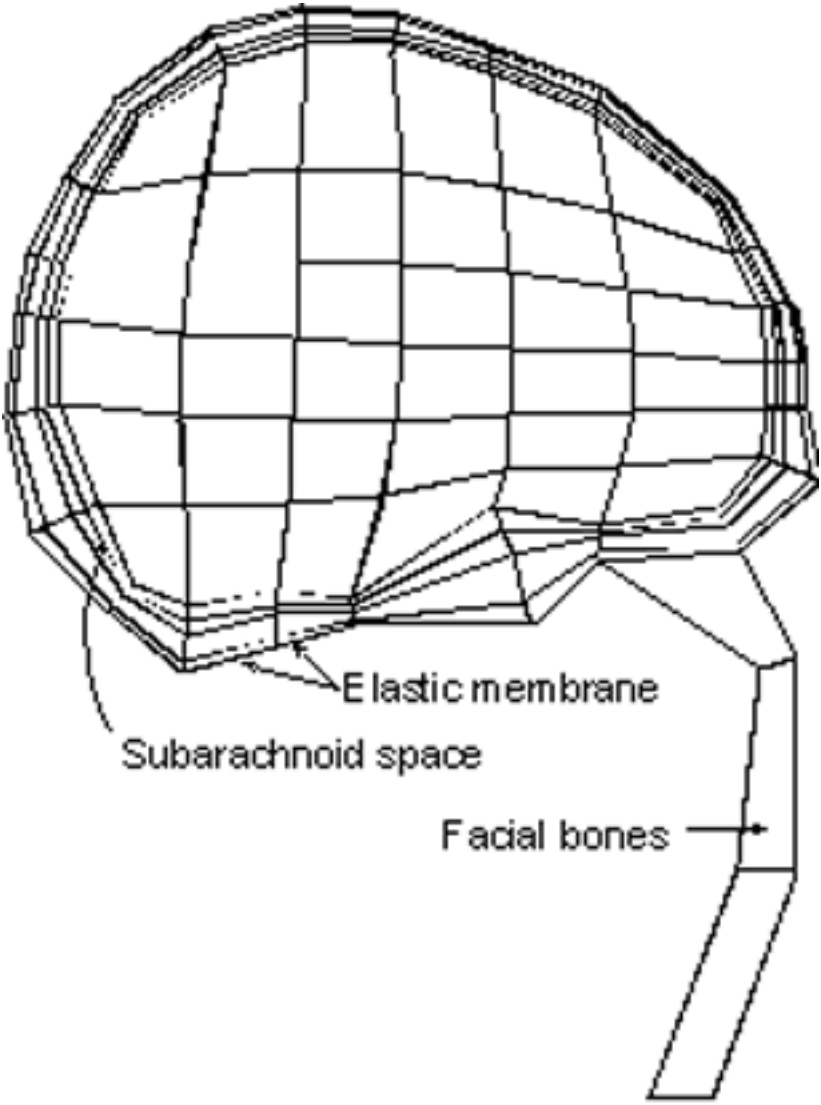

Fig. 5.1.3.1 **Example of a finite element model simulating the human body: a head model by Shugar [4]**

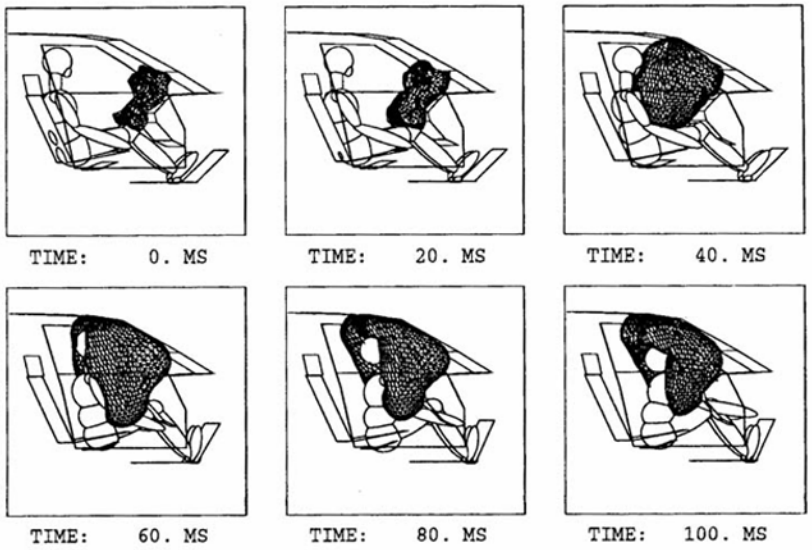

Fig. 5.1.4.1 **Example of an integrated multi-body finite element model: occupant-airbag interaction by Bruijs [5]**

The most important assumption in the airbag model is that the pressure and temperature in the airbag are constant and that inertia effects of the gas are neglected. The finite element airbag model interacts with a multi-body model of the Hybrid III crash dummy modeled in MADYMO 3D.

5.1.5 Chapter Outline

Multi-body models that simulate the complete human body for the purpose of crash analyses are often referred to as Crash Victim Simulation (CVS) models, human body gross-motion simulators or whole body response models. The theoretical basis for this type of model is presented in Section 5.2 – The Multi-body Method for Crash Analyses. The finite element method is assumed to be known here, so it will not be treated further except for the aspect of integrated multi-body finite element simulations in Section 5.2.5 – Integrated Multi-body Finite Element Simulations.

Human body models for crash analyses can be subdivided into models of crash dummies and models of the real human body. Section 5.3 – Crash Dummy Modeling, discusses some aspects of crash dummy models. Real human body models will

be presented in Section 5.4 – Modeling the Real Human Body. In Section 5.5 – Conclusion, future trends are discussed. Topics include model validation in view of the increasing importance of virtual testing.

5.2 The Multi-Body Method for Crash Analyses

5.2.1 Introduction

One of the first human body gross-motion simulation models was developed in 1963 by McHenry [2], see Figure 5.1.1.1. The results of this model were so encouraging that many more sophisticated models have since been developed. The most well known are the two-dimensional 8-segment MVMA-2D model and the three-dimensional 6-segment HSRI occupant model both developed by Robbins et al [6,7], the three-dimensional 12-segment UCIN model [8], and the three-dimensional Calspan 3D CVS (CAL3D), which allowed up to 20 elements [9]. For a review of the status of human body gross-motion simulators up to 1975, see King and Chou [10].

Two models, MVMA 2D and the CAL3D, have gone through extensive validation and development effort since 1975, and are still frequently used. An example of these developments is the ATB (Articulated Total Body) program, which is a special version of CAL3D for aircraft safety studies, developed by the Air Force Aerospace Medical Research Laboratory in Dayton [11].

This section is focused on a more recent program, MADYMO [12], which is a general multi-body/finite element program with a number of special features for crash analyses. The program was developed in Europe by TNO Automotive in Delft, The Netherlands. For a comparison of the basic features between MADYMO, MVMA2D and CAL3D, the reader is referred to reviews of gross-motion simulation programs by Prasad [13,14] and Prasad and Chou [15]. MADYMO has two- and three-dimensional versions referred to as MADYMO 2D and MADYMO 3D, respectively. This section will concentrate on the multi-body part and the force interactions in MADYMO 3D.

5.2.2 MADYMO Set-Up

MADYMO consists of a number of modules (Figure 5.2.2.1). The multi-body module of the program calculates the contribution of the inertia of bodies to the equations of motion. The other modules calculate the contribution of specific force elements such as springs, dampers, muscles, interior contacts and restraint systems or the effect of systems, which are represented as a finite element model. Special models are available for vehicle dynamic applications including tire models. A control module, which offers the ability to apply loads to bodies dependent on

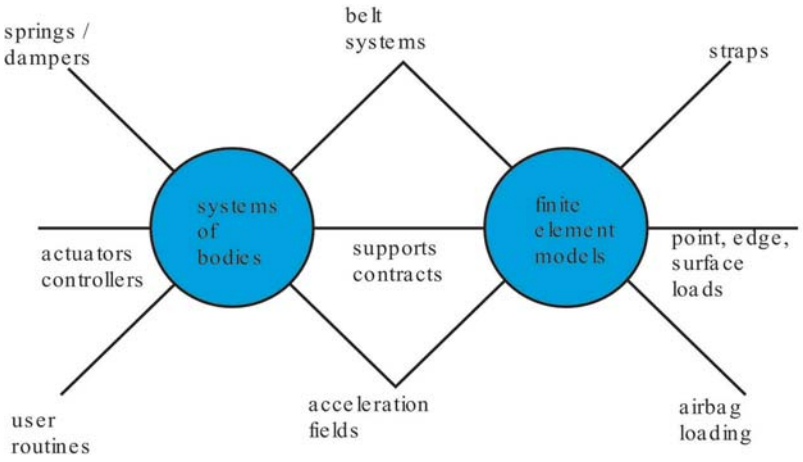

Fig. 5.2.2.1 **MADYMO modules**

the bodies' motions, is available. For this purpose, motion quantities can be extracted from the bodies by sensors. The sensor signals can be manipulated with summers, transformers and controllers, and used as input for actuators, which apply forces or torques to the bodies. In Section 5.2.3 – MADYMO Multi-body Algorithm, the multi-body algorithm is presented, and in Section 5.2.4 – Force Interaction Models, the most important force elements as used for crash analyses. The aspect of integrated multi-body/finite element analyses are introduced in Section 5.2.5 – Integrated Multi-body Finite Element Simulations .

5.2.3 MADYMO Multi-Body Algorithm

The multi-body module analyses the motion of systems of bodies. Bodies can be interconnected by kinematic joints such as spherical joints, revolute joints, universal joints, and translational joints. Moreover, new kinematic joints can be added by user subroutines

5.2.3.1 Topology of a System of Bodies

Consider a system of N bodies with a tree structure (Figure 5.2.3.1.1). A system of bodies has a tree structure if one can proceed from one arbitrary body to another arbitrary body along a unique sequence of bodies and joints. Systems with closed chains of bodies in it (for instance, a four-bar linkage system) are permitted in the later MADYMO versions. For topology specification the chains have to be reduced to a tree structure. The bodies are numbered to specify which bodies are interconnected. One of the bodies is chosen as the reference body and given

number 1. The other bodies are numbered from 2 to N so the numbers of the bodies on the path from the reference body to any other body are lower than the number of that specific body. The configuration of a system is completely defined by specifying for all bodies at the end of the tree (the peripheral bodies), the numbers of the bodies on the path to the reference body. The bodies on such a path form a branch. In the MADYMO input file, the configuration of a system is defined by entering for each branch the numbers of the bodies in decreasing order. This table with branch numbers is called configuration table. For the example in Figure 5.2.3.1.1 the configuration specification is:

Branch 1: 3 2 1
Branch 2: 7 2 1
Branch 3: 6 5 1
Branch 4: 8 4 1

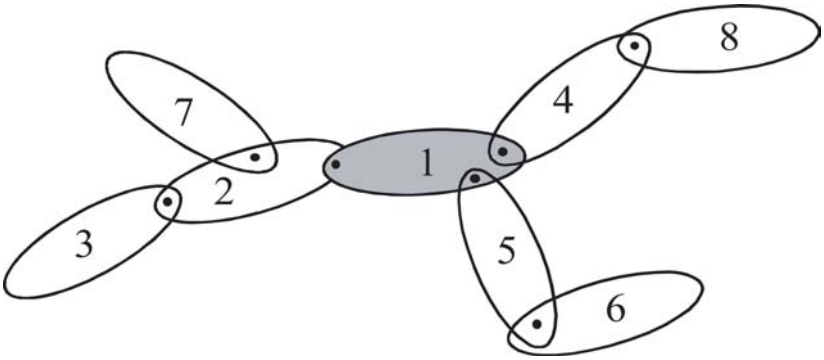

Fig 5.2.3.1.1 **Example of body numbering**

5.2.3.2 Kinematics of a Rigid Body

Consider the rigid body i shown in Figure 5.2.3.2.1 In order to describe its motion relative to an inertial space, a right-handed body-fixed base $\{\boldsymbol{e}\}_i$ is introduced. Its origin is chosen coincident with the center of mass, since the equations of motion of a single body then have their simplest form: the Newton-Euler equations. The motion of the body is defined by the position of the origin and the orientation of the body-fixed base relative to an inertial base $\{\boldsymbol{E}\}$.

The position of the origin of the body-fixed base relative to the origin of the inertial base is given by the vector $\boldsymbol{r}_i$. The orientation of the body-fixed base

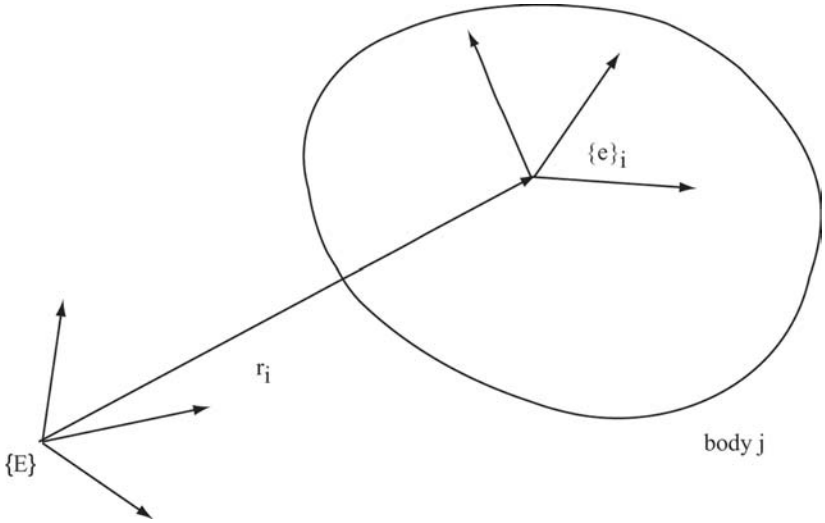

Fig. 5.2.3.2.1 **Specification of the motion of a rigid body**

relative to the inertial base is defined by the rotation matrix A_i. The elements of this matrix consist of scalar products of the inertial base vectors and the body-fixed base vectors.

5.2.3.3 Kinematics of a Flexible Body

In later versions of MADYMO 3D, bodies that experience small deformations can be modeled as flexible bodies. For a flexible body, the motion of a point on a body is considered to be composed of a rigid body motion and a superimposed motion due to the deformation. The motions of the body due to the deformations are approximated by a linear combination of predefined displacement and rotation fields (deformation modes). Only at certain pre-defined points in the body (the nodes), the deformation nodes are defined.

5.2.3.4 Kinematics of a Pair of Bodies Connected by a Joint

A pair of bodies connected by an arbitrary kinematic joint is shown in Figure 5.2.3.4.1. A kinematic joint as defined here can connect only two bodies. The bodies are named *i* and *j*. The number of the lower numbered body, *i,* can be obtained from the configuration table. In MADYMO, the motion of a body, *j*, is described relative to the corresponding lower numbered body, *i*. This is done in terms of quantities that define the motion within the joint, the joint coordinates. Their number, $n_{ij,}$ equals the number of degrees of freedom of the joint. The numbers are placed in the column matrix q_{ij}.

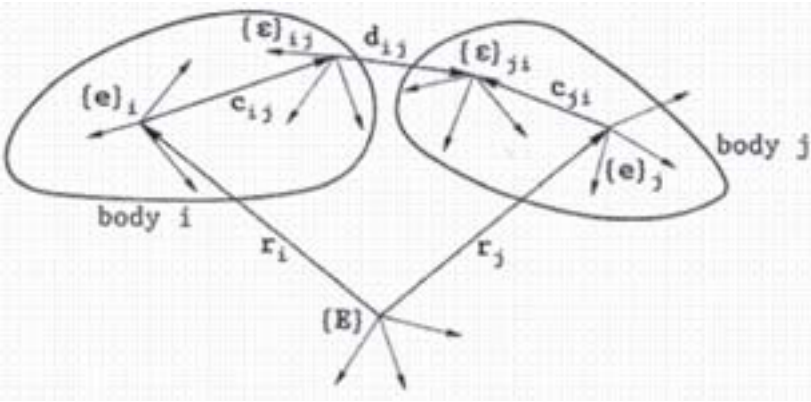

Fig. 5.2.3.4.1 **Pair of interconnected bodies**

On each body, a body-fixed joint base $\{\boldsymbol{\varepsilon}\}$ is introduced to describe the relative motion of body *j* relative to body *i*. The origins of these joint bases are chosen such that the mathematical expression for the relative translation of the joint base origins is as simple as possible. As an example, for a spherical joint, the origins will be chosen coincident with the articulation points on the bodies. Then, the relative translation vector is *0*.

The selection of the orientations of the joint bases is made on the same ground. As an example, for a revolute joint, one of the base vectors of each joint base will be chosen parallel to the rotation axis. The best choice for the origin and the orientation of joint bases depends on the specific joint.

Let the orientation of the joint base on body *i (j)* relative to the body base on body *i (j)* be specified by the time-independent rotation matrix C_{ij} (C_{ji}). Let the orientation of the joint base on body *j* relative to the joint base on body *i* be specified by the rotation matrix D_{ij}. This matrix is a function of the joint coordinates. Using these rotation matrices, the rotation matrix of the base of body j can be written as:

(5.2.3.4.1)

Let c_{ij} and c_{ji} be the position vectors of the origins of the joint bases on body *i* and *j*, respectively, relative to the origin of the base of the corresponding body. For a rigid body, the components of these vectors relative to the corresponding

body base are constant. The vector from the origin of the joint base on body *i* to the joint base on body *j* is given by the vector d_{ij}. The components of this vector relative to the joint base on body *i*, d_{ij}, are functions of the joint coordinates. The position vector of the origin of the body base of body *j* can be written as:

(5.2.3.4.2)

Applying Eqs. (5.2.3.4.1) and (5.2.3.4.2) successively for body *i* until body *N* yields the positions and orientations of all body bases relative to the inertial base. Taking the first time derivative of Eqs. (5.2.3.4.1) and (5.2.3.4.2) yields the following expressions for the angular and linear velocity [16]:

$$\omega_j = \omega_i + \omega_{ij} \tag{5.2.3.4.3}$$

$$\dot{\mathbf{r}}_j = \dot{\mathbf{r}}_i + \omega_i \times \mathbf{c}_{ij} + \dot{\mathbf{d}}_{ij} - \omega_j \times \mathbf{c}_{ji} \tag{5.2.3.4.4}$$

where $\boldsymbol{\omega}_i$ and $\boldsymbol{\omega}_j$ are the angular velocity of body *i* and *j*, respectively, and $\boldsymbol{\omega}_{ij}$ the angular velocity of the joint.

Taking the second time derivative of Eqs. (5.2.3.4.1) and (5.2.3.4.2) yields similar expressions for the angular and linear acceleration [16].

$\mathbf{r}_j = \mathbf{r}_i + \mathbf{c}_{ij} + \mathbf{d}_{ij} - \mathbf{c}_{ji}$

5.2.3.5 Example of a Kinematic Joint

The joint shown in Figure 5.2.3.5.1 allows a relative translation *s* and a relative rotation φ. These joint coordinates are assembled in the column matrix $q_{ij} = [s \ \varphi]^T$. The first base vectors of both joint bases are chosen parallel to the rotation/translation axis. The origin of the joint bases is chosen on the rotation/translation axis and are initially coincident. Then the components of the relative translation vector with respect to the joint base $\{\boldsymbol{\varepsilon}\}_{ij}$ and the rotation matrix are given by:

$$\underline{\mathrm{d}}_{ij} = \begin{pmatrix} s \\ 0 \\ 0 \end{pmatrix} \tag{5.2.3.5.1}$$

$$D_{ij} = \begin{pmatrix} 1 & 0 & 0 \\ 0 & \cos\varphi & -\sin\varphi \\ 0 & \sin\varphi & \cos\varphi \end{pmatrix} \tag{5.2.3.5.2}$$

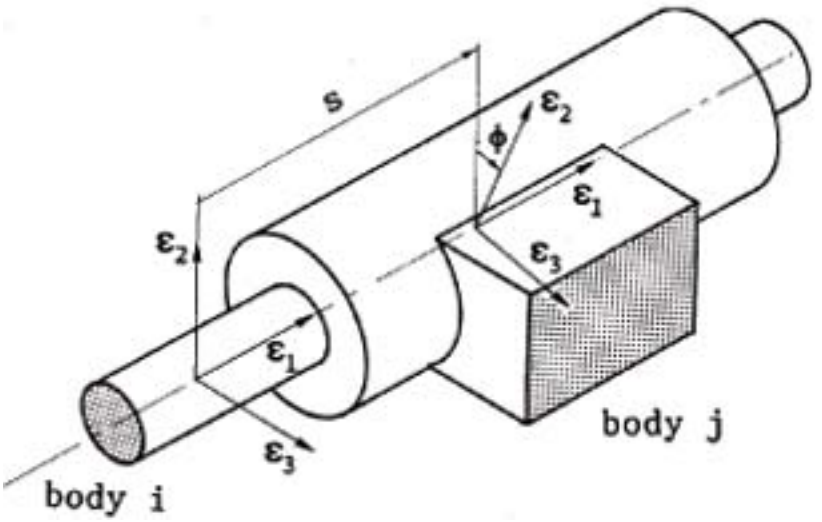

Fig. 5.2.3.5.1 **Translational-rotational joint**

The relative velocity of the origins of the joint bases is obtained by taking the first time derivative of (5). This yields:

$$\underline{\dot{d}}_{ij} = \begin{pmatrix} \dot{s} \\ 0 \\ 0 \end{pmatrix} \tag{5.2.3.5.3}$$

The relative angular velocity of the joint bases is the axial vector of the skew-symmetric matrix $\dot{D}_{ij} D_{ij}^{\ T}$. This yields:

$$\underline{\omega}_{ij} = \begin{pmatrix} \dot{\varphi} \\ 0 \\ 0 \end{pmatrix} \tag{5.2.3.5.4}$$

In MADYMO 3D, a library of kinematic joints is available. Figure 5.2.3.5.2 summarizes several of the most frequently used joint types within MADYMO.

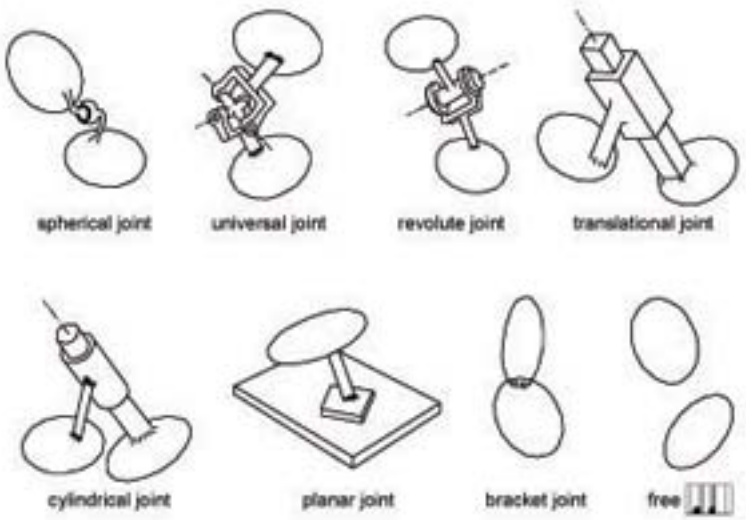

Fig. 5.2.3.5.2 **Examples of kinematic joints**

5.2.3.6 Equations of Motion

The equations of motion (Newton-Euler) of a rigid body *i* referred to its center of mass are [16]:

$$m_i \ddot{\mathbf{r}}_i = \mathbf{F}_i \tag{5.2.3.6.1}$$

$$\mathbf{J}_i \circ \dot{\omega}_i + \omega_i \times \mathbf{J}_i \circ \omega_i = \mathbf{T}_i \tag{5.2.3.6.2}$$

where m_i is the mass, J_i is the inertia tensor with respect to the center of mass, F_i is the resultant force vector, and T_i is the resultant torque vector relative to the center of mass. For a body in a system of bodies, F_i and T_i include the effect of the applied forces and torques acting on the rigid bodies as caused by the force-interaction models as well as the constraint forces and torques due to kinematic constraints in the joints. These constraint forces and torques cannot be determined until the motion of the system is known. This is in contrast with the applied forces and torques that depend only on position and velocity quantities.

The constraint forces and torques can be eliminated using the principle of virtual work. First, Eqs. (5.2.3.6.1) and (5.2.3.6.2) are multiplied by a variation of the position vector, δr_i, and a variation of the orientation, $\delta\pi_i$, and the resulting equations are added for all bodies of the system:

$$\sum[\delta\mathbf{r}_i \circ \{m_i\mathbf{r}_i - \mathbf{F}_i\} + \delta\pi_i \circ \{\mathbf{J}_i \circ \omega_i + \omega_i \times \mathbf{J}_i \circ \omega_i - \mathbf{T}_i\}] = 0 \tag{5.2.3.6.3}$$

In case the variations δr_i and $\delta\pi_i$ of connected bodies are such that the constraints caused by the joint are not violated, the unknown joint forces and torques will cancel (principle of virtual work). Such variations can be obtained from Eqs. (5.2.3.4.1) and (5.2.3.4.2) by varying the joint coordinates. These expressions can be substituted in Eq. 5.2.3.6.3. Starting with bodies at the end of the tree, expressions for the second time derivative of the joint coordinates are obtained:

$$\underline{\ddot{q}}_{ij} = \underline{M}_{ij}\underline{\dot{Y}}_i + \underline{Q}_{ij} \tag{5.2.3.6.4}$$

$\dot{\mathbf{Y}}_i$ is a 6×1 column matrix that contains the components of the linear and angular acceleration of the base of the lower numbered body *i*. The $n_{ij} \times 6$ column matrix M_{ij} and the $n_{ij} \times 1$ column matrix Q_{ij} depend on the inertia of the bodies and the instantaneous geometry of the system. Q_{ij} depends additionally on the instantaneous velocity of the system and the applied loads. The matrices M_{ij} and Q_{ij} are calculated successively, starting with body *N* to body *1*. Then, starting with the joint between the inertial space and body *1*, the second time derivatives of the joint coordinates can be calculated from Eq. 5.2.3.6.4. Note that for this joint, *i* equals 0 and *j* equals 1 and the acceleration of the inertial space, $\dot{\mathbf{Y}}_0 = 0$.

This algorithm yields the second time derivatives of the joint coordinates in explicit form. The number of computer operations is linear in the number of bodies in case all joints have the same number of degrees of freedom. This leads to an efficient algorithm for large systems of bodies.

Time integration of the second time derivatives of the joint coordinates gives the joint coordinates and their first time derivatives at a new point in time. These are used to calculate the motion and velocity of the body bases relative to the inertial base using Eqs. (5.2.3.4.1) and (5.2.3.4.2) and their first time derivatives (5.2.3.4.3) and (5.2.3.4.4). At the start of the integration, the joint coordinates and their first time derivatives must be specified (initial conditions). For the time integration, two explicit numerical integration methods are available: a fourth order Runge-Kutta method that uses a constant time step; and a fifth order Runge-Kutta-Merson method which uses a variable time step that is controlled by the local truncation error.

5.2.4 Force Interaction Models

The motion of a system of joint-connected bodies is caused by applied forces. MADYMO offers a set of standard force-interaction models. The various categories of force-interaction models are summarized below (see also Figure 5.2.2.1):

- Acceleration field model
- Spring-damper elements
- Muscle models
- Contact models
- Belt model
- Dynamic joint models

The user can also make and link his or her own routines to the MADYMO multi-body module.

Forces (and torques) are specified as a (non-linear) function of parameters like deflections, elongations, penetrations and joint rotations. Such functions are defined by means of a set of function pairs, which internally in the program are approximated either by a spline function or by a piece-wise linear interpolation. Generally, quasi-static tests have to be carried out to obtain these characteristics. Differences between loading and unloading responses can be approximated by various hysteresis models.

Often, function characteristics will be rate dependent in a highly dynamic environment like a crash. For this purpose in a number of the force-interaction models, velocity dependent damping can be introduced. Moreover, there is a possibility to prescribe a so-called dynamic amplification factor, which multiplies a statically determined force with a rate dependent factor in order to approximate the dynamic response. For details on the physical background of dynamic amplification in a crash environment see Prasad and Padgaonkar [17]. In MADYMO, several dynamic amplification factors have been implemented, including polynomial and logarithmic function of the rate of deformation (or penetration, elongation or other factors).

5.2.4.1 Acceleration Field Model

The acceleration field model calculates the forces at the centers of gravity of bodies in a homogeneous time-dependent acceleration field a (Figure 5.2.4.2.1). This model can be applied for the simulation of the acceleration forces on a vehicle occupant during an impact. Consider as an example the impact of a vehicle

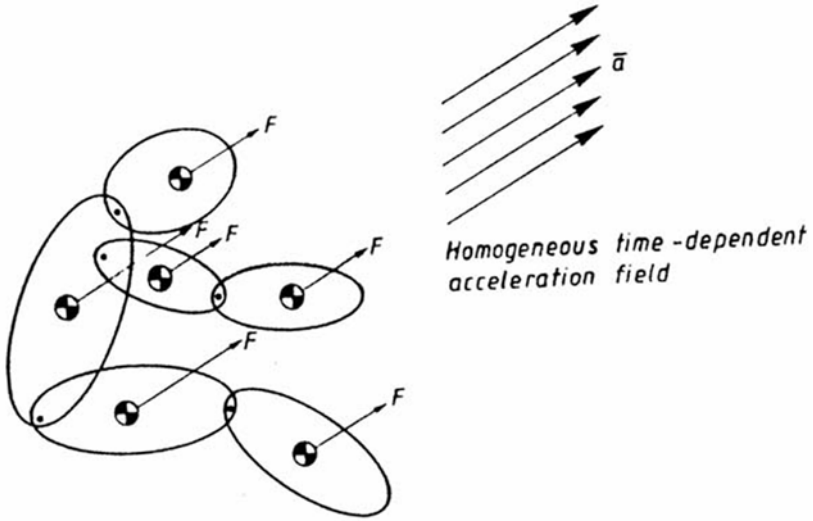

Fig. 5.2.4.2.1 **A homogeneous acceleration field**

against a rigid barrier. If the vehicle does not rotate during the crash, the actual recorded accelerations at the vehicle can be prescribed as an acceleration field acting on the occupant, while the vehicle is connected to the inertial space. The motion of the occupant relative to the vehicle is the same as when the actual recorded motion of the vehicle is prescribed. The components of the vector *a* are defined as a function of time relative to the inertial coordinate system.

5.2.4.2 Spring-damper elements

Three different types of massless "spring-damper" models can be specified: a Kelvin-, a Maxwell- and a point-restraint element (Figure 5.2.4.2.2). The Kelvin element is a uniaxial element that simulates a spring parallel with a damper. The Maxwell element is a uniaxial element that simulates a spring and damper in series. The point-restraint model can be considered as a combination of three Kelvin elements with infinite spring length, each parallel to one of the axes of an orthogonal coordinate system. All spring-damper models can be attached to arbitrary points of any two bodies or between a body and the inertial space.

5.2.4.3 Muscle models

The most common muscle model in biomechanical research is the Hill model (Figure 5.2.4.3.1). The model consists of a contractile element (CE) which describes the active force generated by the muscle, a parallel elastic element (PE) which

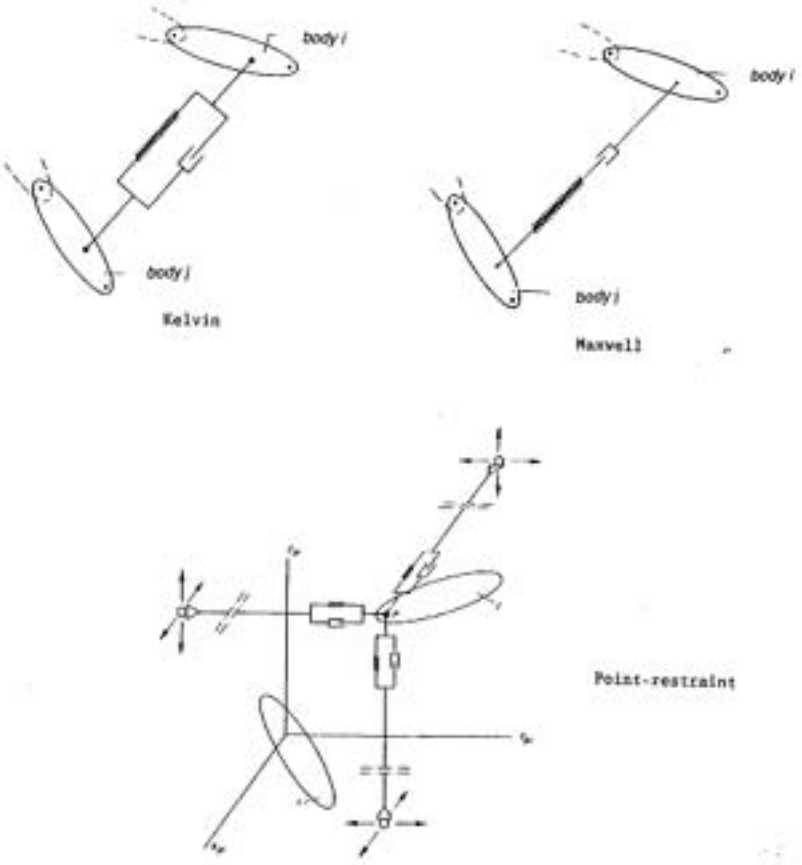

Fig. 5.2.4.2.2 **A Kelvin-, Maxwell- and point- restraint element**

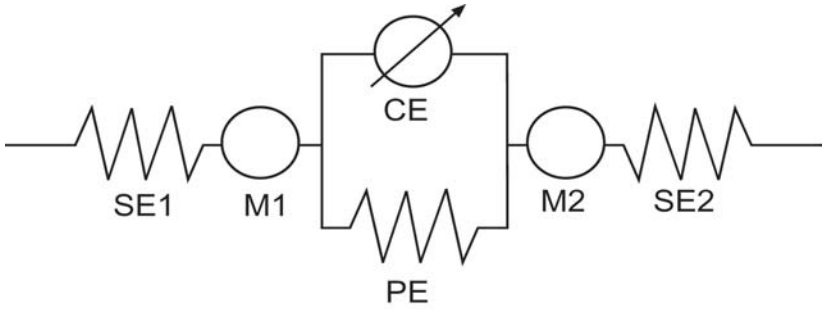

Fig. 5.2.4.3.1 **The Hill-type muscle model**

describes the elastic properties of muscle fibers and surrounding tissue, two elastic elements (*SE1* and *SE2*) which describe the elastic properties of tendons and aponeurosis and two masses (*M1* and *M2*) to account for the muscle mass. The basic muscle model implemented in MADYMO consists of the CE and the PE. Muscles with varying complexity can be formulated using this basic model in combination with the standard MADYMO elements.

5.2.4.4 Contact models

Planes, cylinders, ellipsoids and in later versions of MADYMO, arbitrary shaped surfaces (called facet surfaces) are used to model contact with other bodies or the surroundings. The contact surfaces are of major importance in the description of the interaction of the human body and an impacting surface like the vehicle interior. In addition to standard ellipsoids, which are of the degree 2, higher order ellipsoids can be specified:

$$\left(\frac{|x|}{a}\right)^n + \left(\frac{|y|}{b}\right)^n + \left(\frac{|z|}{c}\right)^n = 1 \qquad (5.2.4.4.1)$$

where *a, b* and *c* are the semi-axes of the (hyper) ellipsoid and *n* is the degree. If the degree *n* increases, the (hyper) ellipsoid will approximate more and more a rectangular shape (Figure 5.2.4.4.1).

Surfaces cannot deform themselves. Instead, surfaces are allowed to penetrate into each other. The basic principle of the contact models in MADYMO (and other human body gross-motion simulators) is that a contact force is generated between two colliding surfaces. That force is a function of the penetration of the two surfaces as well as of the relative velocity in the contact area (Figure 5.2.4.5.1). In this way elastic (including hysteresis and dynamic amplification), damping and friction forces can be specified in the contact. If a facet surface is involved, the contact force, instead of being "force-penetration"–based, may be based on a "stress-penetration" function.

5.2.4.5 The Belt Model

The belt model consists of a chain of connected, massless, spring-type segments (Figure 5.2.4.5.2). The end points of these segments are connected to rigid bodies or the inertial space at so-called attachment points. These attachment points cannot change during a simulation. An important feature is that belt material can slip through an attachment point from one segment to another. The belt model accounts for initial belt slack or pre-tension and rupture of belt segments. Elastic characteristics can be specified separately for each belt segment. Furthermore, a retractor that is either of the vehicle-sensitive type or of the webbing-sensitive

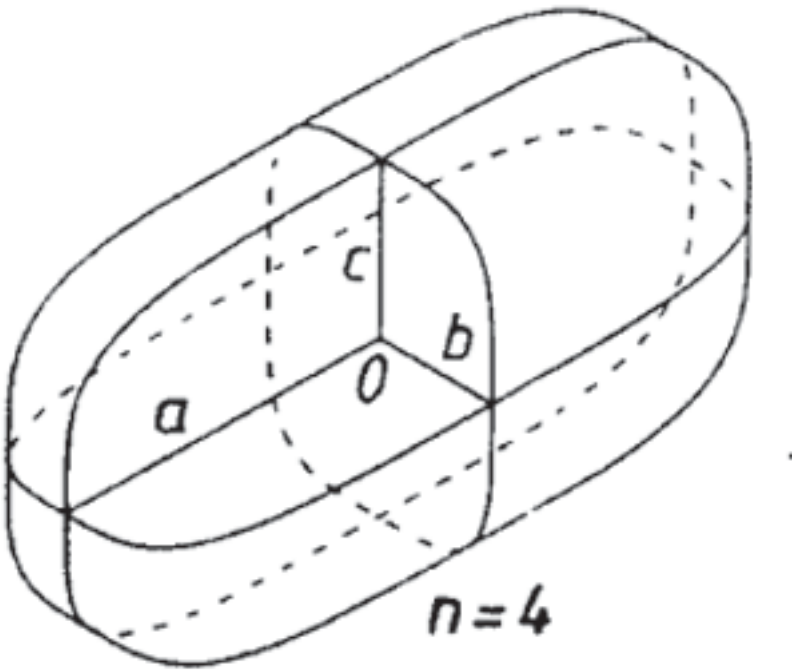

Fig. 5.2.4.4.1 **A hyper-ellipsoid of degree 4**

type can be specified. A vehicle-sensitive reel can lock at a specified time or if a specific component of the calculated linear acceleration at the retractor location exceeds a prescribed level during a certain time interval. A webbing-sensitive reel locks if the belt feed rate exceeds a specified limit. A pretensioner model is also available.

5.2.4.6 Dynamic Joint Models

The last force-interaction models to be reviewed here are dynamic joint models. As described earlier, in a joint, two types of loads are acting: the internal forces and torques caused by the kinematic joint constraints; and the applied loads representing passive loads due to friction or elastic resistance or active loads caused by muscle activity. The applied joint loads are taken into account by the dynamic joint force models. The simplest type generates a force (or torque) as a function of a single joint coordinate. An example is the torque as a function of the rotation in a revolute joint (Figure 5.2.4.6.1). In this model, elastic (including

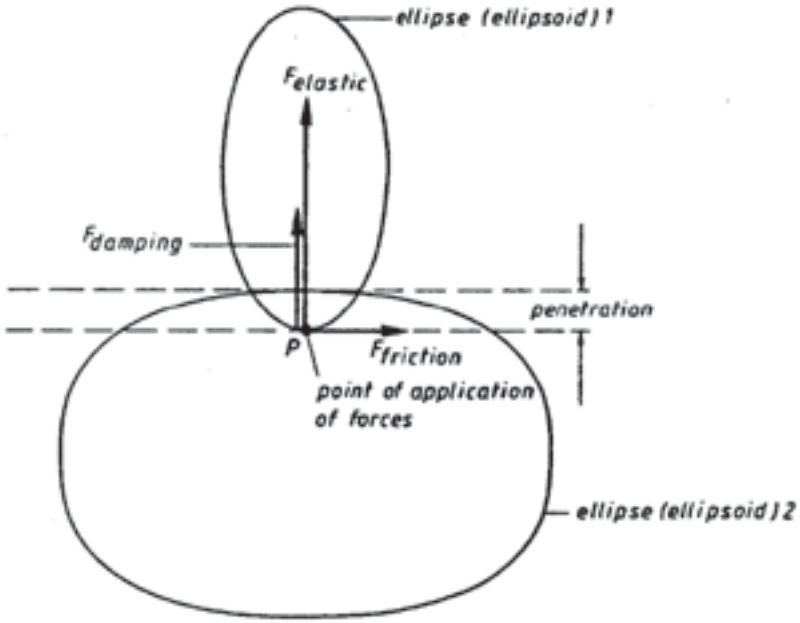

Fig. 5.2.4.5.1 **Contact loads in an ellipsoid-ellipsoid contact (only forces acting on the upper ellipsoid are shown)**

hysteresis and dynamic amplification) as well as damping forces (torques) can be prescribed, as in a spring-damper model. If the joint coordinate is a rotation also a friction torque can be introduced.

A more complicated dynamic joint is the "flexion-torsion restraint" model, which can be applied where spherical joints are used to represent flexible structures such as the neck and spine in crash dummies. In this model, the relative joint position of the joint is considered to be the result of two successive rotations, that is, a "bending" and a "torsion" motion of segment *j* relative to segment *i*. For both the bending and torsion motion, an elastic torque has to be defined where the bending torque can be defined directional dependent. This means that the bending stiffness in forward direction can differ from the stiffness in backward or lateral bending.

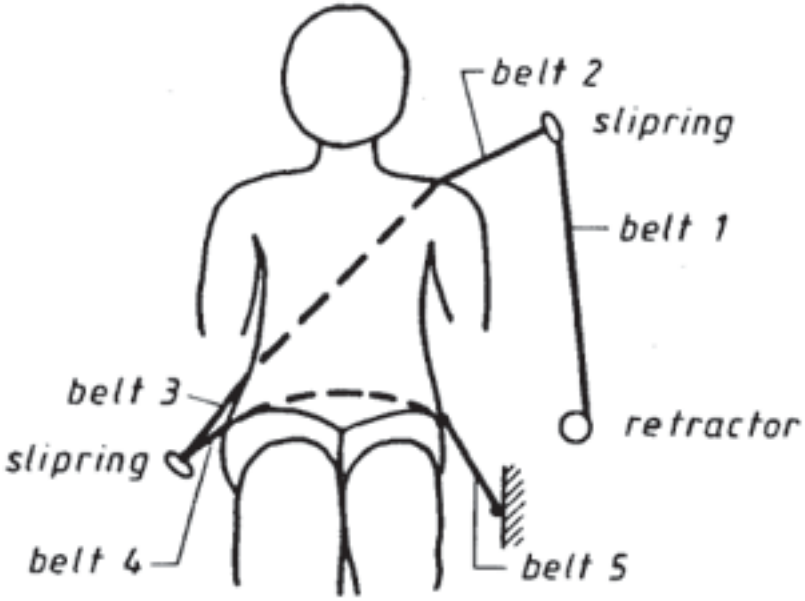

Fig. 5.2.4.5.2 **A 3-point belt with retractor**

5.2.5 Integrated Multi-Body Finite Element Simulations

In the MADYMO finite element module, truss, beam, shell, brick and membrane elements are implemented and material models like elastic, visco-elastic, elasto-plastic, hysteresis and Moonley-Rivlin can be applied. Models also are available for sandwich material, solid foam and honeycomb material. A MADYMO model can be made of multi-body systems, finite element structures or combinations of the two systems.

Figure 5.2.5.1 illustrates the interaction between the multi-body and the finite element module. Two kinds of interactions generate forces between the multi-body and the finite element model: support and contacts. A support is a finite element node rigidly connected to a body of a multi-body system (or to a belt segment of the belt model in order to model belt parts by membrane or truss elements). The necessity of these two types of interactions can be illustrated using the example of a finite element driver airbag simulation. The airbag unit is connected to the steering column, which often is modeled as a multi-body system.

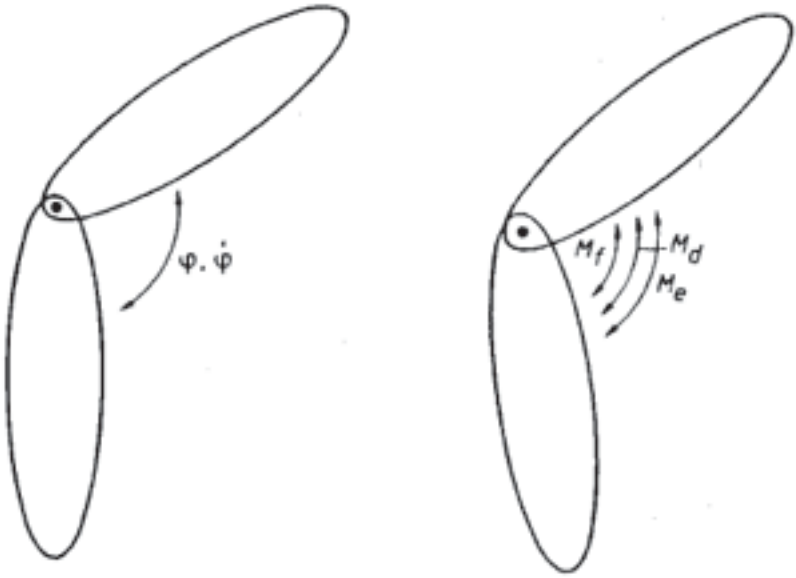

Fig. 5.2.4.6.1 **A revolute joint with joint torques**

The airbag model can be attached to the multi-body steering column using supports while the interaction of the airbag with a multi-body occupant can be handled through contacts.

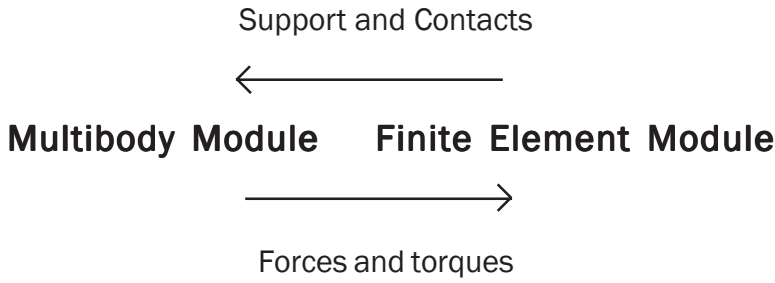

Fig. 5.2.5.1 **Interaction between multi-body and finite element module**

This approach allows the use of different integration methods for the equations of motion of the finite element module and the multi-body module. For an integrated MADYMO analysis, the fourth order Runge-Kutta or Euler method is used for the time integration of the equations of motion of the multi-body system. The central difference method is used for the equations of motion of the finite element model. Actual body positions and velocities at each time step of the central difference method determine the support and contact forces. The forces acting on the multi-body system are accounted for in each mean time point of the fourth order Runge-Kutta and each time step of the Euler method. Due to the fine spatial discritization often required in a finite element model, a much smaller time step is required in finite element model compared to a multi-body model. To improve the efficiency of the integrated analyses, the finite element analysis is subcycled with respect to the multi-body analyses.

In addition to the finite element module within MADYMO using the above principles, external interfaces between MADYMO and finite element programs like PAMCRASH, LSDYNA, RADIOSS and MSC DYTRAN have been developed.

5.3 Crash Dummy Modeling

5.3.1 Introduction

Well-validated human body crash models presented in literature to date have been developed for mechanical models of the human body (crash dummies), rather than for real human beings. The rationale for this is that most model input data in the case of crash dummy models can be measured with relative ease. Moreover, results of experiments with crash dummies often are available for model validation. If not, such experiments, unlike tests with biological models, can be readily carried out in well-equipped crash laboratories. Another reason for the emphasis on modeling crash dummies is the need, particularly from design departments in the automotive industry, for well-validated design tools, which can reduce the number of regulatory tests with crash dummies. This allows for a shorter, optimised development process for new car models. In Section 5.3.2 – Modeling Methodology, the modeling process of a multi-body crash dummy model will be described. In Section 5.3.3 – Examples of Crash Dummy Databases, typical examples of crash dummy models will be presented.

5.3.2 Modeling Methodology

The first step in the modeling process of a crash dummy is to divide the dummy into segments and specify the parts belonging to each segment. Segments are selected by dividing the dummy into functional components. Each part of the dummy having significant mass and a flexible connection with other parts is

considered a segment. Dummy parts, which do not show any relative motion, are usually considered to be part of another segment except if load information is required at the interface between the two segments. In current dummy designs, four types of kinematic connections between segments can usually be distinguished: revolute (or pin joints), translational joints, universal joints and universal joints.

Flexible structures are often present in a dummy. Some are partly or completely made of rubber, as are the lumbar spine and neck. The flexible structures usually are modeled by two universal joints located in the centers of the end planes of these structures or by a 6-degree of freedom joint. Flexible parts like the ribs are usually represented by a number of rigid bodies, flexible bodies or by finite elements.

If the general model set-up has been specified, the geometric parameters have to be determined from technical drawings, CAD files or the parameters have to be measured directly from the dummy. Information needed includes the joint locations within the individual segments, the joint axes orientations and the outside surface geometry. Three-dimensional measurements are usually conducted on a disassembled dummy. Some of the geometric joint data have to be determined in an indirect way since the requested joint data may not be directly accessible to a measuring device. Additional measurements of landmarks specifying segment local coordinate systems must be conducted in order to express the data in a common body-fixed base.

The outside surfaces of the dummy segments are usually represented by means of ellipsoids or arbitrary-shaped surfaces. The ellipsoids or arbitrary surfaces are used for visual presentation of the occupant kinematics and for the contact interactions between dummy segments and environment, such as the vehicle interior.

The second step is to determine the inertial properties. The mass, location of the center of gravity, the principal moments of inertia and the orientation of the principal axes must be determined for each dummy segment. In addition, the position of segment landmarks must be determined to express the inertia data in a body-fixed coordinate system. Experimentally, the moments of inertia can be determined with a torsional vibration table [18]. The object, which is fixed in a box, is measured in several positions in order to get the complete inertia tensor.

The stiffness of the connections (joints) between the different segments is one of the parameters having a major effect on the motions of the dummy segments in a crash environment. These joint resistive properties are determined using various static and dynamic test methods. In these tests, the range of motion corresponding

to a joint coordinate is determined as a function of the externally applied load. Separate measurements for each degree of freedom are conducted if a joint has more than one degree of freedom, as in a universal joint, keeping the other coordinates fixed. Since the actual joint resistance often will depend on the value of multiple joint coordinates, large test series may be required. In practice, this dependency on more than one degree of freedom is neglected and joints are tested with the other degrees of freedom fixed.

The last step is the specification of the surface compliance properties. Static as well as dynamic measurements with several penetrating surfaces must be performed at different locations on the dummy segments. The surface compliance is dependent on the skin covering thickness and density as well as the compliance of the underlying structure. If the dummy part to be modeled will be represented by a finite element model, material parameters describing the involved dummy materials have to be determined. The surface compliance tests can be used for model validation purposes in this case.

On the basis of these measurements, a database of the dummy can be compiled. After formulating a database, verification simulations are carried out to ensure that the database adequately represents the complete dummy. For this purpose, well-controlled impactor tests and sled tests with the assembled dummy at different acceleration levels are used. If results are not completely satisfying, further model refinements with corresponding input measurements may be required. A well-validated computer model allows the user to apply the model for predictive simulations of events outside the range of validated simulations.

5.3.3 Examples of Crash Dummy Databases

Many organizations have recognized the need for well-validated databases of crash dummies. This has resulted in a number of cooperative research efforts to develop such databases. A detailed presentation of these efforts would be out of the scope of this Chapter. However, it is worthwhile to note the activities in the mid-eighties concerning the Hybrid III crash dummy. A series of frontal sled tests using a Hybrid III dummy in a rigid seat at three different severity levels was conducted in 1985 by Prasad [19]. The results were available for a Society of Automotive Engineers, (SAE) subcommittee for the purpose of validation of dummy databases of the ATB and MADYMO programs. These validation efforts were presented at the 1998 SAE congress by several authors [20,21,22] that resulted in a number of recommendations for further improvement of the quality of the Hybrid III dummy database.

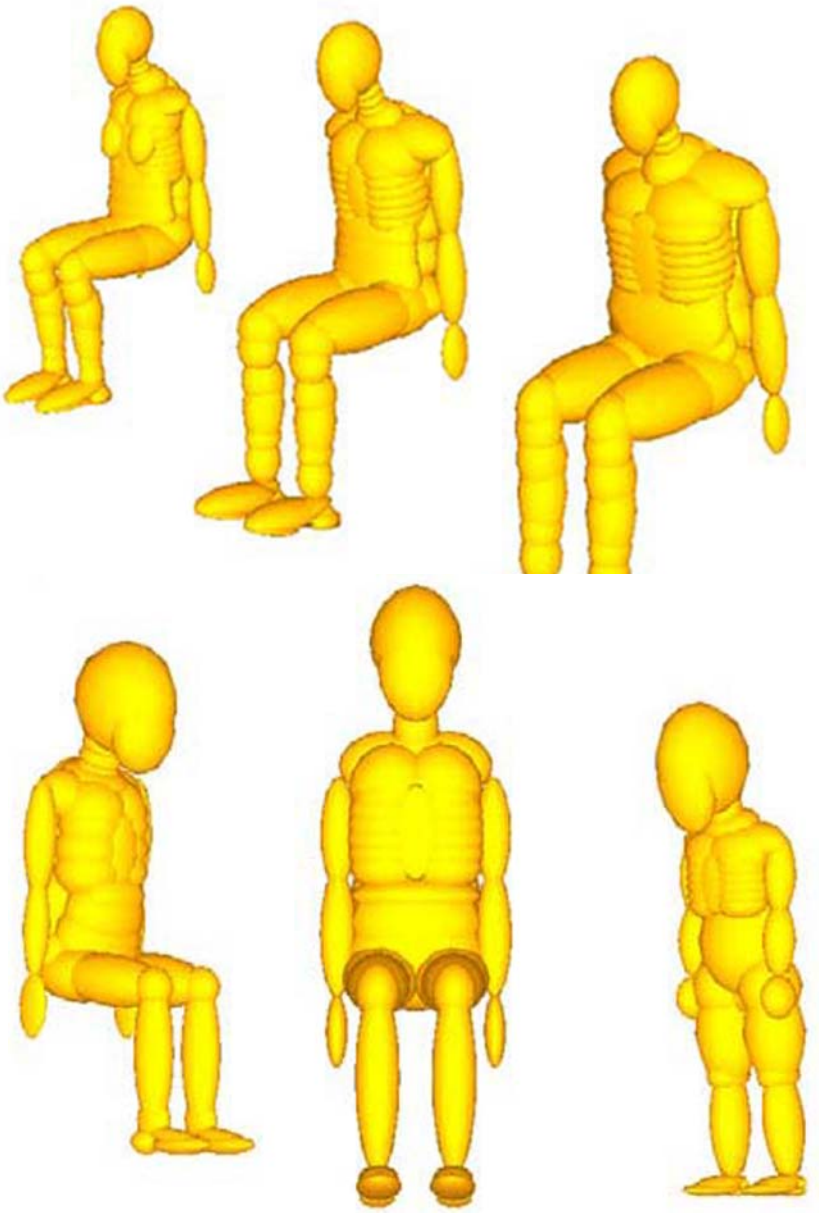

Fig. 5331a **Examples of multi-body crash dummy models Hybrid III dummy family (top) and 5th 50th and 95%, USA child dummies (bottom)**

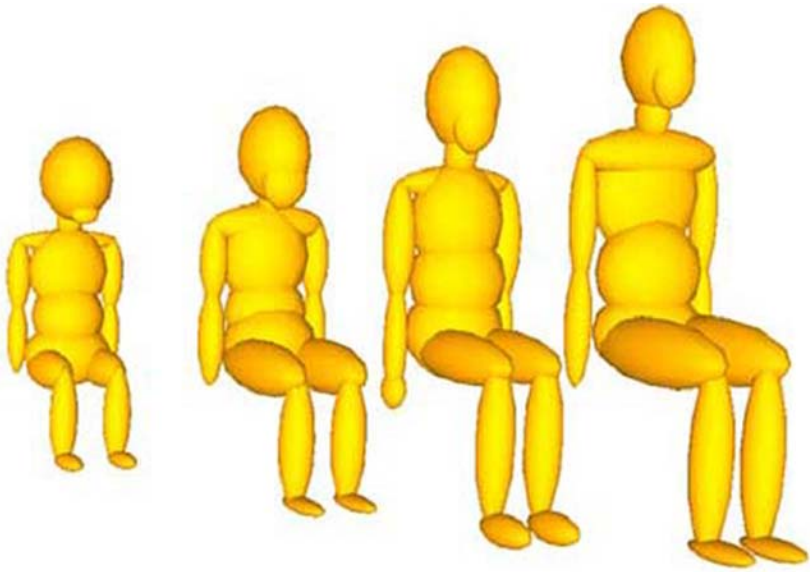

Fig. 5.3.3.1b **Examples of multi-body crash dummy models Hybrid III 3yr, Hybrid III 6yr and Crabi 12 month and TNO child dummies (above): P3/4, P3, P6 and P10)**

Figs. 5.3.3.1 illustrates some of the validated "standard" multi-body dummy databases currently available with the MADYMO program. Models for the Hybrid II dummy, the various side impact dummies (EUROSID, BIOSID and DOT-SID), various headforms and other impactors also are available. Figure 5.3.3.2 shows two different MADYMO models for the EUROSID dummy: a model with arbitrary (facet) surfaces (left) and a finite element model.

5.4 Modelling the Real Human Body

5.4.1 Introduction

A model of the real human body is much more difficult to develop than a model of a physical crash dummy. Mathematical modeling of the real human body potentially offers improved biofidelity compared to crash dummy models and allows the study of aspects like body size, body posture, muscular activity and post fracture

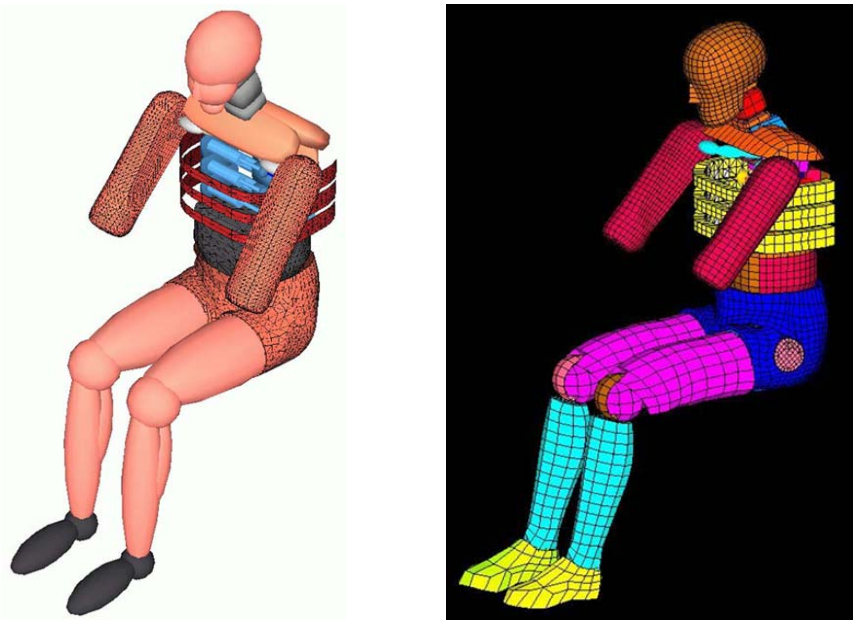

Fig. 5.3.3.2 **MADYMO multi-body facet model (left) and finite element model (right) of the EUROSID dummy**

response. Detailed human body models potentially allow analysis of injury mechanisms on a material level.

A large number of models describing specific parts of the human body have been published but only a few of these models describe the response of the entire human body in impact conditions. Models simulating the response of car occupants have been published for lateral loading by Huang [23,24] and Irwin [25], frontal loading by Ma et al [26] and rear loading by Jakobsson et al [27] and van den Kroonenberg et al [28]. A model for vertical loading has been published by Prasad and King [29]. Pedestrian models have been published by Ishikawa et al [30] and Yang et al [31] and a child model in a child restraint system has been published by Wismans et al [32].

In Section 5.4.2 – Anthropometry, the aspect of anthropometry of human body models will be presented. In Section 5.4.3 – Examples of a Human Body Model, some examples will be shown.

5.4.2 Anthropometry

In occupant crash simulations, the program GEBOD is often used to generate models representing arbitrary human body sizes. GEBOD produces geometric and inertia properties of human beings [33]. Joint resistance models for an adult male GEBOD model are described by Ma et al [26]. GEBOD generates a model consisting of 15 segments: head, neck, upper arms, lower arms, thorax, abdomen, pelvis, upper legs, lower legs and feet. Computations for the geometrical parameters and mass distribution are based on a set of 32 body measurements. From these 32 parameters, body segment sizes and joint locations are derived. Segments are described by ellipsoids, except for the thorax and feet where more complex approximations (so-called elliptical solids) are used. Inertial properties are estimated by calculating the inertial properties of each segment ellipsoid or elliptical solid, assuming homogeneous body density. The parameters can be measured at a subject or can be generated by GEBOD using regression equations on the basis of body height and weight for adult males and females. For children, regression equations are available on the basis of height, weight, age and combinations of these parameters. A major limitation of GEBOD is the approximation of body segments by simple geometric volumes.

More recently, the RAMSIS model [34] has been used anthropometry source for human body models [35]. RAMSIS has primarily been developed for ergonomic analyses and allows the generation of models with a wide range of anthropometry parameters. The RAMSIS model describes the human body as a set of rigid bodies connected by kinematic joints and the skin is described as a triangulated surface. RAMSIS provides a detailed geometric description of the body segments based on extensive anthropometric measurements, including automotive seated postures, on various civilian populations. The skin of the entire body is described as one “continuous” surface. Segment mass and center of gravity are derived in RAMSIS using this realistic geometric description. RAMSIS provides a mathematical prediction for the increase of the average body height of the entire population during a given time period (secular growth).

Anthropometric studies have shown that the body dimensions of each individual can be classified according to three dominant and independent features. These features are body height, the amount of body fat, and body proportion, that is, the ratio of the length of the limbs to the length of the trunk. Using this classification plan, RAMSIS describes the entire population in a realistic way. This method takes into account the correlation between body dimensions, which are disregarded in GEBOD. A translator has been developed to convert RAMSIS models into MADYMO models. The resulting database contains joint locations, joint ranges of motion, segment masses and centers of gravity, and a triangulated

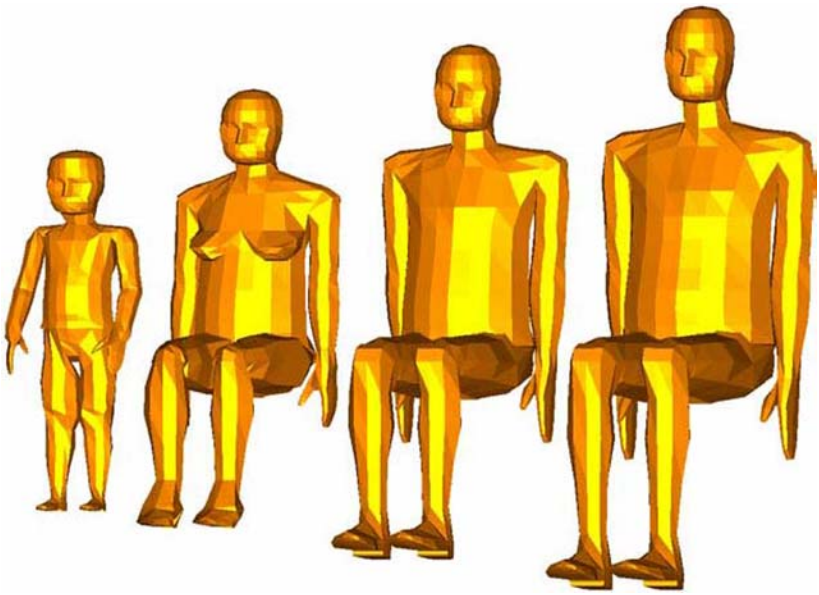

Fig 5.4.2.1 **MADYMO human models of various body sizes generated from the RAMSIS model, from left to right: 3-year-old child, extremely small female, 50th percentile male, extremely large male**

skin connected to various body segments. Inertia properties are derived by integration over segment volume assuming a homogeneous density. The conversion can be performed for any anthropometry specified in RAMSIS, and examples of such models are shown in Figure 5.4.2.1.

5.4.3 Examples of a Human Body Model

This section reviews two examples of human body models: a multi-body model and a full finite element model.

The multi-body model is the 50th-percentile male model from Figure 5.4.2.1. This model has been validated in a number of crash conditions including frontal, rear and side impact volunteer tests, as well as several types of cadaver tests [35]. The simulation shown in Figure 5.4.3.1 is a 15-g frontal sled test with human volunteers

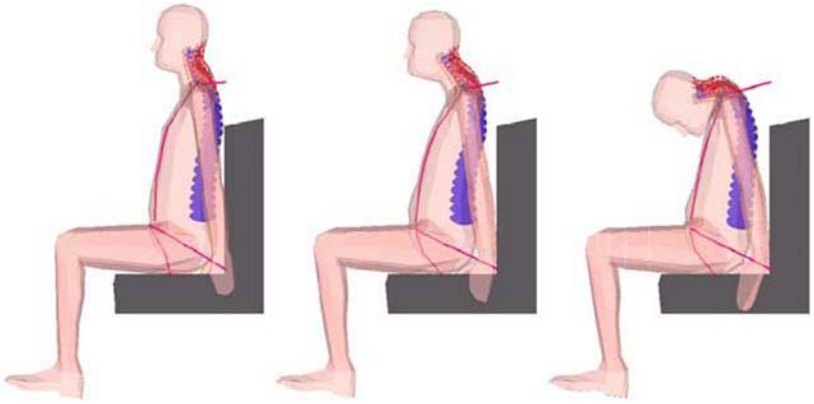

Fig. 5.4.3.1 **Simulation of 50th male human body model in 15g volunteer test [35]**

conducted by the Naval Biodynamics Laboratory in New Orleans. For the neck in this model, a global 7-segment model is available with lumped properties as well as a detailed neck model with separate representations for the facet joints, intervertebral discs, ligaments and active muscle response. Figure 5.4.3.2 shows the response of this neck model in comparison with human volunteer response. In the model, active muscle response was taken into account. The performance of this neck model appears to be much more realistic than the neck behavior of the current Hybrid III crash dummy [36]. For some other body parts, such as the ankle/foot and the head/brain, detailed multi-body and/or finite elements representations are available in this 50th-percentile male model. Figure 5.4.3.3 illustrates a finite element model of the brains developed at Eindhoven Technical University, The Netherlands.

A finite element model is shown in Figure 5.4.3.4. It represents a 50th-percentile male developed by Lizee et al in the RADIOSS program package [37]. Detailed representations of the neck, shoulder, thorax and pelvis have been developed and the resulting model has been validated in more than 30 test configurations. The model has more than 10,000 elements. Head and arms and legs (not shown) were represented as rigid bodies.

5.5 Conclusion

The earliest numerical models of the full human body have been based on multibody techniques. More recently, finite element techniques have been used

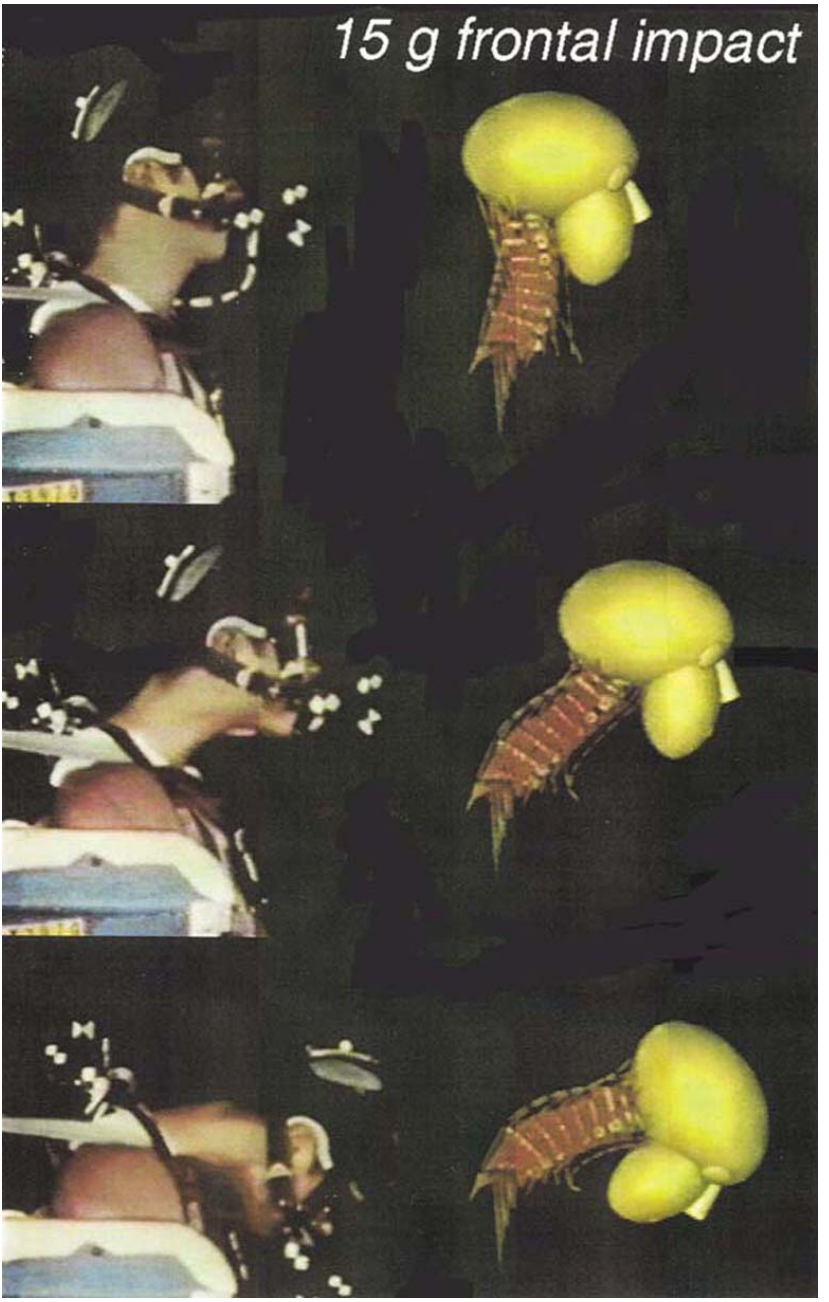

Fig. 5.4.3.2 **Comparison of human neck model response and volunteer response [36]**

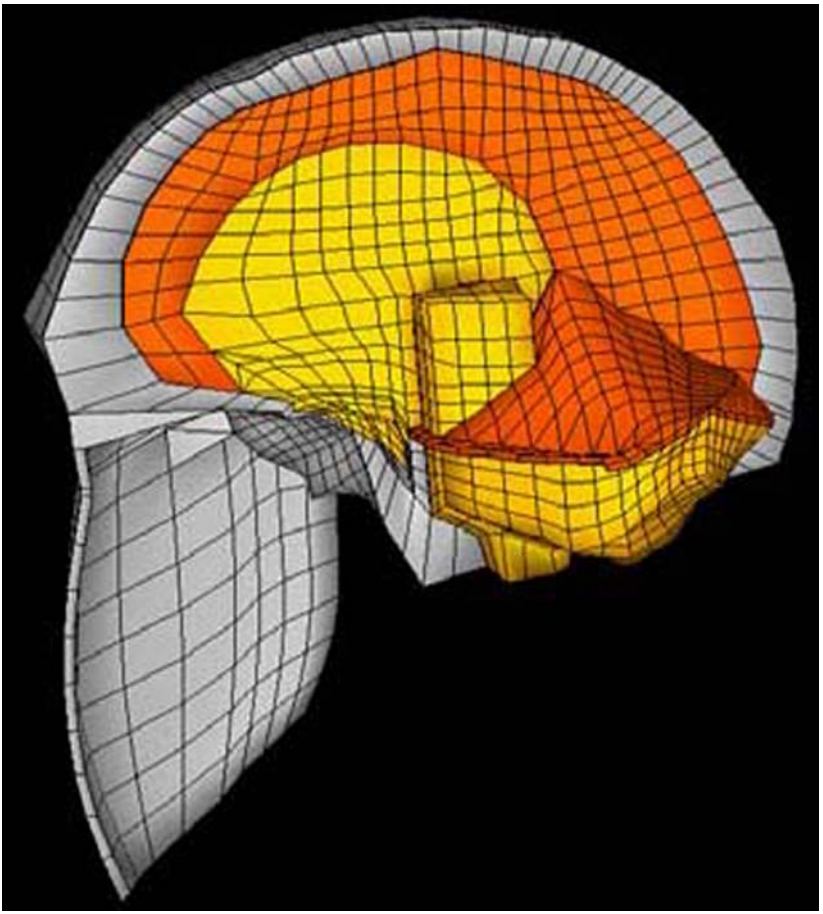

Fig. 5.4.3.3 **MADYMO finite element brain model developed at the Eindhoven Technical University, The Netherlands**

for this purpose. A major advantage of the multibody approach is its capability to simulate, in an efficient way, spatial motions of mechanical systems with complex kinematic connections as present in the human body and in parts of the vehicle structure. The advantage of the finite element method is the capability of describing local structural deformations and stresses in a realistic way. However, the creation of a finite element model is time-consuming, and the availability of realistic material data is limited, particularly in the case of biological tissue response. Furthermore, relatively large amounts of computer time are required to perform a finite element

Fig. 5.4.3.4 **Finite element human body model developed by Lizee et. al.[37]**

Table 5.5.1 **Validation Index proposed by SAE Subcommittee [38]**

Class	Characteristics
Level 0	No agreement between predictions of model and "reference event"
Level 1	Qualitative agreement: a)Trends of predicted parameters same b)Kinematics correspond qualitatively c)Contacts between the occupant and vehicle interior are the same in general
Level 2	HIC and similar indicators predicted by simulation are within 20% of those obtained in reference event
Level 3	Peak values of important occupant responses limited to a relative error of 20% (20% on vector magnitude, 11.31 deg on vector direction)
Level 4	Same as level 3 except 5%
Level 5	Timing of peaks of important vector responses limited to 5% relative difference
Level 6	All peaks and valleys in the duration of time-dependent predictions must match the reference event within 10%
Level 7	Same as level 6 except 5%
Level 8	1% relative error, point-by-point, over the durations of the reference and predicted events

crash simulation, making the method less attractive for complex optimization studies involving many design parameters.

A general advantage of computer crash simulations over crash tests with mechanical human substitutes (crash dummies) is that the safety performance of design concepts and the effect of changes in the design can be studied efficiently, sometimes even without the use of a prototype. Availability of well-validated databases of the human body is an important condition for the use of such models. Continuous efforts are needed to further improve the quality of existing human body models in order to allow for a wider range of applications. Standards for validation procedures and performance criteria are needed to further enhance the applicability of crash simulations. In the past, some attempts have been made to develop such standards. Table 5.5.1—Validation index proposed by SAE subcommittee shows a model Validation Index developed in the early eighties by the “Analytical Human Simulation Task Force” of the SAE Human Biomechanics and Simulation Subcommittee (HBSS) [38]. The Subcommittee agreed upon the

index, but a number of issues were not resolved, including the number and type of tests to be conducted.

Models of the human body can be subdivided into models of crash dummies and models of the real human body. Many models of crash dummies have been developed over the past two decades, and extensive series of validation studies have been conducted with impressive results. Promising results have been achieved in the field of real human body models in the nineties. Real human body models allow the study of the effect of body size, posture influence as well as muscular activity. In the near future, mathematical models may even offer a more realistic representation of the human body than do current crash test dummies. A unique advantage of a design strategy based on real human body crash models over a design strategy based on crash tests with dummies is the possibility to rapidly benefit from new scientific knowledge of injury mechanisms and injury criteria obtained through biomechanical research. With crash test dummy-based design strategies, a long period of time elapses before new findings can be implemented in crash dummy hardware. For example, the Hybrid III, the most-used dummy, is based to a large extent on biomechanical knowledge that is more than twenty years old. New scientific findings have seldom resulted in improvements in the dummy design particularly since safety regulations, which specify the Hybrid III dummy as a regulatory test device, tend to freeze the specifications in the regulation for a long period.

Apart from design studies and the analysis of biomechanical tests, an increased usage of computer models also can be observed in the area of accident reconstruction and litigation. Application of computer models in this field should be handled with much care due to the limited level of development of real human body models for different body sizes, the usually large number of unknown accident parameters and the lack of experimental data available for validation for the case under consideration. Development of a code of practice with guidelines for usage of models in this field is highly recommended.

Several areas can be identified in the field of human body crash simulations where further developments should take place. For crash dummies, realistic models for the foam-type structures (skin and damping material) are required. Areas of future development in the field of real human body models include further improvements in the description of the non-linear dynamic behavior of muscles (including neuromuscular control), the modeling of complex human joints and the study of constitutive equations and parameters for biological materials such as the brain and skin.

This Chapter has concentrated in particular on the usage of multi-body technology for human body modeling. Further refinements of the models using finite element techniques constitute an increase in model complexity, however, with the added advantage that detailed stress and strain analysis can be performed. Particularly for detailed studies of injury mechanisms in specific body parts this is a necessary and feasible approach. Boundary conditions for such segment models may be obtained from experiments or from results obtained through more global models. The usage of finite element techniques coupled with multi-body techniques will allow the user to benefit from the capabilities of both approaches and will offer the flexibility of merging more global multi-body models with, whenever needed, detailed representations for certain parts in his model.

5.6 References

1. Lobdell T.E.: "Impact response of the human thorax," In: Human impact response: Measurement and simulation, pp 201-245, Plenum Press, New York, 1973.

2. McHenry, R.R., "Analysis of the dynamics of automobile passenger restraint systems," Proc. 7th Stapp Car Crash Conference, pp.207-249, 1963.

3. Final report for publication "EU compatibility project," European Commission, Brussel, (in press), 2000.

4. Shugar, T.A.: "A finite element head injury model", Final report Vol 1 Contract DOT HS 289-3-550-IA, NHTSA, Washington DC, July 1977.

5. Bruijs, W.E.M., Subcycling in Transient Finite Element Analysis. Thesis, Department of Mechanical Engineering, Eindhoven University of Technology, Eindhoven, The Netherlands. ISBN 90-9003684-9, 1990.

6. Robbins, D.H., Bowman, B.M. and Bennett, R.O., "The MVMA two-dimensional crash victim simulation," Proc. 18th Stapp Car Crash Conference, pp. 657-678, 1974.

7. Robbins, D.H., Bennett, R.O. and Bowman, B.M., "User-oriented mathematical crash victim simulator," Proc. 16th Stapp Car Crash Conference, pp. 128-148, 1972.

8. Huston, R>L>, Hessel, R. and Passerello, C., "A Three-dimensional vehicle-man model of collision and high acceleration studies, " Paper No. 740725, Society of Automotive Engineers Inc., (1974).

9. Fleck, J.T., Butler, F.E. and Vogel, S.L., "An improved three-dimensional computer simulation of motor vehicle crash victims." Final Technical Report No. ZQ-5180-L-1, Calspan Corp. (4 Vols.), 1974.

10. King, A.I. and Chou, C.C., "Mathematical modeling, simulation and experimental testing of biomechanical system crash response," J. Biomechanics, 9, 301-317, 1976.

11. Wismans, J. and L. Obergefell: "Data Bases and Analytical Modeling," Chapter 8 in AGARD Advisary Report 330 Anthropomorphic Dummies for Crash and Escape system testing, AGARD/AMP/WG21, 1996.

12. MADYMO Theory Manual, Version 5.4, TNO Automotive, Delft, The Netherlands, May 1999.

13. Prasad, P., "An overview of major occupant simulation models," Mathematical simulation of occupant and vehicle kinematics, SAE Publication P-146, SAE paper no. 840855, 1984.

14. Prasad, P., "Comparative evaluation of the MVMA2D and the MADYMO2D occupant simulation models with MADYMO-test comparisons," 10th international technical conference on Experimental Safety Vehicles, Oxford, 1985.

15. Prasad, P. and Chou, C.C., "A review of mathematical occupant simulation models, Crashworthiness and occupant protection inransportation systems," Proceedings AMD-Vol. 106, BED-Vol. 13 of the Winter Annual Meeting of ASME, Dec. 1989.

16. Wittenburg, J., "Dynamics of Systems of Rigid Bodies," B.G. Teubner, Stuttgart, 1977.

17. Prasad, P. and Padgaonkar, A.J., "Static-to-dynamic amplification factors for use in lumped mass vehicle crash models," SAE paper no. 810475, 1981.

18. Kaleps, I., J. Whitestone, "Hybrid III Geometrical and Inertial Properties," SAE 880638, International Congress and Exposition, Detroit, 1988.

19. Prasad P.: "Comparative evaluation of the dynamic response of the Hybrid II and Hybrid III dummies," SAE paper No. 902318, Proc. of the 34th Stapp Conference, 1990.

20. Obergefell, L., Kaleps, I. and S. Steele: "Part 572 and Hybrid III dummy comparisons in sled test simulations," SAE paper No. 880639, SAE PT-44, SAE Int. Congress and Exposition, Detroit, Society of Automotive Engineers Inc., 1988.

21. J. Wismans and J.H.A. Hermans: "MADYMO 3D Simulations of Hybrid III Dummy Sled Tests." SAE paper No. 880645, SAE PT-44, SAE Int. Congress and Exposition, Detroit, Society of Automotive Engineers Inc., 1988.

22. Khatua, T., L. Chang and Pizialli: "ATB simulation of the Hybrid III dummy in sled tests," SAE paper No. 880646, SAE PT-44, SAE Int. Congress and Exposition, Detroit, Society of Automotive Engineers Inc., 1988.

23. Huang Y., A.I. King, J.M. Cavanaugh. "A MADYMO Model of Near-Side Human Occupants in Side Impacts." Journal of Biomechanical Engineering, vol. 116, May 1994, p.228-235, 1994.

24. Huang Y., A.I. King, J.M. Cavanaugh. "Finite Element Modelling of Gross Motion of Human Cadavers in Side Impact." STAPP 1994, SAE 942207, 1994.

25. Irwin A.L. (1994). Analysis and CAL3D Model of the Shoulder and Thorax Response of Seven Cadavers Subjected to Lateral Impacts. Ph.D. Thesis Wayne State University, 1994.

26. Ma D., Obergefell A., Rizer A. "Development of human articulating joint model parameters for crash dynamics simulations," STAPP Conference 1995, SAE 952726, 1995.

27. Jakobsson L., Norin H., Jernstrom C., et al. "Analysis of different head and neck responses in rear-end car collisions using a new humanlike mathematical model," IRCOBI conference 1994 proc., pp. 109-125, 1994.

28. Kroonenberg A. van den, Thunnissen J., Wismans J.: "A human model for low severity rear-impacts." IRCOBI conference, 1997.

29. Prasad P., King A.I.: "An experimentally validated dynamic model of the spine." J Appl Mech, 1974, pp. 546-550, 1974.

30. Ishakawa H., Kajzer J., Schroeder G.: "Computer simulation of impact response of the human body in car-pedestrian accidents." Proceedings of the 37th STAPP Car Crash Conference, SAE-933129, 1993.

31. Yang J.K, Lovsund P: "Development and validation of a human body mathematical model for simulation of car-pedestrian impacts," IRCOBI Conference 1997.

32. Wismans, J., Maltha, J.W., Melvin, J.W. and Stalnaker, R.L., "Child Restraint Evaluation by Experimental and Mathematical Simulation," 23rd Stapp Car Crash Conference, Paper No. 791017, San Diego, USA, 1979.

33. Baughman, L.D., "Development of an Interactive Computer Program to Produce Body Description Data." University of Dayton Research Institute, Ohio, USA, Report number AFAMRL-TR-83-058, NTIS doc. no. AD-A 133 720, 1983.

34. Geuß H. Entwicklung eines anthropometrischen Mebsystems für das CAD-Menschmodel Ramsis. PhD thesis, München University, 1994.

35. R. Happee, M. Hoofman, A.J. van den Kroonenberg, P. Morsink and J. Wismans: "A mathematical human body model for frontal and rearward seated automotive impact loading," in: Proceedings of the 42nd Stapp Car Crash Conference, Tempe, USA, November 2-4, 1998.

36. J. Wismans, A.J. van den Kroonenberg, M.L.C. Hoofman and M.J. van der Horst: "Neck performance of human subjects in frontal impact direction," RTO Specialist' Meeting "Models for aircrew safety assessment: uses, limitations and requirements," Dayton, USA, 26-28 October 1998.

37. E. Lizee, S. Robin, N. Bertholon, J.Y. Le Coz, B. Besnault and F. Lavaste: "Development of a 3D Finite Element Model of the Human Body," in: Proceedings of the 42nd Stapp Car Crash Conference, Tempe, USA, November 2-4, 1998.

Injury Biomechanics from Head to Foot

Albert I. King

6.1 Introduction

This chapter provides the reader with the basics of the biomechanics of impact injury and an up-to-date literature source that can be used for a more detailed study of the subject. The entire body will be covered under the four main branches of impact biomechanics. The branches are injury mechanisms, mechanical response, tolerance and the biofidelity of surrogates. The development of surrogates or test dummies for automotive safety testing depends on a clear understanding of the injury mechanisms involved and of the mechanical response of various body regions to blunt impact. To be able to interpret the measurements made on such a dummy, knowledge of human tolerance to impact is needed. To ensure biofidelity of dummy response, it is necessary to incorporate mechanical components that mimic human response. Dummy design is based on human response data that are obtained largely from testing of human cadavers.

In terms of the design process for a safety system in a vehicle, the dummy is used as a human surrogate in a variety of crash tests and the measurements made on the dummy are compared with established criteria to assess the viability of the design. Thus, the protection afforded to the occupant by the safety system is only as good as the biofidelity of the dummy used. Because of the current proliferation of dummies that represent occupants of different age groups and genders, the reader is cautioned not to assume that all dummies have the same degree of biofidelity and that mechanical response data for dummies are already available. For example, the response of children is not well known but because of the need to evaluate safety and restraint systems for children, child dummies have been developed based on data scaled down from adult responses and not on tests performed on child cadavers.

The specific body regions covered in this chapter are the head, neck, thorax, abdomen, pelvis, spine and the lower extremities. Data on upper extremities are just becoming available and very little is known regarding the response and tolerance of the shoulder.

6.2 Injury Mechanisms

In this branch of impact biomechanics, tests and analyses are conducted to determine the mechanical parameters involved in causing a certain injury. Generally, several reasonable hypotheses are proposed and tested and the one that most consistently produces the same injury emerges as the mechanism of injury. Failure of a long bone occurs as the result of a tensile load being applied to it. In most cases, the tension would come from bending of the bone and thus the mechanism of bony fracture of a long bone is frequently due to the application of a bending moment. In some cases, two different loads or motions can cause the same injury. For example, in the brain, diffuse axonal injury (DAI) can result from angular as well as linear acceleration of the head. In that sense, the injury mechanism for DAI is not unique. However, both of these motions can cause shear stresses to develop in the brain and thus the injury mechanism can very well be shear stress or strain. It is not clear at this time if any injury has a unique mechanism. The mechanisms described below can be found in the literature or are based on recent research results. In the latter case, there will be a cautionary note that no archival literature supporting the mechanism is available.

6.2.1 Head Injury Mechanisms

The major mechanisms of brain injury are discussed in a review article by King et al [1]. They are positive pressure, negative pressure and shear due to pressure gradients or relative motion of the brain with respect to the skull. At the site of impact or the coup site, a positive pressure or compressive stress is developed and a negative pressure occurs at the contrecoup site. These pressures are accentuated by the deformation of the skull; in-bending at the coup site and out-bending at the contrecoup site. Positive pressure can contuse the brain while the mechanism of injury for negative pressure can be due to either tensile loading or cavitation, which is compressive loading due to the collapse of vapor bubbles formed as a result of negative pressure.

Injuries due to relative motion of the brain inside the skull are based on contusions seen on the surface of the brain and on a diffuse form of brain injury called ‘diffuse axonal injury’. This term was first coined by Strich [2], who observed retraction balls forming along injured axons that make up the bulk of the white matter in the brain. She attributed this injury to shear which can be caused by

pressure gradients as well as by motion of the brain inside the skull. This motion is more pronounced when there is a large angular acceleration component of head motion. However, quantitative data of relative brain motion are just becoming available through the work of Hardy et al [3], who used a biaxial high-speed x-ray unit to track radio-opaque targets in an intact and freshly dead cadaveric brain. There is an indication that although relative motion occurs even at mild levels of impact, the extent of the motion is less than that observed in physical models of the brain as well as in previous animal or cadaveric models, such as the 'lexan cavalrium' described by Ommaya et al [4], the sagittal hemisection of Gurdjian and Lissner [5] and the rotational models of Thibault et al [6].

Because of the complex structure of the brain and a possible difference in material properties between the gray and white matter, the development of shear strains or stresses in the brain is not easily visualized. However, axons are apparently stretched in the process and the injury process leads to the enlargement of the axons at locations where there is damage to the microtubules within the axons. Microscopically, this is seen as either retraction balls or enlargements of sections of the axon with the use of appropriate stains.

It has been shown by Gennarelli [7] that although DAI takes a few hours to develop in an injured brain, it is the result of the impact and is not a secondary injury due to other causes, such as ischemia or increased intracranial pressure. Research needs to continue to confirm the injury mechanisms attributed to relative brain motion, as described above. Another severe form of brain injury due to relative brain motion is the rupture of bridging veins that drain blood from the brain into the dural sinus. This short section of vein is stretched when the head experiences a large angular acceleration and the extent of the stretch is particularly large for veins which are directed more anteriorly than medially. This statement is based on a computer model by Zhou et al [8], simulating brain impact. The model predicted that a sudden angular deceleration of a head rotating rearward would tend to cause a bridging vein rupture, such as when a quarterback is sacked and lands on his back, sustaining an occipital impact with a large angular deceleration component.

6.2.2 Neck Injury Mechanisms

Neck injuries can range from mild to catastrophic. Generally, the injuries involving the spinal cord at the higher cervical levels are life threatening while those at the lower levels can result in paralysis. To injure the cord, it is necessary to disrupt the alignment or integrity of the cervical column. Burst fractures of cervical vertebral bodies can propel fragments into the cord and can cause permanent cord damage. Subluxation of one vertebra over another decreases the size of the

spinal canal, again causing cord damage. It is not necessary to sever the cord to produce quadriplegia. If the cord is impacted or crushed temporarily, sufficient damage can be done to paralyze the extremities. In the upper cervical area, separation of the atlas from the occiput is generally a fatal injury. Other life threatening injuries to the upper column are multiple fractures of the arches of C1 and fractures through the pars interarticularis of C2 (hangman's fracture). Milder forms of cervical injury include the so-called whiplash syndrome caused by a rear-end collision. Although clinical literature is frequently portrays this as a real injury, the picture is confused by a multitude of claims of an injury for which the etiology is unknown.

Because of the fact that the neck is slender column which can be subjected to a variety of bending loads in association with an axial load, the injury modes can be classified as compression, tension-extension, tension-flexion, compression-extension, compression-flexion and lateral bending.

6.2.2.1 Compression Injuries

These injuries result from crown impacts to the head which produce a high compressive load on the neck accompanied by bending loads which can depend on the initial orientation of the head, initial orientation of the neck and surface friction. They are not common automotive injuries but can occur in ejections and rollovers. The compression comes from the mass of the body following the head, which is stopped by a resisting surface. It was shown by Pintar et al [9, 10] that for burst fractures to occur, it was necessary to have the neck in the flexed position initially. That is, a high compressive load can only be transmitted from the head to the neck if the cervical spine was straight. Such burst fractures cause fragments of the vertebral body to move out radially in all directions. Those that move posteriorly towards the spinal cord are likely to cause permanent cord injury. Chang et al [11] used a hydraulic sensor to demonstrate that the extent of travel of the fragments exceeds that seen on x-rays and scans following the injury. Nightingale et al [12] showed that fracture dislocation of the cervical spine occurs within the first 10 to 20 milliseconds (ms) of the impact. The subsequent motion of the head depends on its initial orientation as well as on manner in which the neck buckles and on the magnitude of friction between the head and the surface it impacts [13].

6.2.2.2 Tension-Extension Injuries

The whiplash syndrome is frequently associated with this type of injury. It is generally assumed that the injury is result of the hyperextension of the neck, which is also apparently in tension as the neck is stretched out over the headrest or seatback. However, the cervical spine is initially placed in compression by the seatback pushing on the kyphotic thoracic spine. As the thoracic spine tends to

straighten out, it pushes up on the cervical spine and down on the lumbar spine, applying a compressive load on both spines in the process. As a result, the ligaments and tendons holding the cervical spine together are loosened while the vertebrae are required to transmit a large shear force from the torso to the head. Yang and Begeman [14] postulated that this is the mechanism causing soft tissue injuries of the cervical spine. That is, the injury occurs well before the head and neck go into hyperextension. Unpublished data from cadaveric tests at Wayne State University show that there is stretch of the facet capsules within 40 ms after the onset of the impact. Moreover, Bogduk and Marsland [15], Aprill and Bogduk [16] and Lord et al [17] have clinical evidence that the reported neck pain is coming from the facet joint capsules of the neck. Recent volunteer tests by Matsushita et al [18] also show initial compression of the cervical spine and there is anatomical evidence that the facet capsule contains nerve endings which can sense pain [19]. The only possible flaw in this hypothesis is its failure to explain why victims of more severe rear-end impacts do not appear to have as many chronic complaints as those who are involved in minor impacts. If the compression/shear hypothesis is shown to be valid, the most effective manner of preventing whiplash injuries is to redesign the headrest so that it is in constant contact with the head. Preferably, it should be able to push the head forward at the same time as the seatback is pushing the torso, so that the shear force need not be transmitted to the head by the cervical vertebrae.

In more severe impacts, hyperextension injuries do occur. They include teardrop fractures of the anterior-superior aspect of the vertebral body and separation of the disc from the anterior vertebral endplate. At times, a diagnosis of a herniated or bulging cervical disc is made after prolonged complaints of neck pain. Such findings are coincidental and are the result of a pre-existing disc condition, which may have been asymptomatic prior to the crash, or the pain was not constant or severe enough to warrant a visit to the doctor. The basis for this opinion is that intervertebral discs cannot be ruptured as the result of a single loading event in the absence of massive bony fractures of the adjacent vertebrae.

With the advent of the airbag, severe life-threatening injuries to the cervical spine can occur to out-of-position front seat occupants or drivers of short stature. The tension-extension injury is caused by the deploying airbag, a part of which gets under the chin and separates the head from the neck at the atlanto-occipital junction or the C1/C2 junction. A preliminary indication of this hazard was reported by Cheng et al [20], who produced this injury in cadavers using a pre-deployed airbag placed on a vertical steering wheel.

6.2.2.3 Tension-Flexion Injuries

These are relatively uncommon because complaints of chronic or persistent neck pain by belted occupants involved in frontal crashes are rare. In very severe frontal crashes, atlanto-occipital and C2/C2 separation can occur. Thomas and Jessop [21] produced these injuries in subhuman primates that were fully restrained and were subjected to a frontal deceleration of 120 g.

6.2.2.4 Compression-Extension Injuries

These injuries used to occur to unrestrained front seat occupants involved in a frontal crash. When the head impacts the windshield, the neck is placed into extension and compression simultaneously. They are likely to sustain fracture of one or more spinous processes as well as symmetrical lesions of the pedicles, facets and laminae. If there is a fracture-dislocation, the inferior facet is displaced posteriorly and upward and appears to be more horizontal than normal on x-ray [22].

6.2.2.5 Compression-Flexion Injuries

These injuries are similar to those described above under compression injuries when the loading on the head causes the neck to go into flexion. The injuries include burst fractures and fracture-dislocations.

6.2.2.6 Lateral Bending Injuries

Lateral bending occurs when there is a side or oblique impact. This usually is accompanied by shear and axial loading. Lateral wedge fractures of the vertebral body and fractures to the posterior elements on one side of the vertebral column are injuries characteristic of this type of loading. The neck is also frequently subjected to twisting, which can cause unilateral facet dislocations or unilateral locked facets [23]. However, pure torsional loads on the neck are rarely encountered in automotive crashes.

6.2.3 Thoracic Injury Mechanisms

The thorax houses organs essential to life. It is protected to a certain extent by the rib cage and the thoracic spine. The forces encountered in a severe automotive crash are frequently large enough to fracture the ribs and sternum as well as tear the main arteries within the thorax or injure the walls of the heart. At times, high-speed blunt impacts can cause the heart to go into ventricular fibrillation. The lungs can be contused by impact with the chest wall or by the passage of compression waves through the alveolar tissue. Lungs can also be lacerated by the ends of fractured ribs. The various injury types appear to be dependent on the rate of loading because of the viscoelastic nature of the tissues involved. At

low rates of loading, the injury is due to deformation of the rib cage or crushing. At very high rates of loading, such as a pressure wave from an explosion or impact to the chest by a blunt object (non-lethal weapons), the injury is a function of the speed of the wave or of the missile. For automotive crashes, both deformation and rate of loading play a role in injury causation.

6.2.3.1 Low Speed Crush Injuries

For impact speeds below 3 meters per second (m/s) [about 5 miles per hour (mph)], the contents of the thorax are injured by the crushing of the rib cage. As will be shown later, the amount of crush necessary to induce injury is around 35 percent of the depth or width of the thorax [22]. The injury mechanism is compression of the organs.

6.2.3.2 High Speed Impact Injuries

The transmission of a pressure wave through the chest wall by a high-speed blunt projectile or by a blast wave causes the alveolar tissues of the lung to break down. This is because the speed of sound in the tissue is extremely low and the pressure wave is akin to a supersonic wave passing through it. The heart is also susceptible to this type of slap impact, which can either contuse heart walls or septa or disrupt the electrical conduction system of the heart, causing it to go into a fatal ventricular fibrillation. Baseball impacts at speeds of about 100 kilometers per hour (km/hr) [60 mph] to the sternum of Little Leaguers kill a few of them each year [24]. The mechanism is unknown, but there is a possibility that the impact needs to occur during the T-wave of the EKG cycle for the ventricle to go into arrhythmia [25]. The fibrillation occurs almost immediately after impact and attempts at resuscitation by CPR have not been successful. The same situation exists for out-of-position occupants of cars whose chest is impacted by a deploying airbag or for a policeman wearing a bulletproof vested and being struck in the chest by a bullet. In general, the speed of impact is in the range of 35 to 50 m/s or higher.

6.2.3.3 Automotive-Related Chest Injuries

In the range of 5 to 30 m/s, the injury mechanism is compression accompanied by shear and tensile loading. Aortic ruptures can occur in both frontal and lateral impacts to the chest, although, in the cadaver, such ruptures has not been reproduced in simulated frontal impacts. That is, the blood vessels are apparently more vulnerable in a side impact. Since the rupture tends to occur at attachment points of inter-arterial ligaments, it is postulated that these points constitute areas of stress concentration. As for the lung, the extent of damage depends not solely on the degree of compression of the chest but also by the speed of impact. This is based on studies by Viano and Lau [26], who chose the liver as a target organ and performed impacts with different combinations of speed and

compression to establish the dual dependency in this speed range. Animal models were used for this study.

6.2.4 Abdominal Injury Mechanisms

For automotive-related impacts, the same principle of dual dependency on compression and velocity holds. The solid organs appear to be more at risk than the hollow organs. Moreover, injury to the liver and spleen can be life threatening. Simulated frontal impacts of the steering wheel on the thorax and abdomen of unembalmed cadavers by Nusholtz [27] produced injury to the solid abdominal organs. Cadaveric impacts to the lower abdomen with a 25.4-mm diameter impactor [28] did not produce severe injuries to the hollow organs, such as the large and small intestines. Belt-induced injuries to both the hollow and solid organs have been seen in the field. These injuries were attributed by Leung et al [29] to either the shoulder belt or the lapbelt. It was felt that lower abdominal organs could only be injured severely by the lapbelt in association with submarining of the occupant [29].

6.2.5 Injury Mechanisms of the Thoraco-Lumbar Spine

The frequency of injury to the thoraco-lumbar spine is very low (less than 1 percent), based on relatively old data reported by King [30]. However, if the injury involves the spinal cord, paraplegia can result. To understand the mechanisms of injury to the thoraco-lumbar spine, it is necessary to review briefly the contributions made by many investigators in the area of spinal injuries resulting from pilot ejection in which the spine is subjected to a caudocephalad (tail-to-head) acceleration. Anterior wedge fractures of the lower thoracic and upper lumbar are seen in pilots who eject. Vulcan et al [31] determined that the mechanism of injury for these wedge fractures is a combined compressive and bending load. The bending is due to the fact that the center of mass of the torso is anterior to the spine. Prasad et al [32] demonstrated that there are two load paths down the spine to transmit vertical (axial) compression generated by inertial loading, depending on the orientation of the lumbar spine. The two load paths are the discs and the articular facets that transmit compressive load by bottoming the tips the inferior facets onto the laminar of vertebra below. Belted occupants involved in severe frontal crashes can also sustain anterior wedge fractures of the thoracolumbar spine due to the same mechanism but from a different loading source. In this case, there is no vertical inertial loading but the compressive load is generated by the kyphotic thoracic spine, which tends to straighten out against the lap belt during the crash. This mechanism is the same as the one that imposes a compressive load on the cervical spine during a rear-end collision. However, it was first confirmed experimentally by Begeman et al [33] after it was predicted by a two-dimensional spinal model developed by Prasad and King [34].

Another spinal injury involves lapbelted occupants in the rear seat. If the belt is worn above or slips off the iliac crest as the subject submarines, the belt compresses the soft tissues of the lower abdomen and the lumbar spine uses the belt as a fulcrum when it hyperflexes over it. The fracture starts along the posterior aspect of the spine and travels anteriorly. If the fracture goes beyond the laminae, it can cause spinal cord damage. These fractures are known as Chance fractures [35].

In terms of other forms of soft tissue damage, there is a frequent complaint of low back pain following an automotive collision. The impact severity can range of a minor fender bender to a very high-speed crash. In some cases, a herniated disc is diagnosed and the treating physician will almost invariably attribute the rupture to the crash. However, predominant findings in the literature indicate that disc rupture is a slow degenerative process and than an extremely violent single loading event is needed to cause the nucleus pulposus to extrude from the side of the disc. That is, a single load cannot rupture a disc unless there are concomitant fractures of the adjacent vertebrae. Intervertebral discs do not herniate like a balloon and back pain is not solely due to the disc. There are many sources of back pain, including the facet capsules and a causal relationship between an impact and a ruptured disc does not exist. King [36] provides a more detailed discussion.

6.2.6 Pelvic Injury Mechanisms

Common injuries to the pelvis in frontal impacts result from severe knee loading into the dash. As a result, the head of the femur pushes into the acetabulum causing it to displace posteriorly. If the hip is abducted, a rearward impact to the femur can cause an anterior dislocation of hip [37]. Separation of the pelvis from the sacrum at the sacroiliac joint can occur if the knee is wedged between the front seat back and the dash [38]. However, even though high lap belt loads are encountered in severe frontal crashes, they are not known to cause separation of the sacroiliac joint.

In side impact, the door impacts the greater trochanter of the femur, which in turn pushes the acetabulum medially. The most frequent injury in this case is pubic rami fractures followed by acetabular fractures [39]. Rami fractures are the result of bending loads applied through the acetabulum while acetabular fractures are due to compressive forces transmitted through the femoral head. It should be noted that hip fractures, including femoral neck fractures and greater trochanteric fractures, normally associated with falls in the elderly do not occur routinely in side impacts. However, according to surveillance data on falls among the elderly, over 90 percent of those who fall and fracture their hip, fall to the side, and yet of

all of those who fall, less than 2 percent fracture their hip. That is they sustain femoral neck or greater trochanteric fractures. For this reason, Yang et al [40] have proposed an alternate hypothesis that elderly hip fractures are spontaneous and that these spontaneous fractures are more prevalent than the currently accepted figure of 10 percent. The proposed mechanism of muscle loading is being tested at this time.

6.2.7 Injury Mechanisms of the Lower Extremity

Injury to the lower extremities have taken on renewed significance because of the severity of the injuries among unbelted occupants in airbag-equipped cars is high. This phenomenon is due largely to the survival of these occupants in severe frontal crashes that would have killed them had their cars not been equipped with an air bag. Researchers have also identified a major cause of severe lower extremities – offset impacts, which are frontal impacts involving only the driver side of both cars. This partial head-on crash is not as severe as a full frontal crash but there can be major intrusion of the footwell area to cause injuries to the joints and bones of the lower extremities.

The lower extremity is composed of three principal body segments, the thigh, shank and foot, and two highly mobile joints, the knee and ankle. The foot is composed of 27 bones with many articulating surfaces, but the range of motion of the joints of the foot is much less than that of the ankle and knee. The mechanism of injury for bone is generally tension due to some form of bending applied to the bone. This applies to the shaft of long bones as well as to portions of long bones, such as the lateral malleolus of the tibia. Injury to the joints involve disruption of the ligaments and damage to other soft tissues, such as rupture of the tendons, tearing of the menisci of the knees and damage to the articular cartilage.

6.2.7.1 Knee Joint Injuries

In sports, the knee is the most commonly injured joint of the lower extremity. However, it is also frequently injured in motor vehicle crashes when it comes into contact with the instrument panel or dash [41]. In the past, if the shank or leg is impacted just below the knee with no patella contact, the posterior cruciate ligament was frequently ruptured. Current vehicles have a dashboard which slopes down and away from the occupant, ensuring that this ligament is preserved. Current vehicles also have relatively hard surfaces, which can cause patella fractures. Hayashi et al [42] have shown that the dash needs to be covered with a pad that has a stiffness of about 670 kiloPascals (kPa) to prevent both patella fractures as well as a split fracture of the distal femoral condyles. Softer padding will cause the knee to be pocketed in the dash, allowing large bending moments to develop in the femur and causing it to fracture near the mid-shaft. The bending load is in

the plane of the dash and subjects the femoral shaft to bending about the two axes normal to the longitudinal axis. Atkinson et al [43] indicate that sub-fracture level impacts to the patella can result in degeneration of the articular cartilage in the patello-femoral joint. This is due to damage to the subchondral bone that can eventually lead to osteoarthritis.

6.2.7.2 Ankle Joint Injuries

Common bony injuries at this joint include fractures of the medial and lateral malleolus, fracture of the neck of the talus and pylon fracture of the distal tibia. Soft tissue injuries include rupture of the many ligaments around the ankle. In offset impacts, footwell intrusion can place the foot in dorsiflexion as well as in inversion or eversion. These rotational motions can cause talar and malleolar fractures and ligamentous injuries [44, 45]. Pylon fractures appear to be due to the simultaneous application of a large brake pedal load through the mid-foot in concert with the application of a large calf muscle force. This fracture is seen in severe frontal crashes but is difficult to reproduce in cadaveric tibiae due to the need to simulate a constant muscle force along the calf. A recent report by Kitagawa et al [46] describes how this fracture can be reproduced in the laboratory. This is an important finding because pylon fractures constitute one of the most serious lower extremity disabilities.

6.2.7.3 Fractures of the Long Bones

Midshaft fractures of the femur and tibia are generally due to the application of a bending load. For the femur, the bending moment is due to a load applied at the knee after it is pocketed into a soft dash. Tibial shaft fractures are due to a force applied directly to the shaft from such structures as the bottom corner of the dash.

6.2.7.4 Fractures of the Bones of the Foot

Very little work has been done to study the mechanism of injury involving foot fractures. In an attempt to create pylon fractures, Kitagawa et al [46] produced a split fracture of the calcaneus caused by tension in the Achilles tendon. Oddly enough, these muscle-induced fractures occurred at a higher impact force to the mid-foot than those that caused pylon fractures in the tibia. That is, if the distal tibia had a higher tolerance, the calcaneus would fracture instead. Other attempts to cause pylon fractures without the help of the calf muscles were unsuccessful. In one such attempt, a direct compressive load was applied to the tibia through the bottom of the calcaneus. In this situation, the calcaneus sustained a crush fracture and a pylon fracture could not be produced because the fracture limited the magnitude of the peak force that can be transmitted to the tibia.

The talus can be fractured at the neck by dorsiflexing the foot. The brake pedal can fracture the metatarsal bones, but the precise mechanism is unknown.

6.3 Mechanical Response

Mechanical response data obtained from impacts to human cadavers are needed to design more human-like dummies. Response data can also be compared with their human equivalent to determine if that particular region of the animal is a good human surrogate. As in the study of injury mechanisms, response data are collected from individual body regions such as the head, neck, chest, abdomen, and the lower extremities. Response data are just becoming available for the upper extremities and some side impact data are available for the shoulder. In general, response data take the form of a load-deformation curve where the load can be either a force or a moment and the corresponding deformation is either a linear or angular displacement. The early data obtained by biomechanical researchers, such as Yamada [47], provided static response. However, it was determined that the response of many body tissues is dependent on the rate of loading, and dynamic tests at various rates of loading were carried out.

Other forms of response data include force-time histories, displacement-time histories of an impact or force and acceleration as a function of a relevant independent variable, such as drop height. If both sets of time histories are available, a cross-plot of the data would yield a force-deflection curve. Thus, time-histories are rudimentary response curves, which are used in the absence of load-deformation curves. In orthopedic biomechanics, the response of individual tissues, such as compact bone, cartilage and ligaments, are obtained in the form of force-deflection curves and/or stress-strain curves. These data are usually more basic than what are needed for impact biomechanics used in the automotive safety setting.

6.3.1 Mechanical Response of the Head

6.3.1.1 Mechanical Response of the Skull

Early response data of head impact consisted of the response of the entire head as a function of drop height or impact speed. Hodgson and Thomas [48] of Wayne State University (WSU) provided such response data for embalmed cadaveric heads impacting a variety of rigid and padded surfaces. Figures 6.3.1.1.1 and 6.3.1.1.2 show two such response curves, peak force and peak acceleration as a function of free-fall drop height, for impacts against a rigid. When a rigid pendulum impacted the head, the independent variable became the velocity of

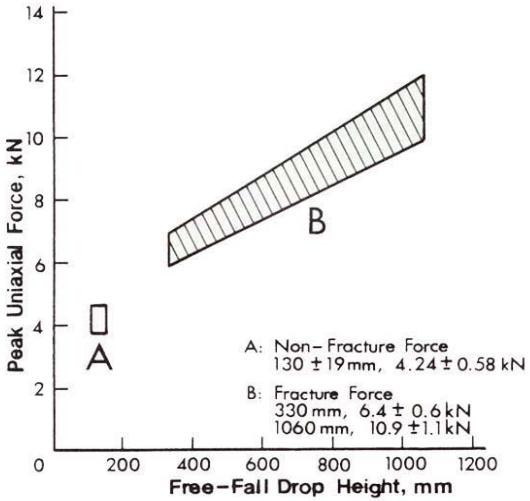

Fig. 6.3.1.1.1 **Head impact response – peak force/drop**

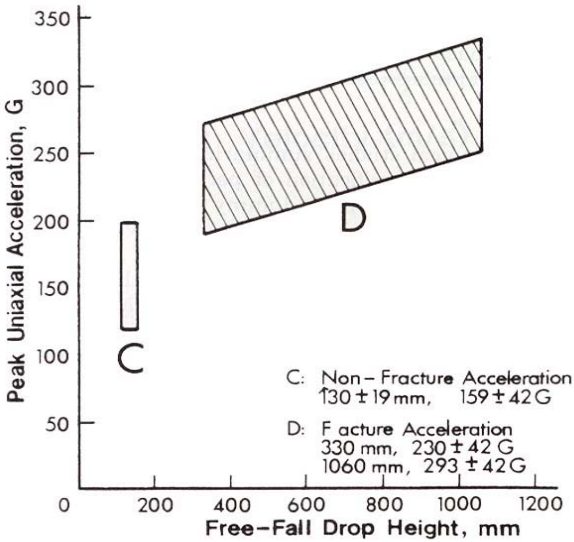

Fig. 6.3.1.1.2 **Head impact response – peak acceleration/ drop height**

impact of the pendulum. Such data were acquired by McElhaney et al [49] at the Highway Safety Research Institute, presently known as Transportation Research Institute, The University of Michigan (UMTRI). In these tests, fresh cadavers were used. These data are shown in Figure 6.3.1.1.3, in which the WSU data have been re-plotted in terms of impact velocity instead of free drop height. The data are not directly comparable, indicating the wide variation in response in biological specimens. It should also be noted that scalp thickness is greater in embalmed heads than in unembalmed ones because some of the embalming fluid is retained

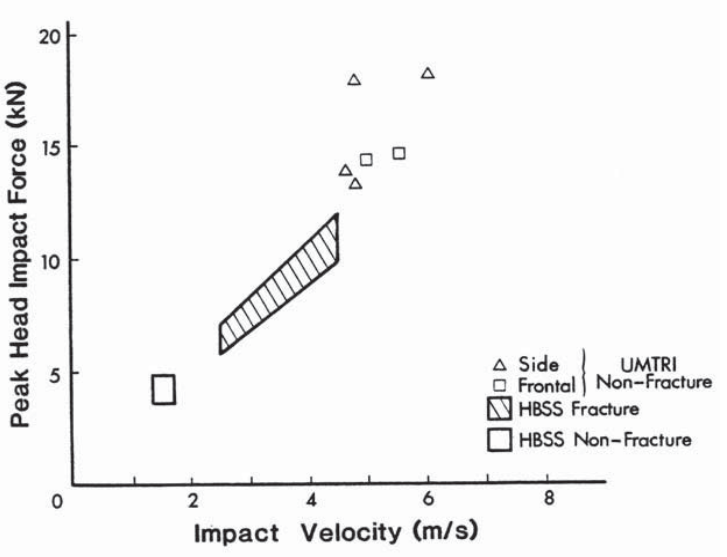

Fig. 6.3.1.1.3 **Head impact response – peak force/ pendulum impact velocity**

in the scalp after the completion of the embalming process. However, this fact alone does not explain the discrepancy in the data shown in Figure 6.3.1.1.3. Data obtained from impacts against rigid surfaces are particularly useful for the design of dummy heads, which are usually metal head forms covered by a soft vinyl cover. The stiffness of the cover can be tuned to mimic head impact against a rigid surface to produce a dummy head with a human-like response. The Hybrid III dummy head was developed based on these data [50].

6.3.1.2 Mechanical Response of the Face

The influence of facial structures on head impact response has received little attention. The primary concern in head injury research has been to prevent serious brain injury. Injury to the face, while presenting the problem of possible disfigurement, has not been considered as serious in nature as that of brain injury. Experiments have been conducted to produce injury to the facial structures but it is not known if fracture of the facial bones can reduce the severity of injury to the brain.

The mechanical response of the face depends on the properties of the overlying soft tissue and the stiffness of the 14 facial bones. While biomechanical studies have been conducted on the major facial bones, the primary thrust was to attempt to establish tolerable force values. As such, the majority of the experiments were not structured to provide impact response directly. There are, however, two exceptions.

The first is a series of sub-fracture experiments on a single instrumented embalmed cadaver was conducted by Hodgson et al [51]. Static loads were applied to the zygoma or the zygomatic arch and the resulting deflections were recorded for both loading sites at loads of up to 445 Newtons (N) (100 lb) for the arch and 890 N (200 lb) for the zygoma. The resulting stiffnesses were found to be 1734 N/mm (9900 lb/in) for the zygomatic arch and 4939 N/mm (28,200 lb/in) for the zygoma. Generally, similar force-deformation relationships were found for both static and dynamic loads.

The second exception is a series of drop tests performed by Tarriere et al [52]. Unembalmed cadaveric faces with and without a rigid mask were dropped onto a flat rigid surface. The mask served to distribute the impact load across the entire face and enabled the researchers to estimate the total energy absorbed by the face during impact. For a drop height of 2.5 mm (8.2 ft), without a mask, the measured peak acceleration was 165 g. With the mask at a drop height of 3.5 m (11.5 ft), the peak head acceleration was reduced to 135 g, but the peak forces were essentially the same. These response characteristics are considerably lower than those of the skull. Thus, impact to the face produces significantly lower head acceleration and force than a similar impact to the skull.

6.3.1.3 Impact Response of the Brain

Although many attempts have been made to determine the relative of motion of the brain inside the skull as a result of a blunt impact, reliable quantitative data were made available by Hardy et al [3] only very recently. Previous studies using the lexan calvarium, sagittal hemi-sections and physical models lacked the assurance that the data would be the same if an intact brain was used. Hardy et al

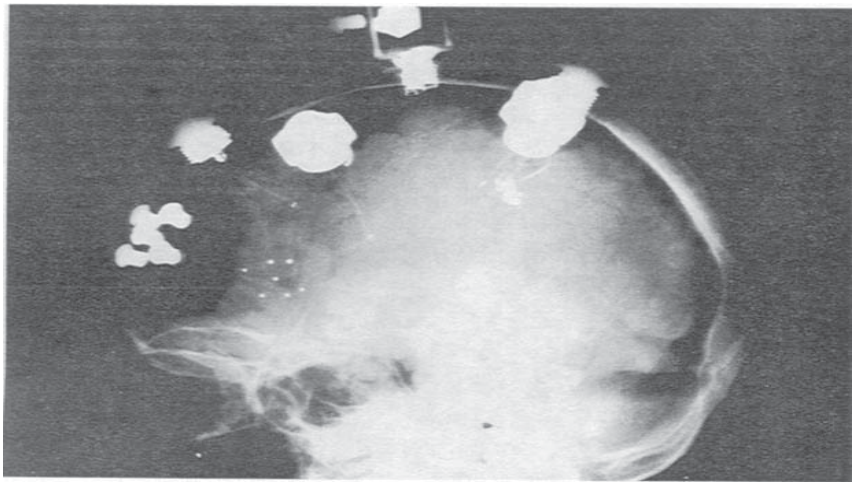

Fig. 6.3.1.3.1 **X-ray of cadaveric brain**

[3] obtained quantitative data by the use of a high-speed biaxial x-ray machine which produced x-ray pictures of an instrumented cadaveric brain at 500 frames per second (fps). Neutral density accelerometers (NDA) and low density radio-opaque targets were inserted into an intact unembalmed cadaveric brain that was exposed to room temperature for a total of less than 24 hours after death. Preliminary data are encouraging. Figure 6.3.1.3.1 shows a single frame of the x-ray image in which the two NDA's (small squares), the two pressure transducers (ovals) and low density targets (small dots) can be clearly seen. Because of the fact that biaxial images were obtained, the precise three-dimensional coordinates of each object can be obtained from each frame. The relative displacement of the brain with respect to the skull measured from the x-ray images matched that computed from acceleration data from the skull-mounted accelerometers and the neutral density triaxial accelerometer. For low-level occipital impacts of 60 to 100 g, the displacement curves computed from the two different methods were identical, as shown in Figure 6.3.1.3.2. The radio-opaque targets yielded strain data that had an approximate resolution of 2 percent. The strain along a posterior-anterior axis due to a 100-g occipital impact was approximately 8 percent. As more of these data become available, it will finally be possible to assess the relationship between brain strain and impact severity. The data are also extremely useful for the validation of finite element models of the brain.

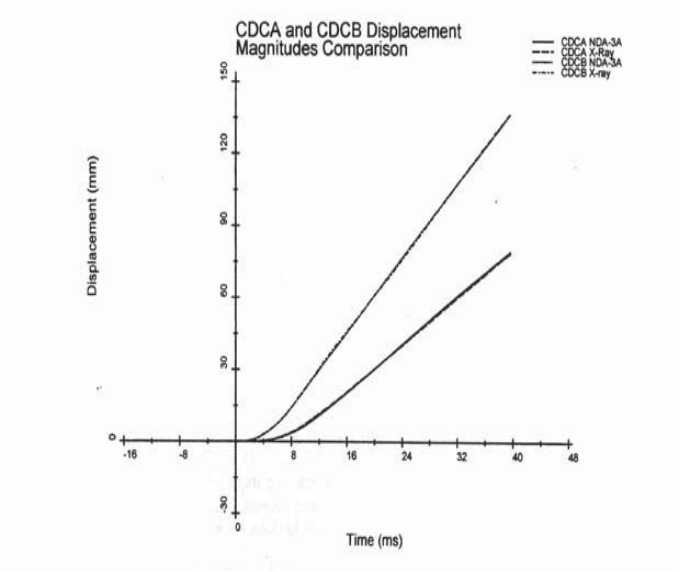

Fig. 6.3.1.3.2 **Comparison: absolute displacement of the brain**

6.3.2 Mechanical Response of the Neck

The response of the cervical spine to loads from different directions has been studied by Mertz and Patrick [53, 54], Patrick and Chou [55], Schneider et al [56], Ewing et al [57] and more recently by Camacho et al [13]. Mertz et al [58] elected to quantify response in terms of rotation of the head relative to the torso as a function of bending moment at the occipital condyles. Loading corridors were obtained for flexion and extension, as shown in Figures 6.3.2.1 and 6.3.2.2. These data form the basis for the design of the Hybrid III dummy neck. Volunteer data on neck bending were obtained by Patrick and Chou [55], using the WSU WHAM III sled. Neck response curves for sagittal flexion and extension, from four test subjects, were found to fall within the loading and unloading corridors established by Mertz and Patrick [53, 54], upon which the loading corridors of Mertz et al [58] were based. Figure 6.3.2.3 is the response envelope for lateral flexion, proposed by Patrick and Chou [55], based on their volunteer data. They did not suggest a corridor for oblique flexion, indicating that further study was necessary. However, they did document ranges of static voluntary motion for all loading directions

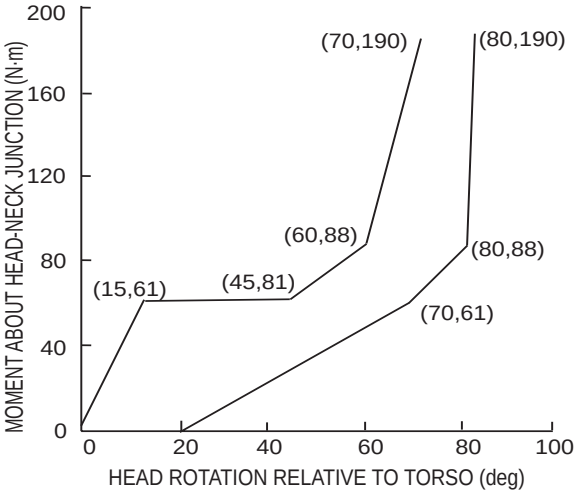

Fig. 6.3.2.1 **Neck response in flexion**

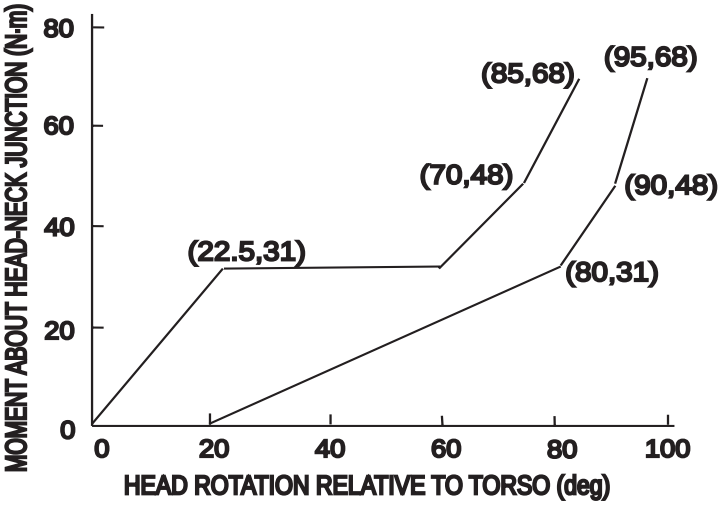

Fig. 6.3.2.2 **Neck response in extension**

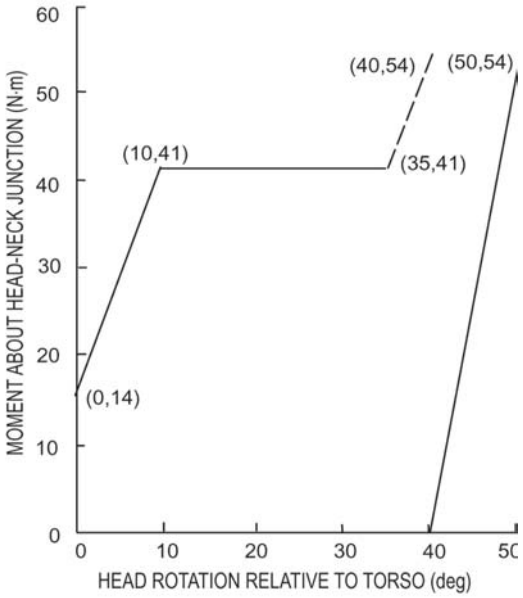

Fig. 6.3.2.3 **Neck response in lateral flexion**

studied. These data are reproduced in Table 6.3.2.1 – Voluntary Range of Static Neck Bending.

Schneider et al [56] have also studied the lateral flexion response properties of the human neck. They tested 96 male and female volunteers, ranging in age from 18 to 74 years. They also documented their head and neck anthropometric information. The three-dimensional range of motion of the head relative to the torso was measured and the response of the head and neck to low level acceleration was studied. Data regarding the stretch reflex time and voluntary lateral isometric muscle force were included. Total planar ranges of motion were reported in the form of averages for various age groups and each gender. The overall averages for sagittal and lateral motion were 103.7 and 71.0 degrees (deg) respectively. Rotation of the head about a superior-inferior axis had an overall range of 136.5 deg. Stretch reflex times varied from about 30 to 70 ms. Average isometric lateral pull forces ranged from 52.5 N (11.8 lb) for elderly females to 142.8 N (32.1 lb) for middle-age males. The authors concluded that, for a complete surprise impact, the total time to reach maximal muscle force is on the order of 130 to 170 ms and is probably too long to prevent injury in a high-speed collision.

TABLE 6.3.2.1: **Voluntary range of static neck bending [55]**

Volunteer	Flexion (deg)	Extension (deg)	Total Range (deg)
LMP	51	82	133
KJD	65	73	138
SAT	63	69	132
Lateral Flexion			
	Left (deg)	Right (deg)	
LMP	42	43	85
SAT	35	39	74
Oblique Flexion 45 Deg Mode			
	Toward (deg)	Away (deg)	
LMP	35	56	91
Oblique Flexion 135 Deg Mode			
	Toward (deg)	Away (deg)	
LMP	53	38	91

The voluminous data acquired at the Naval Biodynamics Laboratory in New Orleans constitute a valuable source of neck response data for volunteers who were tested to relatively high acceleration levels. Some data have been analyzed by Wismans and Spenny [59, 60], but the bulk of the data have not. Frontal response data were analyzed and compared with cadaveric responses by Wismans et al [61]. Head trajectories were found to be comparable but the cadaveric head rotation was larger than that of the volunteer. A new MADYMO neck model simulating volunteer head-neck response was recently reported by van der Horst et al [62]. Curved lines were used to simulate the lines of action of muscles and a delay time for muscle activation was incorporated into the model. However, this delay was not based on muscle stretch or stretch rate. The model was validated against available lateral and frontal impact data. It was concluded that the delay in muscle activation was an important element in producing realistic results and that active muscle behavior was essential to describe human-neck impact response accurately.

There have also been several recent studies involving neck extension in simulated

rear-end collisions. Matsushita et al [18] and Ono et al [63] obtained x-ray movies of volunteer neck motion at 90 fps. It was found that the neck was in compression due to the upward ramping of the torso on an inclined seat back and that there was more relative rotation in the lower cervical vertebrae (C5-6), leading to the hypothesis that the injury could be in the facet capsules in low speed rear-end collisions. More recent unpublished results obtained from cadavers and through the use of a biaxial high-speed x-ray/camera device at frame rates in excess of 250 per second demonstrated that compression began early in the impact event and that there was both relative translation and rotation between adjacent lower cervical vertebrae.

Camacho et al [13] studied the response of the cervical spine due to a crown impact to the head. High-speed video pictures were obtained to show the buckling mode of the cervical spine. The response was characterized by a finite element model of the cervical spine. Figure 6.3.2.2 shows the time course of the buckling for a crown impact against a rigid surface.

6.3.3 Mechanical Response of the Thorax

6.3.3.1 Frontal Thoracic Response

6.3.3.1.1 Response to Flat Impactors

In the automotive environment, the thorax can be loaded frontally by a rigid or deformable surface, such as an instrument panel, steering wheel or shoulder belt. Frontal response was first studied by Patrick et al [64], who tested several embalmed cadavers statically and dynamically. Antero-posterior static stiffness was found to vary from 32.4 to 70.0 kiloNewtons per meter (kN/m) (185 to 400 lb/in) when the chest was loaded by a 102-mm (4-inch) wide bar. Dynamic stiffness prior to rib fracture, based on impacts with a 152-mm (6-inch) diameter padded pendulum, was approximately 175.1 kN/m (1000 lb/in) for loads up to 4 kN (900 lb). The stiffness dropped markedly after the ribs fracture but it recovered to about half the pre-fracture stiffness when the internal organs were compressed. The stiffness increased with loading rate. The static stiffness of an unembalmed thorax was found to vary from 6.3 to 10.9 kN/m (36 to 62 lb/in). Dynamic data were obtained by Nahum et al [65] and Kroell et al [66] using a 152-mm (6-inch) impactor, weighing 227 N (51 lb) or 191 N (43 lb). Response corridors for impact speeds of 4.9 m/s (11 mph) and 7.2 m/s (16 mph) are shown in Figure 6.3.3.1.1.1. They were based on a large number of cadaveric tests and were used to design the Hybrid III dummy chest, as will be discussed in Section 6.5.2 – Mechanical Response.

Patrick [67] performed a courageous study on himself in 1970, using a 10-kg (22-lb) pendulum. Its diameter was 152 mm (6 in) and its surface was padded with 24

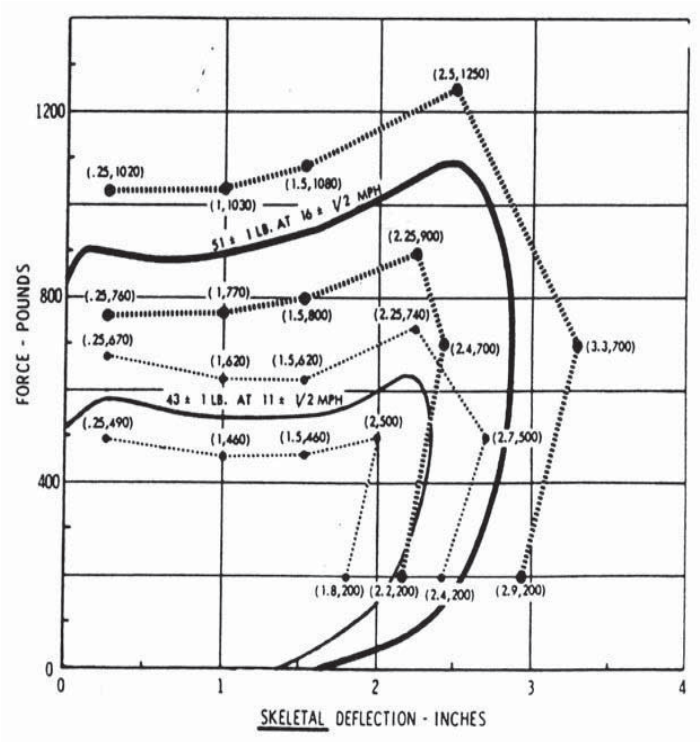

Fig. 6.3.3.1.1.1 **Adjusted force-skeletal deflection curves**

mm (15/16 in) of rubber padding. Impact velocities ranged from 2.4 to 4.6 m/s (8 to 15 ft/s). Tests were conducted with the subject tensed and relaxed, except at the highest velocity, at which only tensed impacts were conducted. Impact force and chest deflection was measured. The data are shown in Figures 6.3.3.1.1.2 and 6.3.3.1.1.3, which compare initial stiffness and plateau force respectively with cadaveric data. Although there is a belief that the cadaveric data needed to be increased to simulate a tensed living human, the data shown in Figure 6.3.3.1.1.2 indicate that Patrick's data agree better with the unadjusted cadaveric data.

6.3.3.1.2 Response to Belt Loading

The diagonal shoulder belt elicits quite a different response from the thorax than a 152-mm (6-inch) diameter impactor. Schmidt et al [68] and Patrick and Levine [69] have reported asymmetric rib fracture patterns in which all of the fractures were in the sternum or the lower in-board rib cage. This difference can be exemplified by

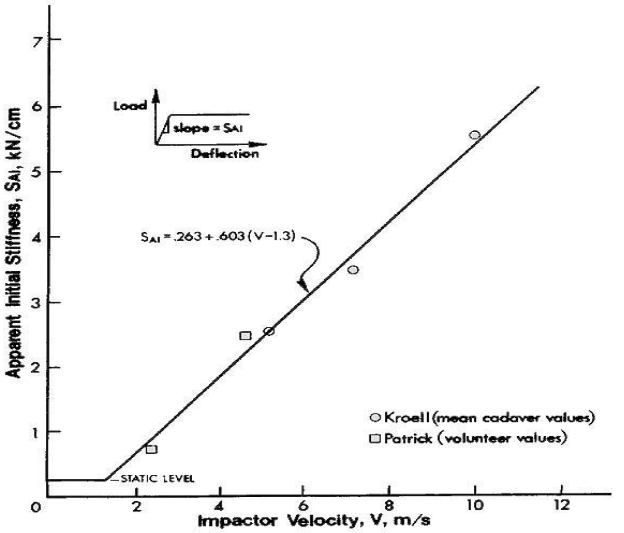

Fig. 6.3.3.1.1.2 **Initial stiffness of the load-deflection response of the chest**

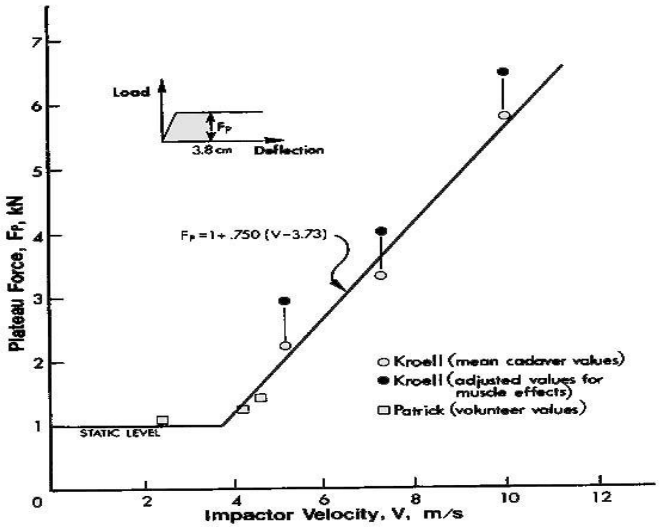

Fig. 6.3.3.1.1.3 **Plateau force versus impactor velocity**

static volunteer data acquired by Fayon et al [70]. Belt loading stiffness at the sternum ranged from 17.5 to 26.3 kN/m (100 to 150 lb/in) while disc loading ranged from 8.8 to 17.5 kN/m (50 to 100 lb/in). The belt loading stiffness of the second rib was from 17.5 to 26.3 kN/m (100 to 150 lb/in) while that of the ninth rib was from 8.8 to 17.5 kN/m (50 to 100 lb/in). L'Abbe et al [71] provided additional volunteer belt-loading stiffness data. For loads of up to 650 N (150 lb) and deflections of 10 mm (0.4 in), the static stiffness under the belt was 67.6 kN/m (386 lb/in) at the mid-sternum, 40.0 kN/m (228 lb/in) at the seventh rib and 94.8 kN/m (541 lb/in) at the clavicle. Their dynamic loads peaked at 3.6 kN (810 lb) and their dynamic deflections were twice the static values. The dynamic belt-loading stiffness averaged 137.5 kN/m (785 lb/in) at the mid-sternum, 123.2 kN/m (703 lb/in) at the seventh rib and 200 kN/m (1142 lb/in) at the clavicle.

Walfisch et al [72] reported a dynamic belt-loading stiffness of about 70.0 to 161.1 kN/m (400 to 920 lb/in). The data are approximate because the deformation was given as a percentage of chest deflection and a 9-inch chest depth was assumed. The mean stiffness was 119.4 kN/m (682 lb/in).

Belt loading response of the pig thorax was studied by Verriest et al [73]. Living and dead pigs were tested dynamically at velocity levels of 40 to 55 km/hr (25 to 34 mph). These mini-pigs had a mean weight of 428 N (96 lb). Their chest depth was larger than that of the human, averaging 0.3 m (11.9 in) while their mean chest breadth was 0.25 m (10 in). All thoracic force-deflection curves exhibited an initial low stiffness region with a concave-upward stiffening behavior up to about 25 to 50 mm (1 to 2 in) of deflection. This was followed by a high stiffness response up a maximum deflection of 100 to 150 mm (4 to 6 in). The dead animals had a low stiffness of 35.7 kN/m (204 lb/in) and a high stiffness of 115.7 kN/m (661 lb/in) – a value remarkably close to the cadaveric data obtained by Walfisch et al [72]. The stiffness of living pigs was slightly over half the value of dead pigs.

It is not clear why the static stiffness values provided by Fayon et al [70] were much lower than corresponding data by L'Abbe et al [71]. One possible explanation is that the supine posture of the subjects used by Fayon et al [70] caused the spine to assume a curved shape, which could have lowered the apparent stiffness of the rib cage.

Corresponding stiffness data obtained from a Hybrid III dummy showed that it was stiffer than volunteer data. Also, the entire dummy chest deflected under a belt load while in the human, there is asymmetric deformation of the rib cage [71].

6.3.3.2 Side Impact Thoracic Response

Stalnaker et al [74] conducted the first side impact tests on the left side of six unembalmed cadavers. A 152-mm (6-inch) diameter flat impactor with a mass of 10 kg (22 lb) was used at two impact speeds – 6.1 and 8.8 m/s (20 and 29 ft/s). The initial dynamic stiffness ranged from 273.6 to 437.8 kN/m (1563 to 2500 lb/in) at 6.1 m/s (20 ft/s). At the higher velocity, the values were 437.8 and 790.0 kN/m (2500 to 4500 lb/in).

Drop tests were then conducted by Stalnaker et al [75] in which the thorax, abdomen and pelvis of unembalmed cadavers were dropped on their sides against rigid or padded surfaces instrumented with load cell. The drop heights were 1.0 m (3.3 ft) for rigid impacts and 2.0 m (6.6 ft) for padded impacts. The dynamic stiffness of the thorax was found to range from 96.8 to 255 kN/m (553 to 1457 lb/in).

Pendulum impacts conducted by Viano et al [76] were directed at a 60-deg angle from the antero-posterior axis to ensure that the photographically measured deflection did not involve any whole-body rotation of the rib cage. The flat impactor used had a rigid surface. It was 152 mm (6 in) in diameter and had a mass of 23.4 kg (51 lb). The three impact speeds used were 4.3, 6.7 and 9.5 m/s (10, 15 and 20 mph). The force-deflection curves for these three speeds of impacts are shown in Figure 6.3.3.2.1. Stiffness values were not computed but the suggested corridors had an initial stiffness of 100 to 140 kN/m.

Chest contour data using a chest band developed by Eppinger [77] were obtained by Huang et al [78] and by Pintar et al [79]. These are plots of the cross-sections of the ribcage in the transverse plane (chest and/or upper abdomen) at discrete instants of time, assuming that the spine is not deformed during impact. They provide a measure of the total chest compression in a side impact, but if a force-deflection curve is to be plotted, additional force data need to be supplied.

6.3.4 Mechanical Response of the Abdomen

Mechanical response data from impacts to the abdomen, particularly frontal impact data, are somewhat sparse. The only published cadaveric response data of the lower abdomen from simulated frontal impacts were provided by Cavanaugh et al [28]. Unpublished frontal impact response data by Nusholtz et al [27] for the lower abdomen are also available in the same velocity range. There were several side impact cadaveric studies beginning with that by Walfisch et al [80] and followed by the work of Viano et al [76] and Cavanaugh et al [81]. Animal (subhuman primate) experiments were conducted by a number of investigators at UMTRI. Some of the data collected in the 1970s were analyzed, scaled and summarized by Stalnaker and Ulman [82]. Normalized stiffness data were provided for the upper, middle and lower abdomen for frontal as well as side impact.

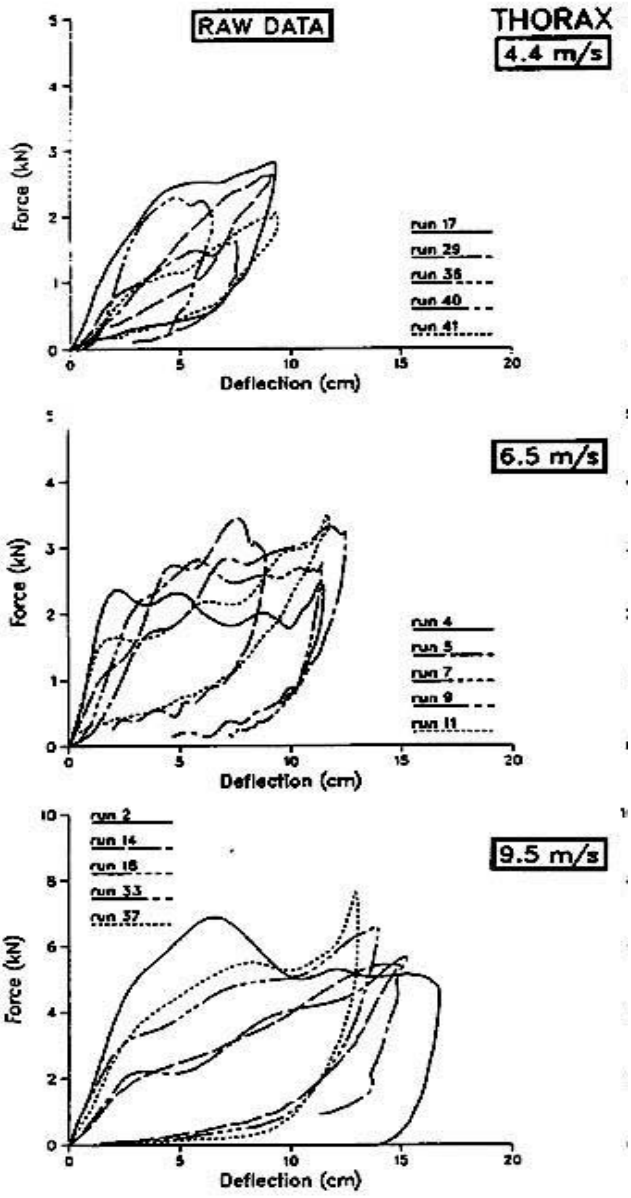

Fig. 6.3.3.2.1.1a **Force-deflection and force-time response for chest impacts--Raw Data**

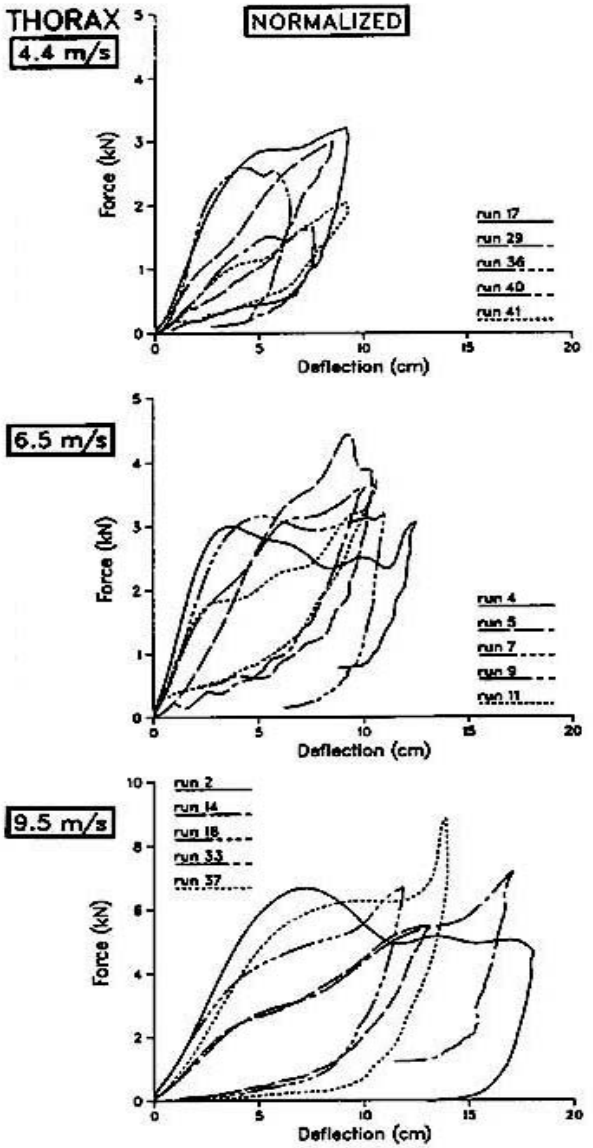

Fig. 6.3.3.2.1.1b **Force-deflection and force-time response for chest impacts--Normalized**

6.3.4.1 Mechanical Response for Frontal Abdominal Impact

It is interesting to make a direct comparison of the available frontal impact response data. The data are comparable because the scaled subhuman primate data provided by Stalnaker and Ulman [82] were done with impactors that are from 12.7 to 50.8 mm in diameters at velocities ranging from 8.4 to 15.7 m/s while the human

TABLE 6.3.4.1.1: **Lower abdominal frontal impact stiffness**

Source	Stiffness (kN/m)
Cavanaugh et al [28]	53.9
Nusholtz et al [27]	52.7
Stalnaker and Ulman [82]	23.0

data were obtained with 25.4 mm diameter impactors at velocities of 4.9 to 13.0 m/s [28] and 3.9 to 10.8 m/s [27] . Lower abdominal frontal impact response data from cadavers and subhuman primates are summarized in Table 6.3.4.1.1 – Lower Abdominal Frontal Impact Stiffness.

Although the average value from Nusholtz et al [27] is approximate, based on the initial slopes of the force-deflection curves provided, it can be seen from Table 6.3.4.1.1 – Lower Abdominal Frontal Impact Stiffness, that the scaled subhuman primate stiffness is less than half of the cadaveric stiffness. It is not clear if this discrepancy is due to the scaling method used [83, 84] or due to the existence of an actual difference between living and dead test subjects. The scaled frontal stiffnesses of Stalnaker and Ulman [82] for the upper and middle abdomen were equally low and it is not clear whether the data are reliable or usable. Rouhana [85] recommends that the lower abdominal response be used for the upper abdomen until more data become available.

As for lower abdominal response to belt loading, the only data available were taken from porcine subjects by Miller [86]. Rouhana et al [87] scaled the data to the human level using the equal stress/equal velocity method. The scaled response curves are shown in Figure 6.3.4.1.1 for an average velocity of 3.7±0.84 m/s.

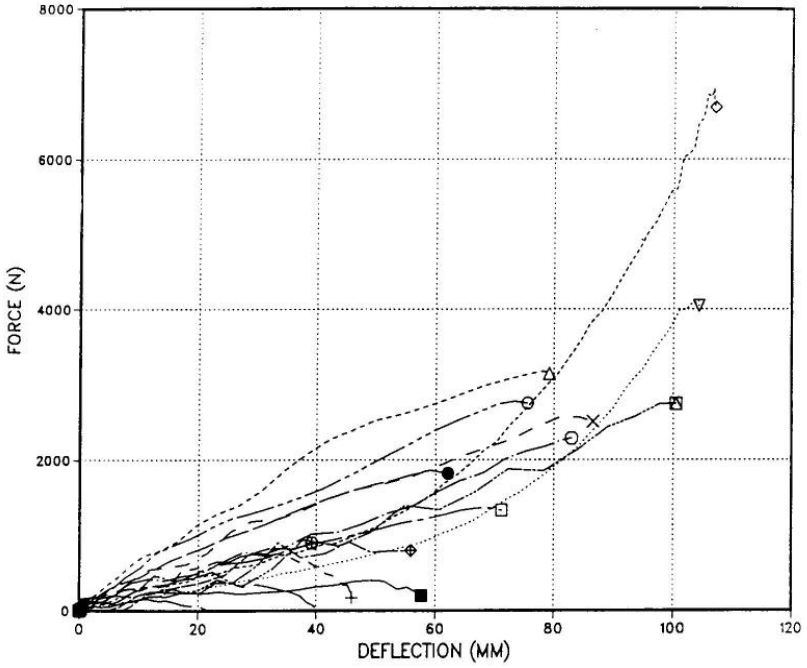

Fig. 6.3.4.1.1 **Lower abdominal response to dynamic belt loading**

6.3.4.2 Mechanical Response for Lateral Abdominal Impact

6.3.4.2.1 Upper Abdominal Response

Pendulum impact data obtained by Viano et al [76] are shown in Figure 6.3.4.2.1.1. On the left are force-deflection curves with initial stiffnesses of 100, 75 and 128.6 kN/m for the three impact velocities of 4.3, 6.7 and 9.5 m/s respectively. Force-time response curves are shown on the right of Figure 6.3.4.1.1. When these force-time histories are compared with normalized data obtained from cadaveric drop tests onto rigid armrests, reported by Walfisch et al [80], distinct differences are obvious.

6.3.5 Mechanical Response of the Pelvis

The pelvis is a ring of bone interposed between the flexible spinal column that it supports and the movable lower limbs upon which it rests. Mechanically, it is the

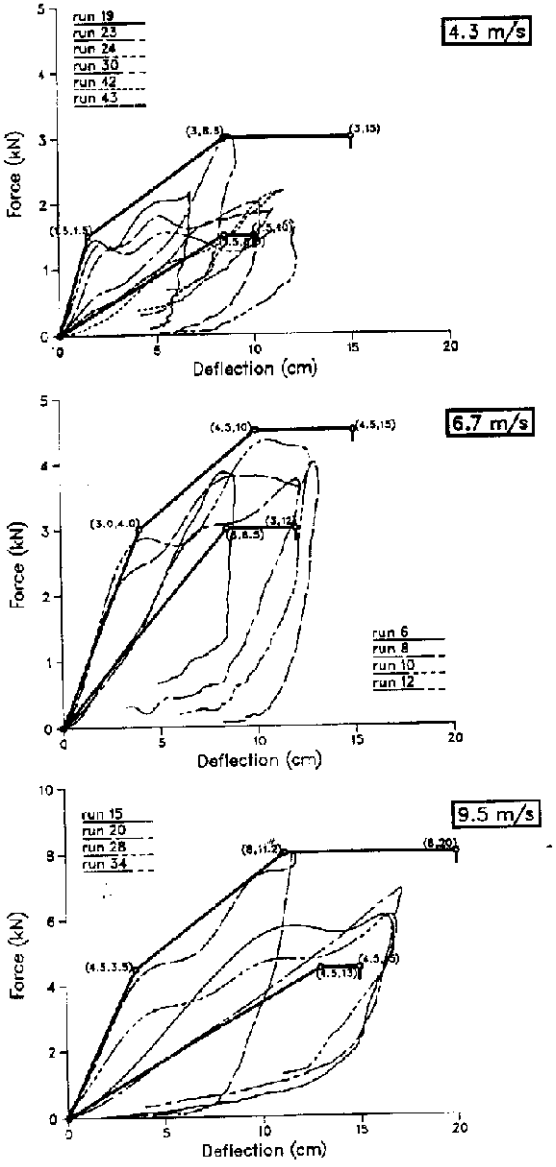

Fig. 6.3.4.2.1.1 **Renormalized force-deflection and force-time response for lateral abdomen impacts**

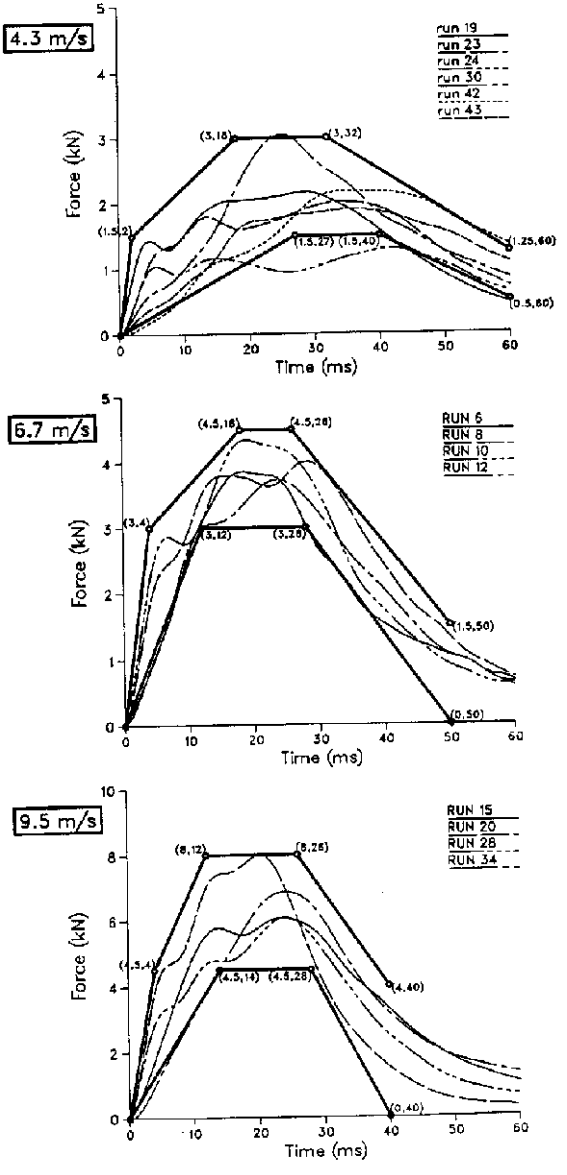

Fig. 6.3.4.2.1.1 **Renormalized force-deflection and force-time response for lateral abdomen impacts**

only load path for the transmission of the weight of the head, arms and torso to the ground. Thus, bilateral disruption of this structure would result in an inability to walk. Pelvic injuries seen in automotive crashes include fracture of the pubic rami and of the iliac bones, acetabular fractures and soft tissue injuries to the blood vessels and organs within the pelvic basin. Many of these fractures result from lateral impacts.

6.3.5.1 Frontal Impact Response of the Pelvis

Frontal impact response cadaveric data in the form of pelvic accelerations resulting from impacts to the knees were acquired by Melvin and Nusholtz [88] and by Nusholtz et al [89]. In the latter study, 37 frontal knee impacts were carried out on 16 cadavers, using a pendulum impactor. The cadaver was suspended in a restraint harness and one knee was impacted. Both the linear and angular acceleration of the pelvis were measured but the angular acceleration about the spinal (z-) axis was not always predominant for this off-axis impact. Initial rotation was about the greater trochanter of the contralateral side and the subsequent motion of the pelvis and femur was rather complex. Mechanical impedance was used as an analytical tool and resonance was estimated to occur between 180 and 280 Hertz. Impedance corridors were plotted for both the pelvis and the trochanter. However, because of the large scatter in the data, it was difficult to obtain average values of the equivalent mass and spring rate of the pelvis.

6.3.5.2 Lateral Impact Response of the Pelvis

Relatively abundant lateral response data are available for pelvic impact. Cesari et al [90] summarized a large body of work performed at INRETS (formerly ONSER). There were 60 impacts on 22 cadavers in this effort, using a 17.3 kg (38 lb) impactor with a diameter of 175 mm (6.9 in) and a spherical face with a radius of curvature of 600 mm (23.6 in). The impact speeds ranged from 21 to 44.6 km/h (13.0 to 27.7 mph). Each cadaver sustained multiple (2 to 5) impacts that were administered at increasing velocities until fracture occurred. In 55 of these tests, the impactor was rigid. The remaining tests were padded impacts. All impacts were aimed at the greater trochanter. Impact force and pelvic acceleration were measured. Peak force data as well as force and acceleration data, except for cumulative durations less than 3 ms (the so-called 3-ms clip), were provided. Tarriere et al [91] summarized all of the response data acquired by the Association Peugeot-Renault (APR). Pelvic acceleration was measured in all of the 26 cadaveric drop tests. Nusholtz et al [89] performed 12 lateral impacts in addition to the frontal tests described above. The impacts were aimed at the greater trochanter. Both impact force and pelvic acceleration were measured. The peak force varied from 3.2 to 14 kN while the peak acceleration ranged from 38 to 135 g for impacts speeds of 18.4 to 31.0 km/h (11.4 to 19.2 mph). Viano et al [76] performed a series of 14 rigid pendulum impact tests on the greater trochanter of unembalmed cadavers. The

mass of the pendulum was 23.4 kg (51 lb). The impact speeds were 16.2 to 33.8 km/h (10 to 21 mph). Force-deflection curves for the 33.8 km/h impacts are shown in Figure 6.3.5.2.1. Finally, the cadaveric study by Cavanaugh et al [81] produced force-time and compression-time histories of lateral pelvic impact. Twelve cadaveric tests were performed on a Heidelberg-type sled.

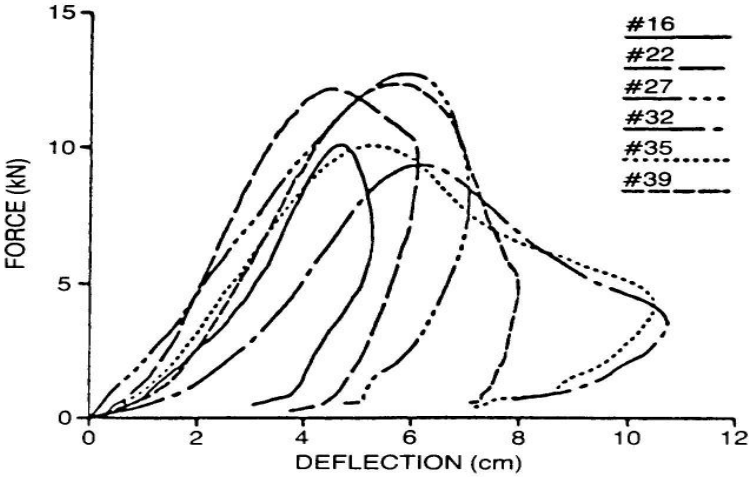

Fig. 6.3.5.2.1 **Force-deflection response of the pelvis**

6.3.6 Mechanical Response of the Lower Extremities

Response data of the lower extremity to impact are needed to design lower extremities for anthropomorphic test devices (ATD). The first concern was the response of the femur in a frontal knee impact because of the Federal regulation on maximum knee loads. The next concern was the protection of the knee when it impacts the dash. A current concern is injury to the foot, ankle and distal tibia due to footwell intrusions.

6.3.6.1 Mechanical Response of the Knee and Femur

Response data in the form of force-time histories were first provided by Patrick et al [64, 92], who conducted a multi-purpose sled experiment to measure head, chest and knee response. These data were subsequently supplemented by additional knee impact data by Horsch and Patrick [93]. Typical cadaveric response

curves in the form of time histories of knee impact force and femur acceleration are shown in Figure 6.3.6.1.1. This was a rigid 5-kg (11-lb) pendulum impact against the knee of a seated cadaver that did not have a back support. The drop height was 0.225 m (8.9 in). Other forms of response data include peak femur acceleration as a function of peak knee impact force and mean peak knee impact force as a function of pendulum mass. These data are useful for dummy design and were provided by Horsch and Patrick [93].

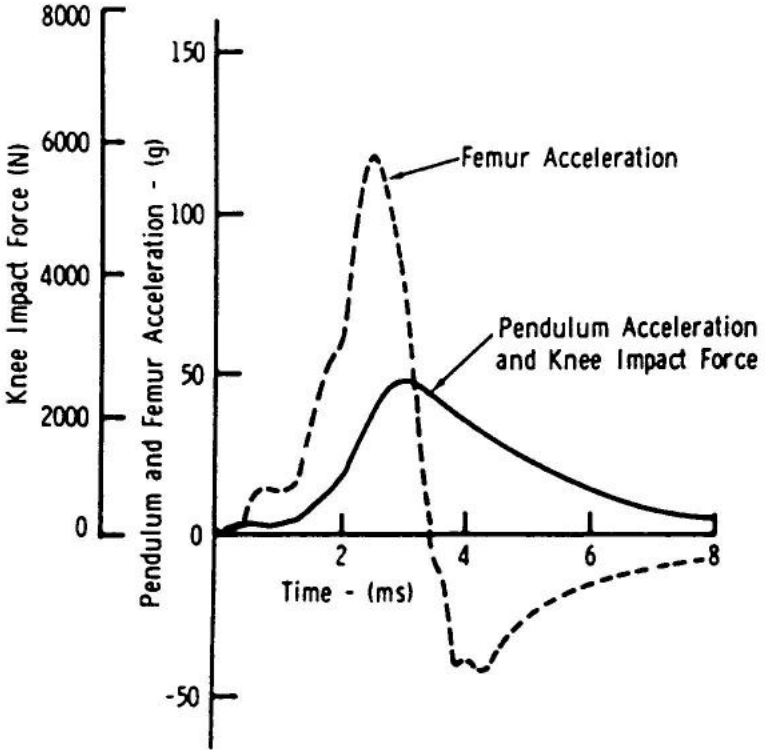

Fig. 6.3.6.1.1 **Knee femur impact response**

For the knee, studies have been conducted to quantify the force-deflection characteristics associated with the human knee being forced into energy-absorbing or crushable materials. Nyquist [94] tested a cross-section of volunteers utilizing Styrofoam of known crush characteristics. Static force-deflection characteristics resulting from knee penetration of the foam were documented along with the anthropometric information of the test subjects. Percentile scaling of both the knee anthropometry and load-deflection results is provided, together with explicit instructions for performing foam crushability qualification tests. The results of this study can be used directly to develop advanced dummies, without any need for further interpretation or analyses.

Hering and Patrick [95] provided a dynamic version of Nyquist's study. They used a padded ballistic pendulum to impact the knees of 13 cadavers to study knee penetration. The padding materials were Styrofoam and aluminum honeycomb. The cadavers' mechanical response was described in detail in order that others can duplicate the responses at a later date. Dynamic force-penetration data are provided, as well as anthropometric information depicting the shape of the knees. The flesh thickness over the patella and over the anterior surfaces of the knee was documented. This research provides an excellent basis for developing advanced dummy knee penetration response for crushable materials. The results are again directly usable, without a need for further analysis.

To prevent soft tissue injuries to the knee in the automotive environment, as discussed above, Viano et al [41] obtained the stiffness the knee joint for static posterior tibia subluxation relative to the femur. The linear range of the stiffness values from the five cadaver specimens tested had an average of 149 kN/m (850 lb/in).

6.3.6.2 Mechanical Response of the Tibia

There is not much dynamic response information on the tibia. Nyquist et al [96] tested 20 tibiae dynamically (with the fibula attached) taken from 11 cadavers. The bones were tested in 3-point bending, 11 of them in the antero-posterior (AP) direction and 9 in the latero-medial (LM) direction. There were 2 static tests, one in each direction. The dynamic load was provided by a 32-kg (70.6-lb) linear impactor at speeds between 2.1 and 6.9 m/s (6.9 to 22.6 ft/s) however, most of the tests were done at 2.9 to 4.7 m/s (9.5 to 15.5 ft/s). The bones had a span of 254 mm (10 in) and were simply supported. The impactor was a 25-mm (1-inch) diameter cylinder placed at right angles to the long axis of the tibia and which impacted the tibia at midspan. Fracture site cross-sectional properties were measured, as was the mineral content of the bone. From the known bending moment, the tensile stress to failure was computed.

The response curve for AP loading had an average stiffness of 282 ± 92 kN/m (1610 ± 525 lb/in) when the impact force was plotted against deflection. The LM response was bi-linear. Its initial stiffness was 105 ± 36 kN/m (600 ± 206 lb/in) and its final stiffness prior to fracture was 265 ± 70 kN/m (1513 ± 400 lb/in). The difference in stiffness is obviously due to the contribution from the fibula which is stronger in the AP direction.

6.3.6.3 Mechanical Response of the Ankle

Dynamic impact response of the ankle in dorsiflexion was first provided by Begeman and Prasad [44]. Moment angle response curves were drawn for some of the 18 specimens tested. Eventually, this data set was supplemented with additional dorsiflexion test results by Crandall et al [97] and Portier et al [98] who did not have any new response data. Responses from inversion and eversion were again first provided by Begeman et al [45]. More data were provided later by Crandall et al [97].

6.3.6.3.1 Ankle Response in Dorsiflexion

Because of the variability in the data, the response curves for dorsiflexion of the ankle are ill-defined, as shown in Figure 6.3.6.3.1.1 [44]. The data provided by Crandall et al [97] were equally scattered and the peak moments reached were only about a third of those shown in Figure 6.3.6.3.1.1.

6.3.6.3.2 Ankle Response in Inversion/Eversion

The only dynamic data obtained by Begeman et al [45] for inversion/eversion are shown in Figure 6.3.6.3.2.1. The data provided by Crandall et al [97] were for quasi-static tests.

6.4 Human Tolerance to Impact

This is the third area of study in impact biomechanics and is closely tied to rule making as well as the design of ATD or dummy instrumentation to ensure that the parameters measured are in the injury range. It is also the most difficult area of study because of the large variation in mechanical properties of human tissue due to age, gender, weight and geometry. All of these factors are in addition to the normal biological variation in tissue strength and the acceptable level of injury. For example, frontal crashes do not cause serious neck problems unless the deceleration is very high. However, minor rear-end collisions can result in long term neck pain. There are several levels of tolerance. These levels range from the "Ouch" level for volunteer subjects to the LD (Lethal Dose) 50 level at which half of the subjects would suffer a fatality. To define a reasonably safe level for the average car occupant without having to make the car unaffordably expensive, a

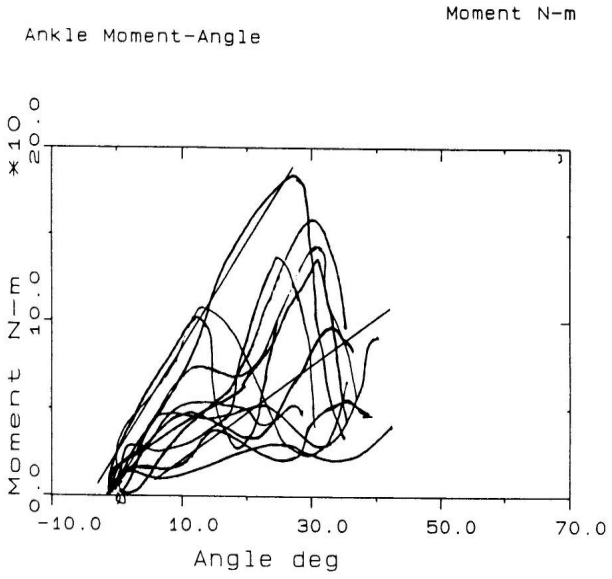

Fig. 6.3.6.3.1.1 **Dynamic ankle response to dorsiflexion**

moderate to severe level of injury is chosen as the tolerance level. That is, the injuries sustained by the average occupant should not be life threatening. There is an Abbreviated Injury Scale (AIS), developed by emergency room physicians and physicians in other medical specialties to quantify the severity of an injury to each body area. Severity is defined as threat to life and is not based on disability or impairment. On the AIS scale, any injury greater than AIS 4 is life threatening. The severity levels of AIS are explained in Table 6.4.1 – The Abbreviated Injury Scale.

Although an injury can be quantified by the use of the AIS, it is still not possible to provide a quantitative description of the agent that caused the injury. Thus, biomechanical engineers need injury criteria to describe the relationship between one or more physical parameters and the injury they caused. These criteria usually take the form of a simple mathematical expression or a force or acceleration level. Generally, the physical parameter should be consistent with the mechanism of injury that most likely caused the injury.

It is perhaps necessary to bring out the difference between an injury criterion and a safety standard, particularly standards set by national or state governments

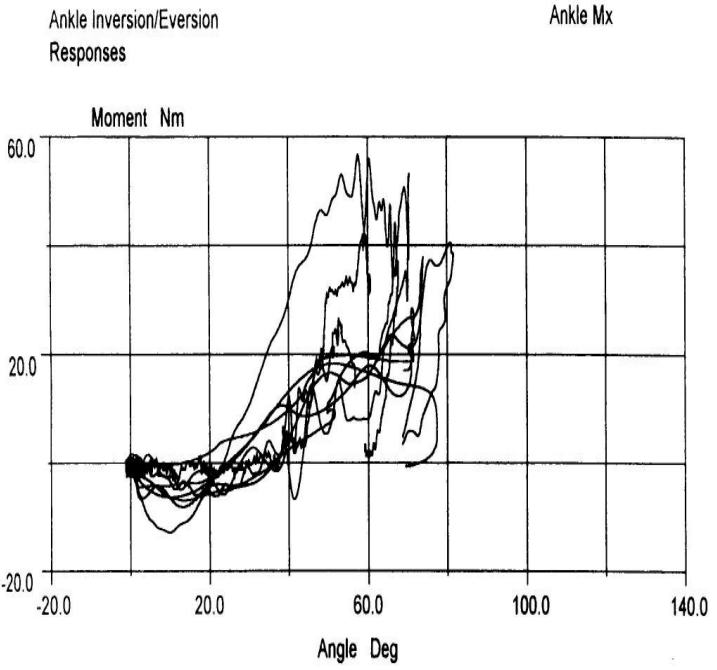

Fig. 6.3.6.3.2.1 **Dynamic ankle response in inversion/ eversion**

which control the sale of cars. In theory, safety standards should be based on scientifically established injury criteria. However, all standards are no longer scientifically sound because much more knowledge on injury mechanisms and injury criteria are now available and standards, once implemented, are hard to change. Examples of this inconsistency will be highlighted in the conclusion of this chapter.

6.4.1 Head Injury Tolerance

The principal concern in head injury is brain injury. One of the first attempts to define tolerance of the brain to linear acceleration was the Wayne State Tolerance Curve (WSTC), proposed by Lissner et al [99]. A more comprehensive version of this curve, taken from McElhaney et al [100], is shown in Figure 6.4.1.1, which shows that the brain can tolerate higher accelerations if the duration of the pulse

TABLE 6.4.1: **The abbreviated injury scale**

AIS	Severity Level
0	No Injury
1	Minor
2	Moderate
3	Serious
4	Severe
5	Life Threatening
6	Maximum
9	Unknown

is shorter. It was based on cadaveric skull fracture data and concussive data from animals, as well as long-duration human sled experiments. Very few data points were used to plot this curve and the instrumentation used was questionable. However, Ono et al [101] confirmed the validity of the curve through a series of experiments on subhuman primates. Gadd [102, 103] converted the WSTC to a severity index based on the WSTC. The equation for the Gadd Severity Index (GSI) is:

$$GSI = \int_0^T a(t)^{2.5}\, dt \pounds 1000 \qquad (6.4.1.1)$$

where $a(t)$ is the acceleration of the head center of mass, t is time, and T is the duration of the impact pulse.

The exponent 2.5 was taken from the WSTC, which could be approximated by a straight line with a negative slope of 2.5 if it was plotted on a log-log scale. Gadd chose this value of 2.5 as a weighting factor for his integral relationship and determined that a limit of 1000 matched some of the data generated at Wayne State. The GSI subsequently was modified to the Head Injury Criterion (HIC) by

Versace [104], but the limit remained at 1000. The final form of HIC adopted by the Federal government as the head injury safety standard (part of the FMVSS 208) is:

$$HIC = [\int_{T_1}^{T_2} a(t)\, dt]^{2.5}/(T_2 - T_1) \leq 1000 \qquad (6.4.1.2)$$

This criterion is valid for linear acceleration impacts, but in most head impacts both linear and angular acceleration are present and no validated injury criterion for angular acceleration is currently available. Despite its deficiencies, no substitute criterion has proven to be acceptable to the government or the biomechanics community. More animal research is needed to find a more effective criterion but ethical and other issues limit such research. An alternative approach is the use of computer models to predict brain injury. A finite element model by Ruan et al [105] showed that HIC correlated well with head linear acceleration, intracranial pressure and parameters associated with linear acceleration but did not correlate well with shear stress in the brain and other rotational parameters. Also, the recent work of Hardy et al [3] may shed some light on the normal and shear strains generated in the brain. The data can be used to validate a comprehensive finite element brain model, which in turn can be used as a possible injury criterion.

6.4.2 Neck Injury Tolerance

There is no widely accepted tolerance for the various loading modes on the neck. The reasons for this inability to set tolerance levels are many. McElhaney and Myers [106] provided some of the more significant reasons. The spine is a multi-segmented column with nonlinear structural properties. Its geometry is complex, it produces large strains at physiologic loading and its constituent elements have nonlinear material properties. Cervical injury mechanisms have been shown to be sensitive to the initial position of the neck, the direction of loading, the degree of constraint imposed by the contact surface and possibly the rate of loading. These factors are in addition to the normal biological variation in the strength of human tissue and the tolerable level of injury. For example, serious neck problems are not encountered in frontal crashes unless the g-level of impact is very high. However, in rear-end collisions, long-term neck pain can result, even though the impact is of low level. Tolerance of the cervical spine will now be discussed for different loading modes, based largely on a review by Myers and Winkelstein [107].

6.4.2.1 Tolerance of the Neck In flexion-Extension

There is ample evidence that the neck can take a fairly high frontal deceleration without injury. Ryan [108], using himself as a test subject, withstood a 23-g impact without injury. He was wearing a single belt with tighteners. Ewing et al [109]

conducted volunteer tests at 10 g and reported only belt contusions from the military harness used. Head accelerations at the mouth mount reached 38.6 ± 6.8 g. Similar tests with male volunteers performed by Cheng et al [110] reached a maximum sled deceleration of 10 g with no reported injuries. However, in the same series, only one of three female volunteers was willing to reach the 10-g level. The main reason given for discontinuing the tests was the intolerable whipping of the head due to weakness in the neck. Volunteer test results reported by Mertz and Patrick [53, 54] are the most frequently cited and widely used. The only volunteer was Prof. Patrick himself. He withstood a flexion moment of 59.4 N.m (43.8 ft-lb) with neck pain. This was defined as the pain threshold. At 87.8 N.m (64.8 ft-lb), he had an immediate onset of pain and prolonged soreness. This was defined as a flexion injury threshold.

Many cadaveric studies on neck flexion have been reported. Lange [111] produced a variety of neck injuries at sled decelerations of 20 to 27 g. In the absence of a steering wheel, the head rotation of three-point belted cadavers reached 123 deg. The simulated rear-end collisions were also severe. The peak accelerations ranged from 19 to 29 g and the heads of the cadaveric subjects rotated rearwards 75 to 108 degrees with respect to the torso when a headrest was used, and 112 to 140 degrees in the absence of a headrest. In both impact modes, severe cervical injuries were reported. There were severe ruptures of ligaments and intervertebral discs. However the ruptures were not bulges or herniations. The disc would separate at the endplate and the separation would invariably be associated with the rupture of longitudinal ligaments.

Clemens and Burow [112], using 53 cadaveric head and torso specimens carried out a set of severe flexion (and extension) experiments. In flexion, there was disc injury associated with the tearing of ligaments and fracture of the bony vertebrae. Kallieris et al [113] subjected 28 cadavers to frontal impacts at deceleration levels of 11 to 17 g. Twenty-two of the 28 cadavers were restrained with a three-point belt and the remaining 6 had a double shoulder belt with a crotch strap. There were injuries to the bony vertebrae, discs, ligaments and joint capsules. It is not clear what the authors meant by disc lacerations. The term appears to be associated with disc hemorrhage, indicating the involvement of the end plates, since the disc itself is avascular. It was not possible for the authors to arrive at a single tolerance value since the AIS ranged from 1 to 5. One of the conclusions was that a large sample was needed to establish the various tolerance levels. The authors found that the maximum head acceleration had the highest correlation with spinal injury ($r = 0.58$). For an AIS of 2, the maximum head acceleration was 22.6 ± 7.1 g. This was contradicted by the opinions of Clemens and Burow [112] and by Ewing et al [109], both of whom reported no injuries in the acceleration range of 31.5 to 45.4 g for the head. A static voluntary limit of 59.4 N.m (43.8 ft-lb) was found by Mertz

and Patrick [54] while a dynamic tolerance of 189 N.m (139.4 ft-lb) at the occipital condyles was also suggested by the same authors. Myers and Winkelstein [107] proposed a flexion limit of 279 N.m (205.8 ft-lb) based on the data provided by Cheng et al [20]. However, this limit was averaged using neck moments that would have caused fatal upper cord injuries in a flexion-tension mode of loading. Using the average of three values which did not result in these catastrophic injuries, the flexion limit is 163 N.m (120.2 ft-lb). This value is more in line with that proposed by Mertz and Patrick [54]. The only conclusion is that a non-injurious limit for flexion is in the range of 163 to 189 N.m (120.2 to 139.4 ft-lb). Of course, this limit is for the absence of macroscopic injury in cadavers and it is probably too high for pain, as evidenced by the pain sustained by Prof. Patrick at 58.9 N.m or 43.5 ft-lb [54]. However, it should be noted that pain is not always indicative of injury, particularly if the subject has a pre-existing degenerative condition and a lowered pain threshold. The average static voluntary tolerance limit measured on 10 volunteers was found to be 27.5 N.m (20.3 ft-lb). The highest voluntary limit, based on the tests done by Ewing et al [114, 115, 116, 57] and by Grunsten et al, [117] was a sled acceleration of 150 m/s^2 or 15.3 g. Some of the flexion data were re-analyzed by Thunnissen et al [118], who reported a peak tolerable flexion moment to be about 70 N.m (51.6 ft-lb) for young Navy enlisted personnel. Parenthetically, it should be noted that the response curves provided by Thunnissen et al [118] all fell within the corridor for neck flexion provided by Mertz and Patrick [54] more than two decades before the results from Thunnissen et al [118] became available.

6.4.2.2 Tolerance of the Neck in Extension

Many studies have been conducted to analyze the problem of whiplash associated disorders (WAD). These were mostly at low impact levels aimed at understanding the causes of neck pain resulting from minor rear-end crashes. On the other hand, there were the studies by Clemens and Burow [112], who created disc injuries that were frequently associated with anterior longitudinal ligamentous rupture. There were also some joint capsular tears and bony fractures. Because of the overly severe input used (approximate sled acceleration of 25 g), it was not possible to establish a threshold for any of the documented injuries. The work of Lange [111] is also at the severe level (19-29 g sled acceleration) and the injuries found were consistent with those reported by Clemens and Burow [112].

Returning to the work of Mertz and Patrick [53, 54], the static limit for Prof. Patrick was 23.7 N.m (17.5 ft-lb) and the average static limit from 10 volunteers was 21.2 N.m (15.6 ft-lb). Their dynamic results show that the moment tolerated at the base of the skull was 16.7 N.m (12.3 ft-lb) for Prof. Patrick. The proposed non-injurious limit is 47.4 N.m (35 ft-lb), or twice the static limit of Prof. Patrick, and the proposed ligamentous injury limit is 57 N.m (42 ft-lb). This limit is based on ligamentous

damage to a small cadaver at 33.4 N.m (24.6 ft-lb), that, when scaled to the size of Prof. Patrick, was 57 N.m. The scaling method used was proposed by Mertz and Patrick [53].

6.4.2.3 Tolerance of the Neck in Lateral Bending

There do not appear to be much tolerance data of the neck in lateral bending. Analysis of volunteer data obtained by Ewing et al [119] and Wismans and Spenny [59] show that there were no obvious injuries from runs made at 5 to 10 g. These tests resulted in a lateral bending moment of 20 to 60 N.m and lateral rotations of 52 deg. Cadaveric studies have been conducted by Kallieris et al [120] simulating three-point belted near-side occupants. The 58 cadavers tested ranged in age from 19 to 65 years and the impact speeds were between 40 and 60 km/hr (25 and 38 mph). A variety of injuries, ranging from AIS 1 soft tissue damage to AIS 3 or higher bony fractures were found, frequently at the C6 level. The maximum head resultant acceleration for these tests was 163 g. Far-side lateral impacts were studied by Horsch et al [121] and by Kallieris and Schmidt [122]. When an in-board shoulder belt was used, some AIS 1 cervical injuries were found in both studies. However, in the older cadavers used by Horsch et al [121], transverse clefts of cervical discs as described above were found. It is not clear whether the tolerance values from this study are valid. The delta V for the Horsch experiments was between 33 and 37 km/hr (21 and 23 mph). In the second study by Kallieris and Schmidt [122], younger cadavers were used and only AIS 1 injuries were found for a delta V of 50 km/hr (31 mph).

6.4.3 Thoracic Injury Tolerance

The study of human tolerance of the chest to blunt impact was initiated to protect the unbelted driver involved in frontal crashes. The information was needed to design energy-absorbing steering wheel columns and deformable steering wheels. Later studies involved the interaction of the lap belt with the rib cage and more recent work concentrated on thoracic tolerance to side impact. Because there are abdominal organs within the rib cage, it is often difficult to separate the discussion of injuries to the thoracic viscera from those of the abdomen. In this chapter, tolerance of the upper abdominal organs such as the liver and spleen will be discussed.

6.4.3.1 Frontal Thoracic Tolerance

Stapp [123, 124] demonstrated that the chest could sustain decelerations of up to 45 g when fully restrained with a double shoulder harness. The computed pressure under the harness was 252 kPa (36.5 psi). Peak accelerations of 30 g at a rate of 1000 g/s were not tolerated. Mertz and Kroell [125] reviewed other early frontal tolerance data. Patrick et al [64, 92] obtained force tolerance values based on tests

TABLE 6.4.3.1.1: **Chest compression injury**

Chest Compression (%)	50th Percentile Chest Compression (mm)	AIS
30	69	2
33	76	3*
40	92	4

*Estimated by Neathery et al (127)

on unrestrained but embalmed cadavers. At a peak dynamic load of 5.96 kN (1340 lb), one cadaver sustained 4 rib fractures, while at 8.23 kN (1850 lb), extensive fractures were observed. These data would be supplemented later by Kroell et al [66, 126] who performed a large number of frontal chest impacts, using a 152-mm (6-inch) diameter rigid pendulum, as described above. The researchers found that chest compression correlated well with AIS (r = 0.730) while the maximum plateau force did not (r = 0.524).

The current FMVSS 208 on chest compression is based on a recommendation by Neathery [127], who analyzed the Kroell data and found that a compression of 76 mm (3 in) would result in an AIS of 3. The compression values in terms of percent of chest depth and compression for a 50th-percentile male and the corresponding AIS values are shown in Table 6.4.3.1.1 – Chest Compression Injury Criteria. An AIS of 4 was assigned to those cases in which the number of rib fractures was sufficient to cause a flail chest, in the opinion of the investigators. Viano et al [41] recommended that the chest compression limit should be 32 percent because at 40 percent, there was severe injury to the thoracic viscera and at 32 percent, there would not be adequate rib stability to protect the internal organs.

Viano and Lau [26] defined an alternate injury criterion for the chest. It is called the Viscous Criterion (V*C) and is the instantaneous product of chest wall velocity (V) and chest compression (C) expressed in percent of chest depth. This criterion

was developed based on studies carried out by Lau and Viano [128] who impacted rabbit livers at speeds of 5 to 20 m/s (16.4 to 65.6 ft/s) at a C_{max} of 16 percent. Liver injury was found to increase with increasing impact velocity. In a second study involving frontal impacts to the chest of 123 anesthetized rabbits, Lau and Viano [129] observed that lung injury increased with C_{max} at velocity levels of 5, 10 and 18 m/s (16.4, 32.8 and 59.1 ft/s). The alveolar region of the lung was more sensitive to velocity than regions of vascular junctions.

Kroell et al [25] confirmed the validity of the viscous criterion through a series of 23 blunt impacts on the chest of anesthetized swine. The average mass of the swine was 53.3 kg (117.5 lb) and the impactor velocities were 15 and 30 m/s (49.2 and 98.4 ft/s). The mass of the impactor was 4.9 kg (10.8 lb) and its diameter was 152 mm (6 in). For heart rupture and maximum AIS (MAIS) thoracic injuries in excess of 3, VC_{max} and $V_{max}C_{max}$ (product of the peak velocity and peak compression) both correlated well with injury. On the other hand, C_{max} did not show a good correlation. Lau and Viano [130] analyzed the data from 39 sternal impacts conducted by Kroell et al [66, 126] on unembalmed cadavers and found that the value for V*C was 1.3 m/s (4.3 ft/s) for a 50% probability of sustaining an AIS injury of AIS 4 or greater. The 25% probability value for VC_{max} was 1.0 m/s (3.3 ft/s). These results were obtained from a probit analysis by Viano and Lau [131].

Lau and Viano [130] concluded that V*C is the best criterion for soft tissue injury that is dependent on compression and the rate of compression. They hypothesized that the viscous criterion could be applied to other body regions besides the chest for impact velocities in the range of 3 to 30 m/s (9.8 to 98.4 ft/s). This velocity range is encountered in automotive type crashes and is intermediate between quasi-static crush loadings and impacts by high-velocity pressure waves caused by explosions.

6.4.3.2 Lateral Thoracic Tolerance

6.4.3.2.1 Velocity and Compression Based Injury Criteria

The cadaveric experiments reported by Viano et al [76] produced reasonable correlation between injury and VC_{max} as well as peak compression, C_{max}. The probability of injury for MAIS ≥ 4 vs. VC and C are shown in Figure 6.4.3.2.1.1. For a 25 probability of injury, VC = 1.5 m/s (4.9 ft/s) and C = 38%. These data were confirmed by tests reported by Cavanaugh et al [81], who found that VC and C were more predictive of injury than force or acceleration based criteria. Seventeen tests were conducted in this series, and it was found that a VC_{max} in excess of 1 m/s (3.3 ft/s) would result in thoracic injuries of AIS 4 to 5 [132]. Cavanaugh et al [132] also proposed an average spinal acceleration (ASA) criterion which is computed by taking the slope of the $T12_y$, the lateral velocity-time curve between

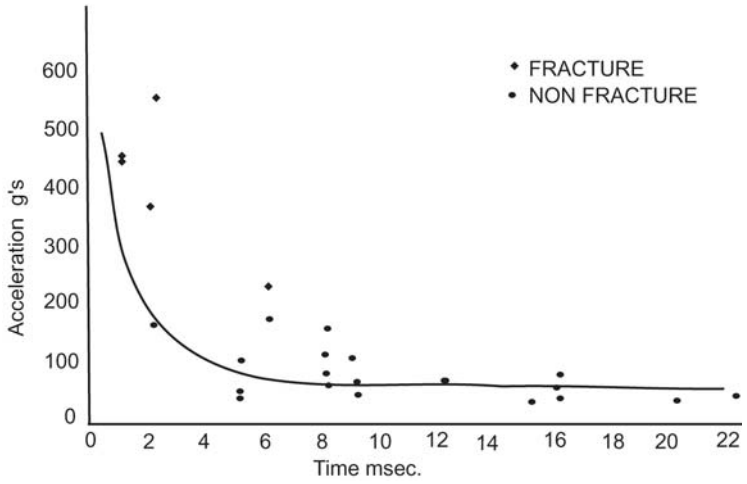

Fig. 6.4.3.2.1.1 **Logist probability curves: pendulum impacts**

a specified range of minimum and maximum spinal velocity. Between 15 and 85 percent, the slope is denoted as ASA15 and if it is normalized with respect to age of the cadaver and to body mass, it is denoted as ASA15N. The normalizing factors for age and mass are Age/45 and Mass/75 respectively where the age is in years and the mass is in kilograms. It was found that although ASA15N was the best predictor among the ASA's selected, it was not as good a predictor as Thoracic Trauma Index (TTI). However, when ASA15 for the SID dummy was computed, it was more sensitive to padding stiffness than TTI. That is, ASA could be used as an alternative criterion to TTI if the SID is to remain as the dummy to be used in certification tests in the United States.

6.4.3.2.2 Acceleration-Based Injury Tolerance

The most well-known acceleration based injury criterion is the TTI proposed by Eppinger et al [84]. The formula to compute TTI for a cadaveric test is given below:

$$TTI = 1.4 \times Age + 0.5 \times (Rib_y + T12_y) \times Mass/Mass_{50} \quad (6.4.3.2.2.1)$$

where Rib_y is the struck side Rib 4 peak acceleration, $T12_y$ is the 12th thoracic vertebral peak acceleration, *Mass* is the mass of test subject, and $Mass_{50}$ is the mass of a 50^{th}-percentile male subject.

This criterion was based on an earlier analysis of data from 30 cadaveric tests reported by Eppinger et al [133]. In 27 of these tests, the cadaveric subjects were instrumented with the 12-accelerometer array on the chest and spine, as specified by NHTSA for all tests done under United States Department of Transportation contracts [134]. The analysis concentrated on the peak accelerations of the struck 4th rib and that of the T12 lateral acceleration. Marcus et al [135] normalized the AIS observed in these tests to a 45-year old subject, using the following relationship:

$$\text{Normalized AIS} = \text{AIS} - 0.025 \times (\text{Age} - 45) \qquad (6.4.3.2.2.2)$$

Data from the University of Heidelberg sled tests were combined with those from Forschungsvereinigung Automobiltechnik (FAT) side impact test series in which a moving deformable barrier struck an Opel Kadett car body containing a seated cadaver. The TTI was revised by using the maximum value of either the Rib4 or Rib8 accelerometer on the struck side in the equation for TTI given above. It has been termed the modified TTI (TTI_m). The AIS was based on both thoracic and abdominal injuries because it took into account organs covered by the entire "hard" thorax, such as the liver and the spleen. Figure 6.4.3.2.2.1 is a plot of the combined data in which the O's are the Heidelberg data and the L's are the FAT data. There does seem to be a correlation between AIS and the formula used to calculate TTI. Figure 6.4.3.2.2.2 shows the probability of AIS4 or greater injury plotted against TTI_m for both left and right-sided impacts. Recently, Pintar et al [79] published tolerance data from 26 side impact cadaveric tests conducted in much the same fashion as that described by Cavanaugh et al [81]. Pintar et al [79] found that TTI, VC_{max}, ASA15N and C_{max} were all good predictors of thoracic injury, but TTI was the best predictor. However, the tests were conducted with the arm down, the choice of peak V and peak C were not always taken from the same location on the chest, the manner in which AIS was assigned based on the number of rib fractures was not carefully described and the nature of injuries sustained by each cadaver was not provided. Because of the considerations, the jury is still out as to whether TTI is a reliable predictor of injury as claimed by Pintar et al [79].

The drop tests first reported by Stalnaker et al [75] did not show a close relationship between the maximum 3-ms lateral acceleration and the number of rib fractures, and there was a lot of scatter in the average 3-ms acceleration at AIS levels between 3 and 5. Thus, the data were not entirely useful in defining a lateral chest acceleration criterion.

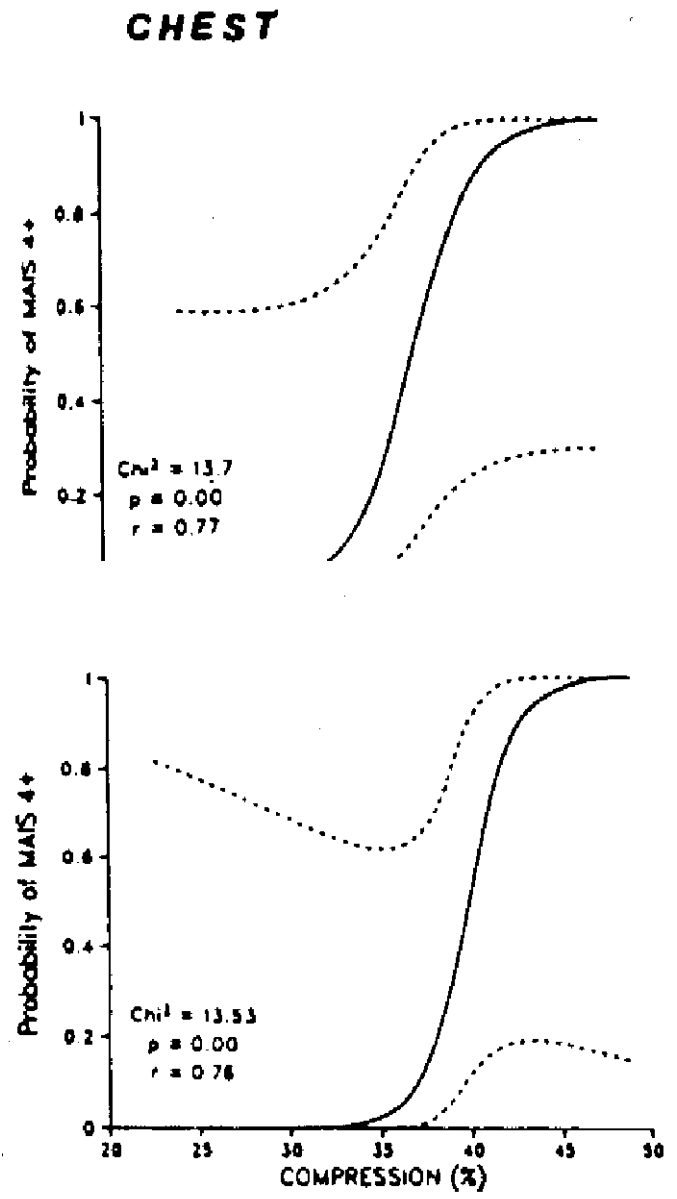

Fig. 6.4.3.2.2.1 **Maximum in AIS to thorax versus TTI**

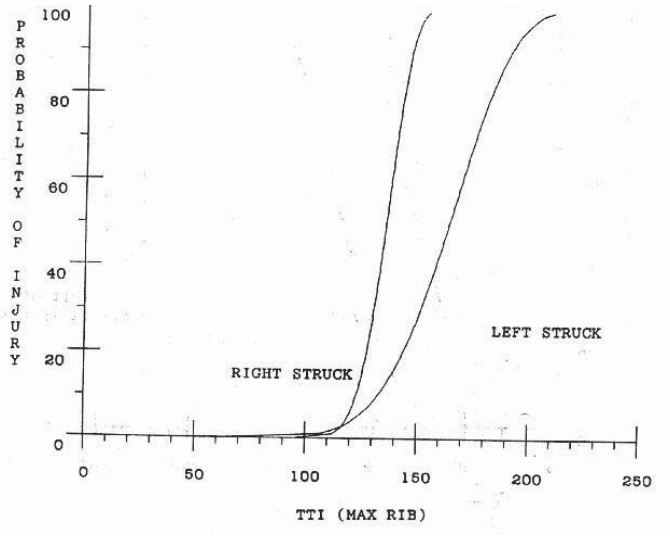

Fig 6.4.3.2.2.2 **TTI for right and left impacts**

6.4.4 Tolerance of the Abdomen

In vehicular crashes, the occupant is subjected to different injury sources depending on the direction of impact as well as the restraints used. In a frontal impact, the primary sources for a restrained occupant are the steering wheel rim and improperly worn safety belts. However, if the occupant is unrestrained, injury sources can come from many vehicular interiors, such as the instrument panel, the shift lever and door structures. In a side impact, the abdomen is exposed to the armrest and other parts of the door and there is evidence that hepatic and renal injuries are far more frequent in side impacts than in frontal impacts [136]. In view of these statistics, it appears that more research is available on abdominal side impact than on frontal impact.

The large number of abdominal organs and the difference in structure and strength between solid and hollow organs render the study of tolerance rather difficult. An additional difficulty is the effect of obesity, age and disease, such as cirrhosis of the liver, and the presence of material in the hollow organs, such as partially digested food in the intestines and a fetus in a uterus.

6.4.4.1 Tolerance of the Abdomen to Frontal Impact

Melvin et al [137] performed some basic strength studies on the liver and kidney of Rhesus monkeys by exposing them to direct impacts while they were being perfused by their original blood supply. The rate of loading was varied from 50 to 5000 mm/s (2 to 200 in/s) and the peak strain level was controlled to vary the severity of injury. A difference in response due to different strain rate was evident in the liver data but not in the kidney data due to the small number of tests conducted on the kidney. The onset of liver injury occurred at 310 kPa (45 psi), but no other tolerance data were provided. McElhaney et al [138] had reported this rate dependency effect in tests which used live anesthetized primates.

Lau and Viano [128] impacted anesthetized rabbits at varying velocities but held the abdominal compression constant. There was a significant increase in hepatic injury with increasing velocity of impact. Cadaveric and subhuman primate data acquired by Stalnaker et al [139] were re-analyzed by Stalnaker and Ulman [82]. Stalnaker et al concluded that V*C is a relevant parameter for predicting injury in subhuman primates and that the values obtained from primates appeared to be useful in predicting abdominal injury in the human. Rouhana [85] indicated that when frontal and side impacts were considered separately and when each abdominal region was considered separately, the correlation of $V_{max}C_{max}$ with AIS 3 or greater injuries was very high. The correlation coefficient, r, ranged from 0.92 to 0.99.

Horsch et al [140] subjected 17 porcine subject to steering wheel impacts. They found that abdominal injury correlated well with the maximum value of V*C, the instantaneous product of velocity and compression.

Miller [86], who applied compressive loads to the abdomen of 25 porcine subjects, studied the effect of belt loading on the lower abdomen. The velocity of impact was in the range of 1.6 to 6.6 m/s (5.3 to 21.7 ft/s). Both compression and belt load were well correlated with injury severity of AIS 3 or greater for these relatively low velocity impacts. Miller [86] also found that C_{max}*F_{max} predicted lower abdominal injuries better than V*C, as shown in Figure 6 of his paper, and not in Table V of the same paper. The tolerance values related to the studies described above for frontal abdominal impact are listed in Table 6.4.4.2.1 – Abdominal Tolerance for Frontal Impact. For a more complete table of tolerance values for various parameters, see [85].

6.4.4.2 Tolerance of the Abdomen to Side Impact

Stalnaker et al [74] also did lateral impact studies on subhuman primates and cadavers and found that abdominal compression was related to abdominal injury severity. The left and right side tolerances were different.

6.4.4.2.1: Abdominal tolerance for frontal impact

Author (ref)	Tolerance	Injury Severity	Organ	Remarks
Melvin et al [137]	p = 310 kPa	AIS 4-5	Liver	Exposed, perfused, N =17 Rhesus monkey, fixed back, V=2.5m/s
Lau and Viano [128,129]	F = 0.24 kN	AIS > 3	Liver	Rabbits, N = 26, Compression 16%, fixed back
Horsch et al [140]	V*C =0.72	AIS > 3	Liver	Steering wheel impact, N = 17,V = 32 km/h
Miller [86]	F = 3.76 kN	AIS > 4	Lower Abdomen	25% prob. of injury, Swine, N=25, Lap belt load
Miller [86]	C = 48.3%	AIS > 4	Lower Abdomen	25% probability of injury, Swine, N = 25, Lap belt load
Miller [86]	Fmax*Cmax = 2.0 kN	AIS > 4	Lower Abdomen	25% probability of injury, Swine, N = 25, Lap belt load

Rouhana et al [141, 142] analyzed 117 abdominal impacts on anesthetized rabbits and concluded that $V_{max}C_{max}$ correlated well with the severity of abdominal injury. This was called the Abdominal Injury Criterion (AIC), which is basically the same as the Viscous Criterion defined by Viano and Lau [26] for thoracic injury.

In terms of tolerance to impact force, Viano et al [76] found that force correlated better than V*C for abdominal injury. This is borne out by the values of r, p and c^2, which are indicators of goodness of fit.

The tolerance values related to the studies described above are listed in Table 6.4.4.2.2 – Abdominal Tolerance for Lateral Impact. For a more complete table of tolerance values for various parameters, see [85].

6.4.5 Tolerance of the Pelvis

For frontal impacts, tolerance data for the pelvis are sparse. This is due in part to the lack of a single study involving a large number of cadaveric subjects. On the

TABLE 6.4.4.2.2: **Abdominal tolerance for lateral impact**

Author (ref)	Tolerance	Injury Severity	Organ	Remarks
Stalnaker et al [74, 139]	C = 60% L C = 54% R	AIS 4-5	Liver	Primates and cadavers, N = 96 Free back, armrest, belt
Rouhana et al (1986)	Vmax*Cmax = 3.15 m/s	AIS > 3	Liver	Rabbits, N = 117, free back 50% probability of injury
Rouhana et al (1986)	Vmax*Cmax = 2.71 m/s R = 3.31 m/s L	AIS > 3	Upper Abdomen	Rabbits, N = 117, free back 50% probability of injury
Viano et al [76]	F = 6.73 kN	AIS > 4	Upper/ Mid Abdomen	25% probability of injury, Cadaver, N = 14, Pendulum
Viano et al [76]	V*C = 1.98m/s	AIS > 4	Upper/ Mid Abdomen	25% probability of injury, Swine, N = 25, Lap belt load

contrary, much more lateral impact data are available as more pelvic injuries are encountered in side impacts after the use of belt restraints became more widespread. Pelvic tolerance data due to vertical loading are also available, but do not have much relevance in automotive-related crashes.

6.4.5.1 Tolerance of the Pelvis to Frontal Impact

The first sled tests involving the pelvis were carried out by Patrick et al [64] who performed frontal impacts on 10 unrestrained, embalmed cadavers. The range of loads for pelvic fracture was 6.2 to 11.8 kN (1400 to 2650 lb). These fracture loads were considered to be conservative by the authors because of the advanced age of the test subjects. Melvin and Nusholtz [88] performed six sled tests on unembalmed cadavers during which knee loads and pelvic accelerations were measured. Hip and/or pelvic fractures resulted from combined knee loads of 8.9 to 25.6 kN (2000 to 5760 lb). In both sets of data, the wide range of fracture loads and the small number of subjects tested precluded any statistical analysis of the data. A larger series of 37 frontal knee impacts on 16 cadavers was carried out by Nusholtz et al [89]. They found no pelvic fractures at force levels as high as 37 kN (8300 lb). Brun-Cassan et al [143] conducted 10 whole-body impacts on

unrestrained and unembalmed cadavers at impact speeds of 49.5 to 67.1km/h (30.7 to 41.7 mph). Peak knee loads from 3.7 to 11.4 kN (830 to 2560 lb). There was only one fracture injury noted, that of the right patella and iliac crest at a knee load of 8.8 kN (1980 lb). Finally, Doorly [144] impacted isolated pelves with a drop weight causing acetabular and hip injuries. The impact force was not measured, but was computed from energy considerations. The computed average force could not be correlated to the observed injuries.

Patrick and Andersson [145] simulated some of the 128 frontal collisions involving restrained occupants in Volvos. The cases were carefully selected and all of the injuries sustained by the 169 occupants were known. The impact speeds ranged from 3.2 to 85.3 km/h (2 to 53 mph). All of the occupants were restrained by a three-point belt and they were simulated by appropriately-sized anthropomorphic test devices available at that time. There were a total of 72 sled simulations during which an attempt was made to measure all belt loads. The maximum total lapbelt load measured on these dummies was 14.3 kN (3220 lb) but no pelvic fractures were reported among 169 belted occupants studied. That is, the lapbelt does cause the iliac wings to separate at the sacroiliac joint.

Although no definitive tolerance level has been established for the pelvis for frontal impact, one can deduce that the 10-kN femoral load limit in FMVSS 208 adequately protects the pelvis and the three-point belt is not likely to cause injury to the sacroiliac joint, even in the absence of an airbag.

6.4.5.2 Tolerance of the Pelvis to Lateral Impact

Cesari et al [90] report on 22 cadaveric tests performed at ONSER. There were a total of 60 tests using a 17.3-kg (38-lb) pendulum impactor with a 175-mm (6.9-inch) diameter impact face having a spherical radius of curvature of 600 mm (23.6 in). The impact speed ranged from 21 to 44.6 km/h (13 to 27.7 mph). Each cadaver sustained multiple (2 to 5) impacts that were administered at increasing velocities until fracture occurred. A rigid impactor was used in 55 of the 60 tests. The other tests used a padded impactor. All impacts were aimed at the greater trochanter. Most of the injuries were multiple fractures of the pubic rami. For males, the force at fracture, at the level of the 3-ms clip, ranged from 4.9 to 11.9 kN (1000 to 2900 lb). The corresponding range for females was 4.4 to 8.2 kN (1000 to1840 lb). The average force for an AIS 2 or 3 pelvic injury was 8.6 kN (1930 lb) for males and 5.6 kN (1260 lb) for females. After making adjustments for body weight of the test subjects, the proposed tolerance force at the level of the 3-ms clip was 10 kN (2250 lb) for a 75-kg person. For a 5th-percentile female, the tolerance was reduced to 4.6 kN (1030 lb). The authors defended their multiple impact procedure vigorously, stating that the force-time histories were consistent in pattern for multiple impacts and that the impact force increased consistently with increasing

impactor speed. In a later paper, Cesari et al [146] proposed the use of an acceleration criterion at the level of the 3-ms clip. They concluded that there was better correlation of injury with pelvic acceleration than with pelvic force.

Tarriere et al [91] reported on a series of 26 cadaveric drop tests during which pelvic responses were measured along with those of the thorax. There were 4 pubic rami fractures out of the 22 cadavers tested. The highest pelvic acceleration measured at the 3-ms clip was 90 g and lowest was 50 g. Ignoring this low outlier, a tolerance level of 80 to 90 g, at the 3-ms clip, was proposed.

Nusholtz et al [89] also impacted the greater trochanter of 12 cadavers, which were suspended in a restraint harness using a pendulum impactor at speeds of 18.4 to 31.0 km/h (11.4 to 19.2 mph). The measured peak accelerations ranged from 38 to 135 g while the measured peak force ranged from 3.2 to 14 kN (720 to 3150 lb). Six of the 12 cadavers sustained pelvic fractures, four of which were to the pubic rami. No tolerance levels were proposed.

Marcus et al [135] presented data from 11 sled tests carried out at the University of Heidelberg. The range of impact forces measured was 3.6 to 28.9 kN at the level of the 3-ms clip. It was concluded that the 10 kN limit proposed by Ramet and Cesari [147] was too conservative.

Viano et al [76] used pendulum impact data to arrive at a displacement-based tolerance level. For a 25 percent probability of sustaining a serious injury (AIS 3), the pelvic compression was found to be 27 percent. Acceleration and force tolerance levels were found to be poor correlates to injury. Cavanaugh et al [81] proposed a displacement limit of 32.6 percent of the struck side half width, based on 12 sled tests, using the Heidelberg-type test setup. Peak impact force and peak acceleration did not perform well as injury indicators. However, pelvic deformation is not possible to measure on dummy pelves and is, therefore, not a practical tolerance limit. At present, in the absence of more reliable data, the 10 kN force limit appears to be the best tolerance for side impact to the pelvis.

6.4.6 Tolerance of the Lower Extremities

Many investigators have studied the tolerance of the femur and tibia over the past century. Weber [148] and Messerer [149] obtained static data. Dynamic data for the femur became available about three decades ago beginning with the work of Patrick et al [64]. Less is known about the dynamic tolerance of the tibia. However, because of current interest in offset collisions and the increase in lower extremity injuries due to airbag inflation, more data regarding the tibia, ankle and foot are becoming available. In Sections 6.4.6.1 through 6.4.6.5, tolerance of the

lower extremities, including the femur, patella, knee, tibia, ankle and foot, are discussed.

6.4.6.1 Tolerance of the Femur

Static failure moments averaged 233 N.m (172 ft lb) for males and 182 N.m (134 ft lb) for females in a series of three-point bending tests by Weber [148]. Static data obtained by Messerer [149] were somewhat comparable – 310 N.m (229 ft lb) for males and 180 N.m (133 ft lb) for females. Torsional failure moments averaged 175 N.m (129 ft lb) for males and 136 N.m (100 ft lb) for females [149]. Yamada [47] summarized the static data of Motoshima in terms of failure load causing a bending failure. Adequate information was provided to convert this information to failure moment. The average value for both sexes was 211 N.m (155 ft lb), ranging from 239 N.m (176 ft-lb) for the 20- to 39-year-old age range to 184 N.m (135 ft lb) for the 70- to 89-year-old age range. Axial compression failure loads of the femoral shaft were 7.72 kN (1735 lb) for males and 7.11 kN (1598 lb) for females if the ends of the bones were padded to prevent local failure. Femoral neck fractures occurred at 7.99 kN (1796 lb) for males and 4.96 kN (1115 lb) for females.

The first attempt to determine dynamic tolerance was made by Patrick et al [64], who tested seated embalmed cadavers on an impact sled simulating a frontal impact. The subjects were unrestrained. In most cases, the knee was targeted to hit a rigid surface covered with 37 mm (1.5 in) of padding. Rigid impact resulted in patella fractures but there were no fractures in more than half of the long bones tested. The fracture types were supracondylar, intertrochanteric fractures as well as shaft fractures. The peak loads ranged from 4.2 kN (950 lb) to 17.1 kN (3850 lb). The authors concluded that the tolerance value in compression should be 6.2 kN (1400 lb). Additional data obtained by Patrick et al [92] revealed that the femur could withstand loads of up to 8.8 kN (1970 lb) without fracture in padded impacts. It was suggested that loads of 8.7 kN (1950 lb) without fracture are not unreasonable.

Brun-Cassan et al [143] tested 10 unrestrained cadavers seated in a buck that was mounted on a sled. The knees were made to impact load cells padded with 25 mm (1 in) of polyurethane foam. At speeds ranging from 49.5 to 67.1 km/h (30.7 to 41.7 mph), there were no femoral fractures. The peak force was normalized using the normalizing relationship proposed by Eppinger [83] in which the measured force was modified by the mass ratio raised to the 2/3 power. The normalized peak force ranged from 3.7 to 11.4 kN (825 to 2563 lb). Rigid pendulum impacts by Powell et al [150, 151] caused femoral shaft or neck fractures at about 11 kN (2473 lb), while condylar fractures occurred from 7.1 to 10.4 kN (1600 to 2340 lb). In 8 of the 15 tests, when the patella was fractured, femoral fracture did not occur.

Melvin et al [152] and Melvin and Stalnaker [153] tested the knees of 26 unembalmed cadavers (15 males) using a pendulum impactor of two different masses (4.3 and 11 kg). The lower torso was free to swing rearward in response to the impact. There were 7 rigid impacts and 28 lightly-padded impacts with a 25-mm (1-inch) Ensolite pad and 5 thick-padding impacts with a 50-mm (2-inch) aluminum honeycomb pad. For the rigid impacts, there were two fractures occurring at an average peak load of 18.8 kN (4240 lb). The five non-fracture peak loads ranged from 16.2 to 22.7 kN (3640 to 5100 lb). For the lightly padded impacts, there were five supracondylar fractures and one undefined fracture. The peak fracture load varied from 13.3 to 28.5 kN (3000 to 6400 lb). For the five thick padding impacts, there were two condylar fractures and one midshaft fracture. The fracture loads for the former were not available and it was 19.7 kN (4420 lb) for the latter. The other two non-fracture loads averaged 14.7 kN (3300 lb).

Finally, Viano and Stalnaker [154] reported on a study by Stalnaker et al [155] in which a series of 13 knee impact tests was conducted on 6 cadavers using the same basic protocol described by Melvin et al [152]. The flesh on the thigh was removed to detect the time of initiation of fracture relative to the time base of the applied force. All 6 rigid tests produced shaft, neck or condylar fractures over a peak force range of 13.4 to 28.5 kN (3010 to 6410 lb) The average peak load for the two lightly-padded tests was 15.7 kN (3530 lb), which caused bilateral condylar fractures in both cases. In the thick padding tests, there were no fractures in three cases for loads ranging from 5.3 to 14.0 kN (1190 to 3150 lb). The authors concluded that the fractures occurred after the peak force was reached. Table 6.4.6.1.1 – Tolerance of the Femur in Axial Compression, summarizes the peak loads and fracture information for the tests described above.

Overall, it can be concluded that male femurs were slightly stronger than female femurs and that osteoporosis could dramatically reduce failure load. This explains the large spread in the data. There is also time dependence of the failure load. Significantly higher forces can be sustained for short duration pulses than can be tolerated under quasi-static loading. This time dependence effect was confirmed by Viano and Khalil [156], who developed a plane strain (2-D) finite element model of the femur which was subjected to a uniformly distributed load on the lateral and medial condyles. The pulse shape was sine-squared. For the same peak magnitude, the stress overshot some 30 percent for durations between 15 and 60 ms. There was a 30 percent undershoot for durations between 3 and 15 ms. The trend of these results are consistent with laboratory data.

Viano [157] proposed a Femur Injury Criterion (FIC) which establishes the axial force required to produce a femoral fracture as function of the primary load force duration, T, as follows:

TABLE 6.4.6.1.1: **Tolerance of the femur in axial compression**

Authors	Test Type	Peak Load Range (kN)	Fracture Type	Percent Fractured	Padding Thick-ness	Duration Range (ms)
Patrick et al (64)	Sled	4.2 – 17.1	Condyl-ar	25	Rigid/ Thin	>30
Patrick et al [92]	Sled	8.8	None	0	36 mm	30
Brun-Cassan et al [143]	Sled	3.7 –11.4	None	0	25 mm	Unknown
Powell et al [150, 151]	Pendulum	11.0	Shaft/ Neck	13	None	10-20
Powell et al [150, 151]	Pendulum	7.1 – 10.4	Condyl-ar	33	None	10-20
Melvin et al [152]	Pendulum	18.8 average	Condyl-ar	29	None	<10
Melvin et al [152]	Pendulum	16.2 – 22.7	None	71	None	<10
Melvin et al [152]	Pendulum	13.6 – 28.5	Condyl-ar	18	25 mm	22 max.
Melvin et al [152]	Pendulum	19.7	Shaft	20	50 mm	<10.7
Melvin et al [152]	Pendulum	14.7	None	40	50 mm	<10.7
Stalnaker et al [155]	Pendulum	13.4 – 28.5	Shaft/ Neck and Condyl-ar	100	None	Unknown
Stalnaker et al [155]	Pendulum	15.7 average	Condyl-ar	33	25 mm	Unknown
Stalnaker et al [155]	Pendulum	5.3 – 14.0	None	60	50 mm	Unknown

$$F\ (kN) = 23.24 - 0.72\ T\ (ms),\ for\ T < 20\ ms \quad (6.4.6.1.1)$$

$$F\ (kN) = 8.90\ for\ T \geq 20\ ms \quad (6.4.6.1.2)$$

Details of the method to arrive at this criterion are given by Viano [157]. Lowne [158] analyzed the available data and concluded that the following criteria are appropriate for avoiding unacceptably high femoral compressive loads proposed another criterion:

- 12 kN (2700 lb) may not be exceeded,
- 10 kN (2250 lb) may not be exceeded for durations of less than 3 ms,
- 7 kN (1575 lb) may not be exceeded for durations of less than 10 ms.

Finally, Nyquist [159] has proposed a criterion called the KTHIC (Knee-Thigh-Hip Injury Criterion) where a Femur Number is computed by integrating an exponentially-weighted femur force over the duration of the pulse and comparing the results to a critical value, analogous to the use of the Gadd Severity Index for head injury. Each of these various techniques has some merit but none is based on the actual mechanism of injury as described above. Namely, shaft fractures are due to lateral or vertical bending loads applied to knee by a well-padded instrument panel and rigid impacts cause patella fractures, while inadequately padded impacts cause condylar fractures.

6.4.6.2 Tolerance of the Patella

The deduction of patella tolerance from the types of knee impacts described above for femoral tolerance is not an easy task. Tolerance implies the minimum load needed to damage a bone or a piece of tissue. Any load above this minimum will also cause damage. Thus, there is no assurance that the forces measured in those knee impacts are close to the tolerance value or have well exceeded this limit. The problem is further complicated by the fact that the forces generated by padded impacts are borne by both the patella and the condylar surfaces around it. Thus, the only data that can be reliably used are the rigid knee impact tests in which there was no patella fracture. Patrick et al [64] reported 9 rigid impacts with no patella fractures below 8.9 kN (2000 lb). The peak loads ranged from 4.2 to 11.8 kN (944 to 2653 lb). Similar data from 3 non-fracture tests by Powell et al [150, 151] show a range of 6.7 to 8.8 kN (1500 to 1980 lb). There was only one data point from the pendulum tests of Melvin et al [152] and Melvin and Stalnaker [153]. One patella survived multiple impacts to a load of 22.7 kN (5100 lb). These results have a wide range of 4.2 to 22.7 N (950 to 5100 lb), a five-fold range. There is one possible explanation. The higher loads that were tolerated by the patella in some

of the rigid impacts may not have impacted the patellae directly and thus a higher load was needed to fracture them.

Melvin et al [160] performed concentrated impacts on the patella at different speeds. Three different impactors were used. Two were flat-surfaced circular contact surfaces and had diameters of 15.5 and 10.9 mm (0.61 and 0.43 in). The third was ring-shaped with an outer diameter of 12.7 mm (0.5 in) and an inner diameter of 6.4 mm (0.25 in). Minimum fracture loads ranged from 2.5 to 3.1 kN (560 to 700 lb) and the average failure load ranged from 4.6 to 5.9 kN (1030 to 1320 lb). The damage pattern varied dramatically with impact speed. Clean punch-through fractures occurred at impact velocities of 16 and 32 km/h (10 to 20 mph). Tolerance of the patella is probably closer to these values than the values obtained from knee impact.

6.4.6.3 Tolerance of the Knee

In the automotive setting, soft tissues of the knee are susceptible to injury from impact with the instrument panel. There are two such scenarios. One is damage to the posterior cruciate ligament (PCL) from impacts to the tibia just below the knee. Viano et al [41] simulated this impact with a 150-mm square impactor positioned or centered approximately over the center of rotation of the joint. The lower leg was flexed 90 deg and the cadaveric subject was seated. The impactor face was vertical and hit the tibial tubercle of the tibia, driving the tibia rearward and causing a posterior subluxation of the joint. The impact speed was 6.0 m/s (20 ft/s) and the average impact force was 5.2 kN (1160 lb). Of the 7 cadavers tested, there was a single case of a PCL rupture and two cases of no injury. Other injuries include tibial fractures and avulsion of the lateral ligament. Subsequently, Viano and Culver [161] did a couple of sled tests in which the knee restraint was placed sufficiently low to engage the proximal femur rather than the knee. In both case, there were stretching and tearing of the PCL. The solution to the problem is to ensure that contact with the instrument panel does not occur initially with the tibial tubercle and the question of tolerance does not arise if the instrument panel design is properly executed.

The other issue is post-traumatic osteoarthritis in the patellofemoral joint, which can result from knee impact with the instrument panel. Much of the recent work has been done at Michigan State University. In their latest paper, Atkinson et al [43] tested 12 knees from 6 cadavers. One knee was subjected to a rigid impact while the contralateral knee sustained a padded impact. Hexcel, rated at 1.35 MPa (196 psi) crush strength, was used. The impactor mass was 4.8 kg (10.6 lb) and the impactor speed was adjusted to deliver approximately the same impact force to the knee whether the impactor was padded or not. Rigid impacts resulted in an average peak force of 5.0 kN (1124 lb) while the average for the padded impacts

was 5.8 kN (1304 lb). Out of the 6 rigid impacts, there were 4 transverse fractures of the patella with two concomitant fractures of the femoral condyles. In terms of microtrauma, 4 of the 6 patellae sustained horizontal and/or vertical occult microcracking of the trabecular bone. For the padded impacts with a slightly higher peak load, there were no gross patella fractures and there was no histological evidence of microcracking. There was evidence of a more even distribution of the load in the padded impacts and possible sharing of the load by the condyles. The peak patellofemoral contact pressure averaged 13.5 MPa (1958 psi) in the rigid impacts and only 11.4 MPa (1653 psi) in the padded tests. Comparing these test results with those of Hayashi et al [42], the microtrauma problem as well as the problem of patellar and distal femoral fractures can be avoided if a reasonably stiff padding is used in instrument panels. That is, the padding should have crush strength of 0.69 to 1.35 MPa (100 to 200 psi).

6.4.6.4 Tolerance of the Tibia

Static failure moments averaged 165 N.m (122 ft lb) for males and 125 N.m (92 ft lb) for females in a series of three-point bending tests by Weber [148]. Static data obtained by Messerer [149] were somewhat comparable – 207 N.m (153 ft lb) for males and 124 N.m (91 ft lb) for females. Torsional failure moments averaged 89 N.m (66 ft lb) for males and 56 N.m (41 ft lb) for females [149]. Yamada [47] summarized the static data of Motoshima in terms of failure load causing a bending failure. In the same manner as described for the femur, the failure moment was computed. The average value for both sexes was 184 N.m (136 ft lb), ranging from 208 N.m (153 ft lb) for the 20- to 39-year- old age range to 164 N.m (121 ft lb) for the 70- to 89-year-old age range. Axial compression failure loads of the tibial shaft were 10.4 kN (2329 lb) for males and 7.5 kN (1684 lb) for females if the ends of the bones were padded to prevent local failure. Yamada [47] states that the bending strength is not significantly different between the anteroposterior and the mediolateral direction.

Dynamic tolerance information was first acquired because of tibial injuries associated with car-pedestrian impacts. Kramer et al [162] carried out over 200 pendulum impact tests on cadaveric lower legs at impact speeds of 4 to 8 m/s (13 to 26 ft/s). The spread in the failure data was extremely wide. At 4 m/s, the tibia failed at a load of 1 kN (225 lb) while at 7.1 m/s (23.3 ft/s), some tibias survived loads of 5.8 kN (1304 lb). These failure loads were obtained with a 145-mm (5.7-inch) diameter impact cylinder. At 7.1 m/s, 50 percent of the tibias failed at 4.3 kN (967 lb). With a 216-mm (8.5-inch) diameter cylinder, the 50 percent failure level was 3.3 kN (742 lb) at 6.3 m/s (20.7 ft/s). However, because of the spread in the data, it is not possible to arrive at a tolerance criterion. An extensive series of cadaveric car-pedestrian experiments was conducted by Pritz et al [163, 164]. However, bumper-knee impacts are not pure bending tests. A substantive

compressive load is developed in the tibia during the impact and the measured bumper load cannot be easily used to define bending tolerance.

Tolerance data provided by Nyquist et al [96] show that there was a difference between male and female tibias and there was also a difference between anteroposterior and lateromedial loading, primarily due to the presence of the fibula. The tolerance data are tabulated in Table 6.4.6.4.1– Tolerance Data for Tibial Bending Impacts.

If the females-only data are considered to be too scanty and are not used in analyzing Table 6.4.6.4.1 – Tolerance Data for Tibial Bending Impacts, it can be seen that LM tolerance is higher than the AP tolerance for the combined data as well as the male-only data. The force data were generated by a 25-mm (1-inch) diameter cylinder. However, the failure loads are well within the range of the dynamic data obtained by Kramer et al [162]. The dynamic moment data appeared to be slightly higher than the static data generated by Weber [148] and Messerer [149].

6.4.6.5 Tolerance of the Ankle

The first known tests on the ankle were performed by Culver [165], who loaded the foot and distal tibia in axial compression in an Instron materials testing machine at 4.2 mm/s (0.17 in/s). The right and left feet of a single cadaver were tested. In each case, the foot rotated medially and fracture of the anterior calcaneus occurred at an average rotation of 36 deg. The failure loads were 5.5 kN (1240 lb) and 3.3 kN (742 lb) for the right and left foot respectively.

The first dynamic tests of the ankle in dorsiflexion were performed by Begeman and Prasad [44]. The distal tibia with the foot attached was held in a fixture while a pendulum impacted the foot. The impact caused the foot to go into dorsiflexion, simulating the braking action during a frontal crash. Forces and moments at the ankle do not appear to be well-correlated with angular deflection or injuries. A logist analysis revealed that the tolerance can be best expressed in terms of the dorsiflexion angle. At 45 deg, there is a 50 percent probability of either bony fracture or ligamentous rupture at the ankle. Begeman et al [45] found that the tolerance of the ankle in inversion and eversion can also be expressed in terms of angular deflection. A logist analysis of the data showed that 60 deg of inversion or eversion will yield a 50 percent probability of injury. Injuries consisted of ligamentous rupture as well as bony fractures and avulsion fractures. Portier et al [98] found that the tolerance level should be expressed in terms of moment at the ankle. They suggested a dorsiflexion moment of 60 N.m. In terms of dorsiflexion angle, they found that injuries occurred at 30 deg instead of 45 deg but had no

TABLE 6.4.6.4.1: **Tolerance data for tibial bending impacts**

Gender	Direction of Loading	Number of Data Points	Bending Moment (N.m)		Total Reaction Load (kN)	
			Mean	S.D.	Mean	S.D.
Males and Females	AP and LM	21	308	79	4.83	1.23
	AP only	11	300	77	4.60	1.37
	LM only	10	317	84	4.86	1.27
Males Only	AP and LM	16	317	88	4.80	1.45
	AP only	8	304	90	4.57	1.59
	LM only	8	330	89	5.03	1.37
Females Only	AP and LM	5	278	30	4.48	0.61
	AP only	3	288	37	4.70	0.74
	LM only	2	264	14	4.16	0.22

explanation for this discrepancy. However, no logist plots were provided. Until more data become available, the ankle tolerance should be expressed in terms of dorsiflexion and inversion/eversion angles.

6.5 Discussion

6.5.1 Injury Mechanisms

Several head injury mechanisms have been proposed, including pressure, shear and relative motion. There is evidence that these mechanisms do indeed cause concussion, DAI and surface contusions as well as bridging vein ruptures. However, it is still not clear how an axon is injured by shear. It appears to be too

flexible to be sheared, except at the neuron/axon level, but it can be injured by the tensile component of a shear tensor or a tensile force can stretch it. This exact mechanism has not been fully explored. Injury mechanisms at the molecular level are still not fully understood. It is known that a traumatic event in the form of mechanical, thermal or electrical energy opens up calcium channels in the membrane, allowing calcium ions to enter the cell. At the end of the traumatic event, the channels close and the excess calcium ions do not leave the cell. Eventually, the cell dies from an enzyme that is formed due to presence of the calcium ions. It is not clear why the calcium pump stopped working as a result of the trauma or how the formation of the enzyme can be stopped.

Neck injury mechanisms of a rear-end impact are still being debated, particularly for low speed crashes that produce no objective signs of injury. One such mechanism was proposed in this paper but there are many proposed theories. Research is in progress to establish the precise mechanism and effective prevention of whiplash injury can only come about when that mechanism is understood.

The most difficult injury to reproduce in the cadaver is aortic rupture due to a frontal chest impact. Several unsuccessful attempts were made at Wayne State University, using cadavers with a pressurized arterial system. It has been hypothesized by Viano and Lau [26] that aortic tears occurred as a result of the development of high pressures within the artery which, when combined with a large stretch will cause the artery to fail. Another hypothesis is that the tears occur due to stresses at the junction of ligaments that hold the arterial system together. Such injuries occurred in cadavers that were subjected to a side impact. The ligamentum arteriosum, connecting the aorta with the pulmonary artery, was responsible for this injury, as described by Cavanaugh et al [81]. Why this injury could not be reproduced in frontal impact is still a mystery. Another unknown injury mechanism is the reason for the heart to go into unrecoverable fibrillation after an impact to the chest by a projectile, such as a baseball. Protective gear can be developed only after the injury mechanism is fully understood.

As for the lower extremities, the mechanism for the pylon fractures of the tibia is still unclear. It is known that calf muscle action is necessary to cause this fracture, but the location of the initiation of this fracture has not been determined. Similarly, the mechanism of fracture of the metatarsal bones (in a foot fracture) needs to be studied.

Injury mechanisms of the lower extremities have been studied extensively. Fracture mechanisms of long bones are known, but the precise mechanism for the failure of the distal tibia in pylon fractures has not been determined. It is suspected that

pylon fractures are due to a tensile stress developing on the inside of the root of the medial malleoulus when the talus is forced into the tibia. The mechanism of foot fractures has not been studied.

6.5.2 Mechanical Response

Although quantitative high-speed x-ray data of cadaveric brain response to impact are becoming available, the response of the entire brain to impact will take a long time to map. One possible way to speed the process is to combine the experiment with a validated computer model which can predict the response of every part of the brain and can simulate a large variety of impact situations that are difficult to accomplish experimentally.

The same can be said of the neck. Although there is a substantial body of knowledge on cervical spine response, much data need to be collected to fully describe its response. The use of a validated model of the cervical spine can extend the study more effectively and in less time. The use of a biaxial x-ray machine to determine relative vertebral motion will provide data that can be the basis for a full understanding of the whiplash phenomenon.

The mechanical response of the shoulder has not been fully characterized. In side impact, Irwin et al [166] has described its motion. More data are needed to determine the stretch of the ligaments and motion of the bones that make up the glenoid joint.

Frontal thoracic response has been studied extensively by Kroell et al [66, 126] and the data form the basis for the design of the Hybrid III dummy. The only troublesome aspect of the thoracic response of the Hybrid III chest is that its stiffness was increased to account for muscle tone in the living human. However, as it can be seen from Figure 6.3.3.1.1.2, there is little difference in stiffness between cadaveric data and those from a single volunteer, Professor Patrick. This author was present during the experiments described by Patrick [67] and there was no question that his muscles were tense just prior to impact.

Scaled abdominal stiffness data from animals are not comparable to human cadaveric data. Human abdominal stiffness was found to be over twice as high as the data scaled up from animal testing. Whether this is due to the scaling method used, differences in the methods of impact or actual difference between the human species and the other animal species is not clear.

6.5.3 Human Tolerance

Historically, brain injury tolerance was divided into tolerance to linear and angular acceleration, even though the head is usually subjected to both types of acceleration in any given impact. The Head Injury Criterion (HIC) was developed based on the linear acceleration of the skull, impacting a rigid surface. However, since the standard was adopted about 25 years ago, the automobile industry has used HIC with a certain degree of success despite the fact that most impact involve an angular acceleration component. At present, a reliable angular acceleration tolerance limit has not been established. This value may range from 5,000 to over 10,000 rad/s^2. Future standards may require the use of a computer model to compute the distribution of strain in the brain and the tolerance limit will be a pre-set strain limit that should not be exceeded.

Neck tolerance is defined in terms of the various modes of loading. In the absence of additional data, the data generated by Mertz and Patrick [53, 54] remain as the most reliable guide for neck flexion and extension. Reliable dynamic lateral flexion tolerance data do not appear to be available.

Frontal thoracic tolerance can be expressed in terms of acceleration, V*C or displacement. The current standard using the 60-g, 3-ms clip and the 3-inch deflection appears to work well, but the V*C limit of 1.0, as proposed by Viano and Lau [130] , is being verified using the voluminous cadaveric data obtained by Kroell et al [66, 126]. For side impact, the competing injury criteria are TTI, V*C and compression, each of which is based on a different test dummy. The problem lies more with the selection of the dummy than with the injury criterion. It will be up to the harmonizers of international standards to settle on a single standard using a single dummy.

In the absence of a Federal Standard on abdominal injury, the current criteria for frontal impact are either impact force, V*C or compression. Since it was difficult to cause injury to cadaveric abdominal organs, animal data were used as the basis for abdominal injury limits. The same limits apply in lateral impact but they are based in part on human data.

Frontal tolerance of the pelvis does not appear to have been measured directly. The lack of injury from lap belt loads, in the absence of an airbag, indicates that pelvic tolerance is relatively high for frontal impact. Many parameters have been suggested for lateral tolerance of the pelvis. However, when used in conjunction with a test dummy, criteria such as V*C and compression are not practical. At present, the accepted criterion is a 10 kN impact force limit, at the 3-ms clip for the 50th-percentile male and 4.6 kN for the 5th-percentile female.

The femoral load limit of 10 kN is not consistent with how a femur fractures because no bending moment is associated with this limit. However, with the advent of belt and airbag restraint, this is issue is now moot. For designers of instrument panels who want to protect the unbelted front seat occupant in an airbag-equipped car, the use of a padding of optimal stiffness is essential for the protection of the knee and the femur. Ankle tolerance should be based on the extent of dorsiflexion and inversion/eversion. For the distal tibia, pylon fractures can be avoided if the brake pedal load is kept at about 5 kN even though the distal tibial can withstand loads of 7 kN. A large calf muscle load of 2 kN must be taken into account when considering distal tibial tolerance. Foot fracture tolerance data are not available.

Upper extremity injury data are just becoming available, for the forearm as well as the upper arm. The forearm is at risk during deployment of the steering wheel airbag while the humerus is at risk due to the deployment of a seat-mounted side impact airbag.

6.6 Conclusions

A large amount of data in impact biomechanics is now available as the result of almost 60 years of laboratory research, using a variety of surrogates. The principal source of data is the unembalmed human cadaver. Although more information is still required to cover a few more body regions, there is now adequate biomechanical knowledge to prevent most of the life-threatening and highly disabling injuries. This does not mean that automotive designers and other safety professionals have put all of the knowledge to general use. However, the information is available if an effective and economic means of introducing more protection for the automotive occupant becomes available. For example, footwell design needs to be based on the tolerable limits of the ankle and distal tibia. Perhaps the only solution is to strengthen the footwell to reduce the intrusion and to have a collapsible brake pedal. These features are available in luxury cars but are not in most cars. Other design improvements may require cars be built differently. The problem of potential neck injuries among short drivers in airbag-equipped cars may find a solution in changing the method by which steering and braking mechanisms are designed. These controls will have to be changed to a “fly-by-wire” mode instead of the present mechanical linkages. In this way, the pedals can be adjusted to suit the leg length of the driver who will be seated far enough from the steering wheel to avoid an airbag-related neck injury.

As to the future of impact biomechanics, there are still several areas of study that need to be investigated in the short term. These include the brain, neck, upper extremities, shoulders and the foot. There also is a need to initiate some biomechanical research on the elderly, females and children. This may take some time, especially pediatric research. In the long term, biomechanical research will focus on functional injuries related to the prevention and treatment of minor injuries to important and vital organs. For example, the sequelae to mild traumatic brain injury can be devastating to the victim as well as to his or her family members. We now know that neurons fail to function normally after an injury because calcium ion channels open up during the trauma, allowing a large influx of calcium into the cell, eventually destroying the cell. These problems are associated with the cell membrane, which is only two molecules thick. To understand why the calcium pump in the injured neuron fails to remove the excess calcium from the cells and how the destructive enzyme can be prevented from forming, research needs to be done at the molecular level. Thus, the future trend in biomechanical research is to study functional injury at the molecular level. Researchers in the field of injury biomechanics will have to become familiar with the principles and techniques of molecular biology. More importantly, students interested in impact biomechanics should have a background in molecular biology before embarking on a research career in this field.

This review was based on the work of a large number of investigators. It goes without saying that the work of many has not been included in this survey for a variety of reasons, but principally because this review was not meant to be an exhaustive discussion of the subject matter. An apology is made to those who feel that their work should have been mentioned but was not, as well as to those whose work was referred to but not accurately or fairly. If such omissions and errors are brought to the attention of the authors, amends will be made in future surveys.

6.7 References

1. King, A.I.; Ruan, J.S.; Zhou, C.; Hardy, W.N.; Khalil, T.B. (1995) Recent advances in biomechanics of head injury research. Journal of Neurotrauma. 12:651-658.

2. Strich, S.J. (1961) Shearing of nerve fibers as a cause for brain damage due to head injury. Lancet, 2:443-448.

3. Hardy, W.; Foster, C.D.; King, A.I.; Tashman, S. (1997) Investigation of brain injury kinematics: Introduction of a new technique. *Crashworthiness, Occupant Protection and Biomechanics in Transportation Systems,* pp 241-254. Ed. by H.F. Mahmood, S.D. Barbat, M.B. Baccouche. ASME Publication AMD Vol 225, Book No. H01132.

4. Ommaya, A.K.; Boretos, J.W.; Beile, E.E. (1969) The lexan calvarium: an improved method for direct observation of the brain. Journal of Neurosurgery, 30:25-29.

5. Gurdjian, E.S.; Lissner, H.R. (1961) Photoelastic confirmation of the presence of shear strains at the craniospinal junction in closed head injury. Journal of Neurosurgery, 18:623-634.

6. Thibault, L.E.; Gennarelli, T.A.; Margulies, S.S. (1987) The temporal and spatial deformation response of a brain model in inertial loading. Proceedings of the 31st Stapp Conference, SAE Paper No. 872200.

7. Gennarelli, T.A.; Thibault, L.E.; Adams, J.H.; Graham, D.I.; Thompson, C.J.; Marcincin, R.P. (1982) Diffuse axonal injury and traumatic coma in the primate. Annals of Neurology, 12:564-574.

8. Zhou, C.; Khalil, T.B.; King, A.I. (1995) A new model comparing impact responses of the homogeneous and inhomogeneous human brain. Proceedings of the 39th Stapp Conference, SAE Paper No. 952714. pp. 121-137.

9. Pintar, F.A.; Yoganandan, N.; Sances, A.; Reinartz, J.; Larson, S.J.; Harris, G. (1989) Kinematic and anatomical analysis of the human cervical spinal column under axial loading. Proceedings of the 33rd Stapp Conference, SAE Paper No. 892436.

10. Pintar, F.A., Sances, A.; Yoganandan, N.; Reinartz, J.; Maiman, D.J.; Suh, J.K.; Unger, G.; Cusick, J.F.; Larson, S.J. (1990) Biodynamics of the total human cadaveric cervical spine. Proceedings of the 34th Stapp Conference, SAE Paper No. 902309.

11. Chang, D.C.; Tencer, A.F.; Ching, P., Treece, B.; Senft, D.; Anderson, P.A. (1994) Transient changes in the geometry of the cervical spinal canal during compressive fracture. Spine, 19:973-980.

12. Nightingale, R.W.; Richardson, W.J.; Myers, B.S. (1997) The effects of padded surfaces on the risk for cervical spine injury. Spine, 22:2380-2387.

13. Camacho, D.; Nightingale, R.W.; Robinette, J.J.; Vanguri, S.K.; Coates, D.J.; Myers, B.S. (1997) Experimental flexibility measurements for the development of a computational head-neck model validated for near-vertex head impact. Proceedings of the 41st Stapp Conference, SAE Paper No. 973345.

14. Yang, K.H. and Begeman, P.C. (1996) A proposed role for facet joints in neck pain after low to moderate speed rear-end impacts – Part I: Biomechanics. Proceedings of the Symposium on Injury Prevention through Biomechanics, pp 59-63, Wayne State University.

15. Bogduk, N. and Marsland, A. (1988) The cervical zygapophyseal joints as a source of neck pain. Spine, 13:610-617.

16. Aprill C. and Bogduk, N. (1992) The prevalence of cervical zygapophyseal joint pain: a first approximation. Spine, 17:744-747.

17. Lord, S.; Barnsley, L.; Bogduk, N. (1993) Cervical zygapophyseal joint pain in whiplash. In *Spine: Cervical Flexion-Extension Whiplash Injuries.* 7:355-372.

18. Matsushita, T.; Sato, T.B.; Hirabyashi, K.; Fujimura, S.; Asazuma, T.; Takatori, T. (1994) X-ray study of the human neck motion due to head inertia loading. Proceedings of the 38th Stapp Conference., SAE Paper No. 942208.

19. Bogduk, N. (1982) The clinical anatomy of the cervical dorsal rami. Spine, 7:319-330.

20. Cheng, R.; Yang, K.H.; Levine, R.S.; King, A.I.; Morgan, R. (1982) Injuries to the cervical spine caused by a distributed frontal load to the chest. Proceedings of the 26th Stapp Conference, SAE Paper No. 821155.

21. Thomas, D.Jj and Jessop, M.E. (1983) Experimental head and neck injury. *Impact Injury of the Head and Spine,* pp 177-217. Ed. by C.L. Ewing et al, Charles C. Thomas, Springfield, Illinois.

22. Viano, D.C. and King, A.I. (1997) Injury mechanism and biofidelity of dummies. *Crashworthiness of Transportation Systems: Structural Impact and Occupant Protection,* pp 25-51. Ed. by J.A.C. Ambrosio et al, Kluwer Academic Publishers, the Netherlands.

23. Moffat, E.A.; Siegel, A.W.; Huelke, D.F. (1978) The biomechanics of automotive cervical fractures. Proceedings of the 22nd Conference of the American Association for Automotive Medicine, pp 151-168.

24. Viano, D.C.; Andrzejak, D.V.; Polley, T.Z.; King, A.I. (1992) Mechanism of fatal chest injury by baseball impact: Development of an experimental model. Clinical Journal of Sports Medicine, 2:166-171.

25. Kroell, C.K.; Allen, S.D.; Warner, C.Y.; Perl, T.R. (1986) Inter-relationship of velocity and chest compression in blunt thoracic impact to swine II. Proceedings of the 30th Stapp Conference, SAE Paper No. 861881.

26. Viano, D.C.; Lau, I.V. (1983) Role of impact velocity and chest compression in thoracic injury. Aviation, Space and Environmental Medicine, 54:16-21.

27. Nusholtz, G.S., Kaiker, P.S.; Lehman, R.J. (1988) Steering system abdominal impact trauma. UMTRI Report No. 88-19, Motor Vehicle Manufacturers Association.

28. Cavanaugh, J.M.; Nyquist, G.W.; Goldberg, S.J.; King, A.I. (1986) Lower abdominal impact tolerance and response. Proceedings of the 30th Stapp Conference, SAE Paper No. 861878.

29. Leung, Y.; Tarriere, C.; Lestrelin, D.; Got, C.; Guillon, F.; Patel, A.; Hureau, J. (1982) Submarining injuries of 3 pt. Belted occupants in frontal collisions – Description, mechanisms and protection. Proceedings of the 26th Stapp Conference, SAE Paper No. 821158.

30. King, A.I. (1984) The spine: Its anatomy, kinematics, injury mechanisms and tolerance to impact. *The Biomechanics of Impact,* pp 191-226, Ed. by A. Chapon; B. Aldman, Elsevier, Amsterdam.

31. Vulcan, A.P.; King, A.I.; Nakamura, G.S. (1970) Effects of bending on the vertebral column during $+G_z$ acceleration. Aerospace Medicine, 41:294-300.

32. Prasad, P.; King, A.I.; Ewing; C.L. (1974) The role of articular facets during +Gz acceleration. Journal of Applied Mechanics, 41:321-326.

33. Begeman, P.C.; King, A.I.; Prasad, P. (1973) Spinal loads resulting from -G_x acceleration. Proceedings of the 17th Stapp Conference, SAE Paper No. 730977.

34. Prasad, P.; King, A.I. (1974) An experimentally validated dynamic model of the spine. Journal of Applied Mechanics, 41:546-550.

35. Chance, G.O. (1948) Note on a type of flexion fracture of the spine. British Journal of Radiology, 21:452-453.

36. King, A.I. (1993) Injury to the thoraco-lumbar spine and pelvis. *Accidental Injury: Biomechanics and Prevention,* pp 429-459. Ed. by A. Nahum and J. Melvin, Springer-Verlag, New York.

37. Beaupre, A. (1973) Trochanteric fractures. Proceedings of the 10th Traffic Injury Research Foundation of Canada Annual Meeting, pp 15-18, TIRF, Ottawa.

38. Markham, D.E. (1972) Anterior-dislocation of the hip and diastasis of the contralateral sacroiliac joint: the rear seat passenger's injury: British Journal of Surgery, 59:296-298.

39. Guillemot, H.; Besnault, B.; Robin, S.; Got, C.; Le Coz, J.Y.; Lavaste, F.; Lassau, J.P. (1997) Pelvic injuries in side impact collisions: A field accident analysis and dynamic tests on isolated pelvic bones. Proceedings of the 41st Stapp Conference, SAE Paper No. 973322.

40. Yang, K.H.; Shen, K-L.; Demetropoulos, C.K.; King, A.I.; Kolodziej, P.; Levine, R.S.; Fitzgerald, R.H., Jr. (1997) The relationship between loading conditions and fracture patterns of the proximal femur. Journal of Biomechanics Engineering, 118:575-578.

41. Viano, D.C.; Culver, C.C.; Haut, R.C.; Melvin, J.W.; Bender, M.; Culver, R.H.; Levine, R.S. (1978) Bolster impacts to the knee and tibia of human cadavers and an anthropomorphic dummy. Proceedings of the 22nd Stapp Conference, SAE Paper No. 780896.

42. Hayashi, S.; Choi, H.Y.; Levine, R.S.; Yang, K.H.; King, A.I. (1996) Experimental and analytical study of knee fracture mechanisms in a frontal knee impact. Proceedings of the 40th Stapp Conference, SAE Paper No. 962423.

43. Atkinson, P.J.; Garcia, J.J.; Atiero, N.J.; Haut, R.C. (1997) The influence of impact interface on human knee injury: Implications for instrument panel design and the lower extremity injury criterion. Proceedings of the 41st Stapp Conference, SAE Paper No. 973327.

44. Begeman, P.; Prasad, P. (1990) Human ankle response in dorsiflexion. Proceedings of the 34th Stapp Conference, SAE Paper No. 902308.

45. Begeman, P.; Balakrishnan, P.; Levine, R.; King A. (1993) Dynamic human ankle response to inversion and eversion. Proceedings of the 37th Stapp Conference, SAE Paper No. 933115.

46. Kitagawa, Y.; Ichikawa, H.; Pal, C.; King, A.I.; Levine, R.S. (1998) Lower leg injuries caused by dynamic axial loading and muscle tensing. To appear in Proceedings of the 16th ESV Conference, Paper No. 98-S7-O-09.

47. Yamada, H. (1970) *Strength of Biological Materials.* Ed. by F.G. Evans. Williams and Wilkins, Baltimore.

48. Hodgson, V.R.; Thomas, L.M. (1975) Head impact response. Vehicle Research Institute, SAE, Warrendale, Pennsylvania.

49. McElhaney, J.H.; Stalnaker, R.L.; Roberts, V.L. (1973) Biomechanical aspects of head injury. *Human Impact Response – Measurement and Simulation, Proceedings of the Symposium on Human Impact Response,* pp 85-110. Ed. by W.F. King, H.J. Mertz. Plenum Press, New York.

50. Foster, J.; Kortge, J.; Wolanin, M. (1977) Hybrid III – A biomechanically-based crash test dummy. Proceedings of the 20th Stapp Conference, SAE Paper No. 770938.

51. Hodgson, V.R.; Nakamura, G.S.; Talwalker, R.K. (1966) Response of the facial structure to impact. Proceedings of the 8th Stapp Conference, pp 229-250, Wayne State University Press, Detroit.

52. Tarriere, C.; Leung Y.C.; Fayon, A.; Got, C.; Patel, A.; Banzet, P. (1981) Field facial injuries and study of their simulation with dummy. Proceedings of the 25th Stapp Conference, SAE Paper No. 811013.

53. Mertz; H.J.; Patrick, L.M. (1967) Investigation of the kinematics and kinetics of whiplash. Proceedings of the 11th Stapp Conference, SAE Paper No. 670919.

54. Mertz, H.J.; Patrick, L.M. (1971) Strength and response of the human neck. Proceedings of the 15th Stapp Conference, SAE Paper No. 710855.

55. Patrick, L.M.; Chou; C.C. (1976) Response of the human neck in flexion, extension and lateral flexion. Vehicle Research Institute Report No. VRI-7-3, SAE, Warrendale, Pennsylvania.

56. Schneider, L.W.; Foust, D.R.; Bowman, B.M.; Snyder, Rm, J.K. (1975) Biomechanical Properties of the human neck in lateral flexion. Proceedings of the 19th Stapp Conference, SAE Paper No. 751156.

57. Ewing, C.L.; Thomas, D.J.; Lustick, L.; Muzzy, W.H. III; Willems, G.C.; Majewski, P. (1978) Effect of initial position on the human head and neck response to +Y impact acceleration. Proceedings of the 22nd Stapp Conference, SAE Paper No. 780888.

58. Mertz, H.J.; Neathery, R.F.; Culver; C.C. (1973) Performance requirements and characteristics of mechanical necks. *Human Impact Response: Measurement and Simulation,* pp 263-288. Ed. by W.F. King; H.J. Mertz. Plenum Press, New York.

59. Wismans, J.; Spenny, D.H. (1983) Performance requirements for mechanical necks in lateral flexion. Proceedings of the 27th Stapp Conference, SAE Paper No. 831613.

60. Wismans, J.; Spenny, D.H. (1984) Head-neck response in frontal flexion. Proceedings of the 28th Stapp Conference, SAE Paper No. 841666.

61. Wismans, J.; Phillippens, M.; van Oorschot, E.; Kallieris, D.; Mattern, R. (1987) Comparison of human volunteer and cadaver head-neck response in frontal flexion. Proceedings of the 31st Stapp Conference, SAE Paper No. 872194.

62. van der Horst; M.J.; Thunnissen, J.G.M.; van Haaster, R.M.H.P.; Wismans, J.S.H.M. (1997) The influence of muscle activity on head-neck response during impact. Proceedings of the 41st Stapp Conference, SAE Paper No. 973346.

63. Ono, K.; Kaneoka, K.; Wittek, A.; Kajzer, J. (1997) Cervical injury mechanism based on the analysis of human cervical vertebral motion and head-neck-torso kinematics during low speed rear impacts. Proceedings of the 41st Stapp Conference, SAE Paper No. 973340.

64. Patrick, L.M.; Kroell, C.K.; Mertz, H.J. (1965) Forces on the human body in simulated crashes. Proceedings of the 9th Stapp Conference, pp 237-259. University of Minnesota, Minneapolis.

65. Nahum, A.M.; Gadd, C.W.; Schneider, D.C.; Kroell, C.K. (1970) Deflection of the human thorax under sternal impact. *1970 International Automobile Safety Conference Compendium*, pp 797-807, SAE, New York.

66. Kroell, C.K.; Schneider, D.C.; Nahum, A.M. (1971) Impact tolerance and response of the human thorax. Proceedings of the 15th Stapp Conference, SAE Paper No. 710851.

67. Patrick, L.M. (1981) Impact force-deflection of the human thorax. Proceedings of the 25th Stapp Conference, SAE Paper No. 811014.

68. Schmidt, G.; Kallieris, D.; Barz, J.; Mattern, R. (1974) Results of 49 cadaver tests simulating frontal collision of front seat passengers. Proceedings of the 18th Stapp Conference, SAE Paper No. 741182.

69. Patrick, L.M.; Levine, R.S. (1975) Injury to unembalmed belted cadavers in simulated collisions. Proceedings of the 19th Stapp Conference, SAE Paper No. 751144.

70. Fayon, A.; Tarriere, C.; Walfisch, G.; Got, C.; Patel, A. (1975) Thorax of 3-point belt wearers during a crash (experiments with cadavers). Proceedings of the 19th Stapp Conference, SAE Paper No. 751148.

71. L'Abbe, R.J.; Dainty, D.A.; Newman, J.A. (1982) An experimental analysis of thoracic deflection response to belt loading. Proceedings of the 7th International Conference on the Biokinetics of Impacts, pp 184-194. IRCOBI, Bron, France.

72. Walfisch, G.; Chamouard, F.; Lestelin, D.; Fayon, A.; Tarriere, C.; Got, C.; Guillon, F.; Patel, A.; Hureau, J. (1982) Tolerance limits and mechanical characteristics of the human thorax in frontal and side impact and transposition of these characteristics into protection criteria. Proceedings

of the 7th International Conference on the Biokinetics of Impacts, pp 122-139. IRCOBI, Bron, France.

73. Verriest, J.P.; Chapon, A.; Trauchessec, R. (1981) Cinephotogrammetrical study of porcine thoracic response to belt applied load in frontal impact: Comparison between living and dead subjects. Proceedings of the 25th Stapp Conference, SAE Paper No. 811105.

74. Stalnaker, R.L.; Roberts, V.L.; McElhaney, J.H. (1973a) Side impact tolerance to blunt trauma. Proceedings of the 17th Stapp Conference, SAE Paper No. 730979.

75. Stalnaker, R.L.; Tarriere, C.; Fayon, A.; Walfisch; G.; Balthazard, M.; Masset, J.; Got, C.; Patel, A. (1979) Modification of Part 572 dummy for lateral impact according to biomechanical data. Proceedings of the 23rd Stapp Conference, SAE Paper No. 791031.

76. Viano D.C.; Lau, I.V.; Asbury, C.; King, A.I.; Begeman, P. (1989) Biomechanics of the human chest, abdomen, and pelvis in lateral impact. Proceedings of the 33rd Annual Conference, Association for the Advancement of Automotive Medicine, pp 367-382. AAAM, Des Plaines, Illinois.

77. Eppinger, R.H. (1989) On the development of a deformation measurement system and its application toward developing mechanically based injury indices. Proceedings of the 33rd Stapp Conference, SAE Paper No. 892426.

78. Huang, Y.; King, A.I.; Cavanaugh, J.M. (1994) Finite element modeling of gross motion of human cadavers in side impact. Proceedings of the 38th Stapp Conference, SAE Paper No. 942207.

79. Pintar, F.A.; Yoganandan, N.; Hines, M.H.; Maltese, M.R.; McFadden, J.; Saul, R.; Eppinger, R.; Khaewpong, N.; Kleinberger, M. (1997) Chestband analysis of human tolerance to side impact. Proceedings of the 41st Stapp Conference, SAE Paper No. 973320.

80. Walfisch, G.; Fayon, A.; Tarriere, C.; Rosey, J.P. ; Guillon, F., Got, C.; Patel, A.; Stalnaker, R. (1980) Designing of a dummy's abdomen for detecting injuries in side impact collisions. Proceedings of the 5th International Conference on the Biokinetics of Impacts, pp 149-164. IRCOBI, Bron, France.

81. Cavanaugh, J.M.; Walilko, T.J.; Malhotra, A.; Zhu, Y.; King, A.I. (1990) Biomechanical response and injury tolerance of the thorax in twelve sled side impacts. Proceedings of the 34th Stapp Conference, SAE Paper 902307.

82. Stalnaker, R.; Ulman, M. (1985) Abdominal trauma – Review, response, and criteria. Proceedings of the 29th Stapp Conference, SAE Paper No. 851720.

83. Eppinger, R.H. (1976) Prediction of thoracic injury using measurable experimental parameters. Proceedings of the 6th ESV Conference, pp 770-780. NHTSA, Washington, DC.

84. Eppinger, R.H., Marcus, J.H.; Morgan, R.M. (1984) Development of dummy and injury index for NHTSA's thoracic side impact protection research program. SAE Paper No. 840885. Government/Industry Meeting and Exposition, Washington, DC.

85. Rouhana, S.W. (1993) Biomechanics of abdominal trauma. *Accidental Injury – Biomechanics and Prevention,* pp 391-428. Ed. by A.M. Nahum; J.W. Melvin, Springer-Verlag, New York.

86. Miller, M.A. (1989) The biomechanical response of the lower abdomen to belt restraint loading. Journal of Trauma, 29:1571-1584.

87. Rouhana, S.W.; Viano, D.C.; Jedrzejczak, E.A.; McCleary, J.D. (1989) Assessing submarining and abdominal injury risk in the Hybrid III family of dummies. Proceedings of the 33rd Stapp Conference, SAE Paper No. 892440.

88. Melvin, J.W.; Nusholtz, G. (1980) Tolerance and response of the knee-femur-pelvis complex to axial impacts. Report No. UM-HSRI-80-27, University of Michigan Highway Safety Research Institute, Ann Arbor.

89. Nusholtz, G.; Alem, N.M.; Melvin, J.W. (1982) Impact response and injury to the pelvis. Proceedings of the 26th Stapp Conference, SAE Paper No. 821160.

90. Cesari, D.; Ramet, M.; Bouquet, R. (1983) Tolerance of human pelvis to fracture and proposed pelvic protection criterion to be measured on side impact dummies. Proceedings of the 9th ESV Conference, pp 261-269, NHTSA, Washington, DC.

91. Tarriere, C.; Walfisch, G.; Fayon, A.; Rosey, J.P.; Got, C.; Patel, A.; Delmas, A. (1979) Synthesis of human tolerance obtained from lateral impact simulations. Proceedings of the 7th ESV Conference, pp. 359-373, NHTSA, Washington, DC.

92. Patrick, L.M.; Kroell, C.K.; Mertz, H.J. (1967) Cadaver knee, chest and head impact loads. Proceedings of the 11th Stapp Conference, SAE Paper No. 670913.

93. Horsch, J.D.; Patrick, L.M. (1976) Cadaver and dummy knee impact response. SAE Paper No. 760799.

94. Nyquist, G.W. (1974) Static force-penetration response of the human knee. Proceedings of the 18th Stapp Conference, SAE Paper No. 741189.

95. Hering, W.E.; Patrick, L.M. (1977) Response comparison of the human cadaver knee and a Part 572 dummy knee to impacts by crushable materials. Proceedings of the 21st Stapp Conference. SAE Paper No. 770939.

96. Nyquist, G.W.; Cheng, R.; El-Bohy, A.; King, A. (1985) Tibia bending strength and response. Proceedings of the 29th Stapp Conference, SAE Paper No. 851728.

97. Crandall, J.; Hall, G.W.; Bass, C.R.; Klopp, G.S.; Hurwitz, S.; Pilkey, W.D.; Portier, L.; Petit, P.; Trosselle, X.; Eppinger, R.H.; Lassau; J.P. (1996) Biomechanical response and physical properties of the leg, foot and ankle. Proceedings of the 40th Stapp Conference, SAE Paper No. 962424.

98. Portier, L.; Petit, P., Domont, A., Troiselle, X.; Le Coz; J.Y.; Tarriere, C.; Lassau, J.P. (1997) Dynamic biomechanical dorsiflexion responses and tolerances of the ankle joint complex. Proceedings of the 41st Stapp Conference, SAE Paper No. 973330.

99. Lissner, H.R.; Lebow, M.; Evans, F.G. (1960) Experimental studies on the relation between acceleration and intracranial pressure changes in man. Surgery, Gynecology, and Obstetrics, 111:329-338.

100. McElhaney, J.H.; Roberts, V.L.; Hilyard, J.F. (1976) *Handbook of Human Tolerance,* p. 289. Japan Automobile Research Institute, Inc.

101. Ono, K.; Kikuchi, A.; Nakamura, M.; Kobayashi, H.; Nakamura, N. (1980) Human head tolerance to sagittal impact reliable estimation deduced from experimental head injury using subhuman primates and human cadaver skulls. Proceedings of the 24th Stapp Conference, SAE Paper No. 801303.

102. Gadd, C.W. (1962) Criteria for injury potential. *Impact Acceleration Stress Symposium* pp 141-144, National Academy of Sciences, National Research Council, Publication No. 977.

103. Gadd, C.W. (1966) Use of weighted-impulse criterion for estimating injury hazard. Proceedings of the 10th Stapp Conference, SAE Paper No. 660793.

104. Versace, J. (1971) A review of the severity index. Proceedings of the 15th Stapp Conference, SAE Paper No.710881.

105. Ruan, J.S.; Khalil, T.B.; King, A.I. (1993) Finite element model of direct head impact. Proceedings of the 37th Stapp Conference, SAE Paper No. 933114.

106. McElhaney, J.H.; Myers, B.S. (1993) Biomechanical aspects of Cervical Trauma. *Accidental Injury – Biomechanics and Prevention,* pp 311-361. Ed. by A.M. Nahum; J.W. Melvin, Springer-Verlag, New York.

107. Myers, B.S.; Winkelstein, B.A. (1995) Epidemiology, classification, mechanisms, and tolerance of human cervical spine injuries. *Critical Reviews in Bioengineering,* 23: 307-410.

108. Ryan, J.J. (1962) Human crash deceleration tests on seat-belts. Aerospace Medicine, 33:167-174.

109. Ewing, C.L.; Thomas, D.J.; Patrick, L.M.; Beeler, G.W.; Smith, M.J. (1969) Living human dynamic response to $-G_x$ impact acceleration II, accelerations measured on the head and neck. Proceedings of the 13th Stapp Conference, SAE Paper No. 690817.

110. Cheng, R.; Mital, N.K.; Levine, R.S.; King, A.I. (1979) Biodynamics of the living human spine during -Gx impact acceleration. Proceedings of the 23rd Stapp Conference, SAE Paper No. 791027.

111. Lange, W. (1971) Mechanical and physiological response of the human cervical vertebral column to severe impacts applied to the torso. *A*

Symposium on Biodynamic Models and Their Applications, pp 141-167. Wright-Patterson Air Force Base, Ohio.

112. Clemens, H.J.; Burow, K. (1972) Experimental investigations on injury mechanisms of cervical spine at frontal and rear-front vehicle impacts. Proceedings of the 16th Stapp Conference, SAE Paper No. 720960.

113. Kallieris, D.; Mattern, R.; Miltner, E.; Schmidt, G.; Stein, K. (1991) Considerations for a neck injury criterion. Proceedings of the 35th Stapp Conference, SAE Paper No. 912916.

114. Ewing, C.L.; Thomas, D.J. (1973) Torque versus angular displacement response of human head to $-G_x$ impact acceleration. Proceedings of the 17th Stapp Conference, SAE Paper No. 730976.

115. Ewing, C.L.; Thomas, D.J.; Lustick, L.; Becker, E.; Becker, E.; Willems, G.; Muzzy, W.H. III (1975) The effects of the initial position of the head and neck on the dynamic response of the human head and neck to $-G_x$ impact acceleration. Proceedings of the 19th Stapp Conference, SAE Paper No. 751157.

116. Ewing, C.L.; Thomas, D.J.; Lustick, L.; Muzzy, W.H. III; Willems, G.; Majewski, P.L. (1976) The effect of duration rate of onset and peak sled acceleration on the dynamic response of the human head and neck. Proceedings of the 20th Stapp Conference, SAE Paper No. 760800.

117. Grunsten, R.C. et al., (1989) The Mechanical Effects of Impact Acceleration on the Unconstrained Human Head and Neck Complex, Contemp. Orthop., Vol. 18, pp. 199-202.

118. Thunnissen, J.G.M.; Wismans, J.S.H.M.; Ewing, C.L.; Thomas, D.J. (1995) Human volunteer head-neck response in frontal flexion: A new analysis. Proceedings of the 39th Stapp Conference, SAE Paper No. 952721.

119. Ewing, C.L.; Thomas, D.J.; Lustik, L.; Muzzy, W.H. III; Willems, G.C.; Majewski, P. (1977) Dynamic response of the human head and neck to $+G_y$ impact acceleration. Proceedings of the 21st Stapp Conference, SAE Paper No. 770928.

120. Kallieris, D.; Schmidt, G.; Mattern, R. (1987) Vertebral column injuries in 90-degrees collisions: A study with post-mortem human subjects.

Proceedings of the 12th International Conference on the Biokinetics of Impacts, pp 189-202. IRCOBI.

121. Horsch, J.D., Schneider, D.C.; Kroell, C.K.; Raasch, F.D. (1979) Response of belt restrained subjects in simulated lateral impact. Proceedings of the 23rd Stapp Conference, SAE Paper No. 791005.

122. Kallieris, D.; Schmidt, G. (1990) Neck response and injury assessment using cadavers and the US-SID for far-side lateral impact of rear seat occupants with inboard-anchored shoulder belts. Proceedings of the 34th Stapp Conference, SAE Paper No. 902313.

123. Stapp, J.P. (1951) Human exposure to linear decelerations. Part 2. The forward-facing position and the development of a crash harness. AFTR 5915, pt. 2. Wright-Patterson Air Force Base, Dayton, Ohio.

124. Stapp, J.P. (1970) Voluntary human tolerance levels. *Impact Injury and Crash Protection,* pp 308-349. Ed. by E.S. Gurdjian, W.A. Lange, L.M. Patrick, L.M. Thomas. Charles C. Thomas, Springfield, Illinois.

125. Mertz, H.J.; Kroell, C.K. (1970) Tolerance of the thorax and abdomen. *Impact Injury and Crash Protection,* pp 372-401. Ed. by E.S. Gurdjian, W.A. Langee, L.M. Patrick, L.M. Thomas. Charles C. Thomas, Springfield, Illinois.

126. Kroell, C.K.; Schneider, D.C.; Nahum, A.M. (1974) Impact tolerance and response of the human thorax II. Proceedings of the 18th Stapp Conference, SAE Paper No. 741187.

127. Neathery, R.F. (1975) Prediction of thoracic injury from dummy responses. Proceedings of the 19th Stapp Conference, SAE Paper No. 751151.

128. Lau, I.V.; Viano, D.C. (1981a) Influence of impact velocity on the severity of nonpenetrating hepatic injury. Journal of Trauma, 21:115-123.

129. Lau, I.V.; Viano, D.C. (1981b) Influence of impact velocity and chest compression on experimental pulmonary injury severity in an animal model. Journal of Trauma, 21:1022-1028.

130. Lau, I.V.; Viano, D.C. (1986) The viscous criterion – bases and applications of an injury severity index for soft tissues. Proceedings of the 30th Stapp Conference, SAE Paper No. 861882.

131. Viano, D.C.; Lau, I.V. (1985) Thoracic impact: A viscous tolerance criterion. Proceedings of the 10th ESV Conference, pp 104-114. Oxford, England.

132. Cavanaugh, J.M.; Zhu, Y.; Huang, Y.; King, A.I. (1993) Injury and response of the thorax in side impact cadaveric tests. Proceedings of the 37th Stapp Conference, SAE Paper No. 933127.

133. Eppinger, R.H.; Morgan, R.M.; Marcus, J.H. (1982) Side impact data analysis. Proceedings of the 9th ESV, pp 245-250. Kyoto, Japan.

134. Eppinger, R.H.; Augustyn, K.; Robbins, D.H. (1978) Development of a promising universal thoracic trauma prediction methodology. Proceedings of the 22nd Stapp Conference, SAE Paper No. 780891.

135. Marcus, J.H.; Morgan, R.M.; Eppinger, R.H.; Kallieris, D.; Mattern, R.; Schmidt, G. (1983) Human response to injury from lateral impact. Proceedings of the 27th Stapp Conference, SAE Paper No. 831634.

136. Baxter, C.F.; Williams, R.D. (1961) Blunt abdominal trauma. J Trauma 1:241-247.

137. Melvin, J.W.; Stalnaker, R.L.; Roberts, V.L.; Trollope, M.L. (1973) Impact injury mechanisms in abdominal organs. Proceedings of the 17th Stapp Conference, SAE Paper No. 730968.

138. McElhaney, J.H.; Stalnaker, R.L.; Roberts, V.L.; Snyder, R.G. (1971) Door crashworthiness criteria. Proceedings of the 15th Stapp Conference, SAE Paper No. 710864.

139. Stalnaker, R.L.; McElhaney, J.H.; Roberts, V.L.; Trollope, M.L. (1973b) Human response to blunt trauma. *Human Impact Response: Measurement and Simulation,* pp 181-198. Ed. by W.F. King; H.J. Mertz . Plenum Press, New York.

140. Horsch, J.D.; Lau, I.V.; Viano, D.C.; Andrzejak, D.V. (1985) Mechanism of abdominal injury steering wheel loading. Proceedings of the 29th Stapp Conference, SAE Paper No. 851724.

141. Rouhana, S.W.; Lau, I.V.; Ridella, S.A. (1984) Influence of velocity and forced compression on the severity of abdominal injury in blunt, nonpenetrating lateral impact. GMR Research Publication No. 4763.

142. Rouhana, S.W.; Foster, M.E. (1985) Lateral impact – An analysis of the statistics in the NCSS. Proceedings of the 29th Stapp Conference, SAE Paper No. 851727.

143. Brun-Cassan, F.; Leung, Y.C.; Tarriere, C.; Fayon, A.; Patel, A.; Got, C.; Hureau, J. (1982) Determination of knee-femur-pelvis tolerance from the simulation of car frontal impacts. Proceedings of the 7th International Conference on the Biokinetics of Impacts, pp 101-115. IRCOBI, Bron, France.

144. Doorly, T.P.G. (1978) Forces imposed on the hip-joint in car collisions. Journal of Traffic Medicine, 6:44-46.

145. Patrick, L.M.; Andersson, A. (1974) Three-point harness accident and laboratory data comparison. Proceedings of the 18th Stapp Conference, SAE Paper 741181.

146. Cesari, D.; Bouquet, R.; Zac, R. (1984) A new pelvis design for the European side impact dummy. Proceedings of the 28th Stapp Conference, SAE Paper No. 841650.

147. Ramet M.; Cesari, D. (1979) Experimental study of pelvis tolerance in lateral impact. Proceedings of the 4th International Conference on the Biokinetics of Impacts, pp 243-249. IRCOBI, Bron, France.

148. Weber, C.O. (1859) *Chirurgische erfahrungen und Untersuchungen*. Berlin. (As cited by Messerer).

149. Messerer, O. (1980) Uber Elasticitat und Festigkeit der Menschlichen Knochen. JG Cotta, Stuggart.

150. Powell, W.R.; Advani, S.H.; Clark, R.N.; Ojala, S.J., Holt, D.J. (1974) Investigation of femur response to longitudinal impact. Proceedings of the 18th Stapp Conference, SAE Paper No. 741190.

151. Powell, W.R.; Advani, S.H.; Clark, R.N.; Ojala, S.J., Martin, R.B. (1975) Cadaver femur responses to longitudinal impacts. Proceedings of the 19th Stapp Conference, SAE Paper No. 751160.

152. Melvin, J.W., Stalnaker, R.L., Alem, N.M.; Benson, J.B.; Mohan, D. (1975) Impact response and tolerance of the lower extremities. Proceedings of

the 19th Stapp Conference, SAE Paper No. 751159.

153. Melvin, J.W.; Stalnaker, R.L. (1976) Tolerance and response of the knee-femur-pelvis complex to axial impact. Report No. UM-HSRI-76-33. University of Michigan, Ann Arbor.

154. Viano, D.C.; Stalnaker, R.L. (1980) Mechanisms of femoral fractures. Journal of Biomechanics, 13:701-715.

155. Stalnaker, R.L.; Nusholtz, G.S.; Melvin, J.W. (1977) Femur impact study. Report No. UN-HSRI-77-25. University of Michigan, Ann Arbor.

156. Viano, D.C.; Khalil, T.B. (1976) Considerations for a femur injury criterion. Plane strain analysis of a femur midsection. Proceedings of the 4th New England Bioengineering Conference, Pergamon, Elmsford, New York.

157. Viano, D.C. (1977) Considerations for a femur injury criterion. Proceedings of the 21st Stapp Conference, SAE Paper No. 770925.

158. Lowne, R.W. (1982) A revised upper leg injury criterion. Working Paper No. 42. Transport and Road Research Laboratory, Crowthorne, England (Also ISO.TC22/SC12/WG6 No. 109, April, 1982).

159. Nyquist, G.W. (1982) A pulse-shape dependent knee-thigh-hip injury criterion for use with the Part 572 dummy. Draft Report. ISO/TC22/SC12/WG6, No. 117, International Standards Organization, Geneva.

160. Melvin, J.W.; Fuller, P.M.; Daniel, R.P.; Pavliscak, G.M. (1969) Human head and knee tolerance to localized impacts. SAE Paper No. 690477.

161. Viano, D.C.; Culver, C.C. (1979) Performance of a shoulder belt and knee restraint in barrier crash simulations. Proceedings of the 23rd Stapp Conference, SAE Paper No. 791006.

162. Kramer, M.; Burow, K.; Heger, A. (1973) Fracture mechanisms of lower legs under impact load. Proceedings of the 17th Stapp Conference, Paper No. 730966.

163. Pritz, H.B.; Weis, E.B.; Herridge, J.T. (1975) Body vehicle interaction: Experimental study , Volume II. Battelle Columbus Laboratories. Columbus, Ohio.

164. Pritz, H.B.; Hassler, C.R.; Weis, E.B. (1978) Pedestrian impact: Baseline and preliminary concepts evaluation, Volume II: Technical Discussion. Battelle Columbus Laboratories, Columbus, Ohio.

165. Culver, C.C. (1984) Lower leg axial force studies: Exploratory tests using excised cadaver legs. Biomedical Science Department, General Motors Research Laboratories, Warren, Michigan (unpublished).

166. Irwin, A.L.; Walilko, T.J.; Cavanaugh, J.M.; Zhu, Y.; King, A.I. (1993) Displacement responses of the shoulder and thorax in lateral sled impacts. Proceedings of the 37th Stapp Conference, SAE Paper No. 933124.

Additional References

Lobdell, T.E.; Kroell, C.K.; Schneider, D.C.; Hering, W.E.; Nahum, A.M. (1973) Impact response of the human thorax. Human Impact Response: Measurement & Simulation, pp 201-246. Ed. by W.F. King; H.J. Mertz. Plenum Press, New York.

Melvin, J.W.; Hess, R.L.; Weber, K. (1985) Thorax. Review of Biomechanical Impact response and Injury in the Automotive Environment, pp 93-123. Ed. by J.W. Melvin; K. Weber. National Technical Information Service, Virginia.

Morgan, R.M.; Marcus, J.H.; Eppinger, R.H. (1986) Side impact – The biofidelity of NHTSA's proposed ATD and efficacy of TTI. Proceedings of the 30th Stapp Conference, SAE Paper No. 861877.

Viano, D.C. (1978) Thoracic injury potential. Proceedings of the 3rd International Conference on the Biokinetics of Impacts, pp 142-156. IRCOBI, Bron, France.

Anthropomorphic Test Devices

Harold J. Mertz

7.1 Introduction

Anthropomorphic test devices (ATDs), commonly referred to as dummies, are mechanical surrogates of humans. Crashworthiness engineers use ATDs to evaluate the occupant protection potential of various types of restraint systems in simulated collisions of new vehicle designs. Current ATDs are designed to be biofidelic, meaning they mimic pertinent human physical characteristics such as size, shape, mass, stiffness, and energy absorption and dissipation. The dummies' mechanical responses simulate corresponding human responses of trajectory, velocity, acceleration, deformation, and articulation when the dummies are exposed to prescribed simulated collision conditions. Engineers equip dummies with transducers that measure accelerations, deformations and loading of various body parts. Analyses of these measurements are used to assess the efficacy of restraint system designs.

Dummies are classified according to size, age, sex and impact direction. Adult male and female dummies are of different sizes and child dummies represent different ages. Some dummies are used to assess frontal collision protection and others are used to evaluate side impact collisions. The most current frontal impact dummies have sufficient biofidelity to be used to evaluate rear-end collision protection. However, neither the current frontal nor side impact dummies have the necessary biofidelity, measurement capacity nor durability to evaluate the other's impact direction. Most often, test engineers use the mid-size adult male dummy for automotive restraint testing. It approximates the median height and weight of the 50th-percentile adult male population. The heights and weights of the small female and large male adult dummies are approximately those of the 5th-percentile female and the 95th-percentile male, respectively. Child dummies have the median heights and weights of children of the specific age groups they represent without regard to gender. Table 7.1.1 – Key Dimensions and Weights for Various Size Dummies, includes information on infant, child and adult dummies.

Table 7.1.1 **Key dimensions and weights for various sizes of dummies**

	Infant			Child		Adult		
	6 Mo	12 Mo	18 Mo	3 Yr	6 Yr	5th Female	50th Male	95th Male
Dimensions (mm)								
Erect Sitting Ht	439	480	505	546	635	812	907	970
Buttocks to Knee	170	198	221	284	381	521	589	638
Knee to Floor	125	155	173	221	358	464	544	594
Shoulder to Elbow	130	150	160	193	234	305	366	381
Elbow to Fingertip	175	198	213	254	310	399	465	503
Standing Height	671	747	813	953	1168	1510	1751	1873
Weights (kg)								
Head	2.11	2.49	2.72	3.05	3.48	3.68	4.54	4.96
Neck	0.29	0.34	0.35	0.43	0.41	0.81	1.54	2.04
Torso	3.04	4.38	5.22	6.61	10.7-6	24.14	40.23	53.00
Upper Ext.	0.85	1.18	1.31	1.79	1.98	4.76	8.53	10.94
Lower Ext.	1.53	1.31	1.60	2.63	4.28	13.52	23.36	31.79
Total Weight	7.82	9.70	11.-20	14.5-1	20.9-1	46.82	78.20	102.73

Authors have summarized the history of dummy development in a number of publications (1-3). Table 7.1.2 – Chronology of Notable Dummies Used by the United States Auto Industry, gives a chronology of the dummies that have been

Table 7.1.2 – **Chronology of notable dummies used by the United States auto industry**

Year	Dummy	Key Features	Deficiencies	Current Usage
1949	Sierra Sam 95th Male (Frontal Impacts)	Human-like exterior shape and body weight. Articulated limb joints. Durable.	Stiffness not biofidelic. Limited instrumentation. Poor reproducibility.	None
1966	VIP Series (Very Important People) 5th Female, 50th & 95th Male (Frontal Impacts)	Human-like shape and body weight. Articulated limb joints. Rubber neck. Human shaped pelvis. Instrumented to measure head and thoracic spine accelerations and femur loads.	Stiffness not biofidelic. Limited instrumentation. Poor repeatability and reproducibility.	None
1967	Sierra Stan 50th Male (Frontal Impacts)	Human-like shape and body weight. Articulated limb joints. Segmented neck. Plastic shell for rib cage. Instrumented to measure head and thoracic spine accelerations and femur loads.	Stiffness not biofidelic. Limited instrumentation. Poor neck bending response.	None
1968	Sophisticated Sam 50th Male (Frontal Impacts)	Easily broken clavicles, humeri, radii, ulna, femurs, tibiae, fibulae and patellae.	Fracture levels of bones poorly controlled.	None
1970	Sierra Susie 5th Female	Same features as Sierra Stan from which it was scaled.	Same as Sierra Stan	None
1972	GM Hybrid II 50th Male (Frontal Impacts)	Uses parts from VIP - 50 and Sierra Stan. Human-like shape, body weight and ranges of motion of some articulated joints. Repeatable, durable and reproducible. Specified for use in FMVSS 208 until 9/97.	Stiffness not biofidelic. Limited instrumentation.	None
1976	GM Hybrid III 50th Male (Frontal & Rear Impacts)	Based on GM ATD-502 which was developed under NHTSA contract. Human-like shape and weight. Biofidelic response for head, neck, chest, knee. Exten-sively instrumented. Human-like automotive seated posture. Excellent biofidelity, repeatability, reproducibility and durability.	Not appropriate for side impact studies.	Worldwide Reg.

Table 7.1.2 (Cont.) – **Chronology of notable dummies used by the United States auto industry**

Year	Dummy	Key Features	Deficiencies	Current Usage
1979	NHTSA / SID 50th Male (Side Impact)	Modified Hybrid II with chest design for side impact loading.	No shoulder or arm. Not biofidelic in response. Limited instrumentation. Not recommended by ISO for side impact testing.·	USA & Australia Reg.
1982	GM 3-Year-Old "Air Bag" Dummy	Modified ARL VIP-3C Dummy with foam filled rib cage and segmented neck structure tuned to give human-like response. Instrumented to measure loads associated with air bag deployment injuries.		Passenger AirbagTests
1985	Hybrid II Type 3 and 6-Year-Old Dummies	Modified ARL - 3 & 6C child dummies. Specified by NHTSA in Part 572 for child restraint testing.	Not biofidelic in impact response. Limited instrumentation.	USA Reg.
1987	Hybrid III Type Small Female (5th), Large Male (95th) and 6-Year-Old. (Frontal and Rear Impacts)	Scaled from Hybrid III mid-size male with same level of biofidelity and measurements capacity. Being incorporated into Part 572 by NHTSA.	Not appropriate for side impact tests.	Worldwide
1989	EUROSID-1 50th Male (European Side Impact Dummy)	Hybrid III dummy modified for side impact testing. Unique neck, chest, abdomen and pelvis.	Marginal biofidelity. Shoulder designs blocks rib deflection. Limited instrumentation.	Europe, Australia, Japan Reg.
1989	BIOSID 50th Male (Side Impact)	Hybrid III dummy modified for side impact testing. "Far Side" mounted rib concept used for shoulder, thorax and abdomen design. Pelvis is modified EUROSID-1 design. Extensively instrumented. Acceptable biofidelity.	Biofidelity could be improved. Side impact testing only.	Exp. Worldwide
1990	CRABI6-, 12-,& 18-Month	Designed to evaluate air bag interactions with rear facing infant restraints. Biofidelic neck. NHSTA is incorporating into Part 572.	Head impact response may not be biofidelic.	Exp. Worldwide

Table 7.1.2 (Cont.) – **Chronology of notable dummies used by the United States auto industry**

Year	Dummy	Key Features	Deficiencies	Current Usage
1997	TNO - Q3 (3-Year Old Child Dummy for Frontal & Side Impacts)	Improved biofidelity and instrumentation. Designed for frontal and side impacts. Developed to replace TNO - P3 in European Reg.	Not designed for air bag interaction testing.	Exp. Worldwide
1998	SID - H III 50th Male (Side Impact)	SID dummy with head and neck of Hybrid III mid-size male. Developed by NHTSA for side-impact pole test.	Same as SID, but head and neck are now biofidelic.	USA Reg.
1999	SID IIs 5th Female (Side Impact)	Scaled from BIO SID with improved biofidelity and extensively instrumented. Represents small adult female or 12- to 13-year old.	Not designed for frontal impact testing.	Exp. Worldwide

used in restraint system testing by the domestic automobile industry. Sierra Sam, a 95th-percentile adult male dummy developed by Sierra Engineering Company in 1949, was the first crash test dummy used by the domestic automobile industry for restraint system testing. Sierra Sam was originally developed for ejection seat testing by the U.S. Air Force. Engineers used early versions of dummies to assess the integrity of restraint systems during simulated frontal collisions. These dummies mimicked human shape and weight and were quite durable. However, they lacked human-like stiffness in the importantareas such as the head, neck, thorax and knee. They also were not extensively instrumented to measure responses that could be associated with all pertinent injury concerns. Current dummies have been designed to be biofidelic in their impact responses and are extensively instrumented. The following is a discussion of the pertinent characteristics of the more notable frontal impact dummies (the Hybrid II and III families and the CRABI infant dummies) and side impact dummies (SID, EUROSID-1, BIOSID and SID-IIs).

7.2 Hybrid II Dummy Family

The most used of the early frontal impact dummies was the Hybrid II mid-size adult male dummy developed by GM in 1972 to assess the integrity of lap/shoulder belt systems (1, 2). This dummy mimicked the size, shape, mass and ranges of arm

and leg motion of the 50th-percentile adult male. It was instrumented to measure the orthogonal linear accelerations of the center of gravity of its head and a point prescribed in ts "thoracic spine." Its femurs were instrumented to measure axial-shaft loading. The dummy was quite durable and gave repeatable responses of coefficient of variations of 10 percent or less when subjected to repeat tests. The design of the dummy was sufficiently defined by engineering drawings so that dummies manufactured to the specifications would give similar results under similar test conditions. In 1973, the GM Hybrid II was specified in the FMVSS 208 as the dummy to be used for compliance testing of vehicles equipped with passive restraints (4). It remained as a compliance dummy until 1997. In addition to the mid-size male, Humanoid Systems developed Hybrid II type small adult female and large adult male dummies by scaling the shapes and features of the mid-size male (1, 2). These dummies had instrumentation capabilities similar to the Hybrid II mid-size adult male. At the same time, engineers developed 3-year-old and 6-year-old child dummies. The child dummies, along with the three sizes of adult dummies, became known as the Hybrid II Dummy Family.

The Hybrid II Dummy Family had two major deficiencies that limited their usefulness in assessing the efficacy of restraint systems. They lacked human-like response stiffness for their heads, necks, thoraxes and knees and they were sparsely instrumented.

7.3 Hybrid III Dummy Family

The Hybrid III Dummy Family consists of a small adult (5th percentile) female dummy, a mid-size adult (50th percentile) male dummy, a large adult (95th percentile) male dummy, a 3-year-old child dummy and a 6-year-old child dummy. Figures 7.3.1 – Hybrid III Adult Dummies and 7.3.2 – Hybrid III 3-year-old, 6-year-old and the CRABI 12-month, show the family. These dummies were developed to address the biofidelity and instrumentation deficiencies of the Hybrid II family. Because their necks mimic human bending response in flexion and extension, these dummies can be used in rear as well as frontal collision evaluations. The following is a discussion of the development of the Hybrid III Dummy Family.

In 1972, General Motors initiated a research program to define and develop a biofidelic mid-size adult male dummy, called Hybrid III, to replace the GM Hybrid II dummy. The Hybrid III (5, 6) was designed to mimic human responses for forehead impacts, fore and aft neck bending, distributed sternal impacts and knee impacts. Its head consists of an aluminum shell covered by vinyl skin having constant thickness over the cranium. The thickness of the skin was chosen to give human-like head accelerations when the forehead is impacted. The neck is

Fig. 7.3.1 **Hybrid III adult dummies (small females, mid-size male and large male)**

made up of asymmetric rubber segments bonded to aluminum disks. A braided wire cable attached to end plates passes through the neck center. The top end plate is linked to the head with a single pivot joint to represent the atlanto-occipital joint of the human. This construction allows the neck to mimic human neck bending responses for flexion, extension, and lateral bending. The chest comprises six steel ribs linked on one end to a leather part representing the sternum and on the other end to a rigid spine. Dampening material is bonded to the inside of each rib to copy the energy dissipation of the human thorax. The ribs are sized to mimic the sternal force-deflection response of the human thorax. The shoulder structure was designed to provide an appropriate interface with the shoulder belt. The abdomen is made of plastic foam. The lumbar spine is represented by a cylindrical curved rubber piece with two braided steel cables running through the center and attached to end plates. The curvature gives the dummy a human-like seated posture. The pelvis is an aluminum casting of a human pelvic bone covered with vinyl skin. Femurs and legs are made of steel shafts covered with vinyl skin. Rubber pads are inserted in both knee areas under the skin to give human-like impact response. Ball joints are used for the hip and ankle. Other joints are constant torque pin-joints. Table 7.3.1 – Instrumentation of III Dummies, notes the extensive instrumentation of the dummy.

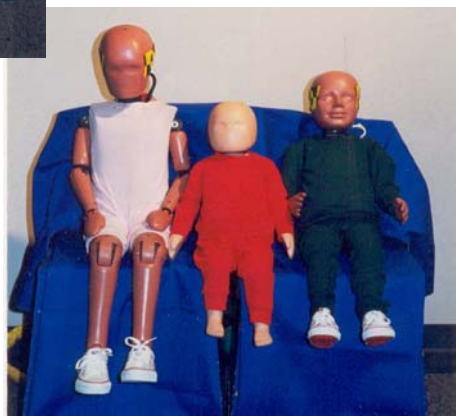

Fig. 7.3.2 **Hybrid III 3-year-old, 6-year-old and the CRABI 12-month**

Because of its excellent biofidelity and measurement capability, General Motors petitioned the National Highway Traffic Safety Administration (NHTSA) in 1983 to allow the use of the Hybrid III mid-size adult male dummy as an alternative test device to the Hybrid II for FMVSS 208 compliance testing of passive restraints. Its use was allowed in 1986. In 1990, General Motors filed a second petition requesting that the Hybrid II dummy be deleted from FMVSS 208 compliance testing. NHTSA deleted the Hybrid II in 1997, making the Hybrid III mid-size adult male dummy the only dummy allowed for FMVSS 208 testing and the only dummy specified for frontal restraint evaluation throughout the world.

Since its creation in 1976, the Hybrid III mid-size male dummy has undergone design changes to improve the biofidelity of its hips and ankles (7) and to increase its measurement capacity (6). Because the Hybrid III is specified in worldwide regulations, several regulatory bodies must approve all design changes. After NHTSA allowed the use of the Hybrid III mid-size adult in FMVSS 208 compliance testing, the Centers for Disease Control and Prevention (CDC) awarded a grant to The Ohio State University in 1987 to develop a multi-sized Hybrid III-based dummy family. To support this effort, the Mechanical Human Simulation Subcommittee of the Human Biomechanics and Simulation Standards Committee of the Society of Automotive Engineers (SAE) formed a Dummy Family Task Group of biomechanics, test dummy, transducer, and restraint-system experts. They defined the specifications for a small adult (5th percentile) female dummy, a large adult (95th percentile) male dummy and a 6-year-old child dummy having the same level of biofidelity and measurement capacity as the Hybrid III mid-size adult male dummy. Key body segment lengths and weights were defined based on anthropometry data for the United States population. Biofidelity response requirements for the head, neck, thorax, and knee of each size of dummy were scaled from the respective biofidelity requirements of the Hybrid III, mid-size adult male dummy (8, 9).

In 1992, the SAE Hybrid III Dummy Family Task Group initiated a program to develop a Hybrid III 3-year-old child dummy. Again, this dummy was designed to have the same level of biofidelity and measurement capacity as the other Hybrid III type dummies, except for the knee impact requirement and the leg instrumentation (8). These items were omitted from the design requirements since knee impact is an unlikely event for a properly restrained 3-year-old child. This dummy was designed to replace the GM 3-year-old “airbag” dummy (10) for evaluating unrestrained child interactions with deploying passenger airbags. It would also be used to assess the efficacy of child restraints. For these reasons, its sternum was instrumented to measure its response to the punch-out forces of deploying passenger airbags. Table 7.3.1 – Instrumentation for III Dummies, summarizes its instrumentation.

Table 7.3.1 Instrumentation for III dummies

Dummy Instrumentation	HIII 3-Yr Child	HIII 6-Yr Child	HIII 5 Female	HIII 50 Male	HIII 95 Male
Head Accelerations (A_x, A_y, A_z)	Yes	Yes	Yes	Yes	Yes
Neck H/CI (F_x, F_y, F_z, M_x, M_y, M_z)	Yes	Yes	Yes	Yes	Yes
C7/TI (F_x, F_y, F_z, M_x, M_y, M_z)	Yes	Yes	Yes	Yes	Yes
Shoulder Loads (F_x, F_z)	No	Yes	Yes	Yes	Yes
Thorax Spine Accel. (A_x, A_y, A_z)	Yes	Yes	Yes	Yes	Yes
Sternal Def. (δ_x)	Yes	Yes	Yes	Yes	Yes
Sternal Acc. (A_x)	Yes	Yes	Yes	Yes	No
Abdomen Lumbar (F_x, F_y, F_z, M_x, M_y)	Yes	Yes	Yes	Yes	Yes
Pelvis Acceleration (A_x, A_y, A_z)	No	No	Yes	Yes	Yes
Ilium (F_y)	No	Yes	Yes	Yes	No
Lower Extremities Femur (F_x, F_y, F_z, M_x, M_y, M_z)	No	Yes	Yes	Yes	Yes
Tibia/Femur Displ. (δ_x)	No	No	Yes	Yes	Yes
Knee Clevis (F_z)	No	No	Yes	Yes	Yes
Tibia Loads & Moments (F_x, F_y, F_z, M_x, M_y, M_z)	No	No	Yes	Yes	Yes

The SAE Hybrid III Dummy Task Group has documented the designs of the Hybrid III small female, large male, 3-year-old child and 6-year-old child dummies so that they can be incorporated into Part 572 of the United States Transportation Regulations, replacing their respective Hybrid II dummies. The dummies are well defined and durable, giving highly repeatable and reproducible results. NHTSA is expected to issue a final rule that incorporates these dummies into Part 572 within the next few months.

7.4 CRABI Infant Dummies

In 1990, a second SAE Task Group of the Human Mechanical Simulation Subcommittee convened to develop instrumented 6-month-, 12-month-, and 18-month-old infant dummies. The dummies would be used to assess the injury potential to infants due to the interactions of deploying passenger air bags and rearward-facing child restraints placed in the front seat of vehicles. 7.3.1 – Hybrid 3-year-old, 6-year-old and the CRABI 12-month shows the 12-month-old dummy. Prototype CRABI (Child Restraint Air Bag Interaction) dummies were available in 1991. The size and weights of the dummies were based on anthropometry studies of the United States child population. Biofidelity response requirements were defined for the head and neck (9). Table 7.4.1 – Instrumentation for CRABI Dummies, shows the instrumentation used with the dummies. The designs of these dummies are currently being documented for incorporation into Part 572 along with the Hybrid III Dummy Family.

Table 7.4.1 **Instrumentation for CRABI dummies**

Dummy Instrumentation	CRABI 6-Mo	CRABI 12-Mo	CRABI 18-Mo
Head Acceleration (A_x, A_y, A_z)	Yes	Yes	Yes
Neck Head/Neck Interface (F_x, F_y, F_z, M_x, M_y, M_z)	Yes	Yes	Yes
Neck/T. Spine Interface (F_x, F_y, F_z, M_x, M_y, M_z)	Yes	Yes	Yes
Shoulder (F_x, F_y)	No	Yes	Yes
Thorax Spine (A_x, A_y, A_z)	Yes	Yes	Yes
Abdomen Lumbar/Pelvis Interface (F_x, F_y, F_z, M_x, M_y, M_z)	Yes	Yes	Yes
Pelvis Acceleration (A_x, A_y, A_z)	Yes	Yes	Yes
Pubic Loads (F_x, F_z)	No	Yes	Yes

7.5 Side Impact Dummies

There are three commercially available 50th-percentile adult male side impact dummies: SID, EUROSID-1 and BIOSID. They are shown in Figure 7.5.1 – 50th Percentile Adult Male Side Impact Dummies. A fourth side impact dummy, SID IIs, has been developed under the Occupant Safety Research Partnership (OSRP) of the United States Council on Automotive Research (USCAR). This dummy is representative of the size and weight of a small adult (5th percentile) female or a 12- to 13-year-old adolescent. Brief descriptions of SID, EUROSID-1, BIOSID and SID IIs follow.

University of Michigan Transportation Research Institute (UMTRI), under contract with NHTSA (11-14) developed SID (Side Impact Dummy) in 1979. SID is

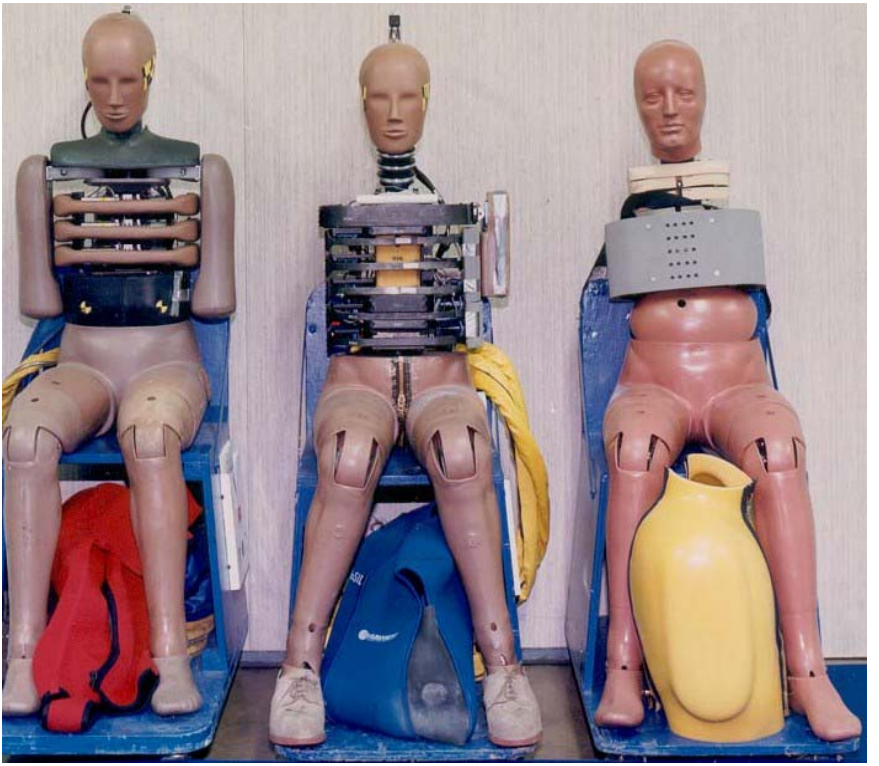

Fig. 7.5.1 **50th percentile adult male side impact dummies (SID, EUROSID-1, BIOSID)**

a Hybrid II dummy modified for side impact testing. It features a unique chest structure including a hydraulic shock absorber that links five interconnected steel ribs to the spine. SID has no arm or shoulder structure. The chest is covered with vinyl. The other body segments are those of the Hybrid II. Exterior size and shape are those of a 50th-percentile adult male. Table 7.5.1 – Instrumentation for Side Impact Dummies shows its instrumentation and includes measurement of linear accelerations of the head, thoracic spine, ribs and pelvis.

Major biofidelic deficiencies of the SID are the lack of a shoulder load path, no elasticity in the thoracic compliance, and a very heavy rib mass. Major instrumentation deficiencies are no measurement of neck, shoulder and abdominal loads and no measurement of rib deflection (18). The dummy does not provide sufficient biofidelity or measurement capacity to be used to either design or assess side impact protection (15-23). Despite these deficiencies, the SID was specified by NHTSA as the only dummy to be used to evaluate side impact protection compliance under FMVSS 214. In 1998, NHTSA updated the SID with the head and neck structures of the Hybrid III mid-size male dummy. This change improved the head/neck biofidelity of the dummy and allowed measurement of neck loads in the compliance testing of head airbags in the NHTSA side impact pole test.

EUROSID-1 (European Side Impact Dummy, Version 1) was developed in 1986 by several European laboratories working together under the auspices of the European Experimental Vehicle Committee (EEVC). Extensive development of EUROSID was performed by Association Peugeot-Renault (APR) and Institute National de Recherché sur les Transports et leur Securite (INRETS) in France, TNO in the Netherlands, and Transport Research Laboratory (TRL) in the United Kingdom. Four prototypes were built and evaluated in 1986. Between 1987 and 1989, governments, the automotive industry, the International Organization for Standardization (ISO), and the SAE (15-17, 23) evaluated this version, known as EUROSID Production Prototype (24-26). Based on this international evaluation, the dummy's biofidelity, dura-bility and instrumentation were improved, and its named was changed to EUROSID-1 (27).

The EUROSID-1 consists of a metal and plastic skeleton covered by foam and rubber. The head is that of the Hybrid III. The neck is a composite of metal discs and rubber elements with special joints to the head and the thoracic spine, which allows a human-like head-to-chest motion. The thorax consists of three separate, identical ribs covered with flesh-simulating foam, attached to a rigid steel spine box by a piston-cylinder assembly and a spring-damper system. The shoulder is designed to rotate forward allowing a direct impact exposure of the chest. The

abdomen is lead-impregnated, skinned foam. A solid rubber cylinder with a steel cable inside simulates the lumbar spine. The pelvis consists of two plastic iliac wings linked by a metal sacrum and covered with a foam and polyvinylchloride skin. The arms are represented by upper arms (plastic skeleton and flesh) only, and the legs are those of the Hybrid III. Table 7.5.1 – Instrumentation for Side Impact Dummies, shows the EUROSID-1 instrumentation including linear accelerometers in the head, spine, ribs and pelvis. Rib-to-spine displacement can be measured for each rib. Loads to the abdomen and pelvis are measured by means of transducers. The dummy represents a 50th-percentile adult male and its final specification was established by EEVC in 1989. EUROSID-1 is the only dummy allowed for compliance testing by the European Side Impact Regulation ECE 48.

Major deficiencies of the dummy are its marginal biofidelity (22), the flat-topping that can occur on its rib deflection measurements due to the inter-action of the arm/and shoulder structure with its ribs (28), and the lack of neck, iliac and acetabulum load measurements (18).

BIOSID (Biofidelic Side Impact Dummy) was developed in 1989 by SAE for side impact testing after international evaluations of EUROSID and SID indicated the need for a more biofidelic dummy with additional measurement capability. Engineers designed the dummy to have impact response biofidelity for the head, neck, shoulders, thorax, abdomen, and pelvis (29-30).

BIOSID uses the Hybrid III head, neck and legs. The chest design is based on a "far side" mounted rib concept which allows 75 mm of rib deflection without permanent rib deformation (31). The shoulder and abdominal constructions are also made using this concept. Only the upper arm is simulated on BIOSID. The pelvis is a modification of the EUROSID pelvis, but is made of metal with a crushable block in the H-point area. Table 7.5.1 — Instrumentation for Side Impact Dummies shows BIOSID instrumentation that measures linear acceleration of the head, shoulders, spine, thoracic and abdominal ribs, and pelvis; neck forces and moments; shoulder force and deflection; rib deflection in the chest and abdominal areas; iliac, sacrum and pubic symphysis forces; and same lower extremity loads as that of the Hybrid III.

The design of the dummy is well documented and quite durable, resulting in excellent repeatability and reproducibility. BIOSIOD has been commercially available since 1990. It is an acceptable test device for assessing side impact protection (18, 22, 23).

SID-IIs is a small (s), second generation (II) Side Impact Dummy (SID) which has the anthropometry of a 5th-percentile adult female. It is represen-tative of a 12- to 13-year-old adolescent. SID-IIs was developed to fill the need for a small dummy to evaluate side impact protection countermeasures, notably air bags (32, 33). The Small Size Advanced Side Impact Dummy Task Group of OSRP first met in 1994 to define the general characteristics of the SID-IIs. The biofidelity response targets were scaled from ISO targets (32, 34) that were de-fined for the 50th-percentile adult male. Since the SID-IIs was to have the anthropometry of the small adult female, many of the parts from the Hybrid III small adult female were incorporated into the design. The thorax, abdomen and pelvis structures are scaled versions of the BIOSID design. Table 7.5.1 – Instrumentation for Side Impact Dummies notes the extensive instrumentation of SID-IIs, which has total measurement capacity of 148 data channels. This includes the use of an Instrumented Arm (35) that has been incorporated into the design. Using the ISO rating scheme (18-21), the SID-IIs biofidelity is rated good and its instrumentation rating is excellent. Final documentation of the dummy in terms of design drawings and calibration requirements are being completed. The dummy is expected to be commercially available in the near future.

7.6 Dummy Harmonization

The Hybrid III mid-size adult male is the only dummy that is used by regulatory bodies worldwide for restraint system evaluation. NHTSA is in the process of incorporating the Hybrid III dummy family and the CRABI infant dummies into its safety standards. While there is a good possibility of other countries adopting the use of the Hybrid III small female and large male dummies into their regulations, there appears to be no worldwide acceptance of the child and infant dummies. TNO has been funded by the European Union (EU) to develop a new family of Q-series child dummies to replace the P-series which are currently specified in European regulations. For side impact regulations, SID is specified by NHTSA as the only dummy allowed for FMVSS 214 compliance testing. Europe and Japan have specified EUROSID-1 for side impact compliance testing. Australia allows either dummy to be used. Recently, the ISO has taken on the task of developing World SID, a side impact dummy acceptable to all regulatory bodies. Development of World SID was completed in 2004.

Clearly, to obtain dummy harmonization for safety regulation there must be an international agreement on the need to improve an existing dummy design, an agreement on the improvements, a cooperative development program to make the changes, and a willingness to accept the upgraded dummy by all interested parties.

Table 7.5.1 **Instrumentation for side impact dummies**

Dummy Instrumentation	SID	SID-HIII	EUROSID-1	BIOSID	SID-IIs
Head Accelerations (A_x, A_y, A_z)	No	Yes	Yes	Yes	Yes
Neck H/CI (F_x, F_y, F_z, M_x, M_y, M_z)	No	Yes	No	Yes	Yes
C7/TI (F_x, F_y, F_z, M_x, M_y, M_z)	No	No	Yes	Yes	Yes
Shoulder Loads (F_x, F_y, F_z)	No	No	Yes	Yes	Yes
Deflection (δ_y)	No	No	No	Yes	Yes
Arm (A_x, A_y, A_z, M_y, M_z)	No	No	No	No	Yes
Thorax Spine Acceleration (A_x, A_y, A_z)	Yes	Yes	Yes	Yes	Yes
Rib Deflection (δ_y)	No	No	Yes	Yes	Yes
Rib Acceleration (A_y)	Yes	Yes	Yes	Yes	Yes
Abdomen Force (F_y)	No	No	Yes	No	Yes
Deflection (δ_y)	No	No	No	Yes	Yes
Lumbar (F_x, F_y, F_z, M_x, M_y)	No	No	F_y, F_z, M_x	Yes	Yes
Pelvis Acceleration (A_x, A_y, A_z)	Yes	Yes	Yes	Yes	Yes
Ilium (F_y)	No	No	No	Yes	Yes
Acetabulum (F_y)	No	No	No	No	Yes
Pubic (F_y)	No	No	Yes	Yes	Yes
Lower Extremities Femur (F_x, F_y, F_z, M_x, M_y, M_z)	No	No	F_z	Yes	Yes
Knee Clevis (F_z)	No	No	No	Yes	Yes
Tibia Loads & Moments (F_x, F_y, F_z, M_x, M_y, M_z)	No	No	No	Yes	Yes

7.7 References

1. Mertz, H. J., "Anthropomorphic Models," The Biomechanics of Trauma, Appleton-Century-Crofts, Norwalk, Connecticut, 1985.

2. Mertz, H. J., "Anthropomorphic Test Devices," Accidental Injury: Biomechanics and Prevention, Springer-Verlag, New York, NY, 1993.

3. *Anthropomophic Dummies for Crash and Escape System Testing*, AGARD-AR-330, ISBN 92-836-1039-3, July 1996.

4. "Anthropomorphic Test Dummy," Code of Federal Regulations, Title 49, Chapter V, Part 572 - Subpart B, Federal Register 1973; 38 (August 1), 147.

5. Foster, J. K., Kortge, J. O. and Wolanin, M. J., "Hybrid III - A Biomechanically Based Crash Test Dummy," 21st Stapp Car Crash Conference, SAE 770938, October 1977.

6. *Hybrid III: The First Human Like Crash Test Dummy*, Edited by S. L. Backaitis and H. J. Mertz, SAE PT-44, Warrendale, PA, 1994.

7. Klinich, K. D., Beebe, M. S. and Backaitis, S. H., "Evaluation of a Proposed Hybrid III Hip Modification," 39th Stapp Car Crash Conference, SAE 952730, November 1995.

8. Mertz, H. J., Irwin, A. L., Melvin, J. W., Stalnaker, R. L. and Beebe, M. S., "Size, Weight and Biomechanical Impact Response Requirements for Adult Size Small Female and Large Dummies," SAE 890756, March 1989.

9. Irwin, A. L. and Mertz, H. J., "Biomechanical Bases for the CRABI and Hybrid III Child Dummies," SAE 973317, 41st Stapp Car Crash Conference, November 1997.

10. Wolanin, M. J., Mertz, H. J., Nyznyk, R. S. and Vincent J. H., "Description and Basis of a Three-year-old Child Dummy for Evaluating Passenger Inflatable Restraint Concepts," 9th International Technical Conference on Experimental Safety Vehicles, November 1982. (Republished as SAE 826040, Automatic Occupant Protection Systems, SP-736, 1988).

11. Melvin, J. W., Robbins, D. H., and Benson, J. B., "Experimental Application of Advanced Thoracic Instrumentation Techniques to Anthropomorphic Test Devices," 7th Experimental Safety Vehicle Conference, Paris, 1979.

12. Donnelly, B. R., "Assembly Manual for the NHTSA Side Impact Dummy," CALSPAN Report No. 7073-V-1, Contract No. DTNH22-82-C-07366, March 1982.

13. Eppinger, R. H., Marcus, J. H. and Morgan, R.M., "Development of Dummy and Injury Index for NHTSA's Side Impact Protection Research Program," SAE 840885, February 1984.

14. Morgan, R. M., Marcus, J. H. and Eppinger, R. H., "Side Impact - The Biofidelity of NHTSA's Proposed ATD and Efficacy of TTI," 30th Stapp Car Crash Conference, SAE 861877, 1986.

15. Bendjellal, F., Tarriere, C., Brun-Casson, F., Foret-Bruno, J. and Caillibot, P., "Comparative Evaluation of the Biofidelity of EUROSID and SID Side Impact Dummies," 32nd Stapp Car Crash Conference, SAE 881717, 1988.

16. "The Biofidelity Test Results on SID and EUROSID," ISO/TC22/SC12/WG5 Document No. 213, JAMA, 1988.

17. Irwin, A. L., Pricopio, L. A., Mertz, H. J., Balser, J. S. and Chkoreff, W. M., "Comparison of the EUROSID and SID Impact Responses to the Response Corridors of the International Standards Organization," SAE 890604, 1989.

18. Mertz, H. J., "Rating of Measurement Capacity of Side Impact Dummies," ISO/TC22/SC12/WG5 Document No. N281, July 1990.

19. "A Method to Calculate a Single, Weighted Biofidelity Value for a Side Impact Dummy," ISO/T22/SC12/WG5 Document N253, March 1990.

20. "Proposed Weighting Factors for Rating the Impact Response Biofidelity of Various Side Impact Dummies," ISO/TC22/SC12/WG5 Document N278, June 1990.

21. "Ballot Results on Biofidelity Weighting Factors for Side Impact Dummies," ISO/TC22/SC12/WG5 Document N284, August 1990.

22. Resolution No. 1, ISO/TC22/SC12/WG5 Document N298, November 1, 1990.

23. Mertz, H. J. and Irwin A. L., "Biofidelity Ratings of SID, EUROSID and BIOSID," ISO/TC22/SC12/WG5 Document No. N288, October 1990.

24. Neilson, L., Lowne, R., Tarriere, C., Bendjellal, F., Gillet, D., Maltha, J., Cesari, D. and Bouquet, R., "The EUROSID Side Impact Dummy," 10th International Technical Conference on Experimental Safety Vehicles, June 1985.

25. Lowne, R. W., and Neilson J. D., "The Development and Certification of EUROSID," 11th International Technical Conference on Experi-mental Safety Vehicles, May 1987.

26. Janssen, E. G., and Vermissen, A. C., "Biofidelity of the European Side Impact Dummy - EUROSID," 32nd Stapp Car Crash Conference, SAE 881716, October 1988.

27. "The EUROSID-1," Technical Information from the TNO Crash Safety Research Center, Delft, 1995.

28. "EUROSID-1 Developments," ISO/TC22/SC12/WG5 Document N533, November 1997.

29. Beebe, M. S., "What is BIOSID?" SAE 900377, February 1990.

30. Beebe, M. S., "BIOSID Update and Calibration Requirements," SAE 910319, 1991.

33. Kirkish, S. L., et al, "Status of Prove-Out Testing of the SID-IIs Alpha – Prototype," 15th International Technical Conference on Enhanced Safety of Vehicles, No. 96-510-0-15, May 1996.

34. "Road Vehicle - Anthropomorphic Side Impact Dummy - Lateral Impact Response Requirements to Assess the Biofidelity of the Dummy," ISO TR9790, ANSI, New York, NY 1998.

35. Saul, R. A., Backaitis, S. H., Beebe, M. S. and Ore, L. S., "Hybrid III Dummy Instrumentation of Arm Injuries During Air Bag Deployment," SAE 962417, 40th Stapp Car Crash Conference, November 1996.

American Iron and Steel Institute

American Iron and Steel Institute
2000 Town Center, Suite 320
Southfield, Michigan 48075
1-877-STEELINDUSTRY
www.autosteel.org